UNIVERSITY COLLEGE LONDON

Faculty of Mathematics and Physical Sciences

Department of Physics & Astronomy

A Herschel study of AGB stars in the Milky Way

Thesis submitted for the Degree of Doctor of Philosophy at University College London

by

Sílvia Martinavarro Armengol

Supervisors:

Prof. Bruce Swinyard

Prof. Mike Barlow

Examiners:

Dr. Mark Thompson

Dr. Jeremy Yates

July 28, 2015

In loving memory

of Bruce Swinyard

I, Sílvia Martinavarro Armengol, confirm that the work presented in this thesis is my own. Where information has been derived from other sources, I confirm that this has been indicated in the thesis.

Abstract

The Asymptotic Giant Branch (AGB) stars are low to intermediate-mass post-MS stars that undergo thermal pulses characterized by a strong wind-driven mass-loss from its surface into the interstellar medium. They are responsible for the majority of the dust contained within the Galactic plane and thus, their study is crucial to understand the life cycle of dust in our Galaxy. The Hi-GAL Survey constitutes the perfect survey to detect and study AGB stars since it uses the PACS and SPIRE Herschel instruments in parallel mode to map the $|l| < 60°$; $|b| < 1°$ region of the Galactic plane in the 70 μm, 160 μm, 250 μm, 350 μm and 500 μm bands, which trace the emission of the dust in which AGB stars are embedded. In this thesis I use the Hi-GAL 1 maps processed with the ROMAGAL Pipeline to create a total of four catalogues:

The *SMA Hi-GAL 1 Point Source Catalogue* - this is, to date, the most reliable Hi-GAL 1 PSC published. It contains the position and fluxes of all the Hi-GAL 1 compact sources detected by CUTEX in the 70 μm Herschel band and the corresponding counterparts found in the other Herschel bands.

The *SMA Hi-GAL 1 PSC AGB star candidate catalogue* - this is the first catalogue including a list of possible Hi-GAL 1 AGB star candidates. The source classification was done by means of colour cuts that efficiently separate 95 reference Hi-GAL 1 AGB stars from 205 reference YSOs, 178 HII regions and 59 PNe. This is, to date, the largest sample of reference Hi-GAL 1 sources used on colour-colour separation methods. These colour cuts involve the Herschel 70 μm band and prove that this band plays a decisive role in identifying AGB stars and that it is highly effective in distinguishing AGB stars from other stellar types.

The *SMA Hi-GAL 1 PSC C-rich and O-rich AGB star candidate catalogues* - these are the first two catalogues including a list of possible Hi-GAL 1 PSC C-rich and O-rich AGB star candidates and constitute the largest compilation of AGB stars detected within the Hi-GAL 1 Galactic region. The source classification was done by means of colour cuts that successfully separate 101 reference OH/IR-stars from 56 reference C-stars. These colour cuts involve the MSX 8.28 μm band, the AKARI 9 μm and 18 μm bands and the WISE 12 μm and 22 μm bands, which cover the silicate and carbonaceous features of O-rich and C-rich AGB stars, and prove that these bands are highly efficient in distinguishing C-rich from O-rich AGB stars.

The analysis of the stellar properties derived for the Hi-GAL 1 PSC C-rich and O-rich AGB star candidates allowed us to define a series of equations that establish the relation between the stars' mass-loss rates and their colour temperatures, NIR [J]-[K] colour, luminosities and outflow velocities. These equations are of great importance since they enable us to derive the mass-loss rates of unknown AGB stars using only their colour temperatures.

Acknowledgements

Foremost, I would like to express my deepest appreciation to my supervisors, Prof. Bruce Swinyard and Prof. Mike Barlow for their excellent guidance, enthusiasm, caring, support and patience. It has been a tremendous honour to work with you. I feel extremely lucky for having been able to learn from such knowledgeable researchers with such charismatic personalities. I simply cannot imagine having had better supervisors.

I would also like to thank Dr. Sergio Molinari, Dr. Michele Pestalozzi, Dr. Eugenio Schisano and Dr. Stefano Pezzuto for providing me with the Hi-GAL 1 maps, the *CUTEX* code and the flux correction factors used in this thesis and most of all, for making my trips to Rome an unforgettable experience.

Special thanks to Dr. George Bendo for providing me with the *Timeline Source Fitter* used in this thesis and for sharing his love for walks with me.

My sincere thanks also goes to Dr. Tanya Lim and Dr. Ismael Pérez who, four years ago, gave me the incredible opportunity to come to Oxford to work on what I like the most.

I am also in debt to Dr. Chris Pearson, Dr. Ed Polehampton, Dr. Mireya Etxaluze and Dr. Sarah Leeks for the help and the excellent atmosphere they provided me with during my previous internship at the Rutherford Appleton Laboratory - the institution whose financial support, together with that of UCL, has made this research possible.

Many thanks to Dr. Mikako Matsuura for the many insightful comments and invaluable suggestions she has given to me throughout these years. Thanks also to my examiners, Dr. Jeremy Yates and Dr. Mark Thompson, for their very helpful comments, which this thesis has greatly benefited from.

I would also like to express my gratitude to Prof. Glenn White who turned my childhood dream of observing in Hawaii and seeing lava into a reality.

I now proceed to thank the long list of fantastic people that have blessed me with their friendship. First of all, I would like to thank Anna and Griselda for always making sure that our friendship does not weaken despite the years and the distance.
A special thanks to Harps, Steph and Nic for being my family abroad. Being able to share my days with you has been an immense gift.
A distant thanks also goes to all those good friends (Roger, Cris, Cam, Japh, Tomek, Foteini and the lovely Paul and Angela) that left UCL, and also to those friends that I left behind in Oxford (Aina, Blanca, Montse and Alberto), in Tenerife (Ana, Andrés, Carol, Juanma, María, Txell and Rubén) and in Barcelona (Car and Javi). Not a day goes by without me missing you.
I should also thank my flatmates and my current, former and next-door office mates who have put up with my rambling, singing, popcorn craves, mood changes and shouts of despair. A general thank you also for all the people in the department who make this research group so uniquely friendly and quirky.

Last but not least, I would like to thank the people whose unconditional love and support has sustained me and kept me strong at all times. Many thanks to my mum and dad, Pilar and Carlos, for the many sacrifices you have done for me throughout the years, for believing in me and in the choices I do and for always encouraging me to pursue my goals. Special thanks to my two amazing brothers, Edgar and Àlex, for the many enjoyable times we have lived together and the many more that are to come. Thanks also to Anabel and Alba, for making my brothers so happy and for being such a wonderful company.
Finally, I want to thank Luke, whose love has brought me the greatest happiness I have ever experienced. Words cannot express how I much I love you and how grateful I am for every laugh and hug you have given me, for every tear you have dried and for every time you have stopped me from falling. *Us estimo moltíssim!*

Coelorum Perrupit Claustra.
(He broke through the confines of the heavens.)

Latin inscription in William Herschel's
tomb Epitaph in Upton Church, Slough.

Contents

List of Figures

List of Tables

Chapter 1

Introduction: The universe according to Herschel

"It really was a beautiful spacecraft."

Micha Schmidt

1.1 William Herschel and the discovery of Infrared

The existence of non-visible radiation was first discovered in 1800 by the astronomer Sir William Herschel while he was investigating the heating effect of different colours of light. In his experiment, Herschel directed sunlight through a glass prism to create a spectrum and measured the temperature of each colour with three different thermometers: one placed in one of the spectrum colours and the other two placed beyond the spectrum, to be used as control samples (see Fig. 1.1). Having finished his measurements, he realised that the temperature of the colours increased as he went from the blue end to the red end of the spectrum.

Figure 1.1: Portrait of Sir William Herschel.

After noticing this pattern, Herschel decided, in a moment of inspiration, to place a fourth thermometer just beyond the red portion of the spectrum in a region apparently devoid of sunlight. The results were astonishing: the temperature of the fourth thermometer was not only higher than that of the control samples but also higher than that measured in the red spectrum colour. In light of this discovery, Herschel concluded that beyond the red, there was a form of radiation which was invisible to the human eye. Although Herschel originally called this type of radiation *calorific rays*, its name was later changed to be *Infrared* (i.e. below red).

Table 1.1: Properties of the NIR, MIR and FIR spectral regions.

Spectral range	**Acronym**	**Wavelength (μm)**	**Temperature (K)**	**Observable objects and features**
Near-Infrared	NIR	0.7-5	700-5000	cold stars dust is transparent
Mid-Infrared	MIR	5-30	100-700	very cold stars planets asteroids warm dust and gas
Far-Infrared	FIR	30-300	10-100	extremely cold stars cold dust and gas

1.2 The Near-, Mid- and Far-Infrared

Nowadays, the infrared (IR) is defined as the region of the spectrum expanding from $\lambda = 0.7$ μm to $\lambda = 300$ μm, which, in astronomy, is commonly divided into three different spectral regions termed: Near–Infrared (NIR), Mid–Infrared (MIR) and Far–Infrared (FIR). Listed in Table 1.1 are the wavelength and temperature ranges covered by each of these spectral regions along with a brief description of some of the objects and features visible at these wavelengths.

Figure 1.2: View of the Horsehead Nebula in the (a) visible, (b) NIR and (c) MIR.

(a) (b) (c)

The set of images in Fig. 1.2 demonstrate how observations taken in (a) visible, (b) NIR and (c) MIR light reveal dramatically different and complementary views of an object. Shown in these images are: the star Alnitak (top right), the blue reflection nebula NGC 2023 (centre), the Barnard 33 dark cloud commonly known as the Horsehead Nebula (bottom left) and the IC 434 emission nebula (bottom right).

From these images we can see that: (i) at visible wavelengths dust is opaque (see Fig. 1.2a), (ii) at NIR wavelengths dust is transparent (see Fig. 1.2b) while (iii) at MIR (FIR and sub–mm) wavelengths dust is very bright (see Fig. 1.2c). As a result: (i) at optical wavelengths, sources embedded or behind clouds of dust are not visible or heavily obscured (see Fig. 1.2a), (ii) at NIR wavelengths, these sources are clearly visible (see Fig. 1.2b), while (iii) at longer wavelengths (MIR and FIR), only a few sources are visible (see Fig. 1.2c). The observational differences between visible and NIR, MIR and FIR images are a direct consequence of the two processes starlight undergoes when it hits the dust grains: *scattering* and *absorption*. The combination of these two processes is known as *extinction*.

Dust scattering causes the starlight to be redirected out of the original direction of the starlight propagation. Scattering is a function of λ^{-4} and so, the level of scattering of the starlight will be higher for shorter wavelengths and much lower for longer wavelengths (see Draine 2011). Moreover, the higher the dust density along the line of sight between the observer and a source, the more scattering the starlight will suffer and the dimmer and redder the source will appear to be. This effect is known as *reddening* and it increases with distance. Dust absorption, on the other hand, causes the removal of part of the starlight, which is transferred into another form of energy. Dust absorption can be a function of λ^{-1} or λ^{-2} (depending on the absorbent properties) and so, the level of absorption of the starlight will be higher for shorter wavelengths and much lower for higher wavelengths. The dependence between the level of absorption and the starlight wavelength accounts for the differences observed in the images shown in Fig. 1.2. In the case of the optical observations, dust appears opaque and optical starlight is not observable because the dust grains absorb the optical starlight coming from the sources within or behind the dust cloud. In the case of the NIR observations, dust appears transparent and the embedded sources are visible because the dust grains hardly absorb the NIR starlight and therefore, the light goes through the grains. Finally, in the case of MIR and FIR observations, dust appears bright because the optical starlight that was absorbed by the dust is re-emitted in the MIR and FIR. At these wavelengths, the dust emission is often so strong that it outshines the emission from the embedded sources. As a result, in the MIR and FIR, only those sources with temperatures lower or similar to that of the dust will come into view.

1.3 IR observations from ground and space-based telescopes

Images like those shown in Fig. 1.2b and 1.2c can be taken with both ground and space IR telescopes. For ground telescopes, however, this is only possible for a few narrow IR wavelength ranges, termed *IR atmospheric windows*, for which the Earth's atmosphere is transparent enough not to block or outshine the IR light coming from stellar objects. These atmospheric windows are centred in the NIR 1.25 μm (J), 1.6 μm (H), 2.2 μm (K) and 3.6 μm (L) bands, in the MIR 5.0 μm (M), 10.2 μm (N) and 21 μm (Q) bands and in the FIR 350 μm and 450 μm bands. In Table 1.2 we provide a brief description of the IR space and ground–based observatories most relevant for this work including details of their duration, spacecraft payload, on board instruments and scientific goals.

Table 1.2: List of the IR space and ground–based observatories most relevant for this work.

Name	Image	Duration	Spacecraft Payload / Instruments	Scientific goals
IRAS		Jan. 1983 – Nov. 1983	(i) a 60-cm Ritchey–Chrétien telescope (ii) a cryogenic liquid helium system (10 K) (iii) three instruments: Survey Array Low–Resolution Spectrometer Chopped Photometric Channel	To map the whole sky (96%) in four bands (*I1,I2,I3,I4*) centred at: 12 μm, 25 μm, 60 μm and 100 μm.
WISE	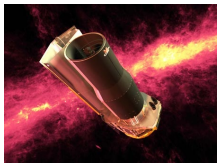	Dec. 2009 – Oct. 2010	(i) a 40-cm Ritchey–Chrétien telescope (ii) scan mirrors (iii) beam splitters (iv) a two–stage solid–hydrogen cryostat (8 K–32 K)	To map the whole sky (99%) in four bands (*W1,W2,W3,W4*) centred at: 3.4 μm, 4.6 μm, 12 μm and 22 μm.
MSX		Apr. 1996 – Apr. 1998	(i) the 35-cm SPIRIT III infrared telescope (ii) a solid-hydrogen cryostat (250 K) (iii) three instruments: UVISI (UV and Visible and Spectrographic imagers) SBV (Space-Based Visible instrument) OSDP (On-board Signal and Data Processor)	To map the Galactic plane in four bands (*B1,B2,A,C,D,E*) centred at: 4.29 μm, 4.35 μm, 8.28 μm, 12.13 μm, 14.65 μm and 21.3 μm.
Spitzer		Aug. 2003 – May 2009	(i) a 85-cm Ritchey–Chrétien telescope (ii) a superfluid liquid helium cryostat (1.4 K) (iii) three instruments: IRAC Infrared Array Camera IRS Infrared Spectrograph MIPS Multiband Imaging Photometer	To conduct a survey (GLIMPSE) of the inner part of the Milky Way ($-65^\circ < b < 65^\circ$, $2^\circ < l < 4^\circ$) in the four IRAC bands (*G1,G2,G3,G4*) centred at: 3.6 μm, 4.5 μm, 5.8 μm and 8.0 μm. Spitzer also conducted the MIPSGAL Survey.
AKARI	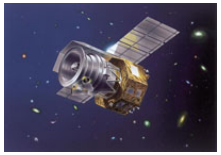	Feb. 2006 – Aug. 2007	(i) a 68.5 cm Ritchey–Chrétien telescope (ii) superfluid liquid helium cryostat (6 K) (iii) two instruments: IRC Infrared Camera FIS Far–Infrared Surveyor	To map the whole sky (94%) in the 2 IRC bands (*A1,A2*) centred at: 9 μm and 18 μm and the 4 FIS bands (*A3,A4,A5,A6*) centred at: 65 μm, 90 μm, 140 μm and 160 μm.
2MASS		Jun. 1997 – Feb. 2001	Two 1.3-m equatorially mounted Cassegrain reflector ground telescopes located at Mount Hopkins, Arizona and Cerro Tololo, Chile	To map the entire sky (95%) in three bands (*J,H,K*) centred at: 1.25 μm, 1.65 μm and 2.17 μm.

1.4 The Herschel Space Observatory

Launched in 14 May, 2009, the *Herschel* [1] *Space Observatory* (Pilbratt et al. 2010) is the latest and largest IR space–based telescope ever launched into space.

1.4.1 Launch and orbit

Herschel was launched together with *Planck*[2] (Tauber et al. 2010) on board of an Ariane 5 ECA launcher from the *Guiana Space Centre* in Kouru (see Fig. 1.3).
After a roughly 50–day journey from Earth, Herschel entered its operational orbit: a large Lissajous orbit around the second Lagrange point of the Sun–Earth system (L2), with a period of about 178 days, an average amplitude of about 700,000 km and a position of 1.5 million km away from the Earth (see Fig. 1.4).

1.4.2 Spacecraft

The Herschel spacecraft consisted of five main parts (see Fig. 1.5):

- Telescope

  The Herschel telescope was a Cassegrain design with a 3.5 m diameter primary mirror that was made from twelve silicon carbide sections which were joined, polished and coated with aluminium. The Herschel telescope is, to date, the largest single mirror ever built for use in space: more than four times larger than any previous IR space telescope, (almost one and a half times larger than the *Hubble Space Telescope*), and the most sensitive: it is able to collect almost 20 times as much radiation as any previous IR space–based telescope.

- Sunshield

  The sunshield protected the telescope from solar radiation and Earth straylight and also supplied the spacecraft with electric power from the solar cells.

- Service module

  The service module housed the instrument electronics and the components responsible for satellite function, such as the communication hardware.

[1] Named after Sir William Herschel.
[2] A microwave observatory which is studying the Cosmic Microwave Background and is named after Max Planck.

- Three instruments

  > SPIRE

  The *Spectral and Photometric Imaging REceiver* (SPIRE, Griffin et al. 2010) comprised: (i) a 3–band imaging photometer operating at 250 μm, 350 μm and 500 μm[3], constituted of 288 pixels, with a field of view of 4 x 8 arcmin and a resolution of 20-30 arcsec and (ii) an imaging Fourier Transform Spectrometer simultaneously covering its whole operating range of 194 μm - 671 μm, constituted of 56 pixels, with a field of view of 2.6 x 2.6 arcmin and a resolution of 20-50 arcsec.

  > PACS

  The *Photoconductor Array Camera and Spectrometer* (PACS, Poglitsch et al. 2010) comprised: (i) a 2–band imaging photometer operating at 70 μm or 100 μm and 160 μm[4], constituted of 2,560 pixels, with a field of view of 1.75 x 3.5 arcmin and a resolution of 5 arcsec and (ii) an Integral–field Spectrometer covering the 51 μm to 220 μm range, constituted of 400 pixels and bolometer arrays operating at 300 mK and with a field of view of 50 x 50 arcsec and a resolution of 10 arcsec.

  > HIFI

  The *Heterodyne Instrument for the Far Infrared* (HIFI, de Graauw et al. 2010) was a very high resolution heterodyne spectrometer covering the frequency range of 490 GHz–1,250 GHz and 1,410 GHz–1,910 GHz.

- Cryostat

  The instruments were mounted in a common optical bench contained within the Herschel cryostat: a sophisticated vacuum flask filled at launch with more than 2,300 litres of superfluid helium, which cooled and kept the instruments at very low and stable temperatures ($\sim$1.6 K) to ensure the instruments' high sensitivity. The cryostat's helium evaporated at a constant rate (about 200 grams per day) and the tank gradually emptied over the following $\sim$4 years up until its complete evaporation on 29 April, 2013 - the end of Herschel's mission.

[3]The 250 μm, 350 μm and 500 μm bands are often referred to as *Photometer Short*, *Medium* and *Long Wavelength* bands (*PSW*, *PMW*, *PLW*), respectively.

[4]In this work, we use PACS 70 μm and 160 μm bands, which are often referred to as *blue* and *red* bands, respectively.

Figure 1.3: Herschel and Planck's shared launch on board of an Ariane 5 ECA.

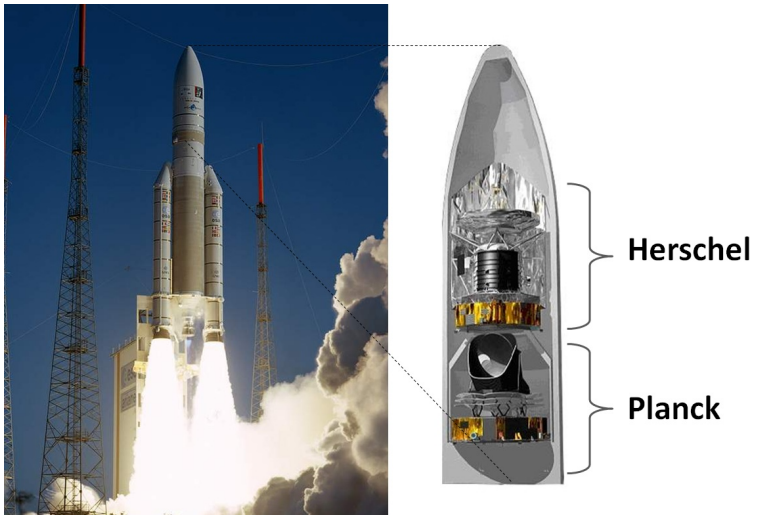

Figure 1.4: Herschel's orbit.

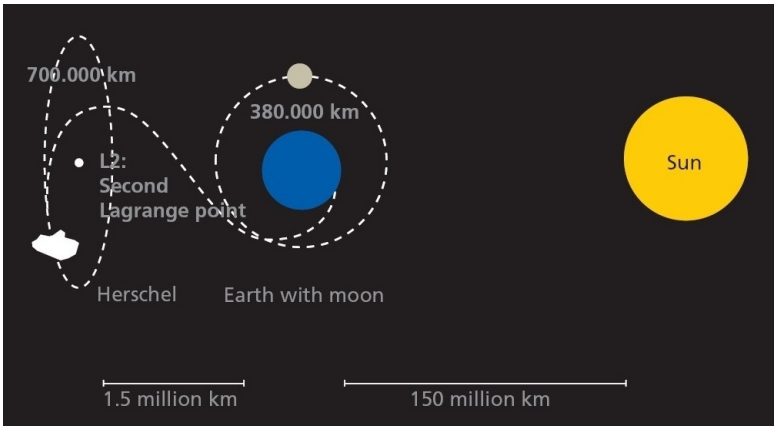

Figure 1.5: Herschel's spacecraft components.

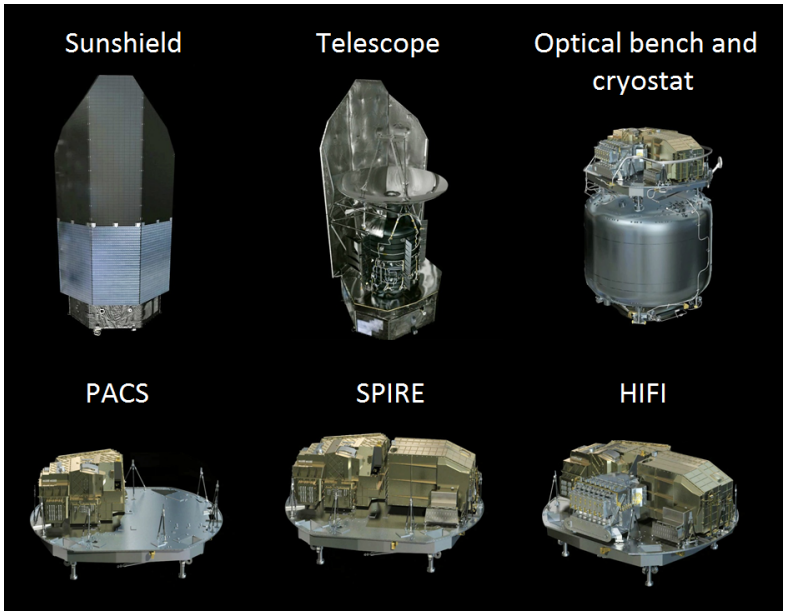

Figure 1.6: Herschel's Parallel Mode scanning strategy.

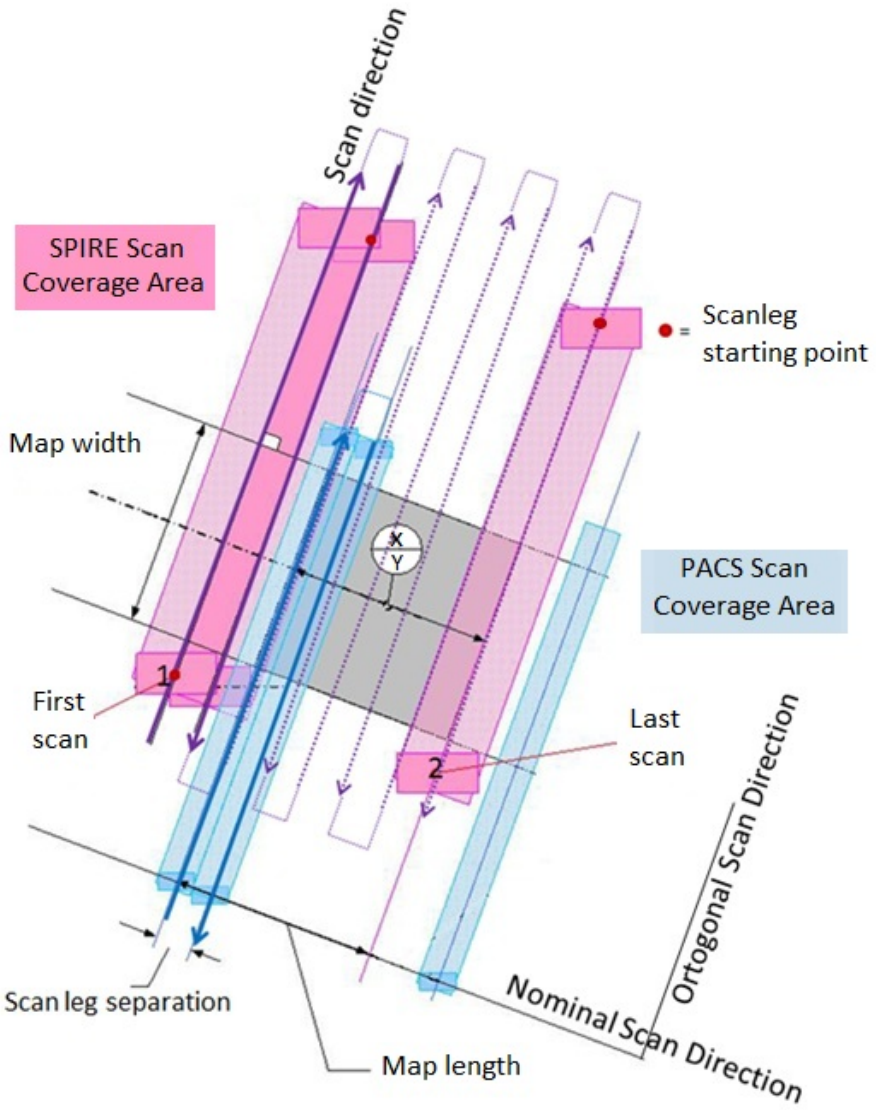

1.4.3 Parallel Scanning Mode

Although PACS, SPIRE and HIFI operated independently, Herschel offered the possibility of using PACS and SPIRE together in a scanning mode called *Parallel Scanning Mode*. In this configuration, PACS and SPIRE photometric cameras were operating simultaneously, carrying out observations, in the 70 μm and 160 μm PACS bands and the 250 μm, 350 μm and 500 μm SPIRE bands, covering very large areas of sky. Shown in Fig. 1.6 is a detailed illustration of the spacecraft scanning scheme when operating in Parallel Mode.

During an observation, the spacecraft slewed from position 1 to 2, at a constant speed of 60 *arcsec/sec* (*fast mode*) or 20 *arcsec/sec* (*nominal mode*), along lines (*scanlegs*) parallel to the *Nominal scan direction*, i.e. $\theta = +42.4°$ [5]. It then performed a turn manoeuvre and continued observing along scanlegs parallel to the *Orthogonal scan direction*, i.e. at $\theta = -42.4°$. The image in Fig. 1.6 shows the different paths followed by PACS (in blue) and SPIRE (in pink) during the first and last scan along the Orthogonal scan direction. The different positions of PACS and SPIRE in the Herschel optical bench resulted in the two instruments pointing at different places on the sky, which were separated by 21 arcminutes.

The complete PACS and SPIRE Parallel Mode scanning footprint is shown in Fig. 1.7. Here, the SPIRE and PACS scanlegs are indicated in pink and green respectively while the common region surveyed by both instruments is indicated in yellow.

Figure 1.7: Complete PACS and SPIRE Parallel Mode scanning footprint.

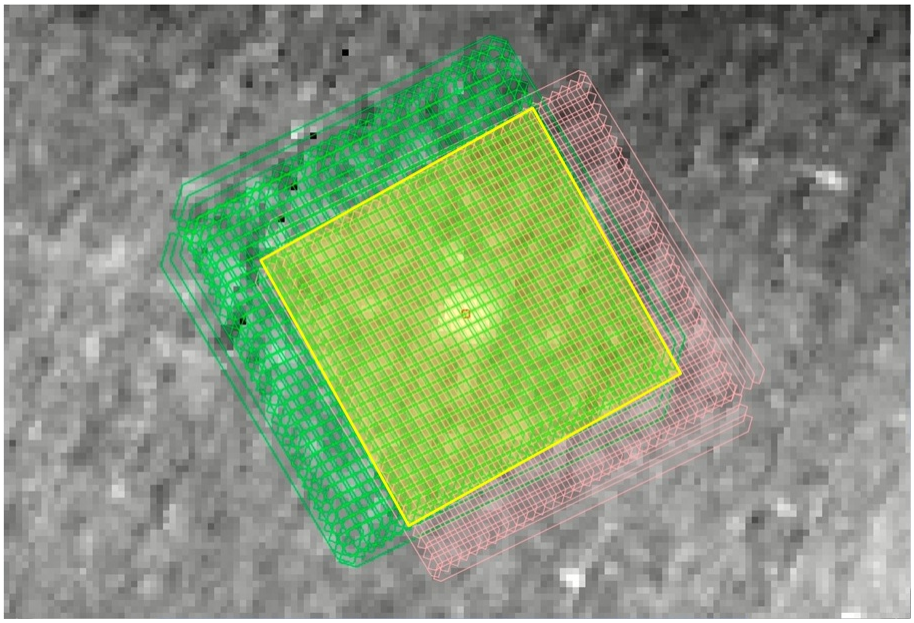

Although Parallel Mode observations were made without significant degradation in the individual instruments' performance, the speed of scan in the fast mode was sufficiently high that some telescope movement occurred before the detector's readout was complete, giving rise to a small degree of Point Spread Function (PSF)[6] smearing in the scan direction (see Sect. 3.2 and Sect. 4.3.2.1).

[5] These angles are measured with respect to the short axis of the SPIRE photometer arrays (see SPIRE PACS Parallel Mode Observers' Manual).

[6] The PSF can be defined as the response of the measuring instrument to a compact source.

1.4.4 Herschel Data Products

The data collected by PACS and SPIRE during an observation were processed by the instruments' processing software, which generated the so-called *Herschel Data Products* (HDP) and the *Meta Data*.
The HDP were grouped in four different product classes:

- *Auxiliary Products*
  Herschel non-science spacecraft data required directly or indirectly in the processing and analysis of the scientific data.
- *Quality Control Products*
  Summary of the information required to evaluate the technical quality of the observations and the products generated.
- *Calibration Products*
  Group of parameters that characterise the behaviour of the satellite and the instruments.
- *Observation Products*
  Scientific data resulting from a Herschel observation.

The Observation Products are the products of most interest for observers. They are classified depending on the level of the processing of the data they contain. We distinguish between:

- *Level 0*
  Raw telemetry data as measured by the instruments.
- *Level 1*
  Detector readouts that are calibrated and converted to physical units.
- *Level 2*
  Level 1 data further processed from which scientific analysis can be performed and maps can be generated.

The Meta Data provides us with information about the observations' start and end date and about the instrument/s used in the observation.

1.4.4.1 HIPE

The HDP and the Meta Data generated during an observation are stored in what is called the *Observation Context*, which can be defined as an inventory or catalogue of the products generated in an observation.

The Observation Context of an observation can be accessed through the main interface to the Herschel data processing software: *Herschel Interactive Processing Environment* (HIPE), a program that provides the tools to interactively reduce from raw data to publishable products and visualise and manipulate data in order to perform science analysis. Shown in Fig. 1.8 is the HIPE Observation Context panel from which users have access to the Meta Data, the Auxiliary, the Calibration and the Quality Control products of an observation. Also accessible are the level 0, 0.5[7], 1 and 2 Observation Products, which are stored in a total of 12 units labelled from 0 to 11 and called *Photometer Scan Products* (PSP).

Each PSP contains 5 individual XY–table datasets, termed *Timeline dataset* (TD), in which the X–values correspond to the Sample Time (in sec) and the Y–values correspond to either:

- *Signal TD*

  The signal from every PSW, PMW and PLW photometer array bolometer, including both detector (in Jy/beam) and non detector (e.g. thermistor, resistor; in V) channels.

- *Mask TD*

  The mask value corresponding to which processing flags have been raised for every PSW, PMW and PLW photometer array bolometer (including both detector and non detector channels).

- *RA/dec TD*

  The RA/dec on the sky (in degrees) for each PSW, PMW and PLW photometer array bolometer (excluding non detector channels).

- *Temperature TD*

  The temperature (in K) for each thermistor channel.

[7] The level 0.5 Observation Products are data with a level of processing somewhere between level 0 and level 1. In this work, we only considered the level 0,1 and 2 Observation Products.

Figure 1.8: Observation Context of a Herschel Parallel Mode observation as seen through HIPE - the main interface to the Herschel data processing software.

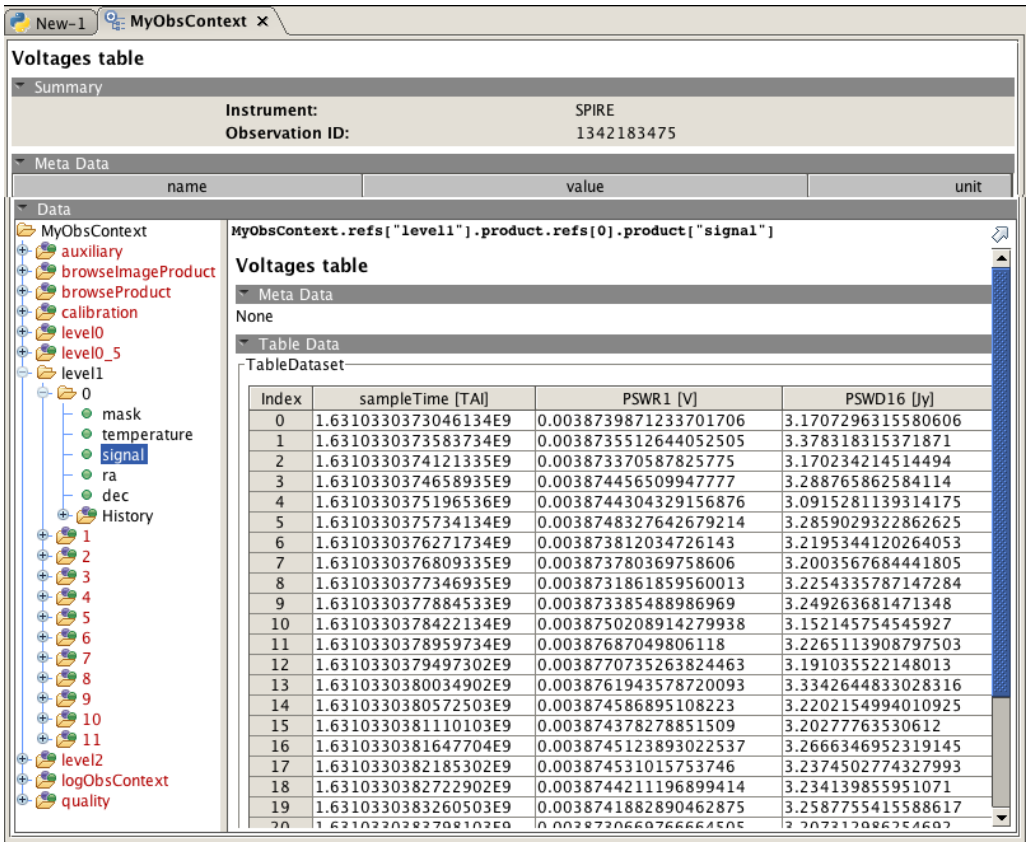

Index	sampleTime [TAI]	PSWR1 [V]	PSWD16 [Jy]
0	1.6310330373046134E9	0.00387398712337017 06	3.17072963155806 06
1	1.6310330373583734E9	0.0038735512644052505	3.378318315371871
2	1.6310330374121335E9	0.0038733705878257 75	3.170234214514494
3	1.6310330374658935E9	0.0038744565099477 77	3.288765862584114
4	1.6310330375196536E9	0.0038744304329156876	3.09152811393141 75
5	1.6310330375734134E9	0.0038748327642679214	3.2859029322862625
6	1.6310330376271734E9	0.0038738120347261 43	3.2195344120264053
7	1.6310330376809335E9	0.0038737803697586 06	3.2003567684441805
8	1.6310330377346935E9	0.0038731861859560013	3.2254335787147284
9	1.6310330377884533E9	0.0038733854889869 69	3.249263681471348
10	1.6310330378422134E9	0.0038750208914279938	3.152145754545927
11	1.6310330378959734E9	0.0038768704980611 8	3.2265113908797503
12	1.6310330379497302E9	0.0038770735263824463	3.191035522148013
13	1.6310330380034902E9	0.0038761943578720093	3.33426448330283 16
14	1.6310330380572503E9	0.0038745868951082 23	3.22021549940109 25
15	1.6310330381110103E9	0.0038743782788515 09	3.202777635306 12
16	1.6310330381647704E9	0.0038745123893022537	3.2666346952319145
17	1.6310330382185302E9	0.0038745310157537 46	3.2374502774327993
18	1.6310330382722902E9	0.0038744211196899414	3.234139855951071
19	1.6310330383260503E9	0.0038741882890462875	3.2587755415588617
20	1.6310330383798103E9	0.0038730669766664505	3.2073129862546 92

1.5 The Herschel Infared Galactic Plane Survey

1.5.1 Project description

The *Herschel Infared Galactic Plane Survey* (Hi–GAL, Molinari et al. 2010a) was a Herschel Open Time Key–Project, which used Herschel's PACS and SPIRE instruments, working in Parallel Scanning Mode configuration, to map the $0° \leq |l| < 360°$; $|b| \leq 2°$ region, centred on the warped Galactic Plane, in the 70 μm, 160 μm, 250 μm, 350 μm and 500 μm Herschel bands.

1.5.2 Galactic coverage

Hi-GAL surveyed the complete Galactic plane in three stages:

- Hi–GAL 1

  In a first stage, Hi–GAL covered, in 63 fields of 2° x 2° square degrees, the Galactic regions centred at $|b| \leq 1°$ on the warped Galactic Plane and expanding from $l = 0°$ to $l = 66°$ and from $l = 290°$ to $l = 358°$. The Hi-GAL 1 Survey is also referred to as *Hi-GAL KP* Survey.

- Hi–GAL 2

  In a second stage, Hi–GAL covered, in 56 fields of 2° x 2° square degrees, the Galactic regions centred at $|b| \leq 2°$ (following the Galactic warp) and expanding from $l = 127°$ to $l = 233°$. The Hi-GAL 2 Survey is also referred to as *Hi-GAL OT1* Survey.

- Hi–GAL 3

  In a third and final stage, Hi–GAL covered, in 51 fields of 2° x 2° square degrees, the Galactic regions centred at $|b| \leq 2°$ (following the Galactic warp) and expanding from $l = 68°$ to $l = 125°$ and from $l = 235°$ to $l = 288°$. The Hi-GAL 3 Survey is also referred to as *Hi-GAL 2π* Survey and the group of Hi-GAL 2 and Hi-GAL-3 surveys is also known as the *Hi-GAL 360* Survey.

Shown in Fig.1.9 is a face–on and an edge–on image of the Milky Way in which we have indicated the Galactic coverage of the Hi–GAL 1, Hi–GAL 2 and Hi–GAL 3 surveys.

Figure 1.9: Galactic coverage of the Hi–GAL 1 (in purple), Hi–GAL 2 (in yellow) and Hi–GAL 3 (in red) surveys.

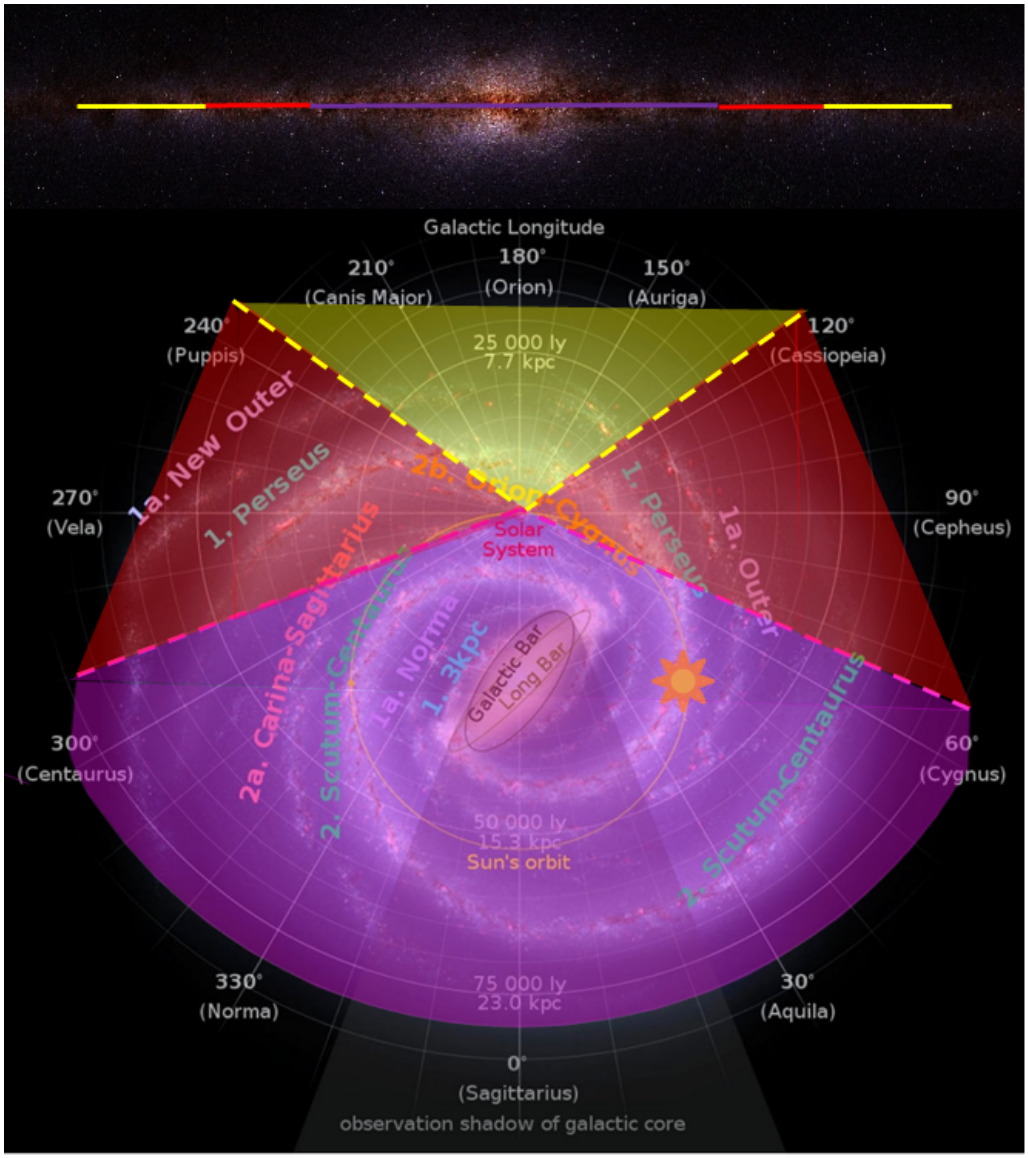

1.5.3 Scientific goals

The main scientific goals of Hi-GAL were: (i) to detect the earliest phases of the formation of molecular clouds and high-mass stars and (ii) to deliver an homogeneous census of the different Galactic dusty environments. These include: the *interstellar medium*, the *interstellar clouds* and the *interstellar filaments* as well as *HII regions*, *Young Stellar objects*, *Asymptotic Giant Branch stars* and *Planetary Nebula*.

1.5.4 Galactic environments observed with Hi-GAL

1.5.4.1 The insterstellar medium

The interstellar medium (ISM) is defined as the matter that occupies the space between the stars of our Galaxy. The main constituents of the ISM are: gas (99% in mass), dust (1% in mass), cosmic ray particles and magnetic and radiation fields (Whittet 2003).
The ISM gas is composed of helium (25%) and hydrogen (75%) (Carroll and Ostlie 1996), which may be in one of the four following phases: *Cold molecular*, *Cool atomic*, *Warm* and *Hot ionized*. Each of these phases is characterised by different temperature and density ranges, which are listed in Table 1.3.
The ISM dust is composed of grains belonging to one of the following grain populations: *Polycyclic Aromatic Hydro-compounds (PAHs)*, *Very Small Grains (VSG)* and *Big Grains (BG)*. Each of these grain populations is characterised by different grain sizes, which are listed in Table 1.3. The difference on the grain sizes of these three populations results on differences on the wavelength of the emission re-emitted by the PAHs, VSG and BG grains (Desert et al. 1990). Listed in Table 1.3 and shown in Fig. 1.10 are the wavelengths for which such emission is maximum. Here, we can see that the PACS and SPIRE wavelengths are ideal for the detection of dusty Galactic structures containing VSG and BG since the instruments' spectral bands sample the peak of the VSG and BG emission.
The ISM gas and dust are acted upon by the ISM cosmic rays, electromagnetic radiation and magnetic fields as well as by gravity and shock waves (Whittet 1992), which shape them into the vast range of dusty Galactic environments presented in the following sections.

Table 1.3: Main constituents of the ISM.

Gas (99% in mass)			
Component	**Phase**	**T (K)**	**n (m^{-3})**
Cold molecular	H_2	∼15	$> 1 \times 10^8$
Cool atomic	H I	∼80	$> 3 \times 10^7$
Warm	H I, H II	∼8000	$> 3 \times 10^5$
Hot ionized	H II	$\sim 5 \times 10^5$	$> 5 \times 10^3$

Dust (1% in mass)		
Component	**Radius**	**Emission lines**
PAHs	0.5 nm	3.3 μm, 6.2 μm 7.7 μm, 8.6 μm 11.3 μm
VSG	10 nm	60 μm
BG	100 nm	100 μm

Cosmic ray particles and magnetic and radiation fields

Figure 1.10: IR emission spectrum of the three ISM dust grain populations

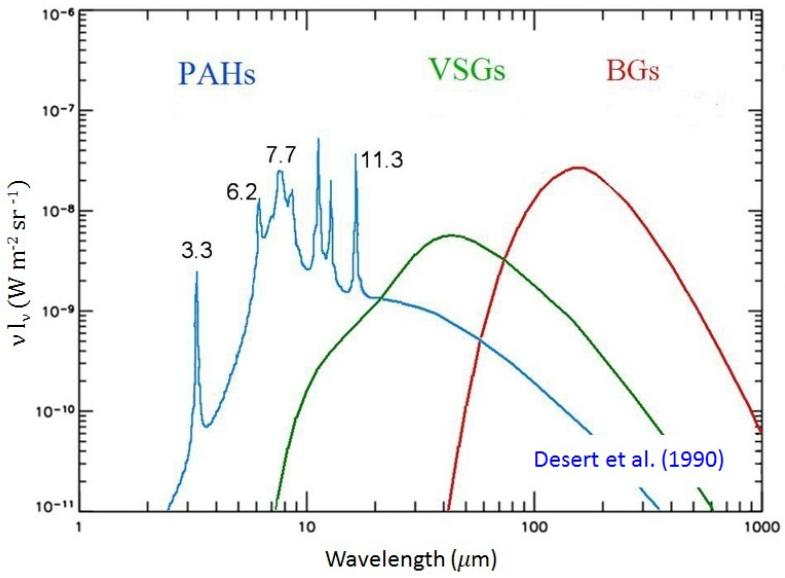

1.5.4.2 Interstellar clouds

These are regions of higher density within the ISM where dust and gas have accumulated. The hydrogen contained in these clouds can be found in any of the phases listed in Table 1.3. Depending on which phase is more abundant in the clouds, we distinguish between *diffuse* and *dense clouds*. Those clouds in which the hydrogen is mostly in atomic phase (molecular phase) are referred to as *diffuse clouds* (*dense clouds*). H I regions and molecular clouds (MC) are examples of diffuse and dense clouds, respectively. While diffuse clouds typically have densities, sizes and masses of $n \sim 10^8\ m^{-3}$, $\varnothing \sim 5\ pc$ and $m \sim 10\ M_\odot$ respectively, dense clouds have densities of $n{>}10^8\ m^{-3}$ and their size and mass can range from $m = 10^6\ M_\odot$ and $\varnothing = 100$ pc (*Giant MC*) to $m{<}10\ M_\odot$ and $\varnothing{<}1\ pc$ (*Small MC*) (Tielens 2005). Giant MC contain most of the ISM material and are dominant sites of star-formation. The large quantities of dust present in these clouds make them be highly opaque at optical wavelengths but extremely bright at FIR wavelengths, to the extent that their FIR and sub–mm emission often exceeds that of the stars embedded within. Thanks to the Herschel wavelength coverage, it was possible to compile a definitive inventory of MC, which allowed the study of their physical properties, their origin and evolution as well as their star-formation activity. Hi-GAL also allowed, for the first time in the FIR, the detection of Infrared Dark Clouds (IRDCs) and the study of their Galactic distribution. IRDC are structures exhibiting similar properties to MC, (n$>10^5\ cm^{-3}$, $\varnothing{\sim}$5 pc and m$\sim 10^3\ M_\odot$; Egan et al. 1998), and are believed to be the precursors of cluster-forming molecular clumps.

1.5.4.3 Interstellar filaments

Galactic MC contain complex networks of tangled gaseous elongated filaments termed *interstellar filaments*. Although the presence of some filaments was already detected with AKARI (Doi et al. 2012, Doi et al. 2015), Hi-GAL's observations have revealed that these filaments are nearly everywhere in the Galactic ISM. The Hi-GAL maps show an interconnected maze of overlapping filaments with a wide range of lengths, densities and brightness levels yet similar widths (Molinari et al. 2010a). Thanks to Herschel's higher resolution and increased sensitivity, it has been possible, for the first time, to determine precisely the filaments' structure and physical properties and to study the filaments' formation mechanisms as well as their connection with star-formation.

In a recent publication, Schisano et al. (2014) used the Hi-GAL observations to carry out a study of ∼500 filaments that were detected, with their filament identification algorithm, in four Hi-GAL maps located within the $l = [216.5°, 225.5°]$ Galactic range. The results from Schisano et al. (2014) established the filaments' length and width to be within $[0.5, 30]$ pc and $[0.1, 3]$ pc, respectively. On the other hand, the average column densities of the filaments were found to be between 10^{20} cm^{-2} and 10^{22} cm^{-2}.

In order to establish the amount of filaments with associated star-formation, Schisano et al. (2014) cross-correlated the filaments' positions with the position of the clumps that Elia et al. (2013) found in the same Galactic region with the NANTEN telescope.

The results showed that despite the majority of the clumps (74%) identified by Elia et al. (2013) were found to be located within the borders of Schisano et al. (2014) filament sample, some of the clumps were located outside the filaments. This result implies that although interstellar filaments seem to be the preferred sites for stellar birth, star formation does not occur exclusively in the filaments.

Moreover, Schisano et al. (2014) found that the clumps outside the filaments had lower surface densities than the clumps inside the filaments. For all the inner clumps, the surface densities were found to be above the value necessary for high-mass star formation (Krumholz and McKee 2008, Butler and Tan 2012). On the other hand, for the majority of the outer clumps, the surface densities were found to be below such value and thus, these clumps are expected to fragment into clusters of low-mass stars. This result suggests that the formation of massive stars might occur only within these filaments where there is a greater amount of raw material available.

The previous findings agree with those found by Polychroni et al. (2013) in the L1641 molecular clouds in the Orion A complex. In this paper, the authors found a difference between the mass distribution of the pre-stellar sources located inside and outside the identified filaments. Whereas the mass distribution of the sources on the filaments was found to peak at 4 $M_{\odot}$, that of the sources off the filaments was found to peak at 0.8 $M_{\odot}$. The results from Schisano et al. (2014) also showed that a considerable amount of filaments did not host any clumps. The existence of filaments with no signs of on-going star formation was already detected in the Polaris Flare by André et al. (2010), who established that interstellar filaments precede the onset of star formation.

Finally, Schisano et al. (2014) found that while the filaments without clumps had a mass per unit length (M_{line}) lower or equal to 16 $M_{\odot}/pc$, the filaments with clumps had M_{line} = $[1, 100]$ $M_{\odot}/pc$. Moreover, Schisano et al. (2014) found higher values of M_{line} in filament branches with pre-stellar clumps than in filament branches with proto-stellar clumps. This suggests that the filaments' M_{line} increases during the evolution of pre-stellar clumps into proto-stellar clumps through contraction and/or accretion. The further analysis of Herschel's images will allow us to continue studying the properties of interstellar filaments, which are key to understand the mechanism of filaments' formation.

1.5.4.4 HII regions

An HII region is defined as a region within a MC in which the molecular hydrogen from the cloud has been ionised by the radiation emitted from a young hot star (e.g. an O or B star) located within the cloud. HII regions can be classified depending on their evolutionary phase into Hypercompact HII (HCHII) regions, Ultracompact HII (UCHII) regions, Compact HII regions and Evolved HII regions. As they age, HII regions expand due to the pressure difference between the ionized gas and the surrounding neutral medium (Dyson and Williams 1997). As a result, the linear diameter (ϕ) of HII regions increases as they age whereas the electron density (n_e) decreases (Kurtz 2005). Typical values of n_e and ϕ are: (i) n_e>10^6 cm^{-3} and ϕ<0.05 pc for HCHII, (ii) $n_e \sim 10^3$–10^4 cm^{-3} and ϕ<0.1–0.5 pc for UCHII and Compact HII regions and (iii) $ne \sim 10^2$ cm^{-3} and a ϕ of several parsecs for Evolved HII regions. While in young HII regions, like HCHII, the star within is fully embedded in a dust cocoon, in Evolved HII regions, most of the material has been ejected from the birth site (Paladini et al. 2012). The different surrounding environment of HII regions results in different emission properties. While HCHII, UCHII and Compact HII regions[8] have an optically thick spectrum for frequencies from a few to several GHz, Evolved HII regions are optically thin at 1 GHz (Paladini et al. 2012). On the other hand, at FIR and submillimeter wavelengths, all HII regions are very bright, being the only exception HCHII (Kurtz 2005). This emission is a result of the presence of dust grains, which are key for the cooling of HII regions as they absorb high energy photons emitted by the O stars and re-emit them in the IR and submillimeter. For UCHII regions, the dust has been estimated to absorb between 42% and 99% of the ionizing photons (Wood and Churchwell 1989 and Kurtz et al. 1994).

[8]Depending on their electron density.

As explained in Anderson et al. (2012c), *the absorption by dust leads to a slower expansion rate and a smaller physical size, stalling the expansion of an HII region earlier than it would otherwise.* Unfortunately, in the past, the lack of IR observations made it impossible to establish *whether dust was directly associated with HII regions or rather with their surrounding photodissociation regions* (PDRs, Paladini et al. 2012). The arrival of the GLIMPSE and MIPSGAL surveys allowed, for the first time, the detection of the different emission properties of HII regions and PDRs. In Povich et al. (2007), the authors used GLIMPSE and MSX data to study the M17 complex and found that the SED of the M17 PDR peaked at a longer wavelength and had a different shape than that of the M17 HII region. Moreover, Povich et al. (2007) established that *the different gas and dust components are mostly distributed in mutually exclusive regions: hot plasma occupies the very inner part of the HII region, warm ionized gas defines the cavity walls, warm dust permeates the ionized gas and PAHs surround the whole star-forming complex, tracing the PDR* (Paladini et al. 2012). On the other hand, the GLIMPSE/MIPSGAL data, together with high-resolution radio continuum VLA data, showed that HII regions are surrounded by a bright 8 μm shell, that traces the PDR they are confined in (Watson et al. 2008), inside which thermal dust emission dominates particularly at 24 μm (Churchwell et al. 2009). Now, thanks to the Hi-GAL Survey and Herschel's high-sensitivity and resolution, it has been possible to distinguish HII regions from their PDRs and to study the properties of these two environments like never before. Studies such as that of Paladini et al. (2012), in which a total of 16 HII regions within the $29°<l<31°$, $|b|<1°$ Galactic region were analysed, have confirmed that there is dust present in the interior of HII regions. Paladini et al. (2012) and Anderson et al. (2012c) remark, however, that the amount of dust contained in HII regions constitutes only $\sim$1% of the total mass.

Herschel has also allowed the study of HII regions as sites of star formation. As HII regions expand, new stars may form in a layer of collected neutral material that forms on the border of the HII region - a process known as "collect and collapse" (Elmegreen and Lada 1977). Studies such as that of Deharveng et al. (2003), Zavagno et al. (2006) and Pomarès et al. (2009) have provided evidence for the collect and collapse in several individual HII regions and have confirmed that this collected layer contains several thousand solar masses. The existence of YSOs in the borders of HII regions has been confirmed by several studies from Deharveng et al. (2005), Churchwell et al. (2006), Churchwell et al. (2007) and Watson et al. (2008).

The new Herschel/Hi-GAL images allow the detection of new YSOs that are too young and embedded to be detected at shorter wavelengths and thus, they offer a new and more complete view of the star formation in HII regions. Moreover, Herschel PACS and SPIRE fluxes allow us to characterize the physical properties of YSOs through their SED fitting and investigate the star formation history in HII regions (Zavagno et al. 2010b).

The are several authors that have already used the Herschel data to study Galactic HII regions where triggered star formation occurs. Some examples are Zavagno et al. (2010a) and Zavagno et al. (2010b), who studied the N49 and RCW 120 Galactic HII regions, respectively. However, with more than 8000 HII regions detected in our Galaxy with WISE (Anderson et al. 2014), there is plenty more to unveil regarding star formation triggered by HII regions in our Galaxy.

1.5.4.5 Young Stellar Objects

Young Stellar Objects (YSOs) are new-born stars that have been formed from the gravitational collapse of GMC. During the clouds' collapse, known as the *collapse-YSO phase*, the in-falling material accumulates in a protostellar disk around the protostar. As the matter accumulates, the temperature of the nucleus increases until thermonuclear reactions are ignited (Whittet 2003) marking the birth of a new star or YSO. The energy released in such reactions gives rise to winds through which matter is expelled to the ISM following a bipolar outflow pattern envelope (Lada 1988). At this stage, the star is said to be in the *embedded-YSO phase* for being embedded within the in-falling envelope of dust and gas that makes the star optically thick yet very bright in the MIR and FIR. When all the material of such envelope is either dispersed into the ISM or accreted into the star's disk, the star is said to become a visible *Pre-Main Sequence (PMS) star* on the *T-Tauri phase*. PMS stars continue evolving until hydrogen nuclear burning begins in their cores and become *Main-Sequence (MS) phase stars* (Bodenheimer 1989); in the case of a star with 1 $M_{\odot}$ that is 40 Myr after the star's initial condensation (Whittet 2003).

Shown in Fig. 1.11 are the four different spectral classes (*Class 0, I, II* and *III*) into which YSOs are classified. This classification is based on the shape and the features of the YSOs' continuum spectrum. These properties are dependent on the YSOs' evolutionary stage and can be characterised by a quantity named *spectral index* α, which is defined as $\alpha = d\log(\lambda F_{\lambda})/d\log(\lambda)$, where λ is the wavelength and F_{λ} is the source flux density.

The YSO classes I, II and III and the α quantity were first introduced by Lada (1988) who established that:

- **Class I YSOs** emit at IR wavelengths and have SEDs that rise in the MIR and FIR ranges, which verify that $\alpha > 0.3$. These YSOs are characterised by a central core surrounded by a circumstellar accretion disk of gas and dust in development (see second panel in Fig. 1.11).

- **Class II YSOs** have SEDs that are flat or are falling in the MIR range, which verify that $-0.3 > \alpha > -1.6$. In these YSOs, the accretion disk is fully developed and contains the majority of the circumstellar gas and dust. As a result, the source within the disk is observable at NIR and MIR wavelengths (see third panel in Fig. 1.11).

- **Class III YSOs** have SEDs that resemble that of a stellar photosphere and verify that $\alpha < -1.6$. In these YSOs, the accretion disk has become sufficiently thin so that its emission becomes negligible. As a result, the central source is now fully revealed and is observable at optical and NIR wavelengths (see fourth panel in Fig. 1.11).

The YSO class 0, on the other hand, was introduced a posteriori by André et al. (1993) who established that:

- **Class 0 YSOs** correspond to an earlier evolutionary stage than class I YSOs. They are characterised for being strong emitters in the millimetre and sub-millimetre ranges, for being undetectable at λ<10μm, for having very low values of L_{bol}/L_{submm} and for having an extremely efficient mass ejection mechanism.

  In these YSOs, the central core is less massive than that of Class I YSOs as the bulk of the final stellar mass has not yet been assembled. This core is deeply embedded in a large "cored-apple" envelope whose mass is greater than that of the central core (see first panel in Fig. 1.11).

The discovery of class 0 YSOs was made whilst carrying out a submillimeter continuum mapping of the ρ Oph A cloud core. The maps obtained by André et al. (1993) revealed the presence of four amorphous clumps, one of which was identified to be the VLA 1623 centimetre radio continuum source. This source was thoroughly studied and established to have the properties of a protostar less evolved than a class 1 YSO. These results led to the definition of a new class of YSOs that André et al. (1993) named class 0 YSOs.

YSOs can also be classified according to their mass: we distinguish between low mass YSOs ($m < 2\ M_{\odot}$), intermediate-mass YSOs ($2\ M_{\odot} \leq m \leq 8\ M_{\odot}$) and massive YSOs ($m > 8\ M_{\odot}$). While the formation of low and intermediate-mass YSOs is relatively well understood, the formation of massive YSOs is still poorly understood. This is due to the fact that MYSOs are difficult to study because they: (i) are rarer, (ii) evolve much more rapidly, (iii) have shorter lifes, (iv) are much farther away and (v) are embedded in larger dust quantities than low mass and intermediate-mass YSOs (Urquhart et al. 2007b).

Within the last few years, the number of identified MYSOs has considerably increased thanks to the work of Molinari et al. (1996), Sridharan et al. (2002), Hoare et al. (2004) and Urquhart et al. (2007b). From these, the Urquhart et al. (2007b) study is the most important and recent contribution. This work is part of the Red MSX Source (RMS) Survey, which is a multi-wavelength programme of follow-up observations designed to distinguish genuine MYSOs (which are relatively radio quiet sources) from other contaminants with similar colours such as UCHII regions and PNe (which are radio loud sources). Using the MYSO colour criteria developed by Lumsden et al. (2002) on the MSX and 2MASS sources, Urquhart et al. (2007b) produced an initial sample of ∼2,000 MYSO candidates. From these sources, Urquhart et al. (2007b) selected a total of 826 sources located in the $235°<l<350°$ Galactic region for which they conducted high resolution radio continuum observations at 3.6 cm and 6 cm using the Australia Telescope Compact Array (ATCA). Their results showed that from the 826 RMS sources observed with ATCA, a total of 627 sources were confirmed to be genuine MYSOs whereas the remaining 199 were identified to be mainly UCHII. In addition, Urquhart et al. (2007b) detected a further 169 discrete radio sources, 42 of which were also identified to be UCHII regions. Thus, in total, Urquhart et al. (2007b) classified 627 MYSOs and 241 UCHII regions.

Although an evolutionary sequence for MYSOs was proposed by Evans et al. (2002) and Kurtz et al. (2000) - in which cold massive cloud cores evolve into hot molecular cores with outflows, IR-bright MYSOs and finally into UCHII regions - such sequence was rather qualitative and was based on small and incomplete samples. Now, thanks to the Hi-GAL Survey and its use of the Herschel instruments, we have been able to trace the SED peak of the dust envelopes of a large amount of YSOs and HII regions (including MYSOs and UCHII regions) in different evolutionary stages (Molinari et al. 2010b). This will allow us to study the evolutionary phases of these objects and to confirm the sequence proposed by Evans et al. (2002) and Kurtz et al. (2000).

Figure 1.11: Image showing the four spectral classes (*Class 0, I, II* and *III*) into which YSOs are classified.

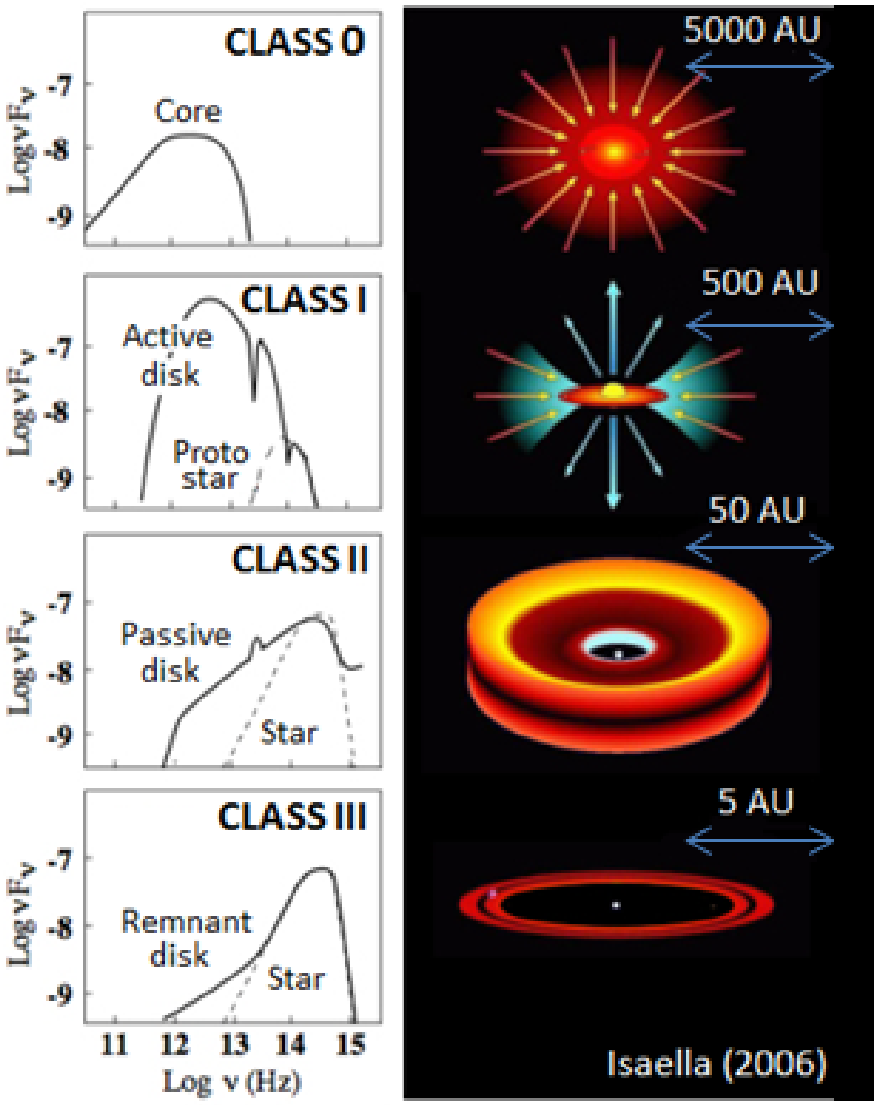

Figure 1.12: The figure below, adapted from Habing and Olofsson (2003), shows the structure of a star when entering the E–AGB phase. This structure is known as *double-shell burning structure* and is constituted by the six following layers: (i) a small, very hot ($T \sim 10^8\ K$), dense ^{12}C - ^{16}O core, (ii) a very thin He-burning shell, (iii) a thin inter-shell layer composed of mostly He, (iv) a very thin H-burning shell, (v) a radiative H-rich layer and (vi) a thick convective outer circumstellar envelope (CSE) composed of H at $T_{eff} \sim 3 * 10^3\ K$.
The radii and mass of these layers are dependent on the star's mass. The quantities shown below are for a low-mass star of M=1 $M_\odot$ and for an intermediate-mass star of M=5 $M_\odot$.

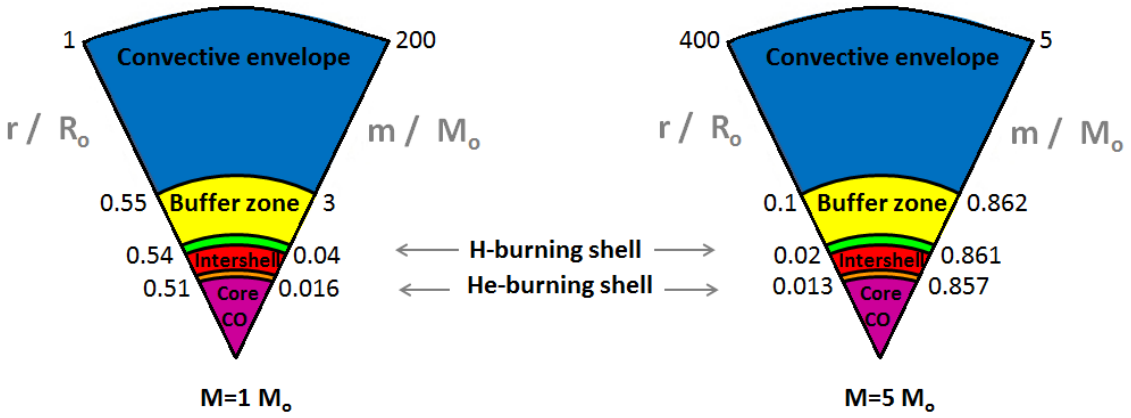

1.5.4.6 Asymptotic Giant Branch stars and Planetary Nebulae

In this section we present a summary of the main evolutionary stages that AGB stars undergo, which is based on the reviews on AGB evolution from Habing and Olofsson (2003), Herwig (2005), Salaris and Cassisi (2006) and Karakas (2010).

Asymptotic Giant Branch stars (AGB stars) are low-mass and intermediate-mass evolved stars ($0.8\ M_\odot < M < 8\ M_\odot$) that are near the end of their existence and whose nuclear fuel is mostly exhausted. These stars are post-MS stars with a *double-shell burning structure* (see Fig. 1.12) that are undergoing the *Asymptotic Giant Branch* phase, which is located in the upper left side of the Hertzsprung Russell (HR) diagram (see Fig. 1.13).

The AGB–phase is normally separated in two sub–phases: the Early AGB (E–AGB) and the Thermally Pulsating AGB (TP–AGB). Although all AGB stars undergo both the E-AGB and TP-AGB phases, the evolutionary tracks and the thermodynamic and chemical processes the stars undergo throughout these sub-phases are different for AGB stars of low and intermediate mass (see Fig. 1.13).

During the E–AGB phase the star's core contracts and heats up while the He–burning shell, the He inter–shell layer and the convective envelope expand and cool in such effective way that also the H–burning shell's temperature decreases. For intermediate–mass stars, the decrease in temperature of the H–burning shell causes the H-burning shell to totally extinguish so that the total stellar luminosity is then provided almost entirely by the

He–burning shell. Meanwhile, the envelope expansion causes the opacity in the envelope to increase, which in turn drives envelope convection. Next, the inner edge of the convective envelope penetrates down into the dormant H–burning shell giving rise to a process known as the 2^{nd} *dredge–up*. During the 2^{nd} dredge–up the H-burning products (mostly ^{4}He and ^{14}N) are mixed with the convective envelope and brought up to the surface, which results in the increase of the ^{4}He and ^{14}N abundances and the decrease of the ^{12}C and ^{16}O abundances.

For low–mass stars, the H–burning shell does not completely extinguish and so, it remains active at a low level, which prevents the convective envelope from penetrating any further than into the H–He discontinuity and stops the 2^{nd} dredge–up from occurring.

Following the 2^{nd} dredge–up occurrence (in intermediate–mass stars) or avoidance (in low–mass stars), the continuous He-burning causes the ^{12}C - ^{16}O core to increase its density until it becomes degenerate. Then, the envelope expansion is halted by its own cooling and it starts contracting and heating until the H-burning shell is reignited. The reignition of the H–burning shell causes the pressure, temperature and luminosity of the He inter–shell to dramatically increase giving rise to a series of thermal instabilities known as *Thermal Pulses* (TP). The onset of the first of these TP marks the beginning of the TP–AGB phase. The number of TP a star undergoes during its lifetime depends on its mass. While low–mass stars undergo around 10 TP within a total lifetime of $\sim 10^{6}$ years, intermediate mass stars undergo several tens of TP within a total lifetime of $\sim 3 * 10^{5}$ years. During a TP, the star suffers:

1. A thermonuclear runaway called *He–shell flash* – during which a convective zone is formed in the He inter–shell and is then flash–driven throughout causing the products of partial He–burning to mix.

2. An expansion of the He inter–shell – during which the He inter–shell luminosity decreases and the He–burning shell expands and cools causing the H–burning shell to extinguish.

3. A 3^{rd} *dredge–up* (in some cases) – during which the outer convective envelope penetrates beyond the extinguished H–burning shell causing the He–burning products (mostly ^{12}C) from the He inter-shell layer to be dragged to the outer envelope.

4. Shock waves that generate strong stellar winds – through which large amounts of dust ($\sim 10^{-6}$ $M_{\odot}$ yr^{-1}) are injected from the AGB star CSE to the ISM.

After several years, the He–shell flash ends and the He–burning becomes stable until, a few hundred years later, the H-burning shell is reignited and the He–burning shell becomes inactive. This marks the end of the TP and the beginning of a new phase, known as *Inter-Pulse* (IP) phase, during which the H–burning shell remains stable while the He inter–shell layer mass continues to grow until a new TP, with greater pulse amplitude, occurs [9]. In low–mass stars the IP lasts $\sim 5 * 10^4$ years whereas in intermediate-mass stars it lasts $\sim 10^3$ years. The AGB–phase is said to be over when the succession of TP causes the star's CSE to decrease to a mass of 10^{-2} – 10^{-3} $M_{\odot}$. Then, the star enters a new phase, known as the *Post-AGB* (P-AGB) phase, during which the star's effective temperature (T_{eff}) and emitted core UV radiation increases while its luminosity remains constant for $\sim 10^4$ years (hence the horizontal track in the HR diagram in Fig. 1.13). Beyond T_{eff}=3*10^4 K, the pressure caused by the UV radiation gives rise to very fast winds of $< v >\sim$25 km s^{-1} (Kwok 1994), which destroy the CSE dust grains, dissociate the present molecules and ionize part of the CSE gas in the shape of a shell. This shell absorbs the UV energy emitted from the nucleus and re-emits it at visible wavelengths turning the star to optically thin. Furthermore, the ionization of the gas and its associated dust makes the star also observable in radio and IR wavelengths. At this point, the P-AGB star is said to have become a Planetary Nebula (PN) whose properties will depend on the chemical and physical circumstances in which the gas has been ionized.

Eventually, after $\sim 10^4$ years (Kwok 1994), when the shell mass drops below $\sim 10^{-5} M_{\odot}$, there will not be enough mass left above the H-burning shell to maintain the temperature required for H-burning (Habing and Olofsson 2003). As a result, thereafter, the star's luminosity will rapidly decrease. When the temperature reaches $T_{eff} \sim 10^5$ K and the mass decreases to 0.5 $M_{\odot} < M <$1.44 $M_{\odot}$, the PN will become a *White Dwarf* (WD) whose structure will consist of a ^{12}C - ^{16}O core surrounded by a thin He–rich envelope of < 0.01 $M_{\odot}$ embedded in a thinner H-rich layer of $\sim 10^{-4}$ $M_{\odot}$ (Althaus et al. 2010). The WD will progressively cool down and lose mass until the density of its envelope equals to that of the ISM.

[9] For stars with m>4 $M_{\odot}$, there is an extra process taking place during the inter-pulse known as *Hot Bottom Burning* (HBB). During the HBB, the temperature at the base of the convective envelope becomes so high ($T > 3 * 10^7$ K) that H-burning reactions are ignited. The reactions cause an increase in the surface luminosity and more importantly, they convert the dredged-up ^{12}C into ^{14}N, thus changing the stellar surface composition.

Figure 1.13: The Hertzprung Russell (HR) diagram is a plot showing the relationship between the stars' absolute magnitudes (M) or luminosities (L) versus their spectral types (O, B, A, F, G, K, M) or B-V colour index or effective temperatures (T_{eff}). This diagram was first created by using stars of known stellar type, distance and luminosity and can serve us as a reference to estimate the stellar type, the spectral type or the M, L, B-V and T_{eff} of unknown stars.
Indicated in this diagram are the two distinct evolution tracks (blue lines) followed by: (i) an AGB of low mass (M=1 $M_{\odot}$, track A) and (ii) an AGB of intermediate mass (M=5 $M_{\odot}$, track B), during their E–AGB and TP–AGB phases. Also indicated are the phases preceding the E–AGB phase: the *MS* phase, and the phases following the TP-AGB phase: *post-AGB*, *PNe* and *WD* phases, together with a numbered list (in green for track A, in pink for track B) of the most important features or events occurring during each phase and an schematic of the evolution of the AGB stellar structure.

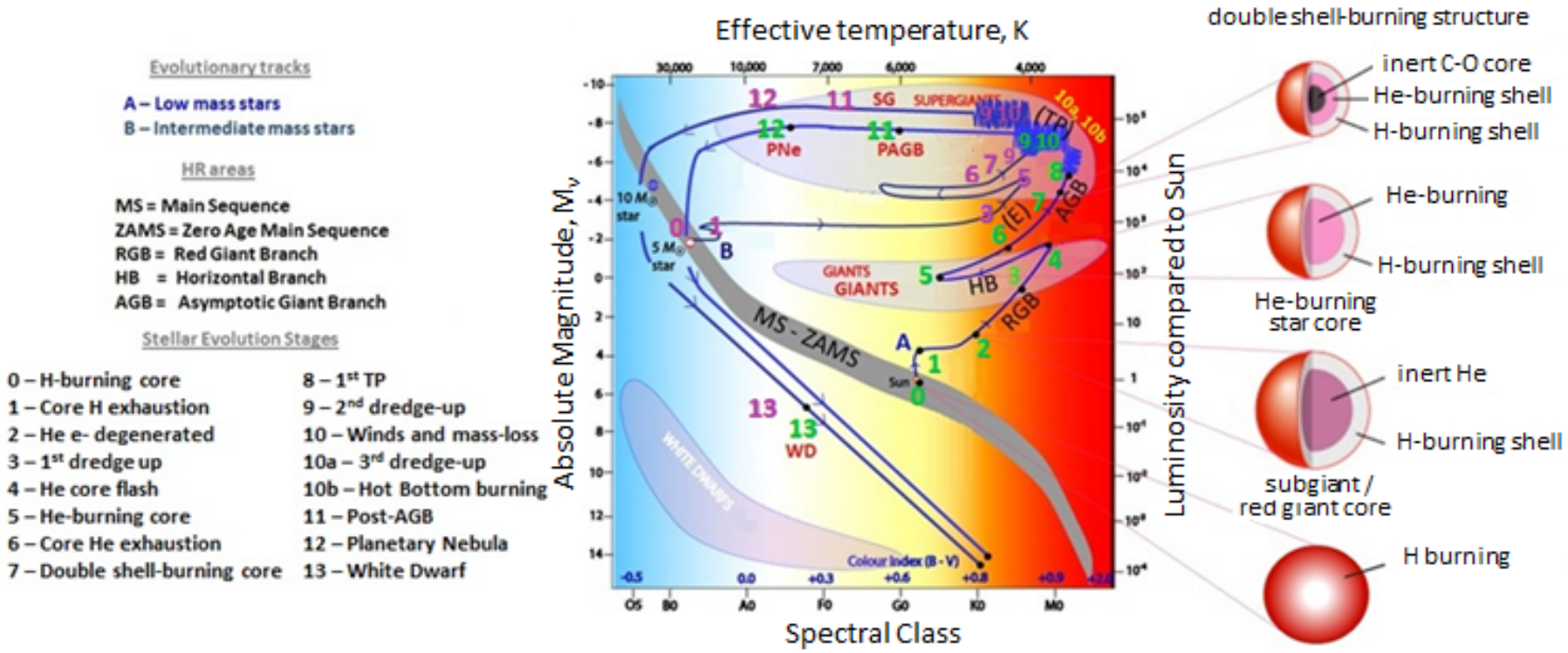

AGB stars can be classified depending on the frequency and amplitude (intensity) of the luminosity variations (LPV) that AGB stars experience with every TP. We distinguish between: (i) Mira - AGB stars with large amplitude and regular LPV, (ii) SRa - AGB stars with small amplitude and relatively regular LPV, (iii) SRb - AGB stars with small amplitude and poorly regular LPV and (iv) L - AGB stars with small amplitude and irregular LPV.

AGB stars can also be classified depending on the ratio between the C and O abundances present on their CSE. We distinguish between: Carbon-rich (C-rich or C-) stars, Oxygen-rich (O-rich or M-) stars and S-stars.

Carbon-rich stars are AGB stars for which the abundance of ^{12}C in their CSE is higher than that of ^{16}O (i.e. $C/O > 1$). This surplus on ^{12}C is a consequence of the large quantities of ^{12}C that are added to the AGB stars' surface with every dredge-up process the stars experience during the TP-AGB phase. The excess of ^{12}C results in the presence of carbon compounds and in the lack of metallic oxides in the dust grains and spectra of these stars.

Oxygen-rich stars are AGB stars for which the abundance of ^{12}C is lower than that of ^{16}O (i.e. $C/O < 1$). This surplus of ^{16}O is due to: (i) the low number of dredge-up processes the star has undergone during their TP-AGB phase or (ii) the conversion of ^{12}C into ^{14}N during the Hot Bottom Burning process (only for $M > 4\ M_{\odot}$). The excess of ^{16}O results in the presence of metallic oxides (e.g. TiO, ZrO and VO) in the dust grains and spectra of these stars.

S-stars are AGB stars for which $C/O = 1$, i.e. the abundance of ^{12}C equals that of ^{16}O. They constitute transition objects between M-stars and C-stars and their spectra is characterised by the presence of ZrO lines. S-stars with TiO-ZrO lines are often referred to as *MS-stars* while S-stars with ZrO-C lines are called *SC-stars*.

As an AGB undergoes the TP-AGB phase its atmosphere can change from C-rich to O-rich and vice versa due to the continuous ^{12}C dredge-up processes that take place in every TP the star experiences. The composition and structure of the star's CSE dust grains will depend on: (i) the abundance of ^{12}C and ^{16}O atoms present in the CSE and available to become dust grains and (ii) on the temperature that the CSE has during the nucleation of the dust grains.

AGB stars are by far the most efficient stellar types that inject dust into the ISM. The contribution of AGB stars to the total amount of injected dust is believed to be of $\sim 93\%$ (Whittet 1992) whereas for other evolved types, such as supergiants (Chiosi and Maeder 1986), PNe and Wolf-Rayet stars (Abbott and Conti 1987), their contribution is believed to be of only $\sim 4\%$, $\sim 0.4\%$ and $\sim 0.2\%$, respectively (Whittet 1992). Other contributors are Supernovae (Matteucci and Greggio 1986) whose contribution on dust constitutes only $\sim$2% of the total dust injected to the ISM (Whittet 1992).

The ejection of dust into the ISM in an AGB star begins during the TP-AGB phase. Every TP is accompanied by shock waves that give rise to stellar winds, which are driven by thermodynamic pressure and are responsible for the very high dust mass-loss rates characteristic of AGBs. The dust ejection process in AGB stars can be separated in two phases. Firstly, the gas and dust particles that escape the stellar gravitational attraction form a circumstellar envelope (CSE) around the AGB star. Secondly, the CSE matter is dispersed into the ISM as the star evolves. This dispersion commences in the TP-AGB but continues during the P-AGB phase until the star enters the PN-phase.

On the other hand, in supernova explosions, the interaction between the mass ejected by the resulting shock waves and the ISM can be separated in three phases (Tielens 2005). In the first phase, the ejected mass is much greater than that of the swept-up ISM and thus, the shock wave advances through the ISM at high velocity without changing its velocity. In the second phase, on the contrary, the mass of the swept-up ISM is greater than that of the ejecta and thus, the ISM starts slowing down the shock, which then becomes adiabatic. In the third and final phase, the shock velocity is greatly reduced, radiative cooling becomes important and the shock becomes isothermal. Eventually, when the pressure of the shock equals to that of the ISM, the supernova remnant will merge with the ISM.

Once injected in the ISM, dust grains undergo a great diversity of processes responsible for their growth and destruction. On the one hand, low velocity grain-grain and gas atom/molecule-grain collisions give rise to grain coagulation and mantle growth, respectively thus increasing the size and mass of the dust grains. On the other hand, high velocity grain-grain collisions generated by SN interstellar shock waves (Seab and Shull 1983) of $\sim 50\, km\, s^{-1}$ (Seab 1988) or higher lead to shattering or evaporation of the grain material. Finally, atom/ion-grain collisions cause the surface of the grains to be eroded in a process called sputtering (Barlow 1978). In the collision, atoms can be removed due to becoming chemically bonded to the impinging grains or due to the energy of the impact.

The dust grains intermix very well with the ISM H I gas to the extend that the distribution of dust has been found to be quite similar to that observed for the H I gas (Schulz 2005). In ISM regions sufficiently dense, (i.e. n $> 10^8\, m^{-3}$), all the H I is converted to H_2 giving rise to dense Giant MC (see Sect. 1.5.4.2). Initially, the MC are supported against their self-gravity by interstellar magnetic fields but eventually, they collapse and fragment into individual pre-stellar nucleus that evolve into YSOs (see Sect. 1.5.4.5), which then evolve into MS stars following the evolutionary sequence described in Fig. 1.11. Finally, those MS stars that arrive to the ZAMS having masses between $0.8M_{\odot} < M < 8M_{\odot}$ will continue their evolution as AGB stars. As a result, the group of processes described in Sect. 1.5.4.6 will take place all over again in a cycle often referred to as the *dust life cycle*. This cycle has been occurring since the first generation of stars, (composed almost exclusively of H and He), were born. As these stars evolved and died, part of their nuclear processed material was returned to the ISM and then used (recycled) in the birth of a second generation of stars. Thereafter, with every new stellar generation, the ISM has been enriched with increasingly heavier elements whose presence has made possible the creation of a great variety of stellar objects.

1.6 Thesis layout

As we mentioned earlier, AGB stars are the major contributors of dust into the ISM. Therefore, their detection and study is crucial to determine the amount of dust contained along the Galactic plane and its distribution, to establish the percentage used in the formation of new stars and to understand the evolution of dust in our Galaxy. The aim of this thesis was to use the Hi-GAL 1 Survey data to compile the largest inventory of Galactic AGB stars detected with Herschel existent to date. In order to achieve this we needed to create a Point Source Catalogue (PSC) for the Hi-GAL 1 Survey and establish a method to separate AGB stars from other stellar types included in the Hi-GAL 1 PSC. This thesis is structured as follows:

- In Chapter 2 I introduce the processing software used to convert the Hi–GAL 1 raw telemetry data into high quality maps.
- In Chapter 3 I find an adequate algorithm for the detection and flux extraction of the point sources present the Hi–GAL 1 maps.
- In Chapter 4 I explain the requirements and steps followed in the creation of the SMA Hi-GAL 1 PSC and describe its properties.
- In Chapter 5 I introduce colour criteria capable of efficiently separating AGB stars from YSOs, HII regions and PNe and OH/IR-stars from C-stars. These colours cuts are applied to our SMA Hi-GAL 1 PSC in order to create the catalogues of SMA Hi-GAL 1 PSC AGB, C-rich AGB and O-rich AGB star candidates.
- In Chapter 6 I study the stellar properties (e.g. bolometric fluxes, nominal distances, colour temperatures, mass-loss rates...etc) of the SMA Hi-GAL 1 PSC AGB star candidates and derive the equations that relate the sources' mass-loss rates with their colour temperatures, luminosities, NIR colours and outflow velocities.
- In Chapter 7 I summarise the work presented and the conclusions drawn in this thesis.

Chapter 2

Choice of a map-making pipeline for the Hi-GAL maps

"All systems are green. We are GO for launch."

John Dodsworth

2.1 Introduction

The aim of this chapter is to select a suitable processing software to convert the Hi–GAL 1 raw telemetry data into high quality maps devoid of artefacts generated by the telescope and electronics. Currently, there are two different programs available for the processing of the Hi–GAL data: the *Parallel Mode Scan* pipeline and the *ROMAGAL* pipeline.
In the following sections I:

(i) analyse the different drift removal, deglitching, destriping, map–making and denoising techniques carried out in these two pipelines,

(ii) review the work presented in Traficante et al. (2011) where the quality of the pipelines' output maps is compared and which provides solid arguments that support our final choice of pipeline and

(iii) describe the terminology, units, pixel size, number of pixels, astrometrical and absolute flux calibration as well as the overall quality of the final Hi–GAL 1 maps.

2.2 Data Processing Pipeline

The group of processing steps through which raw telemetry data is converted into maps is known as *pipeline*. In general, such conversion is achieved in two consecutive phases: a *pre–processing phase*, in which the level 0 data is processed into further processed level 1 data, and a *map–making phase*, in which level 2 products are generated.
The pre–processing phase includes all the operations necessary to accurately remove systematics and random effects in the data. The most important pre-processing operations are: the *drift removal*, the *deglitching* and the *destriping*.

- *Drift removal*

  Drift removal is defined as the process of subtracting *drifts*. These are changes taking place in the detector's responsivity over the course of an observation period. They are caused by the detector's thermal bath and the readout electronics and can occur either on the detector's entire array or on a single detector sub-unit.

  The detection and subtraction of such drifts is necessary to ensure that: (i) there are no pixel-to-pixel offsets, (ii) there are no signal systematic decreases from the start to the end of the observation and to guarantee that (iii) the level 1 PACS and SPIRE data represents the true sky and it is not dominated by the telescope background and the unknown zero level of the electronics.

- *Deglitching*

  Deglitching is defined as the process of removing *glitches*. These are strong and spiky detector bolometers' signal variations caused by cosmic rays hitting the detector (affecting single detectors only) or the detector base plate (affecting multiple detectors at once).

  The detection and rejection of glitches is essential as undetected glitches are a source of map artefacts, which limit the calibration accuracy, the sensitivity and the overall quality of the final data products.

- *Destriping*

  Destriping is defined as the series of corrections done to the level 1 data in order to obtain maps free from *stripes*. During the drift removal process some of the detector's thermal and electronic variations are not properly corrected, which causes residual offsets in the flux calibration from one detector to another in the form of low-frequency noise. Since this noise follows the pattern of the adopted scanning strategy, this results on stripes superimposed on the sky signal in the map.

  An effective removal of the stripes is crucial to guarantee the obtaining of maps of good quality, which in turn dramatically conditions the precision of any map photometric measurements.

The map–making phase includes all the operations necessary to transform the pre–processed data to maps. The most important map-making operations are: the *map-making algorithm* and the *noise estimation*.

- *Map–making algorithm*

  In general, a map–making algorithm uses a series of mathematical operations, with different levels of complexity, to project into a 2D image (map) the signal data collected during the observation time on the detectors' pixels.

  Different algorithms produce different maps generated from the same signal data. Thus, for a specific survey dataset, several map-making algorithms are often generated, each of which delivers different quality maps. The more knowledge is put into the algorithm's operations (e.g. about the imaging instrument, the detector's response, the nature of the astronomical objects observed,...etc), the better the quality of the map made.

- *Noise estimation*

  Due to the limitations of the SPIRE and PACS bolometer detectors used for imaging, random additions to the signal data (noise) occur. Examples of these are: readout noise, dark current noise, flat field noise, glitches, hot spots, dark columns, blooming,...etc. An adequate estimation and removal of undesirable noise is vital for the generation of good quality images.

2.2.1 Parallel Mode Scan Pipeline

The Parallel Mode Scan Pipeline (PMSP), as its name indicates, was created to process the Herschel data acquired when observing in Parallel Mode (see Sect. 1.4.3). This was the official, and only existing, standard reduction strategy for the Hi–GAL data until the ROMAGAL Pipeline (RMP) appearance (see Sect. 2.2.2). The PMSP is written in Jython and can be accessed through HIPE (see Sect. 1.4.4.1).
The main pre–processing phase operations included in the PMSP are:

- *Drift removal corrections*

  These include: (i) the correction of the electric crosstalk between thermistor-bolometer channels, (ii) the detection and flagging of jumps in the signal of the thermistor timelines, (iii) the amendment of the delay in the detector's data timeline with respect to the astrometric pointing timeline imposed by the detector's electronics, (iv) the removal of the low frequency noise from the detector's signal timelines caused by variations of the detector array bath temperature and (v) the time correlation between the spacecraft clock and the Photometer Scan Products.

- *Deglitching methods*

  These include the use of a concurrent deglitcher and a wavelet deglitcher.

  The concurrent deglitcher removes glitches that occur simultaneously in all the bolometer detectors of the photometer arrays. Glitch signatures are identified as Signal Timeline Data values (see Sect. 1.4.4.1) that deviate from a calculated median by some established threshold. Detected glitches are then flagged by replacing the corrupted data with the running median of the input signal.

  The wavelet deglitcher removes glitches due to cosmic ray hits or other impulse-like events. In this case, glitch signatures are assumed to be similar to a Dirac delta function and are detected using a wavelet-based local regularity analysis. Identified glitches are then flagged by reconstructing the signal by means of linear fitting.

Other operations are the addition of the turnarounds to the scanlegs, the production of pointing information and the flux conversion from V to $Jy/beam$.
The final addition of the Photometer Scan Products to the level 1 context brings to a close the PMSP pre–processing phase.

The main map–making phase operations included in the PMSP are:

- *Relative Gain Corrections*

  Each bolometer timeline is divided by a calculated relative gain factor in order to amend the variations in the beam shape between the different bolometers, which affect the quality of the maps with extended emission.

- *Destriping procedures*

  These include the use of median baseline removal or alternatively, of the destriper.

  On the on hand, the median baseline removal creates a map using the median from each detector in the level 1 timelines and is only suitable for flat background regions. On the other hand, the destriper iteratively updates offsets in the timelines until an optimal solution is found and works in flat background regions and in structured regions with cirrus clouds and gradients.

- *Mapper methods*

  These include the use of the *Naïve Scan* mapper or alternatively, of the *Microwave Anisotropy Dataset* (MAD) mapper.

  The Naïve Scan mapper creates a: (i) *Signal map* - by means of directly projecting onto an image plane the full signal power seen by each bolometer onto the nearest image pixel, (ii) *Coverage map* - by counting the number of data samples that contribute to each image pixel, (iii) *Flux density (or Image) map* - by dividing the Signal map by the Coverage map and an (iv) *Error map* - by calculating the standard deviation of the mean of data samples falling in each map pixel.

  In the case of the MAD mapper, further destriping is performed by removing the bolometers' uncorrelated one-over-frequency (1/f) noise. The Signal maps are built using a maximum-likelihood method to minimise the maps' Fourier Transform and the Coverage, Image and Error maps are created as in the Naïve Scan mapper.

The final addition of the maps to the level 2 context brings to an end the PMSP map–making phase.

2.2.2 ROMAGAL Pipeline

The ROMAGAL pipeline (RMP) was created as an alternative to the former PMSP. Contrary to the PMSP, the RMP was optimized and specifically tailored for the reduction of the Hi–GAL data affected by bright and irregular backgrounds (Traficante et al. 2011). Listed in Table 2.1 and 2.2 are the main procedures included in the pre–processing and map–making phases for both pipelines. Processes coloured in yellow and blue are exclusive for the PMSP and RMP respectively while those in green are common for both the PMSP and the RMP. Here, we can see that while the RMP pre–processing phase constitutes an extension of that of the PMSP, the RMP operations during the map–making phase are very different from those performed in the PMSP.

With respect to the pre–processing phase, the two pipelines share more similarities than differences, with the only distinction being that the RMP pre–processing phase has some additional operations listed below:

- *Creation of TODs*

  After having performed all the pre–processing steps (except deglicthing for the PACS data) included in the PMSP, the RMP exports, in fits format, the SPIRE and PACS level 1 Photometer Scan Products outside HIPE in the form of *Time Ordered Data series* (TODs). This is level 1 product data that is rearranged into one time series per detector pixel and includes the calibrated flux and the celestial coordinates.

  Once exported, the PACS TODs are imported into *Interactive Data Language* [1] (IDL) in order to correct them from the changes in responsivity over time, drifts and glitches.

- *Identification and correction of corrupted TODs*

  The random hitting of cosmic rays creates a bias on the bolometer timeline with a low-frequency drift, which is corrected by masking any strong, spiky and/or exponential change along the TODs.

[1] IDL is a scientific programming language used for mathematical data analysis and graphical visualization.

- *Drift removal corrections*

  After masking the corrupted TODs, two additional drift removal corrections are performed on the TODs within IDL.

  Firstly, the effect of pixel–to–pixel offsets is mitigated by calculating and then subtracting the median level for each pixel from each readout so that all pixels have median level equal to 0.

  Secondly, drift behaviour is calculated by fitting a polynomial to the set of minimum median values of the entire bolometer array/unit for all the scanlegs.

- *Deglitching*

  Unlike in the PMSP, deglitching in the RMP is not applied up until this point and is not achieved by means of the PMSP concurrent and wavelet deglitcher.

  Instead, the RMP automatically localises TODs containing exponential–looking glitches using the TOD first derivatives and flags the corrupted portion where the detector's pixel response follows such function.

  Next, TODs outliers are iteratively removed using a sigma–clipping algorithm, which detects and eliminates all the signal values that differ from the mean by more than n standard deviations, where n is defined as in Pezzuto (2010).

With respect to the map–making phase, the two pipelines have no operations in common other than the fact that they both include a mapper method. Whilst in the PMSP, maps are created in HIPE using the Naïve Scan mapper or the MAD mappers, in the RMP, maps are created in Fortran using the:

- *GLS mapper*

  The *Generalized Least Square* (GLS) mapper creates maps with minimum noise variance making use of the GLS algorithm[2].

- *Noise Constraint Realization*

  In order for the GLS mapper to create destriped maps, the gaps originated in the data when flagging the corrupted TODs must be filled with Gaussian Noise Constraint Realizations (NCR)[2].

[2]Further information on both the GLS and the NCR functioning and formalism is available in Traficante et al. (2011).

Table 2.1: List of pre-processing operations included in the Parallel Mode Scan and ROMAGAL pipelines.

PRE-PROCESSING (Level 0→Level 1)	
Parallel Mode Scan Pipeline (PMSP)	**ROMAGAL Pipeline (RMP)**
Add turnarounds to scans	
Pointing information	
Electrical crosstalk correction	
Signal jump detection correction	
Deglitching	-
Low pass filter response correction	
Temperature drift correction	
Bolometer time response correction	
Flux conversion	
Detach turnarounds	
Attach pointing	
Time correlation	
Add Photometer Scan Product to level 1 context	
-	Creation of TODs
-	Correction of corrupted TODs
-	Drift removal
-	Deglitching

Table 2.2: List of map-making operations included in the Parallel Mode Scan and ROMAGAL pipelines.

MAP-MAKING (Level 1→Level 2)	
Parallel Mode Scan Pipeline (PMSP)	**ROMAGAL Pipeline (RMP)**
Relative gain correction	-
Baseline removal or destriping	-
Naïve Scan mapper	GLS mapper
-	NCR
Add maps to level 2 context	

2.3 Quality of the PMSP maps

In most of the cases, the quality of the PMSP maps obtained with the Naïve Scan mapper is very good as they come out of the pipeline. However, as explained in the SPIRE data reduction guide, in occasions, some artefacts get through and show up on the final maps. Listed in the table below are the most common artefacts found in the PMSP maps.

Table 2.3: Artefacts found in the PMSP maps. The images shown below are from the SPIRE data reduction guide.

Map Artefact	**Description**	**Visual effect on the map**
Bright sources	Bright sources can create Airy rings and other artefacts due to diffraction effects from the telescope support structure.	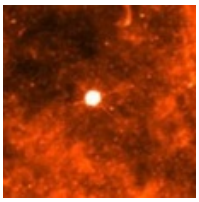
Failure on the baseline removal	Strong extended sources introduce a certain bias into the baseline signal, which leads to the failure of the baseline removal and results in an inefficient map destriping.	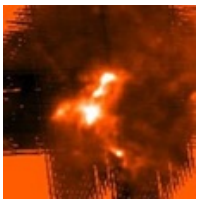
Residual glitches	Although deglitching is carried out within the pipeline, occasionally, glitches get through resulting in a regular pattern of bright pixels on the map.	
Holes	For maps with low coverage (i.e. maps without orthogonal scans or no repetitions) and for maps with residual glitches (that the pipeline was not able to remove or reconstruct), holes (i.e. 0's on the Coverage map, NaN's on the Signal map) may be visible in the final maps.	
Edge defects	Map edges often present defects but since they are out of the guaranteed area they should not be used but ignored.	

2.4 Quality of the RMP maps by Traficante et al. (2011)

In this section we review the work presented in Traficante et al. (2011) where the author compares the quality of the PMSP and RMP output maps and presents solid arguments that support our final choice of pipeline.

Although an experienced user could possibly amend most of the map defects (see Table 2.3) that affect the PMSP output maps by means of interactive analysis within HIPE, Traficante et al. (2011) opted for the creation of their new RMP, with which they aimed to create higher quality maps.

Shown in Fig. 2.1 is a comparison, carried out by Traficante et al. (2011), between the PMSP Naïve Scan maps and the RMP GLS maps of the $l = 30°$ field at 70 μm, 160 μm, 250 μm and 350 μm. Here, we can clearly appreciate that maps processed with the PMSP Naïve Scan mapper have a lower artefact removing power than those processed with the RMP. As discussed in Traficante et al. (2011), the PMSP maps are found to be more affected by:

- *Stripes*

  Results in Fig. 2.1 show that SPIRE, and specially PACS maps, created with the PMSP suffer still from some level of striping. This affects particular regions with low signal–to–noise ratio where only diffuse emission is present and has been observed to be of the same order of magnitude of the signal or even higher.

  On the contrary, maps created with the RMP show very low levels of striping. These results prove that the GLS mapper is capable of removing the 1/f residual noise without losing any signal, both on bright sources and on diffuse emission.

- *Glitches*

  According to Traficante et al. (2011), the deglitching operations performed within the PMSP were suitable for the SPIRE maps. For the PACS data however, such operations appeared to generate false detections, which were visible on the final maps. The new deglitching technique included in the RMP has proven to deliver better results for the PACS maps. Furthermore, when applied to the SPIRE maps, it is capable of removing some weak glitches missed by the PMSP concurrent and wavelet deglitchers.

Figure 2.1: The images shown below are extracted from Traficante et al. (2011) and show the different level of striping present in the PMSP and the RMP output maps. From these images, we can clearly see that GLS mapper generates maps of better quality.

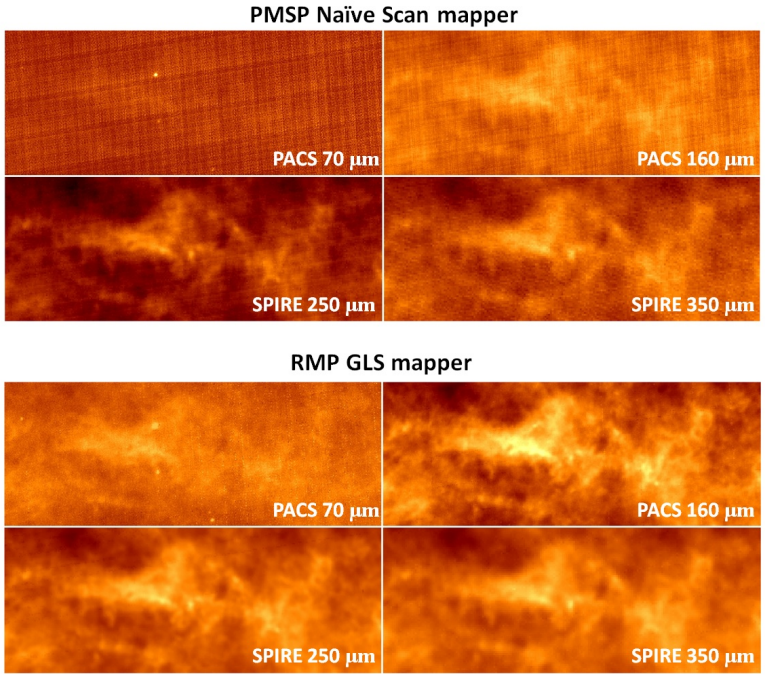

Table 2.4: Shown below are the rms values obtained by Traficante et al. (2011) for the PMSP and ROMAGAL output maps. From these values, Traficante et al. (2011) established that the S/N is higher for the ROMAGAL output maps.

PACS $l = 30°$			
Band	**rms RMP (Jy/pixel)**	**rms PMSP (Jy/pixel)**	**ratio**
70 μm	0.0085	0.026	3.1
160 μm	0.047	0.102	2.2
SPIRE $l = 30°$			
Band	**rms PMSP (Jy/pixel)**	**rms RMP (Jy/pixel)**	**ratio**
250 μm	0.1749	0.2868	1.6
350 μm	0.1569	0.2302	1.5
500 μm	0.2659	0.4065	1.5

- *Background noise level*

  In a statistical analysis of the background noise level of the PMSP and RMP maps, Traficante et al. (2011) showed that the *root mean square* (rms) values in the RMP maps are lower than those found for the PMSP maps. Since the flux between the PMSP and the RMP maps is conserved, lower rms values result in higher *signal–to–noise* (S/N) ratio values in the RMP maps. Listed in Table 2.4 are the rms residuals of the PACS and SPIRE maps, calculated in a diffuse emission area of each map in Fig. 2.1. Here, we can see that the ratio between the PMSP and RMP rms residuals shows an improvement of a factor $\sim$ 2–5 in the PACS RMP maps, and a factor $\sim$ 1–2 in the SPIRE RMP maps.

- *Pixel–to–pixel offsets*

  Finally, Traficante et al. (2011) found that the PMSP-generated PACS level 1 signal is dominated by the telescope background and the zero level of the electronics, which further introduce significant pixel–to–pixel offsets.

The previous results demonstrate that from the two pipelines ROMAGAL's delivers better quality Hi-GAL maps. Therefore, it was decided to use a total of 126 PACS maps (i.e. 63 Hi–GAL 1 mapped fields $\times$ 2 PACS bands) and 189 SPIRE maps (63 Hi–GAL 1 mapped fields $\times$ 3 SPIRE bands), readily processed by ROMAGAL (see Fig. 3.3a for an example).

2.5 General comments on our maps

Below, we provide a general description of the properties of the ROMAGAL-processed maps we used for this work. We discuss the terminology of the maps, their units, the size of the maps' pixels, the number of pixels in the maps, the maps' astrometrical and flux calibration as well as their quality with respect to previous missions.

- Terminology

  The ROMAGAL group assigned a name to each Hi-GAL 1 map in the form of *HIGALllllsbbb_www_RM.fits*, where: *llll* is the galactic longitude of the centre of the map to one decimal place, *s* is the sign of the galactic latitude (p for positive, n for negative), *bbb* is the galactic latitude to two decimal places, *www* is the wavelength of the map in three digits (i.e. 070, 160, 250, 350 and 500, in μm) and *RM* indicates that the pipeline used to create the maps was ROMAGAL's.

- Units

  Both SPIRE and PACS Hi-GAL 1 maps were in units of MJy/sr after converting SPIRE Jy/beam units into MJy/sr (see Appendix A).

- Pixel size

  Map pixel sizes were 3.2", 4.5", 6.0", 8.0" and 11.5" for the 70 μm, 160 μm, 250 μm, 350 μm and 500 μm bands, respectively.

- Number of pixels

  Because scan directions were not always aligned along or across the Galactic plane, the number of pixels in each map varies between tiles and bands. Average sizes in square pixels for the 70 μm, 160 μm, 250 μm, 350 μm and 500 μm Hi-GAL 1 maps were, respectively: 1700×1700, 1200×1200, 1000×1000, 700×700 and 500×500. The edges of the maps were excluded and only the maps' central common PACS and SPIRE area, scanned in both orthogonal and nominal directions, were considered.

- Astrometrical calibration

  The Hi-GAL 1 maps were astrometrically registered by ROMAGAL to ensure astrometric consistency with the MIPSGAL 24 μm data. While the PACS maps were directly registered on the MIPSGAL 24 μm maps (using the measurements of the mean shift of $\sim$10–15 reference objects visible in both data sets), the SPIRE maps were registered on already registered PACS maps using the same procedure.

- Absolute flux calibration

  The Hi-GAL 1 maps were also absolute flux calibrated in order to remove the zero level (or offsets) of the maps. These offsets were obtained by comparing the background emission measured in the Hi-GAL 1 maps, at a given empty sky region, to the emission measured in the same region on a set of model maps created using[3]:

  (i) the sky brightness data measured in the original 60 μm and 100 μm IRIS (Miville-Deschênes and Lagache 2005) maps and the 350 μm and 550 μm Planck HFI (Lamarre et al. 2000) maps, (ii) the differential colour correction between IRAS or Planck and the considered Herschel band and (iii) frequency interpolation.

[3]See Bernard et al. (2010) for a detailed description on the process followed.

The Hi-GAL 1 maps were then smoothed to the common resolution of the IRIS and Planck maps (i.e. 5'), which allowed to compare the integrated emission in the Hi-GAL 1 maps to the predictions of the IRIS-Planck model estimates. Such comparison allowed to finally derive the offset level to be added to the Herschel data to best match the IRIS-Planck data.

- Quality

  The quality of the Hi-GAL 1 maps, with respect to previous missions (e.g. WISE, Spitzer, MSX, IRAS) is staggering. Thanks to its combination of unprecedented wavelength coverage, high sensitivity and resolution, Herschel was capable of mapping the emission from the ISM of the Milky Way at resolutions unmatched by any previous instrument.

  The astonishing accuracy of the Herschel images can be seen in Fig. 2.2 where we show a panoramic view of a fragment of the Galactic plane ($310° < l < 319°$; $-1° < b < 1°$) as seen by Hi-GAL, WISE, Spitzer, MSX and IRAS. The image is centred around $l = 314°$ and $b = 0°$ and expands over a total sky area of $\sim 12° \times 2°$.

Figure 2.2: Panoramic view of a fragment of the Galactic plane ($310° < l < 319°$; $-1° < b < 1°$) as seen by Herschel (Hi-GAL), WISE, Spitzer, MSX and IRAS. The image is centred around $l = 314°$ and $b = 0°$ and expands over a total sky area of $\sim 12° \times 2°$. These are all colour composites created by combining the images in each of the corresponding Herschel, WISE, Spitzer, MSX and IRAS bands. Indicated in the figure are the wavelengths at which these bands are centred and the spatial resolution each of these bands have.

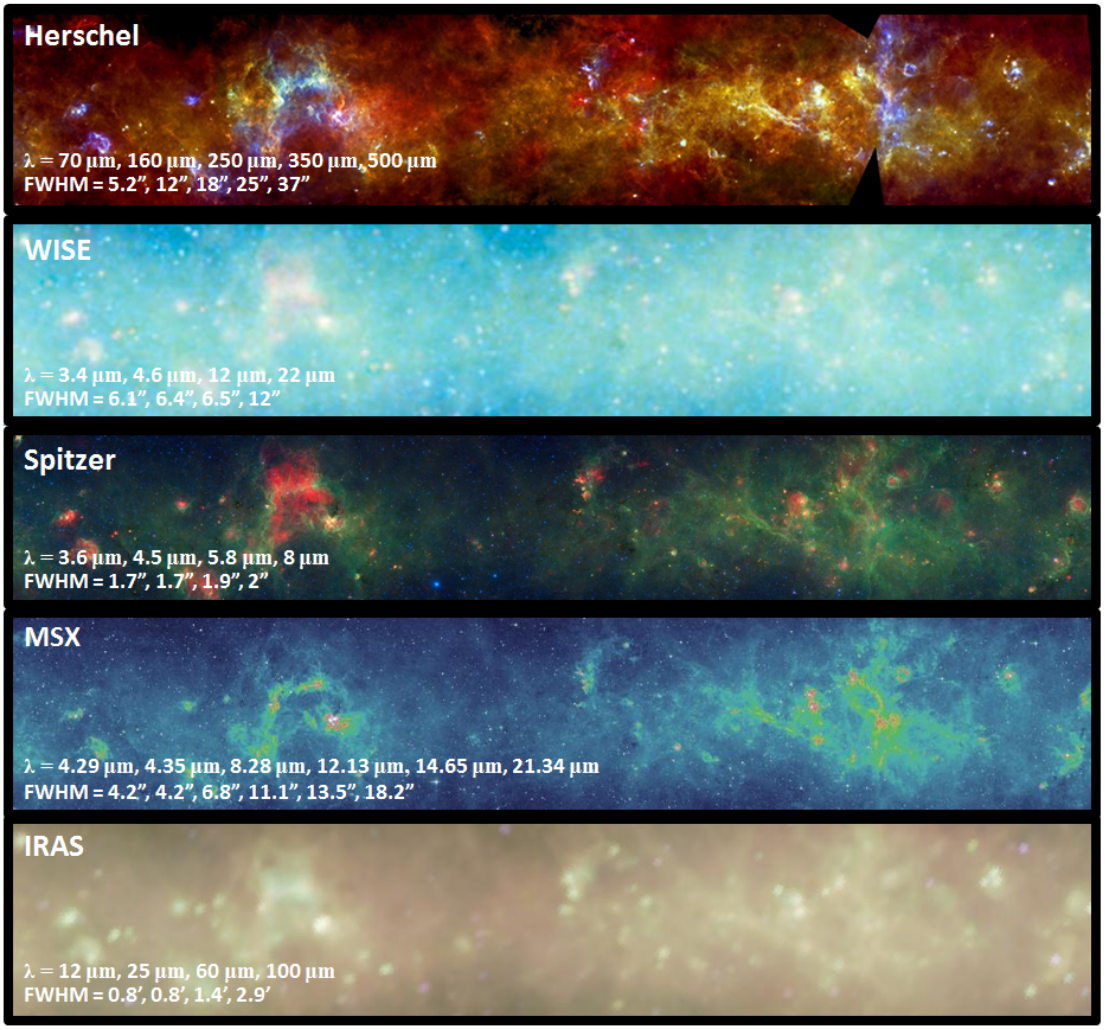

2.5.1 Note on the use of the RMP maps

The RMP is entirely managed by the ROMAGAL group meaning that most members of the Hi–GAL community have no access to the pipeline and therefore cannot process the maps themselves. For a project like ours (that requires the whole set of 63 fields to be processed using the same calibration settings) this fact had dramatic drawbacks regarding our work progress.

At the start of this PhD, only 4 fields were available and it took more than a year for ROMAGAL to deliver all 63 fields. This first set of maps was then found to be in need of calibration changes, which resulted in a second and third maps release. The data used in this thesis is part of this third release, which was dated January 2012. Five months later, that is 1 year and 8 months after starting this project, a fourth new set of maps became available. Unfortunately, by the time this fourth set came out, there was no longer time to redo the work done up until that point. However, whenever it was possible, we updated our results in order to ensure their validity and usability for the new maps. Updates of this nature can be found in Chapter 3 and 4 of this thesis and are duly identified.

2.6 Summary and Conclusions

The purpose of this chapter was to choose an adequate pipeline from the two available pipelines for the creation of the Hi–GAL maps: the Parallel Mode Scan pipeline (PMSP) and ROMAGAL's pipeline (RMP). The two pipelines were described in detail in Sect. 2.2 where we analysed their different drift removal, deglitching, destriping, map–making and denoising techniques.

In order to make such pipeline choice, we visually inspected the output maps obtained with the PMSP and the RMP. We observed that the PMSP-processed maps showed more artefacts (i.e. Airy rings around bright sources, stripes, glitches, holes and edge defects) than the RMP-processed maps and they therefore were of lower quality. We then searched for solid arguments to support our observations, which we found in the work of Traficante et al. (2011). According to Traficante et al. (2011), the superior quality of the RMP maps is due to the fact that the RMP has a higher map artefact removing power. As a result, the RMP-processed maps have a lower presence of stripes, glitches and background noise (S/N) as well as pixel–to–pixel offsets. In light of these results, it was decided to use the maps processed by ROMAGAL.

Chapter 3

Choice of a source and flux extractor for the Hi-GAL maps

"...it was truly amazing - nobody in their right mind would ever have predicted such quality at the very first attempt."

Albrecht Poglitsch

3.1 Introduction

The aim of this chapter is two–fold: to find an adequate algorithm for the detection of the point sources present in the Hi–GAL maps and to find an appropriate algorithm for the extraction of the flux densities of those detected sources. A total of five different algorithms are considered: DAOPHOT, SExtractor, the Wiener Filter, TSF and CUTEX. In the following sections I:

(i) analyse the methods used in these five algorithms,

(ii) test their performance when used on artificial sources,

(iii) define parameters to quantify their efficiency and

(iv) use these parameters to choose the most suitable source and flux extractor.

3.2 Source detection and flux extraction algorithms

On the one hand, a *source extractor* is a routine that automatically: (i) detects astronomical sources from an astronomical image, (ii) obtains accurate astrometric measurements from the earlier detected sources and (iii) builds an output catalogue, usually referred to as *sourcelist*, containing the source positions previously measured, amongst other parameters. The majority of the existing algorithms achieve source detection in two steps. In the first step, termed *image transformation*, a first group of operations are applied to the astronomical image in order to either suppress undesired image distortions or to enhance some of the image features. Depending on the nature of these operations we distinguish between:

- Basic image transformations – noise filtering and estimation of the background level.
- Bayesian approaches[1] – determination of the probability of a pixel to be part of a source or part of the background.
- Multi–scaled strategies – denoising, source highlighting and deblending.

In the second step, termed *source detection*, a second group of operations are applied to the transformed image in order to separate those pixels that belong to sources from those that belong to the background or to noise. Depending on the detection method used we distinguish between:

- Thresholding – sources are identified as those pixels whose intensity exceeds a limit imposed either globally or locally.
- Local peak search – sources are localised in those pixels that constitute a local maximum in their neighbourhood and whose intensity exceeds a limit imposed locally.

Since each detection algorithm employs different image transformations and detection methods, its use will generally only be optimum for (but not restricted to) the original image set that it was created for.

On the other hand, a *flux extractor* is a routine that automatically: (i) accesses the sourcelist previously generated by a source extractor, (ii) performs precise photometric measurements at the positions listed in such sourcelist and (iii) creates a new sourcelist containing the source positions and flux densities amongst other parameters.

[1] The functioning of these methods is based on *Bayesian model selection methods* (see Appendix B).

There are two different techniques for measuring the flux of point sources: *PSF-fitting* [2] and *Aperture photometry*.

- PSF-fitting

  This method works under the assumption that the shape of the image profile of any point source, as recorded in the telescope CCD camera, is given by the telescope PSF and is similar to a Gaussian. With this premise, the program builds a semi–empirical model PSF, which is used later to fit the data. In order to construct a realistic PSF, the program chooses, from across the image, a set of bright, isolated point sources known as the *PSF stars*. The image profile of these stars is then fitted with an analytic function (e.g. Gaussian, Lorentzian or Moffat). Whichever function fits the best is defined as the model PSF. Next, the model PSF is used to fit all the sources in the image. After the fit, the sources are subtracted to analyse the remaining residuals (i.e. sky brightness, background noise,...etc.), which are then used to build a new model PSF, more realistic than the previous. This process is repeated until the residuals are minimised for a given model PSF. The height of the final model PSF is taken as the flux of the source.

- Aperture photometry

  This method obtains the flux of a source by subtracting the background noise from the source total flux (noise + source signal). The program allows the user to define two regions (or *apertures*): the *source* and the *sky* radii. The apertures can be defined either circular or elliptical. The source radius encloses the image of a star while the sky radius includes only background. The total flux is calculated by adding the flux in all the pixels within the source radius and the background noise is calculated as the mode of the flux values found in the pixels within the sky radius.

  Although this method is faster than PSF-fitting, it does not work in the case of blended sources. In this case, the images of the different sources overlap and thus, it is not possible to define an aperture that includes the light of a given star but excludes the light from its neighbours.

While simple flux extractors will include only one of the previous two techniques, programs of higher complexity generally combine the two in order to obtain more accurate results.

[2] The PSF can be defined as the response of the measuring instrument to a point source.

3.3 Photometric packages

Programs that implement both source detection and flux extraction algorithms are often referred to as photometric packages.

3.3.1 Most common photometric packages in the pre-Herschel era

Before Herschel's arrival, three of the most common photometric packages used on IR images were: *DAOPHOT*, *SExtractor* and the *Wiener Filter*.

3.3.1.1 DAOPHOT

DAOPHOT (Stetson 1987) is a stellar photometry package, designed at the *Dominion Astrophysical Observatory* (DAO), that carries out photometry of point sources in stellar crowded fields with relatively uniform background emission conditions.

- Source detection

  In order to detect point sources from an image DAOPHOT inspects each image pixel looking for pixel-centred real stellar sources (i) whose brightness is greater than a user defined global threshold limit and (ii) whose roundness and sharpness levels are within some established limits. The nature of the sources is then checked by convolving a Gaussian profile to each pixel, which allows the program to discriminate cosmic rays and CCD defects and to differentiate stellar point sources from extended sources. In order to estimate the background, DAOPHOT applies iteratively a thresholding technique, which is based on the mean and standard deviation. The statistics derived from this process are then used to calculate the value of the true background with the following expression: $3 \times median - 2 \times mean$.

- Flux extraction

  In order to measure the flux of the sources DAOPHOT makes use of a technique that combines aperture and PSF-fitting photometry. Firstly, the program runs aperture photometry upon all the detected stellar point sources in order to obtain an estimation of the sources' flux. Secondly, DAOPHOT chooses a set of PSF stars from which it builds a semi-empirical model PSF, scaled to the fluxes estimated with aperture photometry. This model PSF is then fit to the sources in order to obtain their precise flux.

3.3.1.2 SExtractor

SExtractor (Bertin and Arnouts 1996) is a stellar photometry package that detects and extracts point and extended sources in homogeneous background emission conditions.

- Source extraction

  In order to simultaneously detect point sources and estimate the background from an image, SExtractor makes use of a Bayesian source filtering technique, which inspects each image pixel to determine whether the pixel data can be described more realistically by:

  (i) An *Empty sky, uniform background* model - solely consisting of a flat uniform background.

  (ii) A *Point source, uniform background* model - consisting of a flat uniform background on top of which sits a pixel–centred point source that is modelled as a circular 2D Gaussian of known FWHM. The height of this Gaussian is taken as the flux of the source, which must be greater than a user–defined global threshold limit.

- Flux extraction

  In order to simultaneously measure the flux, position, local background, the PSF FWHM and determine the nature of the sources, SExtractor makes use of a Bayesian source photometry technique, which inspects each image pixel to determine whether the pixel data can be described more realistically by:

  (i) An *Empty sky, uniform background* model - solely consisting of a flat uniform background.

  (ii) A *Point source, uniform background* model - consisting of a flat uniform background on top of which sits, at a given (parametrized) position (X,Y), a point source that is modelled as a circular 2D Gaussian of known FWHM.

  (iii) An *Extended source, uniform background* model - identical to the second model with the exception that the FWHM is now allowed to vary as a model parameter.

3.3.1.3 The Wiener Filter

The *Wiener Filter* (WF, Vio et al. 2002) is a Fourier Transform (FT) deconvolution filter for 2D images, which can be used to carry source and flux extraction of point sources corrupted by uniform background noise.

- Source extraction

  In order to detect point sources from an image, the Wiener Filter builds a filter to remove the image background noise so that sources are enhanced with respect to the background.

  First, the program measures the power spectrum (S) of the image background. This background is assumed to be isotropic and uncorrelated with the signal of the sources, which are assumed to have a spherically symmetric profile such as that from the telescope PSF ($PSF_{telescope}$).

  Next, the program builds up a filter (P) that is cross–correlated with the signal map in order to obtain a filtered map. In the case of a flat background: $P = PSF_{telescope}$ while for a structured background: $P^{'} = FT(P/S)$.

  The variance of the filtered map is then minimised, which results in the signal–to–noise ratio at the sources' positions being maximised. Finally, sources are located by finding the positions in which the image signal values are above the chosen threshold.

- Flux extraction

  In order to obtain the flux of the sources, the Wiener Filter makes use of PSF fitting. First, the telescope PSF is shifted to a source position and scaled to the source signal. Next, the PSF height is taken as the flux of the source.

3.3.2 New algorithms for the Herschel era

With the arrival of Herschel, a new photometric package, *CUTEX*, and a new flux extractor, the *Timeline Source Fitter*, were created. In the following sections, we describe in detail the functioning of the CUTEX and TSF algorithms.

3.3.2.1 TSF

The *Timeline Source Fitter* (TSF, Bendo et al. 2013) is a Jython routine, which performs photometry exclusively on the 250 μm , 350 μm and 500 μm SPIRE maps at a user-specified source position (i.e. it does not perform source extraction). Prior to running the TSF flux extraction routine, the user must:

(i) Provide TSF with a sourcelist that includes the sources' RA and dec.

(ii) Indicate the SPIRE photometer array used to create the map, either *PSW* (250 μm), *PMW* (350 μm) or *PLW* (500 μm).

(iii) Select a suitable value for the following input parameters that the TSF requires:

* The *rPeak* - which defines the source radius. This radius should include the source's flux peak and should extend to the location of the minima between the peak and the first diffraction ring of the beam profile, thus encompassing the central part of the beam that most closely resembles a Gaussian function.

* The *rBack* - which defines the sky radius. This radius should exclude the rPeak and should be large enough to include a representative area of the source's surrounding background.

* The *FWHM* - which establishes the width (FWHM) and the shape of the Gaussian that the TSF uses to fit the data enclosed within the rPeak. The Gaussian FWHM can be set to be either a free parameter or a fixed parameter while the shape of the Gaussian can be set to be either circular or elliptical.

- Flux extraction

  In order to measure the flux of the sources, TSF makes use of an aperture photometry technique slightly different to that described in Sect. 3.2. Here, the background noise and the total flux are not calculated using the signal measured directly in the maps within the sky and the source radii defined. Instead, these are calculated using the Signal Timeline Data[3] recorded by the bolometers that have scanned along positions falling within the source and the sky radii defined.

[3]In Sect. 1.4.4.1 we defined the Signal Timeline Data as a dataset in which the X–values correspond to the Sample Time (in sec) and the Y–values correspond to the signal from every PSW, PMW and PLW photometer array bolometer.

This signal data (in V) is then converted to flux values (in mJy) and the measured background noise is finally subtracted from the total flux in order to obtain an estimation of the sources' flux (see Bendo et al. 2013 for details).

Finally, TSF fits the sources' signal distribution with the user defined 2D Gaussian function and establishes the sources' flux to be equal to the height of this function.

3.3.2.2 CUTEX

The *Curvature Thresholding Extractor* (CUTEX, Molinari et al. 2011) is an IDL code, designed by the ROMAGAL team for the detection and measurement of compact[4] sources in the Hi–GAL maps.
Before running the source extraction routine, the user can choose to enable the CUTEX *CutEdges* routine. When activated, this routine allows the user to interactively cut the map edges in *ds9* [5] to avoid the map boundary regions whose quality is often very degraded. The original map is then rejected and all following CUTEX steps are performed with the new selected map area.

- Source extraction

  In order to detect point sources from an image, CUTEX builds a set of 4 new images containing the 2^{nd}–order Lagrangian differentiation (i.e. *the curvature*) of the original signal image in 4 different directions: X,Y and the XY and YX bisectors. After differentiation, the diffuse emission has been removed and sources stand out with respect to the background (see Fig. 3.1).

  Next, pixels whose curvature exceeds the chosen threshold in all 4 differentiation directions and are contiguous in space are grouped into clusters. If no local peaks are found on the curvature values within a cluster, the totality of the cluster pixels is considered to constitute a single candidate source. If instead, local peaks are found, the group of cluster pixels are segmented into as many individual candidate sources as local peaks were found.

  The central position of a candidate source is given by the cluster pixel for which the curvature is at least 1σ above the curvature of all the surrounding cluster pixels.

[4] A compact source is defined in the CUTEX User's guide as a source with a size smaller than 3 times the adopted PSF.
[5] ds9 is an astronomical imaging and data visualization application.

Figure 3.1: Example of the CUTEX performance during the source detection step. Panel (a) shows a 24 μm Spitzer/MIPS map of IRAS23385+6053 (Mol160) while panel (b) shows the 2^{nd}–order derivative images of the map above. The derivatives have been computed in 4 different directions: along the x–axis (top–right), y–axis (top–left), and the two diagonals (bottom panels). From these images, we can see that after CUTEX differentiation process, the diffuse emission is successfully removed from the maps, the sources stand out from the background and can be easily extracted. The images shown below were extracted from Molinari et al. (2011). Although in the derivative images the sources' peaks are negative, their sign was deliberately inverted by Molinari et al. (2011) for cosmetic purposes. Thus, in these images the sources' peaks appear in white instead of black.

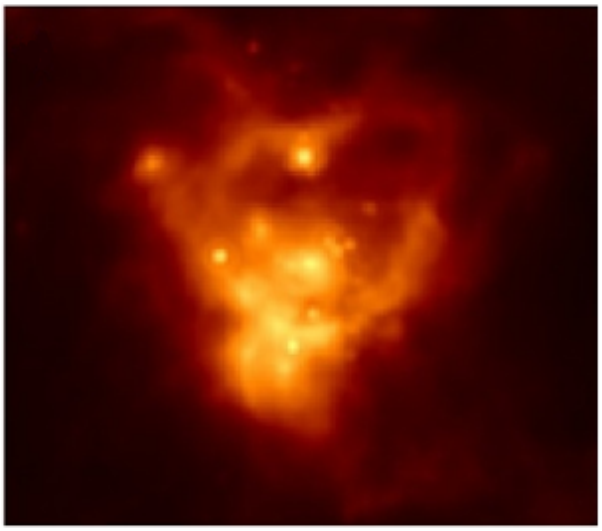

(a)

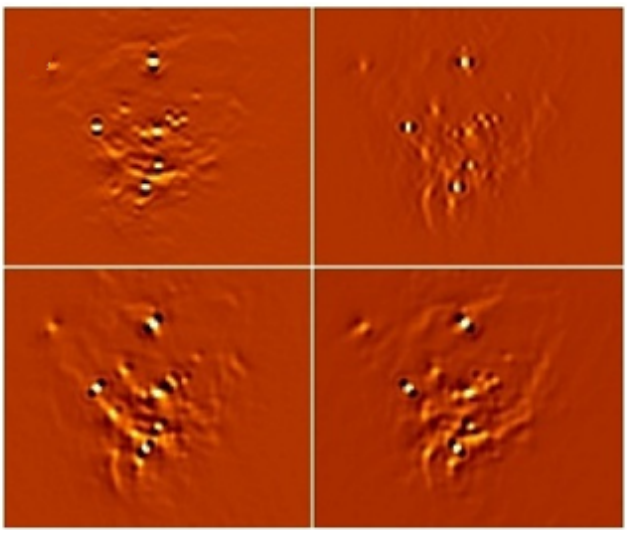

(b)

Figure 3.2: Schematic of the CUTEX source size estimation technique. A total of 8 pixels (2 per each differentiation axis) are used to delimiter the area to which CUTEX fits an ellipse with variable semi-axis a (minor) and b (major) and position angle θ. The distances between any two pixels at a given differentiation axis and the source peak (d_1, d_2) must be within 20% of each other. Otherwise, only the nearest point in such direction is kept.

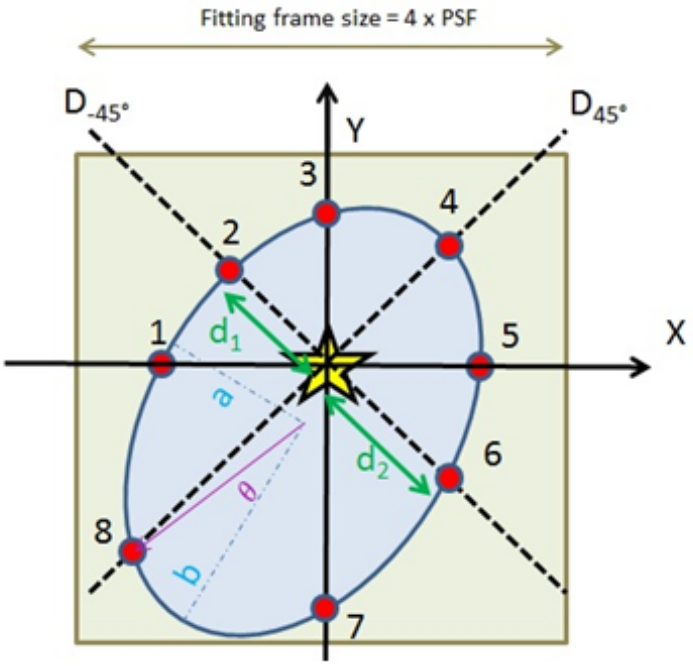

The shape (size and orientation) of a candidate source is given by the area defined by the 8 pixels whose curvature exceeded the chosen threshold in all 4 differentiation directions (see Fig. 3.2). The background emission of the map is defined as the mean of the residual emission left in the maps after subtracting the sources. Once estimated, the background is removed by means of a planar inclined plateau.

Below, we describe the routines, parameters and keywords that are available in CUTEX when source extracting and justify their activation and/or their values.

1. CutEdges

   The *CutEdges* routine, when activated, allows the user to cut the slanted edges[6] present on the Hi-GAL maps in order to prevent CUTEX from extracting sources lying on the map boundary regions where the map quality is greatly degraded. Despite being an optional routine, its activation is strongly recommended by ROMAGAL and so, we manually selected the map boundaries we wanted to reject and ran the rest of CUTEX source detection routines on these new maps.

[6] These edges arise from when the Herschel spacecraft moved from one scanleg to another.

2. PSFPIX and RANGE

   The *PSFPIX* parameter is defined as the number of pixels the user wishes to consider when sampling the PSF of the input image. On the other hand, the *RANGE* parameter is defined as the number of pixels away from the candidate source centre the user wishes CUTEX to check for the 2^{nd} derivative minima (see Sect. 3.3.2.2).

   The choice of low (high) PSFPIX and RANGE values results in CUTEX detecting compact (extended) sources. Therefore, these two parameters can be used to set the size of the sources the user wishes to select. In our case, since we wanted to avoid the inclusion of extended sources in our catalogue, we chose the PSFPIX and RANGE values to be low.

   Following ROMAGAL's recommendation, we selected PSFPIX=(1.56, 2.7, 2.98, 3.125, 3.11) for the 70 μm, 160 μm, 250 μm, 350 μm and 500 μm bands and RANGE=9 for all bands.

3. thr

   The *thr* parameter is defined as the curvature threshold level the user wishes CUTEX to use in order to identify the source candidates.

   Ideally, in order to select an appropriate threshold value to be used in the extraction of sources in a specific Hi–GAL map, one should test "n" possible threshold values on that particular map and then analyse the results obtained for each value in order to verify the authenticity of the extracted sources. This process could be done either by visual inspection of the detected sources or by checking whether those sources have been previously identified in other catalogues.

   In our case, given that we had 63 maps and 5 bands and that we detected around 10^4 sources per tile, we would have a total of $315 * n$ CUTEX run tests to do and around $315 * n * 10^4$ sources to inspect. Since we had neither the time nor the computing resources to carry out such exhaustive tests, we adopted a much simpler strategy in which a total of 20 thresholds around thr=2 (i.e. CUTEX default configuration) were tested in the l=290°, b=0° Hi-GAL 1 field (see Fig. 3.3a).

From the visual inspection of these results we chose the threshold values that were the most adequate for each band. We selected: thr=1.8, 2.5, 3.5, 3.2 and 3 for the 70 μm, 160 μm, 250 μm, 350 μm and 500 μm bands, respectively. This selection of threshold values was then used on two other fields and confirmed to be also appropriate.

4. LOCAL–THRESH

   The *LOCAL–THRESH* keyword, when activated, stops CUTEX from using a single global threshold value on all of the map. Instead, the program will compute a local threshold value considering only the pixels lying within a windows centred in the source and 61×61 pixels wide.

   According to the CUTEX User's guide, the adoption of this approach leads to an increase of the number of faint sources detected by CUTEX and so, we activated this keyword.

5. NPIXMASK

   The *NPIXMASK* parameter establishes the minimum number of closest-neighbour pixels above the threshold to be found by CUTEX to define a source candidate. Following ROMAGAL's recommendation, we selected NPIXMASK=3.

Other methods or keywords include: ABSCURV and SMOOTHING, which were kept in the CUTEX default configuration. The definitions of these parameters as well as further information about their use can be found in the CUTEX User's guide.

- Flux extraction

  In order to find the flux of a source, CUTEX fits the source signal distribution with a 2D elliptical Gaussian whose shape is given by the source shape previously determined.

  CUTEX returns two flux values: a *peak* flux value and an *integrated* flux value. While the peak flux is given by the maximum flux found by the 2D elliptical Gaussian used in the fit, the integrated flux corresponds to the flux density integrated within the ellipse used in the fit.

  Next, we describe the routines, parameters and keywords that are available in CUTEX when flux extracting and justify their activation and/or their values.

1. DMAX–FACTOR

   The *DMAX–FACTOR* parameter is used in order to define the size of the window, centred on a source, where CUTEX fits a Gaussian to the source flux distribution. The choice of an inappropriate window size can lead to CUTEX making an incorrect estimation of the source flux and background and so, it is very important to select an adequate window size. In the CUTEX default configuration, this window is a square with a size given by:
   $[n*(2*PSF)+1] \times [n*(2*PSF+1)]$; where n=2 and PSF is in pixels but following ROMAGAL's recommendation, we selected DMAX–FACTOR=3.

2. CLOSEST–NEIGH

   In cases where a source (say, A) is found to be associated with other sources (say, B and C) CUTEX, in its default configuration, will simultaneously obtain the flux of all of the sources by simultaneously fitting a Gaussian to all of them. The *CLOSEST–NEIGH* keyword, when activated, stops CUTEX from doing such simultaneous fitting. Instead, the program will fit first source A and its closest neighbour (say, source B). Then, it will simultaneously fit source A, B and C, but storing only the flux for source B, and it will repeat this process for source C to obtain its flux. According to the CUTEX User's guide, the adoption of this approach leads to fluxes of higher accuracy and so, we activated this keyword.

3. BACKGFIT

   The *BACKGFIT* keyword, if activated, stops CUTEX from using a planar approximation to fit the background so that $flux_{bg} = C_1 * x + C_2 * y + C_3$. Instead, the program uses a 2^{nd} order polynomial so that:

   $$flux_{bg} = C_1 * x^2 + C_2 * y^2 + C_3 * x * y^2 + C_4 * x + C_5 * y + C_6$$

   In the previous expressions, x and y are the coordinates of the pixel considered in the fit and $C_1 - C_n$ are coefficients. According to the CUTEX User's guide, the use of a 2^{nd} order polynomial provides a better estimation of the background flux and so, we activated this keyword.

Other keywords are: *MAX–DIST–FAC*, *DTRH*, *PSFLIM* and *SMOOTHING*, which we kept in default configuration (see CUTEX User's guide for definitions).

3.4 Application on the Hi-GAL maps

With the aim of finding a suitable source extractor and flux extractor for the Hi–GAL maps, we proceeded to test the previous photometric packages on the 250 μm l=290°, b=0° Hi–GAL 1 map[7] (see Fig. 3.3a).

This process allowed us to detect and discard those algorithms unable to adequately perform source detection and flux extraction on the Hi-GAL maps as well as to identify the most efficient algorithm/s. The successful algorithm/s was then run through the 70 μm, 160 μm, 250 μm, 350 μm and 500 μm l=290°, b=0° Hi–GAL 1 maps into which we injected a total of 121 identical synthetic sources with 2D circular Gaussian shape PSF. These maps are hereafter referred to as *tests maps*.

The artificial sources were uniformly distributed across the maps and their flux level was set to be the same for all the sources and was changed, in each test, to be either 0.1, 0.2, 0.5, 1, 2, 5, 10, 20, 50, 100 or 200 Jy. We then extracted the sources from the maps and compared the algorithm's readout source position and flux to the input source position and flux level.

The use of synthetic sources sitting on top of a real Hi–GAL map background was preferred over the use of real known sources (or synthetic sources) sitting on top of a synthetic map background for three reasons. Firstly, with real sources one can never be sure of knowing their exact position and flux density since there is always a discrepancy between the values returned by different algorithms, whereas with synthetic sources these variables are absolutely accurate. A second advantage is that one can choose the PSF of a synthetic source to be a perfect 2D Gaussian whereas with real sources, their PSF is always distorted by the telescope and electrical readout effects. Finally, with a synthetic map it is not possible to fully recreate the real maps' strong and highly variable foreground and background emission. The number of artificial sources added to the maps, (i.e. 121 sources), is a result of having imposed a distance of 380 arcsec between the artificial sources. This distance was established:

(i) so that the TSF was able to perform aperture photometry within a sky radius large enough, (i.e. *rBack* 360 arcsec), to enclose a representative area of the sources' background and,

(ii) to ensure there was no contamination between the artificial sources.

[7] The l=290°, b=0° field was one of the two first non–SDP fields released to the Hi–GAL community.

The maximum flux given to the artificial sources, (i.e. 200 Jy), was set taking into account that, with the exception of the $l = (+2, 0, -2)^\circ$ Hi-GAL 1 fields, the majority of the Hi-GAL 1 fields were scanned without the *Bright Source Setting*[8] enabled. This setting is required when observing sources brighter than 200 Jy to avoid the detectors' saturation. As a result, with the exception of the $l = (+2, 0, -2)^\circ$ Hi-GAL 1 fields, all the sources detected in the remaining Hi-GAL 1 fields should have fluxes lower than 200 Jy. The fluxes selected between the [0,200] Jy range were chosen with the only condition of being a representative flux sample and convenient.
The tests described above provided us with a mean to compare the algorithms' performance when source-extracting and flux-extracting and to establish whose extraction was more suitable and whose photometry was the most accurate.
The algorithms' efficiency was quantified by means of three parameters:

(i) the *Source Extraction Limit* (SEL),

(ii) the *Source Flux Fitting Limit* (SFFL) and

(iii) the *Source Flux Accuracy Limit* (SFAL).

Furthermore, the tests also allowed us to:

(iv) establish *Flux Correction Factors* (FCF) when needed,

(v) analyse the statistical outliers present in the output fluxes and,

(vi) derive the flux uncertainties associated to the fluxes returned by the algorithm.

In the next sections we show the results obtained when testing DAOPHOT, SExtractor, the Wiener Filter, TSF and CUTEX in the tests maps, with and without artificial sources. We first present those algorithms found to be inadequate (see Sect. 3.4.1). Next, we introduce those that were found to be suitable (see Sect. 3.4.2).

3.4.1 Inadequate algorithms

Shown in Fig. 3.3b-d are the results obtained when running DAOPHOT, SExtractor and the Wiener Filter through the 250 μm l=290°, b=0° Hi–GAL 1 map, which we discuss in the following sections.

[8] See Sect. 2.4.2 in the SPIRE PACS Parallel Mode Observers' Manual

Figure 3.3: Images showing the sources extracted (yellow circles) from the (a) 250 μm l=290°, b=0° Hi–GAL 1 map when using (b) DAOPHOT, (c) SExtractor and (d) the Wiener Filter.

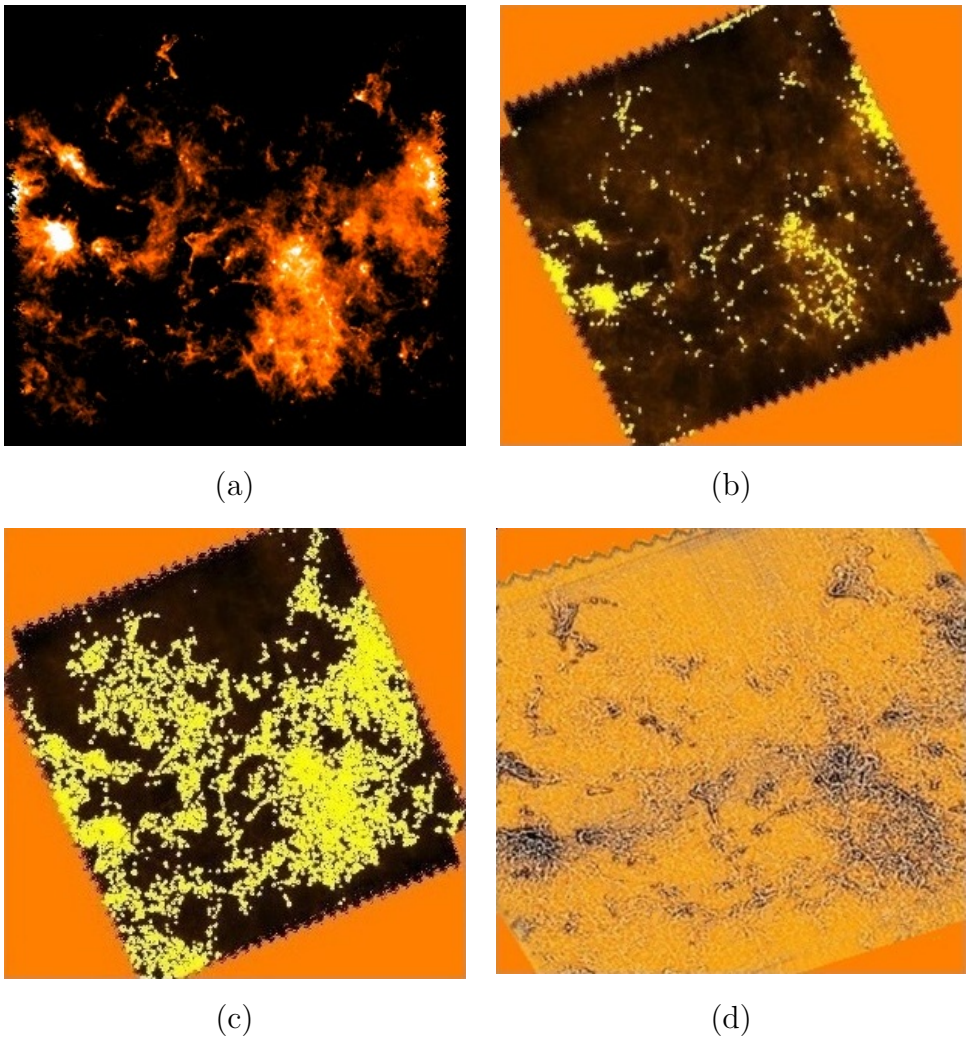

(a) (b)

(c) (d)

3.4.1.1 DAOPHOT

- Source extraction

  The results in Fig. 3.3b show that although DAOPHOT was able to extract some real isolated sources, located all over the test map, most of the sources extracted by DAOPHOT were: (i) concentrated within the brightest regions, (ii) following the ISM filamentary structures or (iii) located at the edges of the map - all these being signs of a faulty source extraction.

  The previous effects are a direct consequence of DAOPHOT's use of a global threshold, which is only adequate when applied to maps with a uniform background emission. However, such conditions are rarely met in the Hi–GAL maps where the background emission is so strong and variable that no general threshold can be found to be appropriate for every region in the map.

  For instance, let us consider a first case where a faint source s_1 is embedded in a map region A with low background emission and a second case where a different source s_2, brighter than source s_1, is embedded in a map region B whose (background) emission is higher than that of region A and source s_1 but lower than that of source s_2 (see Fig. 3.3b).

  Under these circumstances, if we chose a low threshold, DAOPHOT would detect source s_1, despite its faintness, but it would also misread the strong emission in region B as a collection of several clustered (or aligned) unreal sources (i.e. false positives).

  On the contrary, if we chose a high threshold, DAOPHOT would then detect source s_2 and would reject the emission in region B but it would not detect the source s_1 despite being a real source (i.e. false negative).

  Therefore, although increasing the threshold would minimise the presence of false positives it would also lead to many false negatives.

- Flux extraction

  DAOPHOT was found to return incorrect fluxes, this being a result of its inadequate: (i) source extraction and (ii) use of global source and sky radii – which are not suitable for the Hi–GAL maps where there are sources with a high level of blending and a great variety of sizes and shapes.

3.4.1.2 SExtractor

- Source extraction

  The results in Fig. 3.3c show that SExtractor was not capable to cope with the strong background emission present in the Hi-GAL maps. Like DAOPHOT, SExtractor erroneously misread such emission as a collection of highly clustered sources, most of which are expected to be false positives. In the case of SExtractor, however, the number of extracted sources was found to be higher than that of DAOPHOT. As a result, the number of false positives detected by SExtractor is expected to be much higher than that of DAOPHOT. These results indicate that SExtractor has a higher sensitivity than DAOPHOT, which makes SExtractor's source extraction even more inadequate than that of DAOPHOT.

  The previous effect is due to: (i) SExtractor's use of a Bayesian source filtering technique – in which only models with uniform background are considered, and (ii) SExtractor's use of a global threshold – which is inappropriate for the Hi–GAL maps as discussed in the previous section.

- Flux extraction

  SExtractor was found to return incorrect fluxes, this being a result of: (i) SExtractor's inadequate source extraction and (ii) SExtractor's use of a Bayesian source photometry technique – in which only models with uniform background are considered.

3.4.1.3 The Wiener Filter

- Source extraction

  The results in Fig. 3.3d show that, in general, the Wiener Filter was able to remove most of the map's background diffuse emission except for some ISM filamentary structures. Unfortunately, in order to successfully remove such emission from the map, the threshold had to be set so high that also the map sources were filtered in the process and only the filamentary structures remained. For this reason, the Wiener Filter was established to be inadequate for the extraction of sources from the Hi–GAL maps.

- Flux extraction

  The Wiener Filter was found to return incorrect fluxes, this being a result of: (i) the Wiener Filter's inadequate source extraction and (ii) the preservation of the ISM filamentary structures.

3.4.2 Adequate algorithms

Shown in Fig. 3.4 is the result obtained when running CUTEX through the 250 μm l=290°, b=0° Hi–GAL 1 map, which we now discuss together with the TSF results.

3.4.2.1 TSF

- Flux extraction

  The TSF use of Signal Timeline Data was found to return fluxes much more accurate than those obtained with DAOPHOT, SExtractor and the Wiener Filter – which use the signal data directly read from the map and are therefore affected by the smearing effects of pixelisation. The accuracy of these fluxes was assessed on artificial sources and is discussed and compared to that of the CUTEX fluxes in Sect. 3.5.

3.4.2.2 CUTEX

- Source extraction

  The results in Fig. 3.4 show that CUTEX was able to efficiently separate the sources from the background emission and the ISM filamentary structures thanks to its: (i) image differentiation method – through which CUTEX removes the map's diffuse emission and (ii) source finding strategy – which ensures that the filamentary structures are not misread as sources.

- Flux extraction

  CUTEX tailoring of the Gaussian function used to fit each of the detected sources, combined with CUTEX's highly efficient source extraction, were found to result in fluxes of high accuracy. The accuracy of these fluxes was assessed on artificial sources and is discussed and compared to that of the TSF fluxes in Sect. 3.5.

Figure 3.4: Images showing the sources extracted (blue circles) from the 250 μm l=290°, b=0° Hi–GAL 1 map when using CUTEX.

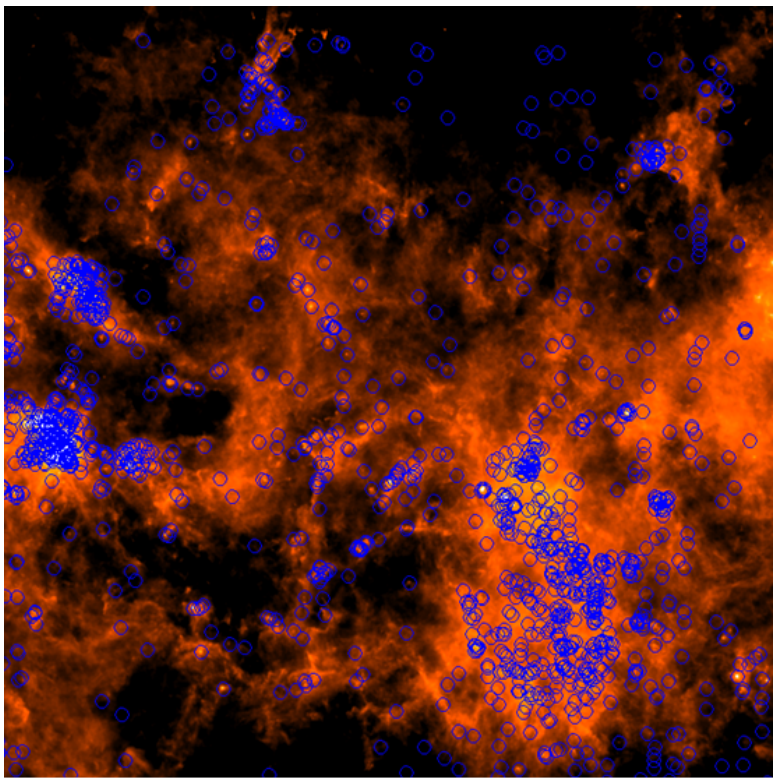

3.5 Determination of the efficiency of TSF and CUTEX

In light of the results presented in the previous sections, we concluded that neither DAOPHOT, nor SExtractor nor the Wiener filter were suitable for the source and flux extraction of sources in the Hi–GAL maps.

On the contrary, both TSF and CUTEX were found to be adequate and so we proceeded to run them through the 70 μm, 160 μm, 250 μm, 350 μm and 500 μm l=290°, b=0° Hi–GAL 1 maps with artificial sources (see Fig. 3.5).

In the following sections we establish the definitions of the *Source Extraction Limit*, the *Source Flux Fitting Limit* and the *Source Flux Accuracy Limit* and present the values found in TSF and CUTEX for these parameters (see Sect. 3.5.1, 3.5.2 and 3.5.5). Moreover, we present the Flux Correction Factors that we derived from the analysis of the fluxes returned by the algorithms (see Sect. 3.5.3). Also, we examine the distributions of the fluxes returned by TSF and CUTEX in order to identify statistical outliers (see Sect. 3.5.4). In addition, we determine the flux uncertainties associated with the output TSF and CUTEX fluxes (see Sect. 3.5.6). Finally, we compare our findings on CUTEX performance with the results established later on by the ROMAGAL group (see Sect. 3.5.7).

Figure 3.5: Image showing the 121 artificial sources injected in the 250 μm l=290°, b=0° Hi–GAL 1 map and successfully extracted with CUTEX.

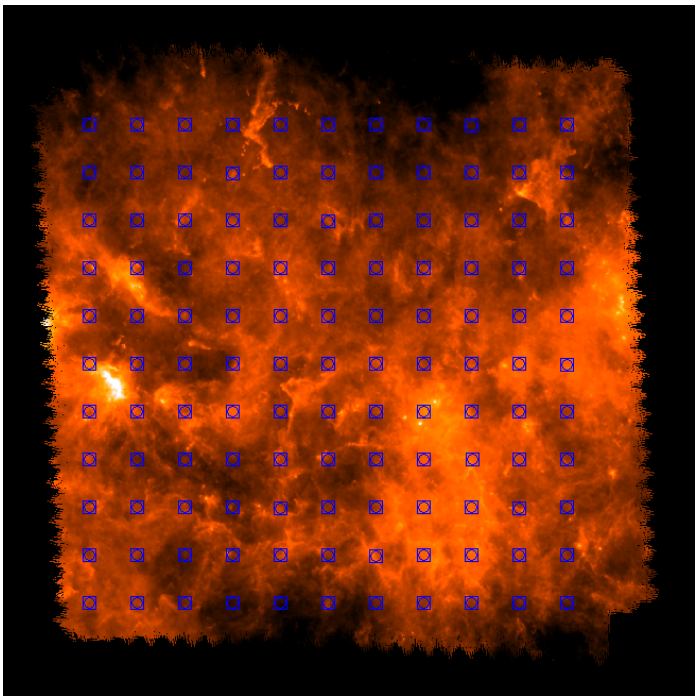

3.5.1 Source Extraction Limit

- Definition

  When using CUTEX to extract the synthetic sources from the maps, it was found that there were sources which CUTEX did not extract. The number of non extracted sources was observed to increase as the injected flux level decreased and to vary for each band.

  The *Source Extraction Limit* was introduced in order to establish the minimum flux level, in each band, for which CUTEX was able to extract the total 121 injected sources, i.e. the 100% of the injected source sample.

  The importance of this parameter relies on the fact that it provides us with an absolute measure of the completeness of the output sourcelist generated by CUTEX.

  For instance, if CUTEX, in a specific band, cannot detect sources fainter than 1 Jy, the generated sourcelist for that band will only include sources brighter than 1 Jy.

  Furthermore, should a new real point faint source be detected in one band, its mis–detection on the other bands could lead to its mis–classification as a false positive.

- Results

  Shown in Fig. 3.7 is a plot indicating the percentage of sample sources extracted by CUTEX for the different injected flux densities on each band. Here, we see that the minimum flux levels for which CUTEX was able to extract 100% of the injected source sample in the 70 μm, 160 μm, 250 μm, 350 μm and 500 μm bands are: 0.5 Jy, 1 Jy, 0.1 Jy, 0.1 Jy and 2 Jy, respectively.

- Conclusions

  CUTEX Source Extraction Limits for the 70 μm, 160 μm, 250 μm, 350 μm and 500 μm bands were found to be: 0.5 Jy, 1 Jy, 0.1 Jy, 0.1 Jy and 2 Jy, respectively.

  Thus, while CUTEX 250 μm and 350 μm band output sourcelists are complete within the [0.1 Jy, 200 Jy] flux range, CUTEX 70 μm, 160 μm and 500 μm band output sourcelists are only complete within the [0.5 Jy, 200 Jy], [1 Jy, 200 Jy] and [2 Jy, 200 Jy] flux ranges, respectively.

3.5.2 Source Flux Fitting Limit

- Definition

  When using TSF and CUTEX to extract the flux of the maps' sources, it was found that there were cases in which CUTEX and TSF would return null or negative fluxes. The number of sources with null or negative fluxes was observed to increase as the injected flux level decreased.

  The *Source Flux Fitting Limit* was introduced in order to establish the flux level, in each band, for which the number of positive fluxes returned by TSF and CUTEX was maximised while the number of null and negative fluxes were minimised.

  This parameter provides us with an idea of the limitations that TSF and CUTEX have when flux-extracting faint sources.

- Results

  Shown in Fig. 3.6, 3.8 and 3.9 and also listed in Table 3.1 and 3.2 are:

  (i) The percentage of sample sources for which TSF and CUTEX returned a null or negative flux in each band - labelled $Flux = 0$ and $Flux < 0$, respectively.

  (ii) The percentage of artificial sources for which TSF and CUTEX returned a positive flux density in each band - labelled $Flux > 0$.

  (iii) Also indicated (for CUTEX only) is the percentage of sample sources CUTEX failed to extract - labelled *Not extracted*. These sources are not included in CUTEX output sourcelists whereas $Flux = 0$ sources are included but have been mistakenly attributed a null flux.

  Here, we see that the flux levels for which the number of TSF positive fluxes is maximised and the number of TSF null and negative fluxes is minimised, in the 250 μm, 350 μm and 500 μm bands, are: 1 Jy, 1 Jy and 1 Jy, respectively. In the case of CUTEX, these are: 1 Jy, 2 Jy, 0.1 Jy, 0.2 Jy and 2 Jy, respectively.

- Conclusions

  The TSF Source Flux Fitting Limit for the three SPIRE bands is 1 Jy, while CUTEX Source Flux Fitting Limits for the 70 μm, 160 μm, 250 μm, 350 μm and 500 μm bands are: 1 Jy, 2 Jy, 0.1 Jy, 0.2 Jy and 2 Jy, respectively.

Figure 3.6: Percentage of sample sources for which TSF returned a null ($Flux = 0$), negative ($Flux < 0$) or positive ($Flux > 0$) flux in the 250 μm, 350 μm and 500 μm bands. The dotted grey lines indicated in the plots correspond to the established TSF Flux Fitting Limits. These are: 1 Jy, 1 Jy and 1 Jy for the 250 μm, 350 μm and 500 μm bands, respectively.

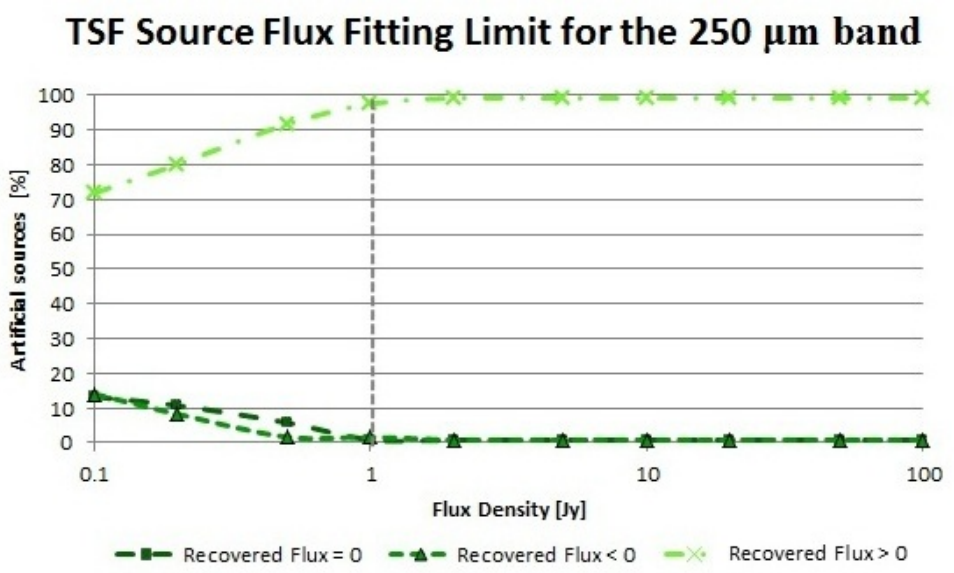

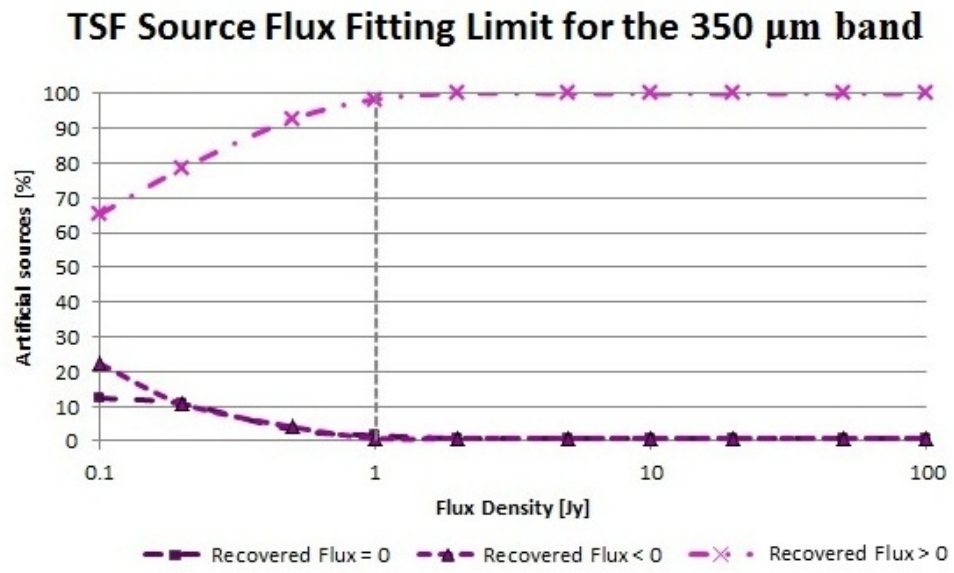

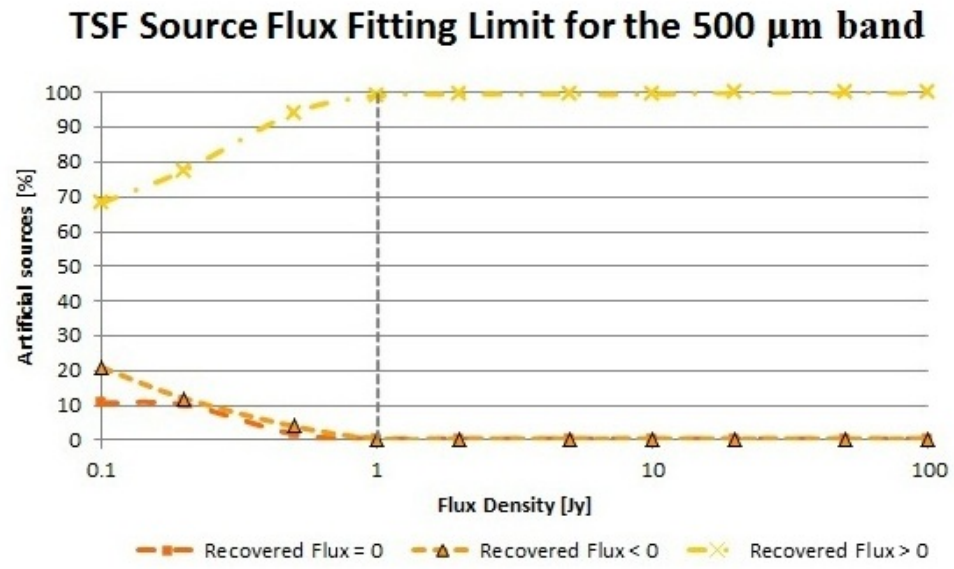

Figure 3.7: Percentage of sample sources extracted by CUTEX in the 70 μm, 160 μm, 250 μm, 350 μm and 500 μm bands for the different injected flux densities. CUTEX Source Extraction Limits are: 0.5 Jy, 1 Jy, 0.1 Jy, 0.1 Jy and 2 Jy for the 70 μm, 160 μm, 250 μm, 350 μm and 500 μm bands, respectively.

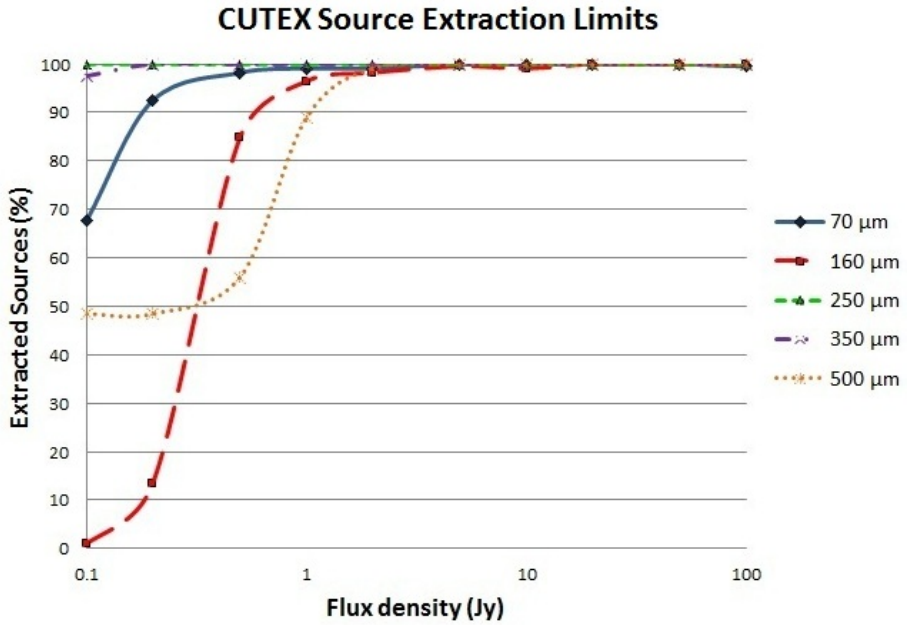

Figure 3.8: Percentage of sample sources for which CUTEX returned a null ($Flux = 0$), negative ($Flux < 0$) or positive ($Flux > 0$) flux in the 70 μm and 160 μm bands for the different injected flux densities. Also shown are the percentage of sample sources which CUTEX was not capable to extract (*Not extracted sources*). The dotted grey lines indicated in the plots correspond to the established CUTEX Flux Fitting Limits. These are: 1 Jy and 2 Jy for the 70 μm and 160 μm bands, respectively.

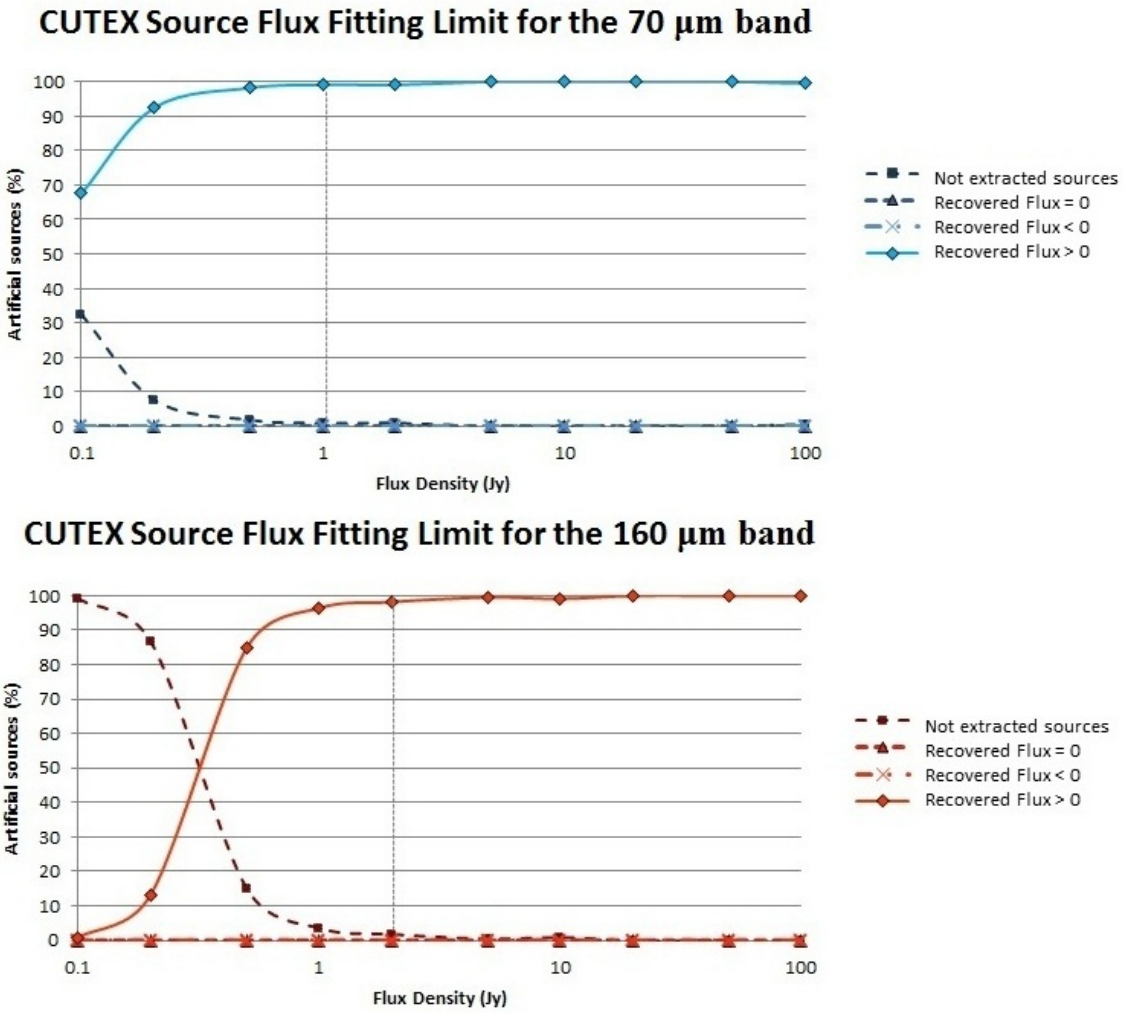

Figure 3.9: Percentage of sample sources for which CUTEX returned a null ($Flux = 0$), negative ($Flux < 0$) or positive ($Flux > 0$) flux in the 250 μm, 350 μm and 500 μm bands for the different injected flux densities. Also shown are the percentage of sample sources which CUTEX was not capable to extract (*Not extracted sources*). The dotted grey lines indicated in the plots correspond to the established CUTEX Flux Fitting Limits. These are: 0.1 Jy, 0.2 Jy and 2 Jy for the 250 μm, 350 μm and 500 μm bands, respectively.

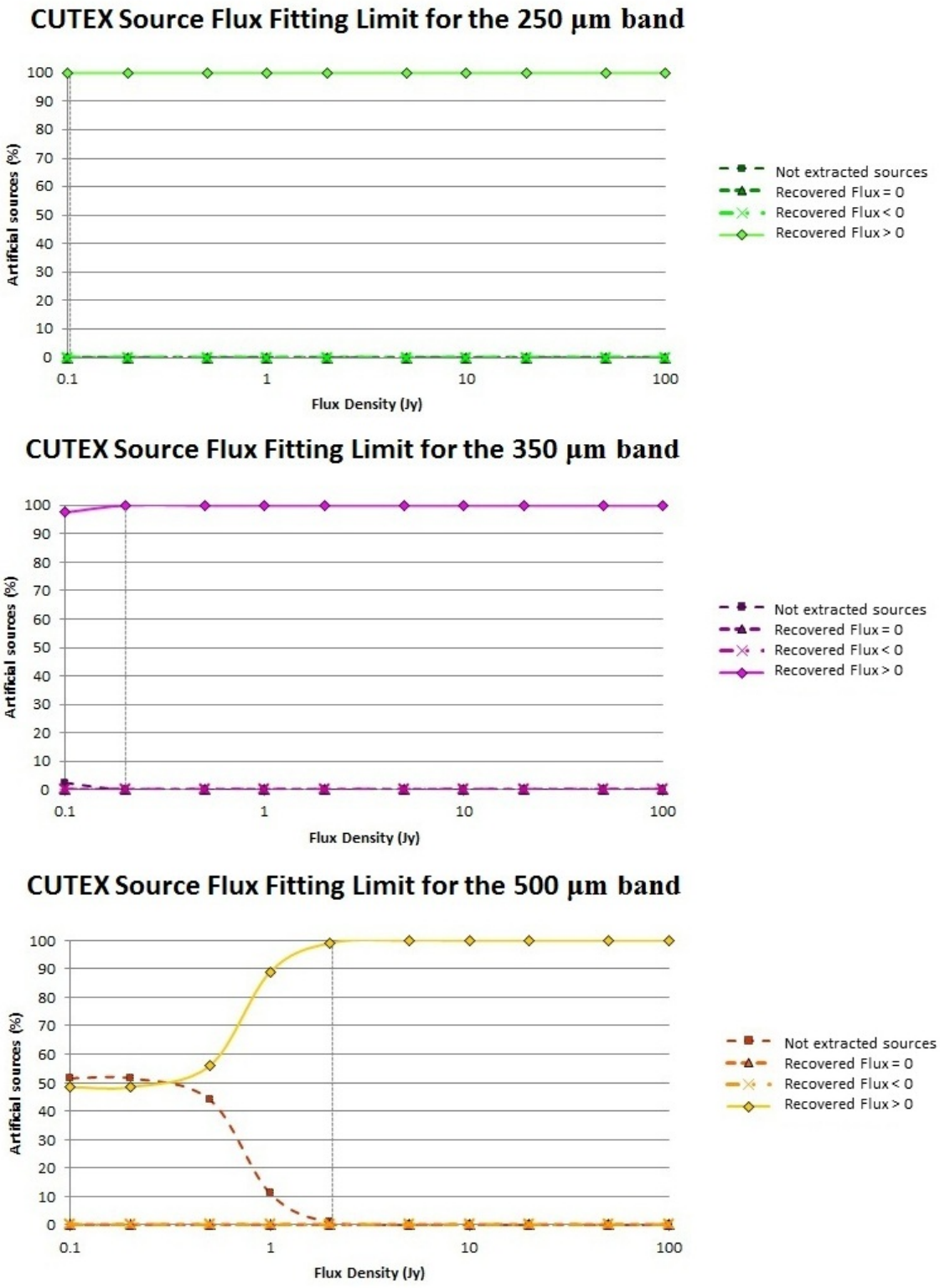

Table 3.1: Percentage of sample sources for which TSF returned a null ($Flux = 0$), negative ($Flux < 0$) or positive ($Flux > 0$) flux in the 250 μm, 350 μm and 500 μm bands.

250 μm band					
Injected Flux (Jy)	**0.1**	**0.2**	**0.5**	**1**	**2–200**
Flux > 0	71.90	80.17	91.74	97.52	99.17
Flux = 0	13.22	10.74	5.79	0.83	0.83
Flux < 0	14.05	8.26	1.65	1.65	0.83
350 μm band					
Injected Flux (Jy)	**0.1**	**0.2**	**0.5**	**1**	**2–200**
Flux > 0	65.29	78.51	92.56	98.35	100
Flux = 0	12.40	10.74	3.31	1.65	0.83
Flux < 0	22.31	10.74	4.13	0.83	0.83
500 μm band					
Injected Flux (Jy)	**0.1**	**0.2**	**0.5**	**1**	**2–200**
Flux > 0	68.30	77.68	94.20	99.11	99.55
Flux = 0	10.71	10.27	1.79	0.45	0.45
Flux < 0	20.98	12.05	4.02	0.45	0.45

Table 3.2: Percentage of sample sources for which CUTEX returned a null ($Flux = 0$), negative ($Flux < 0$) or positive ($Flux > 0$) flux in the 70 μm, 160 μm, 250 μm, 350 μm and 500 μm bands for the different injected flux densities. Also shown are the percentage of sample sources which CUTEX was not capable to extract (*Not extracted*).

70 μm band											
Injected Flux (Jy)	**0.1**	**0.2**	**0.5**	**1**	**2**	**5**	**10**	**20**	**50**	**100**	**200**
Not extracted	32.44	7.56	1.78	0.89	0.89	0	0	0	0	0.44	0
Flux > 0	67.56	92.44	98.22	99.11	99.11	100	100	100	100	99.556	100
Flux = 0	0	0	0	0	0	0	0	0	0	0	0
Flux < 0	0	0	0	0	0	0	0	0	0	0	0
160 μm band											
Injected Flux (Jy)	**0.1**	**0.2**	**0.5**	**1**	**2**	**5**	**10**	**20**	**50**	**100**	**200**
Not extracted	99.11	86.67	15.11	3.56	1.78	0.44	0.89	0	0	0	0
Flux > 0	0.89	13.33	84.89	96.44	98.22	99.56	99.11	100	100	100	100
Flux = 0	0	0	0	0	0	0	0	0	0	0	0
Flux < 0	0	0	0	0	0	0	0	0	0	0	0
250 μm band											
Injected Flux (Jy)	**0.1**	**0.2**	**0.5**	**1**	**2**	**5**	**10**	**20**	**50**	**100**	**200**
Not extracted	0	0	0	0	0	0	0	0	0	0	0
Flux > 0	100	100	100	100	100	100	100	100	100	100	100
Flux = 0	0	0	0	0	0	0	0	0	0	0	0
Flux < 0	0	0	0	0	0	0	0	0	0	0	0
350 μm band											
Injected Flux (Jy)	**0.1**	**0.2**	**0.5**	**1**	**2**	**5**	**10**	**20**	**50**	**100**	**200**
Not extracted	2.48	0	0	0	0	0	0	0	0	0	0
Flux > 0	97.52	100	100	100	100	100	100	100	100	100	100
Flux = 0	0	0	0	0	0	0	0	0	0	0	0
Flux < 0	0	0	0	0	0	0	0	0	0	0	0
500 μm band											
Injected Flux (Jy)	**0.1**	**0.2**	**0.5**	**1**	**2**	**5**	**10**	**20**	**50**	**100**	**200**
Not extracted	51.56	51.56	44.00	11.11	0.89	0	0	0	0	0	0
Flux > 0	48.44	48.44	56.00	88.89	99.11	100	100	100	100	100	100
Flux = 0	0	0	0	0	0	0	0	0	0	0	0
Flux < 0	0	0	0	0	0	0	0	0	0	0	0

3.5.3 Flux Correction Factors

- Definition

  At this stage, those cases for which TSF and CUTEX returned either null or negative values were rejected and only the sample of positive fluxes was considered.

  When inspecting the distribution of the fluxes returned by TSF and CUTEX, it was found that all the CUTEX 70 μm fluxes were systematically overestimated and that all the TSF 250 μm, 350 μm and 500 μm fluxes were systematically underestimated, regardless of the flux level of the injected sources.

  In order to correct the overestimation and underestimation that affected the CUTEX 70 μm fluxes and the TSF 250 μm, 350 μm and 500 μm fluxes respectively, we defined a total of four *Flux Correction Factors* that, when multiplied to the original fluxes, correct the flux uncertainties introduced by the highly bright and variable background emission present in the maps.

- Results

  Shown in Fig. 3.10 are the CUTEX and TSF (uncorrected) fluxes originally recovered for the 10 Jy sources extracted in the 70 μm band (CUTEX) and in the 250 μm, 350 μm and 500 μm bands (TSF). These plots show that the uncorrected CUTEX (TSF) fluxes are somewhat overestimated (underestimated) but can be corrected when multiplying the original CUTEX 70 μm and TSF 250 μm, 350 μm and 500 μm fluxes by 0.77, 1.18, 1.21 and 1.13, respectively. As a result, the previous values were established to be our Flux Correction Factors.

- Conclusions

  The following Flux Correction Factors were found to correct the flux underestimation detected in the CUTEX 70 μm fluxes and the flux overestimation detected in the TSF 250 μm, 350 μm and 500 μm fluxes.

$$FCF_{CUTEX(70\mu m)} = 0.77$$
$$FCF_{TSF(250\mu m)} = 1.18$$
$$FCF_{TSF(350\mu m)} = 1.21$$
$$FCF_{TSF(500\mu m)} = 1.13$$

Figure 3.10: Plots showing the effect of our Flux Correction Factors on the *Uncorrected* fluxes (diamonds) recovered for the 10 Jy sources extracted in the 70 μm band (CUTEX) and in the 250 μm, 350 μm and 500 μm bands (TSF). Here we can see that after applying the Flux Correction Factors the resulting *Corrected* fluxes (squares) are successfully shifted to the injected flux level (red line at 10 Jy).

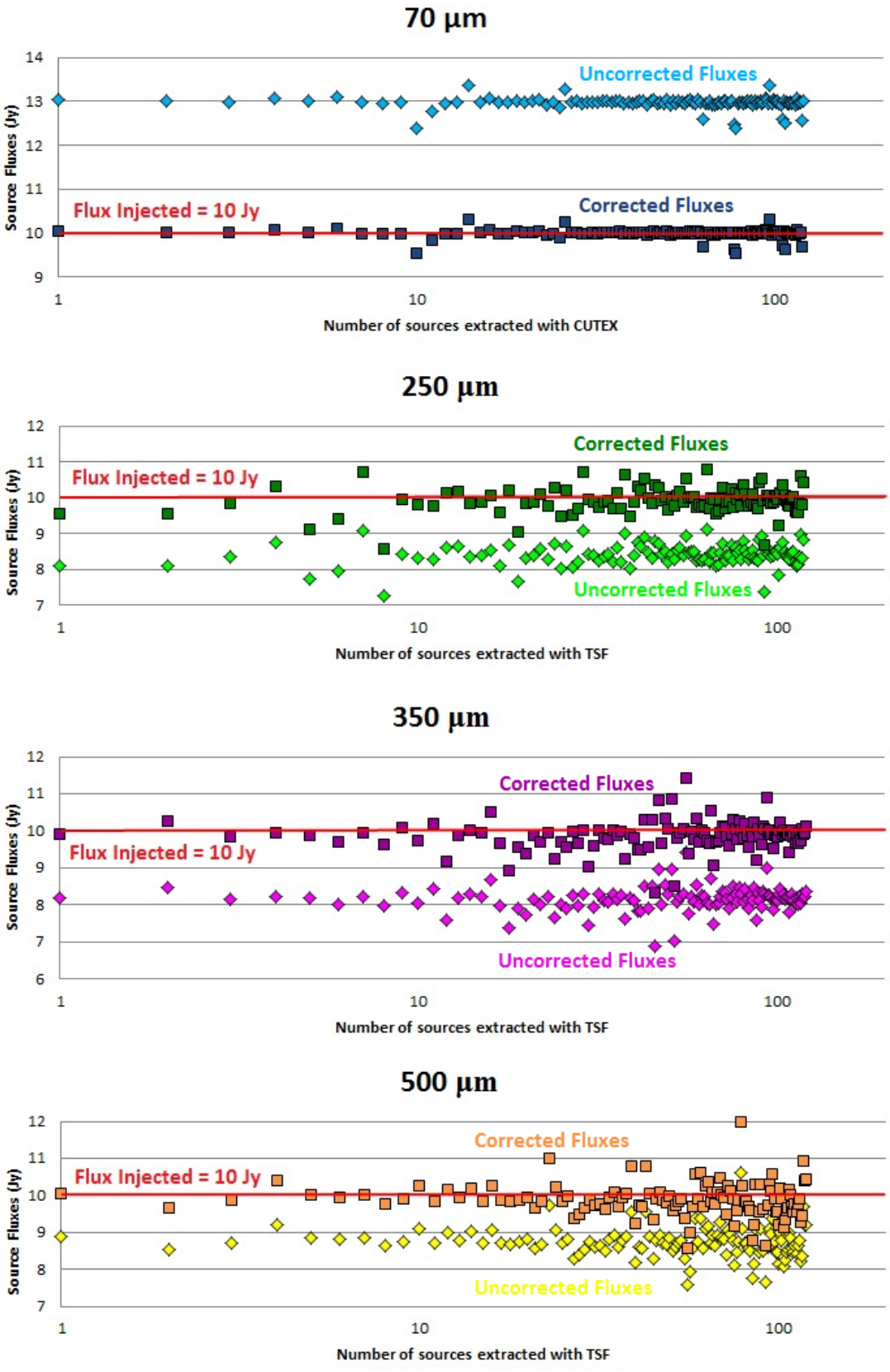

3.5.4 Detection of statistical outliers

- Definition

  The Flux Correction Factors introduced in the previous section were applied to all the fluxes extracted by TSF in the 250 μm, 350 μm and 500 μm bands and CUTEX in the 70 μm band. The resulting *corrected* flux distributions were then analysed in order to investigate the presence of statistical outliers within the distributions. These outliers provide us with information regarding the accuracy of the CUTEX and the TSF fluxes and can be detected using the sample's Mean (μ) and Standard Deviation (STDEV, σ). For instance, let us consider the hypothetical case where the flux sample returned by an algorithm follows a normal (or Gaussian) distribution[9], such as that shown in Fig. 3.11. In this example:

  (i) $\simeq$68% of the flux values lay within $|1\sigma|$ of the sample μ.

  (ii) $\simeq$95% of the flux values lay within $|2\sigma|$ of the sample μ.

  (iii) $\simeq$99.7% of the flux values lay within $|3\sigma|$ of the sample μ.

  (iv) $\simeq$100% of the flux values lay within $|4\sigma|$ of the sample μ.

  (v) Each nσ outlier (where n=1,2,3,..) contains fluxes (f) whose value is in the $\mu + ((n-1) \times \sigma) < f < \mu + (n \times \sigma)$ range.

  (vi) Each -nσ outlier (where n=1,2,3,..) contains fluxes (f) whose value is in the $\mu + (n \times \sigma) < f < \mu + ((n+1) \times \sigma)$ range.

  From the previous expressions we see that the lower the $|n|\sigma$ deviation of a flux value from the sample mean, the more accurate the flux is. Thus, the higher the percentage of fluxes lying within the $|1\sigma|$ outlier, the more precise the flux extractor results will be. Although in a normal distribution, all the flux values lie within $|4\sigma|$ of the μ, and the percentage of sample points lying in each outlier is symmetrical about the μ, distributions of other kinds may be contained in less or more outliers which might also not be necessarily symmetrical. In our case, we considered up to 6 different sample outliers: the $\pm$ *1*σ, $\pm$ *2*σ and $\pm$ *3*σ outliers and calculated the percentage of sources whose flux value fell within these ranges. The previous process was repeated per each band for all the TSF and CUTEX fluxes returned at each injected flux level.

[9] A Gaussian distribution is a data distribution with a bell–shaped curve symmetrical about the μ.

Figure 3.11: Statistical outliers for a normal distribution.

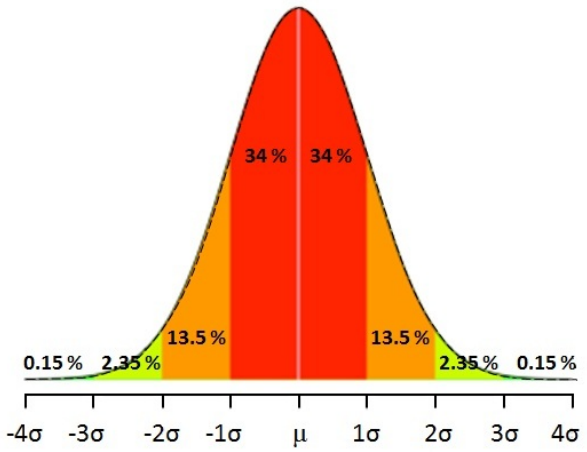

- Results

  Shown in Fig. 3.12–3.14 and Fig. 3.15–3.19 are the corrected distributions of the fluxes returned by TSF and CUTEX respectively, for each band and at each injected flux density. The previous distributions were used to calculate the samples' μ and σ (i.e. the mean and the STDEV of the sample of sources extracted for a given flux level). These values are listed in Table 3.3 (TSF) and Table 3.7 (CUTEX)[10].

  Finally, the μ and σ values were used to identify the percentage of sample sources whose TSF and CUTEX fluxes were found to lie within $\pm$ 1σ, $\pm$ 2σ and $\pm$ 3σ of the samples' μ. These percentages are listed in Table 3.5-3.6 (TSF) and in Table 3.9-3.11 (CUTEX). Also included in the tables is the mean percentage for each outlier from which we calculated the average values listed in Table 3.17[11]. The meaning of the "–" symbol included in Tables 3.3-3.11 is discussed later on in Sect. 3.5.5.

- Conclusions

  From the results presented in Table 3.17 we can see that for CUTEX: (i) the number of sources with fluxes within the $|1\sigma|$ outlier was found to be ∼7% higher than for TSF while (ii) the number of sources with fluxes within the $|2\sigma|+|3\sigma|$ outliers was found to be ∼8% lower than for TSF. These results provide evidence that CUTEX returns more accurate fluxes than the TSF for ∼7% of the source sample, which leads to the conclusion that CUTEX fluxes are overall more accurate.

[10] These μ and σ values were established for the corrected fluxes.
[11] These percentages were established for the corrected fluxes.

Figure 3.12: Distributions of the (corrected) 250 μm TSF fluxes for the different injected flux densities.

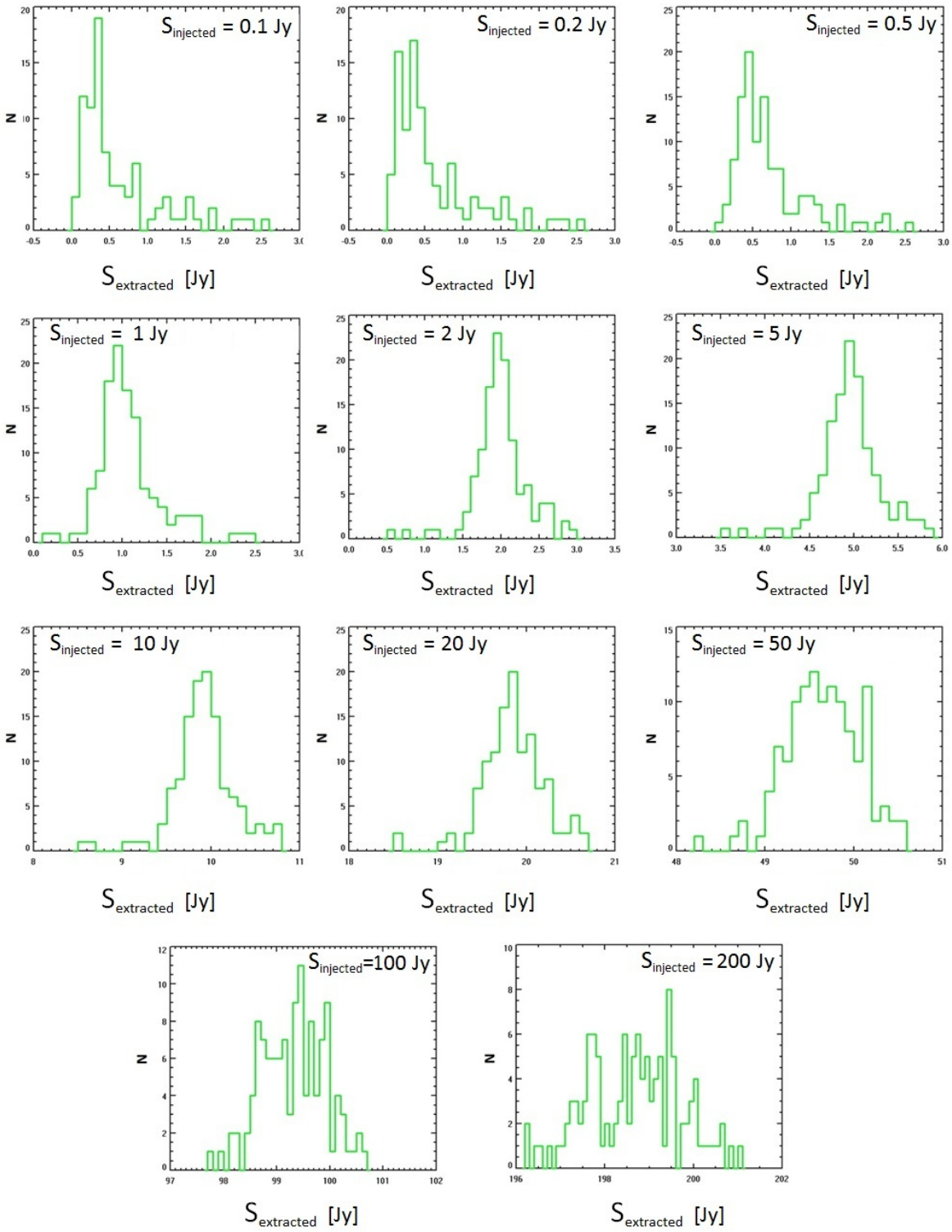

Figure 3.13: Distributions of the (corrected) 350 μm TSF fluxes for the different injected flux densities.

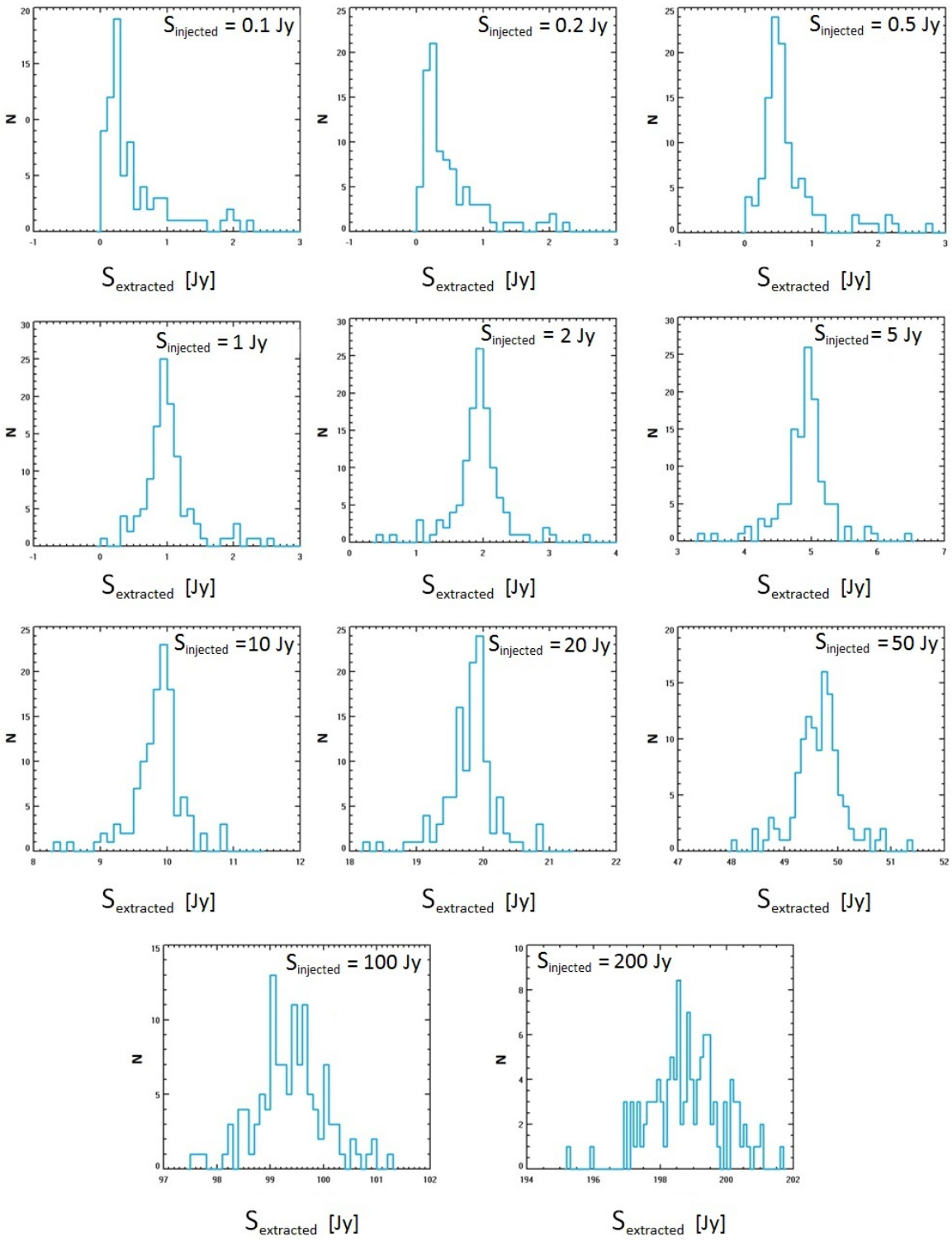

Figure 3.14: Distributions of the (corrected) 500 μm TSF fluxes for the different injected flux densities.

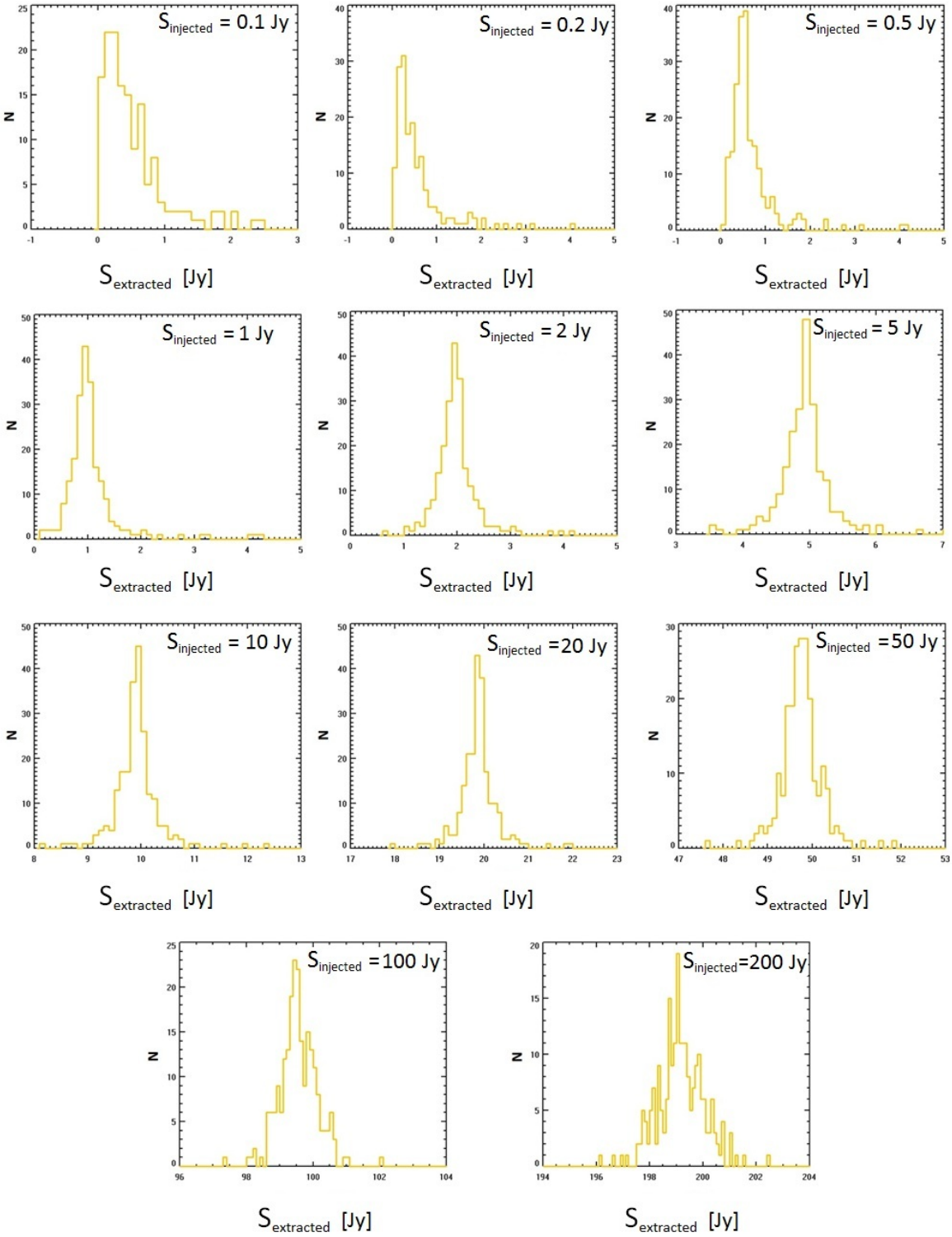

Table 3.3: The TSF flux mean and STDEV for the 1σ outlier in the 250 μm, 350 μm and 500 μm bands for the different injected flux densities.

Flux [Jy]	**250 μm**		**350 μm**		**500 μm**	
	μ	σ	μ	σ	μ	σ
0.1	–	–	–	–	–	–
0.2	–	–	–	–	–	–
0.5	–	–	–	–	–	–
1	1.06	0.29	0.99	0.32	0.98	0.31
2	2.04	0.29	1.94	0.33	1.96	0.33
5	5.00	0.29	4.91	0.32	4.91	0.35
10	9.96	0.28	9.88	0.33	9.88	0.34
20	19.90	0.29	19.82	0.34	19.85	0.36
50	49.66	0.40	49.63	0.46	49.74	0.38
100	99.32	0.59	99.40	0.59	99.53	0.51
200	198.65	1.06	198.83	1.11	199.18	0.78

Table 3.4: The TSF S/N values for the 1σ outlier in the 250 μm, 350 μm and 500 μm bands for the different injected flux densities.

Flux [Jy]	**250 μm**	**350 μm**	**500 μm**
	S/N	**S/N**	**S/N**
0.1	–	–	–
0.2	–	–	–
0.5	–	–	–
1	4	3	3
2	7	6	6
5	17	15	14
10	36	30	29
20	69	58	55
50	124	108	131
100	62	168	195
200	187	179	255

Table 3.5: Percentage of sample sources whose TSF returned flux was found to lie within ± 1σ, ± 2σ and ± 3σ of the samples' μ (see Table 3.3) in the 250 μm and 350 μm bands for the different injected flux densities. Also included is the mean percentage for each outlier.

250 μm band

Flux [Jy]	-3σ	-2σ	-1σ	1σ	2σ	3σ
0.1	–	–	–	–	–	–
0.2	–	–	–	–	–	–
0.5	–	–	–	–	–	–
1	0	12.39	44.25	28.32	7.96	7.08
2	0	12.93	44.83	27.59	9.48	4.31
5	0.86	12.07	43.97	29.31	8.62	5.17
10	0	12.17	45.22	26.96	9.57	6.09
20	0	16.52	38.26	28.70	10.43	6.09
50	2.52	13.45	33.61	31.93	16.81	1.68
100	1.67	15.00	30.83	37.50	12.50	2.50
200	2.50	14.17	30.00	37.50	14.17	1.67
Mean	0.94	13.59	38.87	30.98	11.19	4.32

350 μm band

Flux [Jy]	-3σ	-2σ	-1σ	1σ	2σ	3σ
0.1	–	–	–	–	–	–
0.2	–	–	–	–	–	–
0.5	–	–	–	–	–	–
1	0	11.40	42.11	35.09	6.14	0
2	3.42	8.55	39.32	36.75	8.55	0.85
5	3.39	9.32	33.05	42.37	8.47	1.69
10	4.24	7.63	33.05	42.37	9.32	1.69
20	5.08	6.78	32.20	44.92	7.63	2.54
50	2.50	7.50	35.00	42.50	7.50	3.33
100	0.86	12.93	35.34	32.76	14.66	3.45
200	0.83	14.05	33.06	33.88	14.88	2.48
Mean	2.54	9.77	35.39	38.83	9.64	2.00

Table 3.6: Percentage of sample sources whose TSF returned flux was found to lie within $\pm$ 1σ, $\pm$ 2σ and $\pm$ 3σ of the samples' μ (see Table 3.3) in the 500 μm band for the different injected flux densities. Also included is the mean percentage for each outlier derived from the mean values obtained for the 250 μm, 350 μm and 500 μm bands.

500 μm band

Flux [Jy]	-3σ	-2σ	-1σ	1σ	2σ	3σ
0.1	–	–	–	–	–	–
0.2	–	–	–	–	–	–
0.5	–	–	–	–	–	–
1	2.84	10.43	39.34	35.55	8.06	2.84
2	2.79	9.30	38.60	37.67	7.91	2.33
5	1.83	6.88	35.78	42.66	8.26	2.29
10	2.78	6.02	34.26	43.06	8.80	3.24
20	2.29	7.80	33.95	41.28	9.63	3.21
50	3.69	10.60	36.87	34.10	11.52	3.23
100	2.30	13.82	35.94	31.34	14.29	2.30
200	0.93	16.20	36.11	30.09	12.96	3.24
Mean	2.43	10.13	36.36	36.97	10.18	2.84

Average results

TOTAL=98.99					
$\lvert 1\sigma \rvert$		$\lvert 2\sigma \rvert$		$\lvert 3\sigma \rvert$	
72.47		21.50		5.02	
-3σ	-2σ	-1σ	1σ	2σ	3σ
1.97	11.16	36.87	35.59	10.34	3.05

Figure 3.15: Distributions of the (corrected) 70 μm CUTEX fluxes for the different injected flux densities.

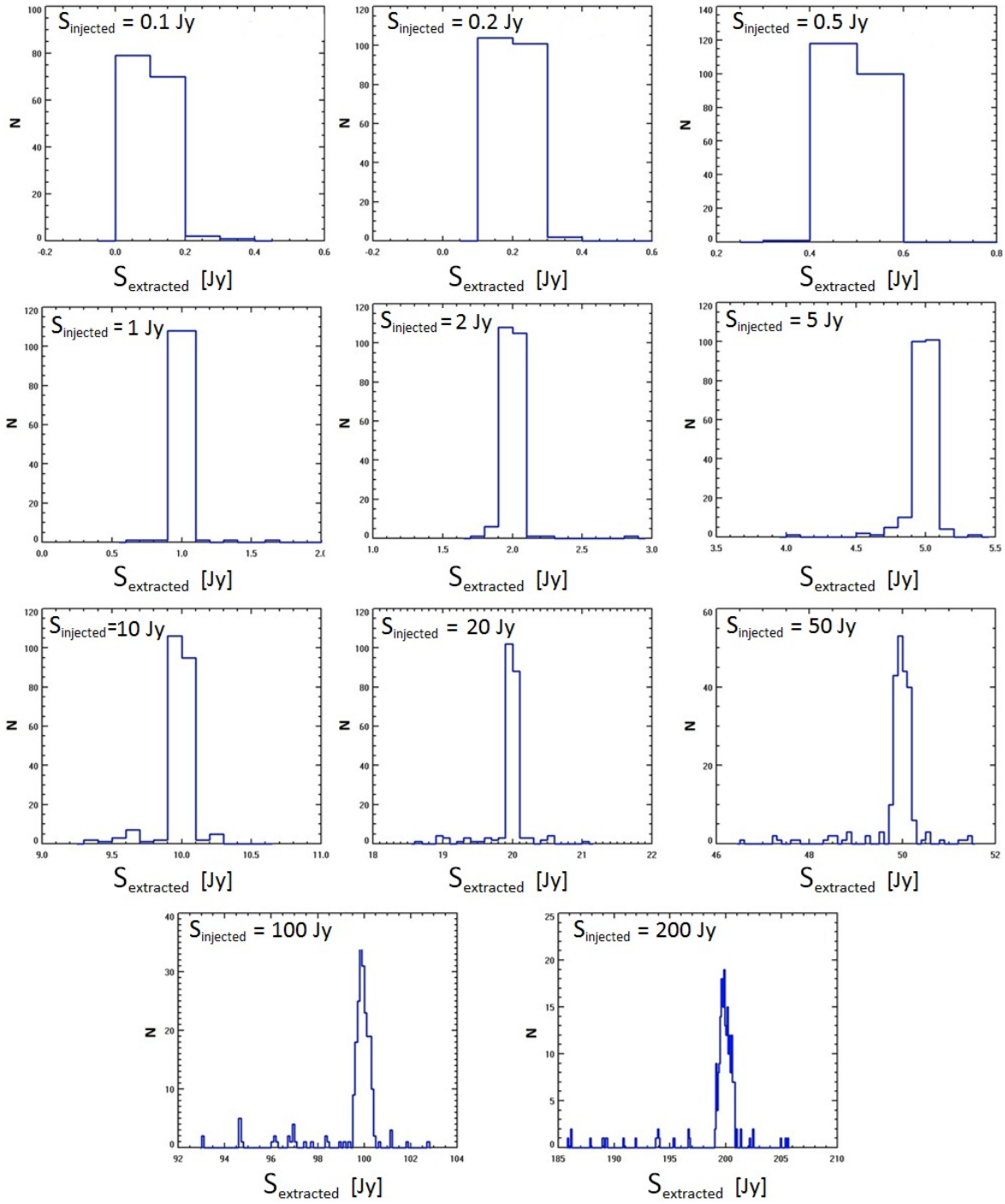

Figure 3.16: Distributions of the (corrected) 160 μm CUTEX fluxes for the different injected flux densities.

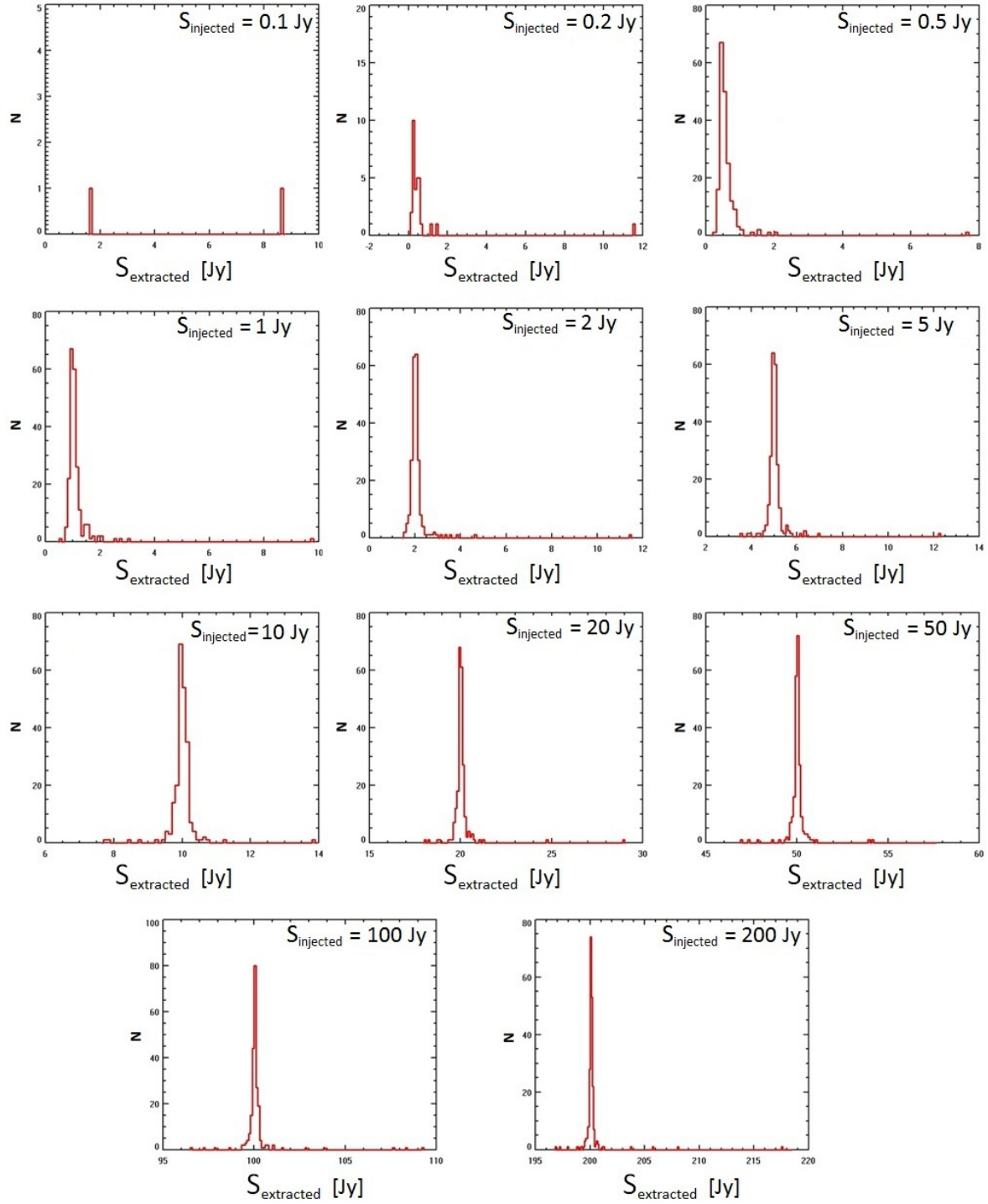

Figure 3.17: Distributions of the (corrected) 250 μm CUTEX fluxes for the different injected flux densities.

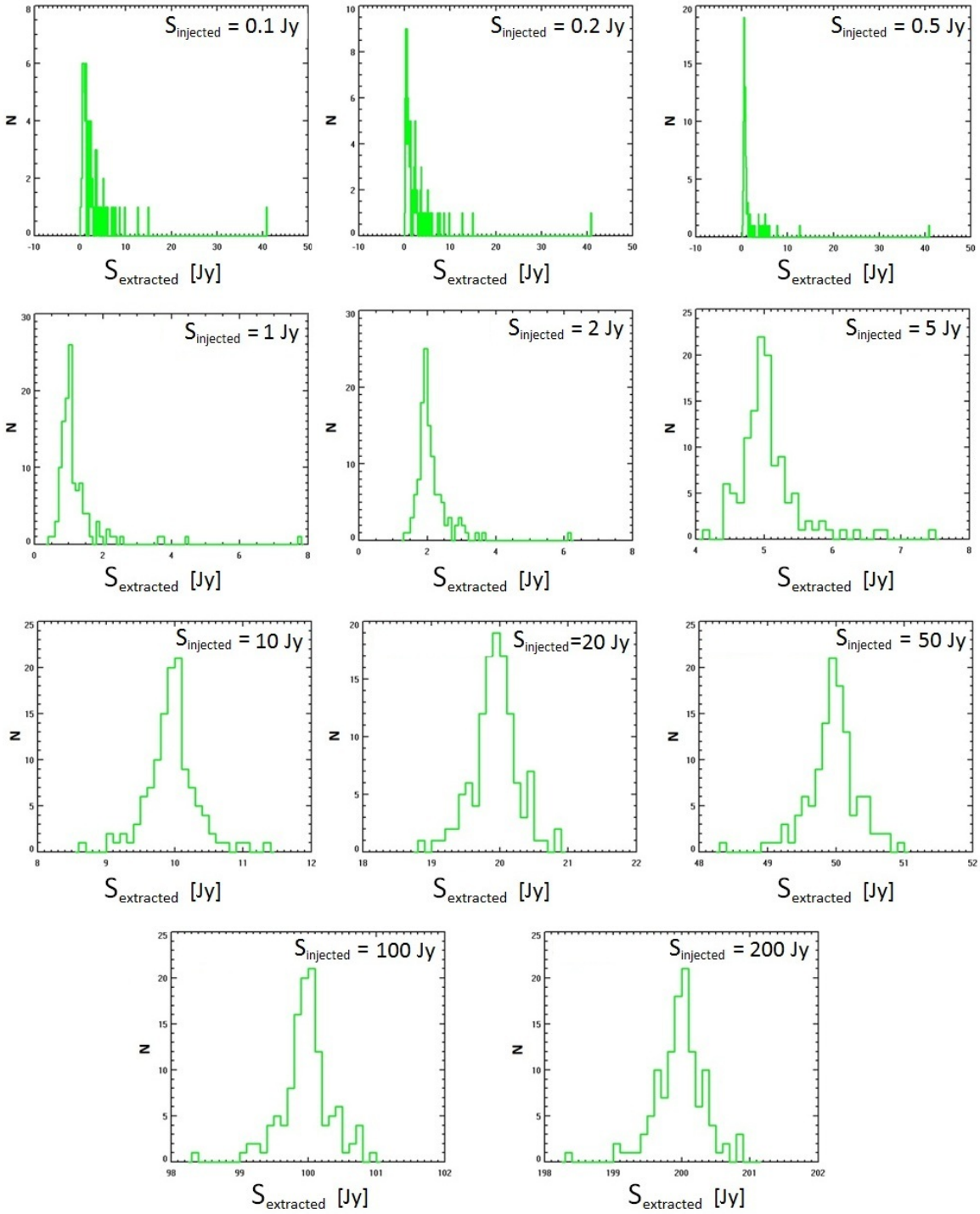

Figure 3.18: Distributions of the (corrected) 350 μm CUTEX fluxes for the different injected flux densities.

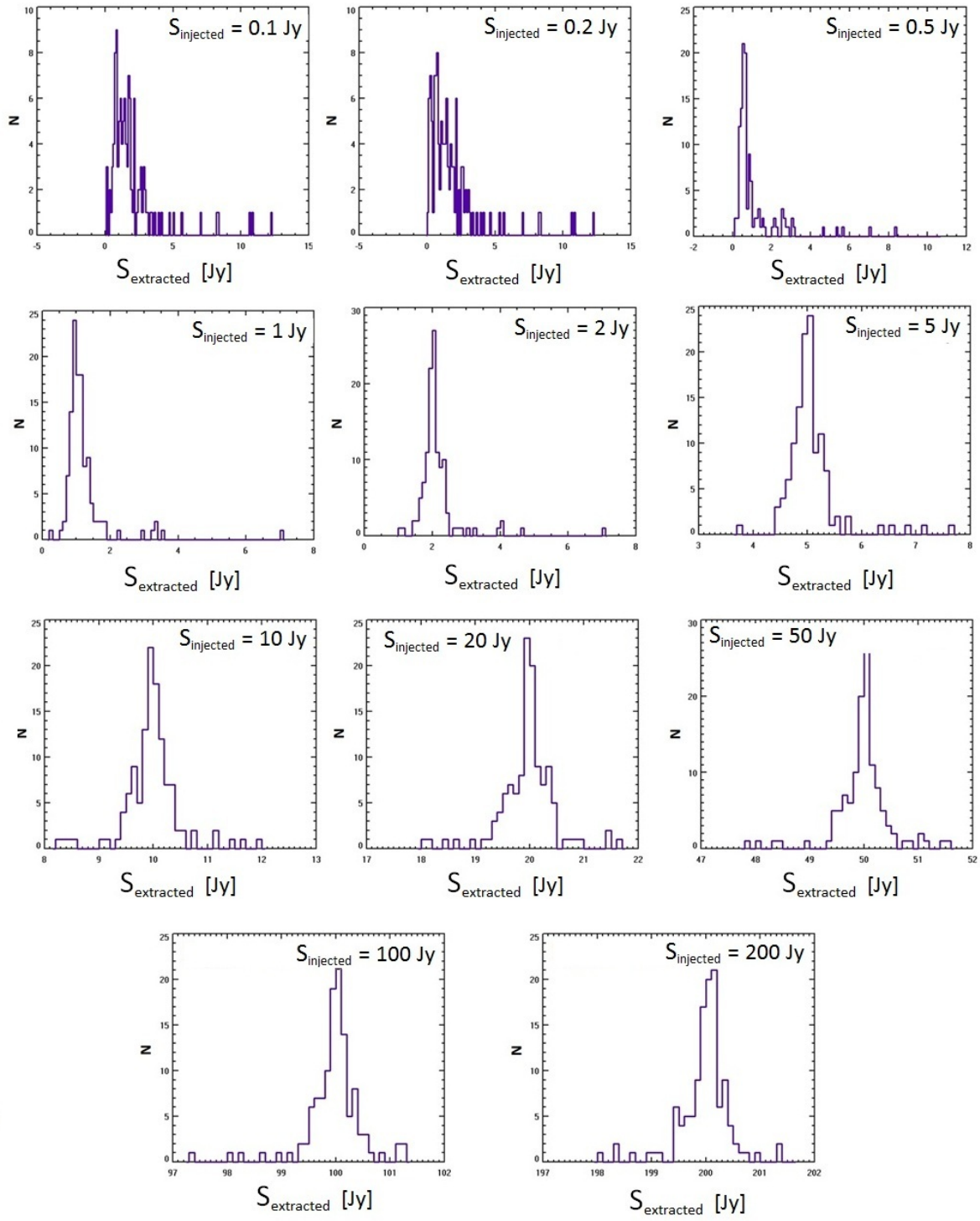

Figure 3.19: Distributions of the (corrected) 500 μm CUTEX fluxes for the different injected flux densities.

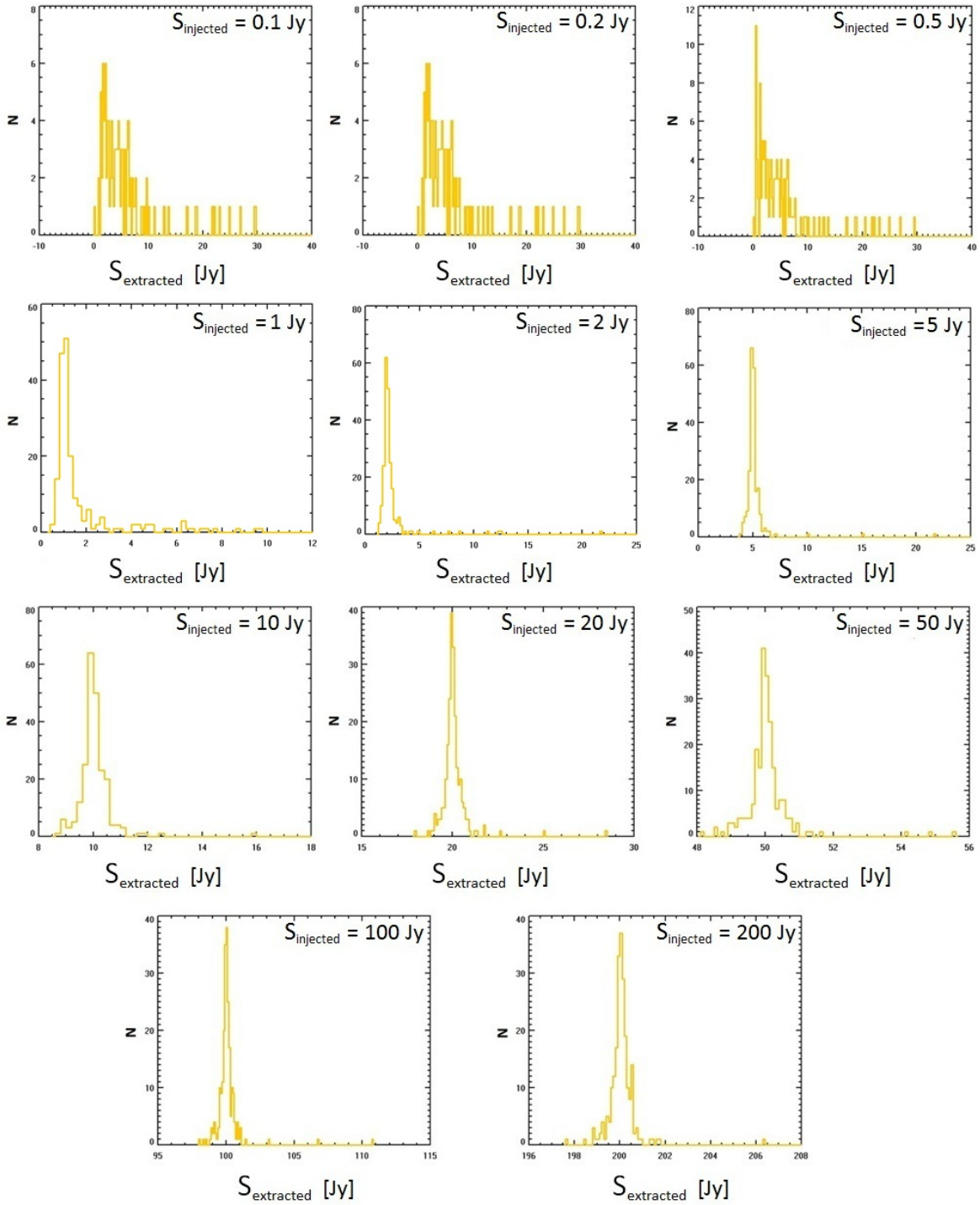

Table 3.7: The CUTEX flux mean and STDEV for the 1σ outlier in the 70 μm, 160 μm, 250 μm, 350 μm and 500 μm bands for the different injected flux densities.

Flux [Jy]	**70 μm**		**160 μm**		**250 μm**		**350 μm**		**500 μm**	
	μ	σ	μ	σ	μ	σ	μ	σ	μ	σ
0.1	0.11	0.03	–	–	–	–	–	–	–	–
0.2	0.20	0.02	–	–	–	–	–	–	–	–
0.5	0.50	0.02	–	–	–	–	–	–	–	–
1	1.00	0.04	1.07	0.22	1.10	0.33	1.15	0.46	1.19	0.46
2	2.00	0.04	2.02	0.19	2.00	0.21	2.08	0.36	2.08	0.38
5	4.99	0.07	5.02	0.18	5.00	0.26	5.01	0.22	5.04	0.41
10	9.98	0.12	10.01	0.18	9.96	0.27	10.00	0.28	10.00	0.40
20	19.96	0.22	20.01	0.19	19.98	0.28	20.02	0.34	20.02	0.42
50	49.90	0.53	50.02	0.20	49.66	0.23	50.02	0.28	50.00	0.37
100	99.55	1.35	100.03	0.20	100.00	0.28	100.04	0.32	100.02	0.38
200	199.40	2.78	200.08	0.18	200.02	0.29	200.03	0.36	200.02	0.36

Table 3.8: The CUTEX S/N values for the 1σ outlier in the 70 μm, 160 μm, 250 μm, 350 μm and 500 μm bands for the different injected flux densities.

Flux [Jy]	**70 μm**	**160 μm**	**250 μm**	**350 μm**	**500 μm**
	S/N	**S/N**	**S/N**	**S/N**	**S/N**
0.1	4	–	–	–	–
0.2	10	–	–	–	–
0.5	25	–	–	–	–
1	25	5	3	3	3
2	50	11	10	6	5
5	71	28	19	23	12
10	83	56	37	36	25
20	91	105	71	59	48
50	94	250	216	179	135
100	74	500	357	313	263
200	72	1112	690	556	556

Table 3.9: Percentage of sample sources whose CUTEX returned flux was found to lie within ± 1σ, ± 2σ and ± 3σ of the samples' μ (see Table 3.7) in the 70 μm and 160 μm bands for the different injected flux densities. Also included is the mean percentage for each outlier.

70 μm band

Flux [Jy]	−3σ	−2σ	−1σ	1σ	2σ	3σ
0.1	0.00	1.32	61.18	30.26	3.29	1.32
0.2	1.45	3.38	47.83	40.58	4.83	0.48
0.5	0.91	6.39	36.99	41.55	11.42	1.37
1	0.45	2.27	38.64	53.64	3.18	0.00
2	0.90	3.60	31.53	56.76	3.60	0.00
5	1.81	3.17	17.19	71.49	2.71	0.45
10	3.15	0.45	21.62	68.47	0.90	2.25
20	1.81	2.26	23.53	65.16	1.36	2.71
50	3.60	1.35	25.23	63.96	1.80	1.80
100	3.14	3.14	4.04	83.86	1.79	0.45
200	0.90	2.69	11.21	78.03	1.35	1.79
Mean	1.65	2.73	29.00	59.43	3.29	1.15

160 μm band

Flux [Jy]	−3σ	−2σ	−1σ	1σ	2σ	3σ
0.1	–	–	–	–	–	–
0.2	–	–	–	–	–	–
0.5	–	–	–	–	–	–
1	0.00	5.66	62.74	21.23	4.72	3.30
2	1.40	7.91	46.05	37.21	4.19	0.93
5	0.00	0.00	25.93	18.52	18.52	22.22
10	3.70	7.41	41.20	37.50	7.41	0.46
20	0.92	9.68	40.09	38.71	5.07	2.76
50	1.85	7.87	44.91	35.65	4.63	2.31
100	2.82	6.57	36.62	40.85	9.39	0.94
200	3.23	5.07	40.55	39.17	5.53	1.38
Mean	1.74	6.27	42.26	33.61	7.43	4.29

Table 3.10: Percentage of sample sources whose CUTEX returned flux was found to lie within $\pm 1\sigma$, $\pm 2\sigma$ and $\pm 3\sigma$ of the samples' μ (see Table 3.7) in the 250 μm and 350 μm bands for the different injected flux densities. Also included is the mean percentage for each outlier.

250 μm band

Flux [Jy]	-3σ	-2σ	-1σ	1σ	2σ	3σ
0.1	–	–	–	–	–	–
0.2	–	–	–	–	–	–
0.5	–	–	–	–	–	–
1	0.48	6.19	61.90	19.05	6.19	3.81
2	1.48	9.36	43.84	30.54	7.88	4.93
5	2.79	8.84	44.65	30.70	7.44	3.72
10	2.30	8.29	33.64	43.32	7.37	3.23
20	2.71	8.60	39.82	36.20	9.50	1.81
50	4.76	9.52	22.22	52.38	9.52	0.00
100	2.30	8.29	36.41	40.55	7.37	4.61
200	2.27	9.55	30.00	46.36	5.91	3.64
Mean	2.39	8.58	39.06	37.39	7.65	3.22

350 μm band

Flux [Jy]	-3σ	-2σ	-1σ	1σ	2σ	3σ
0.1	–	–	–	–	–	–
0.2	–	–	–	–	–	–
0.5	–	–	–	–	–	–
1	0.00	1.87	70.56	19.16	4.67	0.93
2	0.00	5.58	62.33	24.65	2.33	2.79
5	1.40	10.28	42.52	32.71	8.41	2.80
10	1.41	11.27	40.85	36.15	6.57	2.35
20	1.37	9.59	45.66	32.88	5.94	1.83
50	1.40	11.16	44.19	32.09	6.98	2.33
100	1.83	9.63	42.66	36.24	5.50	0.92
200	2.26	6.79	32.58	48.87	6.33	0.90
Mean	1.21	8.27	47.67	32.84	5.84	1.86

Table 3.11: Percentage of sample sources whose CUTEX returned flux was found to lie within ± 1σ, ± 2σ and ± 3σ of the samples' μ (see Table 3.7) in the 500 μm band for the different injected flux densities. Also included is the mean percentage for each outlier derived from the mean values obtained for the 70 μm, 160 μm, 250 μm, 350 μm and 500 μm bands.

500 μm band

Flux [Jy]	-3σ	-2σ	-1σ	1σ	2σ	3σ
0.1	–	–	–	–	–	–
0.2	–	–	–	–	–	–
0.5	–	–	–	–	–	–
1	0.00	5.95	62.70	17.84	8.11	2.16
2	0.95	11.90	46.67	25.71	8.57	4.29
5	2.73	8.18	45.00	30.00	10.45	2.27
10	4.55	7.73	39.55	33.64	11.36	3.18
20	3.18	7.73	42.73	33.18	10.00	1.82
50	4.65	8.37	35.81	36.74	11.16	3.26
100	4.59	8.72	36.24	35.78	11.01	3.67
200	3.69	7.83	35.02	38.25	12.44	1.38
Mean	3.04	8.30	42.97	31.39	10.39	2.75

Average results

TOTAL=97.53					
$\lvert 1\sigma \rvert$		$\lvert 2\sigma \rvert$		$\lvert 3\sigma \rvert$	
79.12		13.75		4.66	
-3σ	-2σ	-1σ	1σ	2σ	3σ
2.01	6.83	40.19	38.93	6.92	2.65

3.5.5 Source Flux Accuracy Limit

- Definition

  From the corrected flux distributions shown in Fig. 3.12– 3.19 we can see that for the 160 μm, 250 μm, 350 μm and 500 μm bands:

  (i) The fluxes returned by TSF and CUTEX for the 0.1 Jy, 0.2 Jy and 0.5 Jy sources lie within large $|n|\sigma$ outliers (n=5 and higher) from the expected mean values (i.e. $\sim$0.1, $\sim$0.2 and $\sim$0.5, respectively). This implies that for sources fainter than 1 Jy the fluxes returned by the TSF and CUTEX have large uncertainties associated.

  (ii) The maximum value of the 0.1 Jy, 0.2 Jy and 0.5 Jy flux distributions is found to strongly deviate from the expected mean values.

  (iii) The 0.1 Jy, 0.2 Jy and 0.5 Jy flux distributions are strongly skewed to the right instead of being quasi symmetrical as for the other cases.

  As a result, for the 160 μm, 250 μm, 350 μm and 500 μm bands, it was not possible to calculate neither the μ and σ values of the 0.1 Jy, 0.2 Jy and 0.5 Jy flux distributions nor the percentage of sources lying within the $\pm$ *1*σ, $\pm$ *2*σ and $\pm$ *3*σ outliers of such distributions. This fact is indicated in Tables 3.3–3.11 with a "–" symbol and demonstrates that for sources fainter than 1 Jy the flux values returned by TSF and CUTEX are, in general, highly inaccurate and therefore unreliable.

  In the case of the 70 μm band, we can see from Fig. 3.15–3.19 that, thanks to the application of the Flux Correction Factor $FCF_{CUTEX(70)} = 0.77$, the fluxes returned by CUTEX for the 0.1 Jy, 0.2 Jy and 0.5 Jy sources have relatively small uncertainties associated and are therefore reliable. Without such flux correction, the 70 μm 0.1 Jy, 0.2 Jy and 0.5 Jy fluxes would have large uncertainties associated and therefore they would be, like for the other bands, unreliable.

  The *Source Flux Accuracy Limit* was introduced in order to establish the flux level, in each band, below which the fluxes returned by TSF and CUTEX were not reliable. This parameter provides us with an idea of the TSF and CUTEX limitations when flux-extracting faint sources.

- Conclusions

  For the corrected fluxes, the TSF Source Flux Accuracy Limit for the 250 μm, 350 μm and 500 μm bands[12] is 1 Jy, 1 Jy and 1 Jy while the CUTEX Source Flux Accuracy Limit for the 70 μm[13], 160 μm, 250 μm, 350 μm and 500 μm bands is 0.1 Jy, 1 Jy, 1 Jy, 1 Jy and 1 Jy, respectively. For the uncorrected fluxes, the CUTEX Source Flux Accuracy Limit for the 70 μm band would also be 1 Jy as for the rest of the bands. Thus, in general the fluxes returned by CUTEX and TSF for sources fainter than 1 Jy are unreliable.

3.5.6 Flux uncertainties

- Definition

  The detection of statistical outliers carried out in Sect. 3.5.4 allowed us to establish the flux uncertainties associated to the fluxes returned by TSF and CUTEX as the σ values listed in Table 3.3 and Table 3.7, respectively. These values constitute an estimation[14] of the flux uncertainties introduced by the high variability of the background emission present in the Hi-GAL 1 maps and provide us with information about the reliability of the TSF and CUTEX fluxes.

- Results

  Shown in Table 3.4 and 3.8 are the ratios between the flux (μ) and the flux uncertainty (σ),(the S/N values), calculated for the fluxes returned by TSF and CUTEX in each flux level in the 70 μm, 160 μm, 250 μm, 350 μm and 500 μm bands.

  In the case of the 70 μm band, we determined that, when flux corrected, the S/N for the 0.1 Jy, 0.2 Jy and 0.5 Jy sources is 4, 10 and 25, respectively.

  In the case of the 160 μm, 250 μm, 350 μm and 500 μm bands, it was not possible to determine the S/N values corresponding to these fluxes[15]. However, given the large uncertainties associated to the returned fluxes, the S/N of the 0.1 Jy, 0.2 Jy and 0.5 Jy flux levels would be much lower than 3.

[12] In the case of TSF, the fluxes in all three SPIRE bands were corrected.
[13] In the case of CUTEX, only the 70 μm fluxes were corrected.
[14] Especially in the cases where we found that the returned flux distribution was severely skewed.
[15] This fact is indicated in Table 3.4 and 3.8 with a "–" symbol.

Table 3.12: Level of reliability of the fluxes returned by TSF.

Flux reliability	**Flux quality flag q_Flux**	**Flux range**		
		250 μm	**350 μm**	**500 μm**
Low	1	<1 Jy	<1 Jy	<1 Jy
Moderate	2	1 Jy	[1,2] Jy	[1,2] Jy
High	3	>1 Jy	>2 Jy	>2 Jy

Table 3.13: Level of reliability of the fluxes returned by CUTEX.

Flux reliability	**Flux quality flag q_Flux**	**Flux range**				
		70 μm	**160 μm**	**250 μm**	**350 μm**	**500 μm**
Low	1	–	<1 Jy	<1 Jy	<1 Jy	<1 Jy
Moderate	2	0.1 Jy	1 Jy	1 Jy	[1,2] Jy	[1,2] Jy
High	3	>0.1 Jy	>1 Jy	>1 Jy	>2 Jy	>2 Jy

If we consider that fluxes with S/N<3, 3≤S/N<7 and S/N≥7 are fluxes with low, moderate and high reliability respectively, we can establish the flux reliability levels for the fluxes returned by TSF (see Table 3.12) and CUTEX (see Table 3.13). Here, fluxes with low, moderate and high reliability are denoted with a flux quality flag (*q_Flux*) equal to 1, 2 and 3, respectively[16].

- Conclusions

  In light of the results presented in Table 3.12 and 3.13 we concluded that, in general, for TSF and CUTEX: (i) fluxes fainter than 1 Jy have S/N<3 and so, they have a low flux reliability, (ii) fluxes in the [1,2] Jy range have 3≤S/N<7 and so, they have a moderate flux reliability and (iii) fluxes brighter than 2 Jy have S/N≥7 and so, they have a high flux reliability.

[16]The flux ranges indicated for the 70 μm band were established for the corrected fluxes. For the uncorrected fluxes, the 70 μm band would have the same ranges as the 160 μm and 250 μm bands.

3.5.7 Comparison with CUTEX ROMAGAL results

In this section we present a review of the results obtained by the ROMAGAL team in a series of tests they conducted with the aim of characterising CUTEX performance when source and flux extracting. Further information regarding ROMAGAL's tests can be found in Molinari et al. (2011) and Molinari et al. (2015), which are the two publications from which we extracted the information here presented.

- **Source Extraction Limit**

  In order to establish the degree of completeness of CUTEX extracted sourcelists, the ROMAGAL team conducted the following tests. First, they selected a total of 30 Hi-GAL 1 fields. Then, they injected 1,000 synthetic sources to the 150 (i.e 30 Hi-GAL 1 fields x 5 Herschel bands) original maps. These sources were set to have an elliptical 2D Gaussian shape and a variable axis ratio up to a maximum of 2. All the sources were assumed to have the same integrated flux and were randomly assigned a value of FWHM between 18" and 36". The sources were randomly distributed through the map, with the only constraint being to avoid overlap with the positions of the real sources.

  Having built the previous test maps, they then run CUTEX through the maps in order to establish the fraction of recovered sources. This process was repeated several times and in each run, the injected sources were given different fluxes in order to determine how the fraction of extracted sources varied with the sources' flux level.

  With the previous tests, the ROMAGAL team was able to determine the minimum flux levels at which the CUTEX extracted sourcelists had a completeness of 90% in each of the 30 tested maps and for each Herschel band. These flux levels are equivalent to our Source Extraction Limits (see Sect. 3.5.1). These results can be found in the *Hi-GAL Data Products Description document* but are reported here in Table 3.14 for readability.

  The tests described above are very similar to those we conducted to establish CUTEX Source Extraction Limit (see Sect. 3.5.1), being the only differences:

  (i) the number of fields in which the tests were carried out - 1 in our case and 30 in ROMAGAL's,

  (ii) the number of sources injected - 121 in our case and 1,000 in ROMAGAL's,

(iii) the shape and the flux of the sources injected - our sources were set to have a 2D Gaussian circular shape (instead of an elliptical shape) and were also given different flux values and

(iv) the fraction of completeness imposed for the Source Extraction Limit - 100% in our case and 90% in ROMAGAL's.

Thus, the ROMAGAL team, with their higher computing resources and less limited time constraints, were capable of carrying out tests that were more exhaustive than ours and so, their table of Source Extraction Limits, with specific values for each one of the 30 Hi-GAL 1 fields, constitutes a more complete, but posterior, version of our results.

- **Flux uncertainties**

  The tests described above were also used by the ROMAGAL team to establish the uncertainties associated with CUTEX extracted fluxes. These uncertainties were determined by comparing the flux injected for the 1,000 test sources with the fluxes returned by CUTEX. Shown in Table 3.14 are the average flux uncertainty values found for the 1000 sources extracted in each of the 30 Hi-GAL fields tested and for each Herschel band. These results can be found in the *Hi-GAL Data Products Description document* but are reported here for readability.

  The results listed in Table 3.14 are different than those we derived when studying the flux uncertainties in Sect. 3.5.6. In the case of ROMAGAL, the team studied how the background emission, in each of the 30 tested Hi-GAL 1 fields, affected the fluxes CUTEX attributed to the field sources, regardless of the sources' flux level. On the contrary, in our case, we studied the effect of the $l = 290°$ field background emission in sources with different flux levels.

  Since our results demonstrate that the uncertainties associated with CUTEX extracted fluxes depend very strongly on the sources' flux, we concluded that, in the $l = 290°$ field, the uncertainties established by ROMAGAL are not as accurate as ours. We believe our results are also valid for the rest of the Hi-GAL 1 fields[17] as the background conditions present in the $l = 290°$ field are representative enough of the background emission levels found in the majority of the Hi-GAL 1 fields.

[17] With the exception of the most inner Galactic fields such as $l = [0°, 4°]$ and $l = [256°, 360°)$, whose background conditions might significantly differ from those found in the $l = 290°$ field.

Table 3.14: Flux levels, found by the ROMAGAL group, at which the CUTEX output sourcelists were found to have a completeness of 90%.

BLUE		RED		PSW		PMW		PLW	
Map Identifier (l)	90% complete at (Jy)	Map identifier (l)	90% complete at (Jy)	Map identifier (l)	90% complete at (Jy)	Map identifier (l)	90% complete at (Jy)	Map identifier (l)	90% complete at (Jy)
l002	1.737	l013	3.959	l002	13.059	l002	15.326	l002	14.375
l006	2.153	l019	3.313	l013	8.149	l006	7.532	l006	8.022
l013	1.645	l026	2.047	l019	5.924	l013	8.11	l019	7.789
l019	1.973	l030	4.762	l026	6.362	l019	6.783	l030	7.877
l026	1.591	l037	2.67	l037	4.411	l026	6.16	l037	4.578
l030	2.043	l044	2.154	l039	3.564	l030	7.75	l044	3.028
l037	1.687	l046	1.902	l044	2.752	l037	4.228	l046	2.981
l041	1.464	l048	2.519	l048	3.315	l044	2.803	l048	3.434
l044	1.656	l050	2.026	l050	3.308	l048	3.196	l050	3.559
l046	1.302	l052	1.74	l052	2.622	l050	3.366	l052	2.986
l048	1.869	l055	1.579	l055	1.789	l052	2.769	l055	2.118
l050	1.584	l057	1.07	l057	1.77	l055	1.951	l057	2.243
l052	1.424	l059	1.508	l059	1.79	l057	1.939	l059	2.402
l055	1.415	l060	1.496	l060	1.681	l059	2.083	l060	2.707
l057	1.2	l061	1.458	l061	1.403	l060	2.174	l061	1.777
l059	1.306	l063	1.276	l063	1.238	l061	1.62	l063	1.647
l060	0.798	l290	2.396	l290	2.5	l063	1.581	l294	2.579
l061	1.113	l294	1.864	l294	5.095	l290	2.781	l301	2.795
l063	1.287	l301	1.806	l301	2.064	l294	2.238	l314	4.453
l290	1.95	l308	2.118	l308	3.114	l301	2.615	l319	3.996
l294	1.559	l314	2.062	l314	3.649	l308	3.051	l321	4.308
l301	1.299	l319	2.904	l319	3.498	l314	3.757	l327	8.969
l308	1.501	l347	3.66	l321	3.61	l319	3.954	l334	12.667
l314	1.529			l327	8.336	l321	4.308	l341	7.301
l321	1.653			l334	8.06	l327	8.212	l354	10.394
l327	2.131			l347	5.145	l334	8.414		
l334	1.834			l354	7.021	l341	6.5		
l347	2.288					l347	5.055		
l354	2.528								

Table 3.15: Flux uncertainties, found by the ROMAGAL group, associated to the fluxes extracted by ROMAGAL and introduced by the highly variable maps' background.

BLUE		RED		PSW		PMW		PLW	
Map Identifier (l)	Uncertainty on flux (Jy)	Map identifier (l)	Uncertainty on flux (Jy)	Map identifier (l)	Uncertainty on flux (Jy)	Map identifier (l)	Uncertainty on flux (Jy)	Map identifier (l)	Uncertainty on flux (Jy)
l002	1.737	l013	3.959	l002	13.059	l002	15.326	l002	14.375
l002	0.195	l013	0.326	l002	1.143	l002	0.745	l002	1.934
l006	0.104	l019	0.203	l013	0.456	l006	0.524	l006	1.317
l013	0.081	l026	2.287	l019	0.200	l013	2.230	l019	0.118
l019	0.018	l030	0.540	l026	0.228	l019	0.105	l030	1.705
l026	0.065	l037	0.168	l037	0.180	l026	0.433	l037	0.304
l030	0.106	l044	0.184	l039	0.18	l030	1.173	l044	0.211
l037	0.063	l046	0.154	l044	0.188	l037	0.384	l046	0.299
l041	0.088	l048	0.150	l048	0.180	l044	0.217	l048	0.190
l044	0.304	l050	0.140	l050	0.170	l048	0.210	l050	0.210
l046	0.138	l052	0.120	l052	0.150	l050	0.220	l052	0.170
l048	0.120	l055	0.120	l055	0.140	l052	0.200	l055	0.150
l050	0.130	l057	0.110	l057	0.150	l055	0.180	l057	0.160
l052	0.120	l059	0.130	l059	0.120	l057	0.210	l059	0.150
l055	0.140	l060	0.130	l060	0.140	l059	0.140	l060	0.140
l057	0.110	l061	0.120	l061	0.130	l060	0.150	l061	0.110
l059	0.110	l063	0.110	l063	0.110	l061	0.150	l063	0.130
l060	0.100	l290	0.110	l290	0.387	l063	0.170	l294	0.242
l061	0.100	l294	0.137	l294	0.034	l290	0.218	l301	0.469
l063	0.110	l301	0.104	l301	0.163	l294	0.106	l314	0.330
l290	0.073	l308	0.194	l308	0.204	l301	0.178	l319	0.064
l294	0.084	l314	0.252	l314	0.225	l308	0.130	l321	0.838
l301	0.118	l319	0.029	l319	0.067	l314	0.272	l327	1.149
l308	0.081	l347	0.388	l321	0.140	l319	0.058	l334	1.243
l314	0.130			l327	0.640	l321	0.838	l341	0.545
l321	0.127			l334	0.842	l327	0.648	l354	2.016
l327	0.167			l347	0.414	l334	0.844		
l334	0.102			l354	0.710	l341	0.948		
l347	0.135					l347	0.639		
l354	0.065								

- **Flux Correction Factors**

  As we explained in Sect. 3.5.3, we found that the fluxes returned by CUTEX for the artificial sources were in general overestimated with respect to the original injected flux values. Such overestimation was attributed to the flux uncertainties introduced by the high variability of the background emission present in the Hi-GAL 1 maps. We showed that in the case of the 70 μm band, this overestimation was found to be systematic and could be amended by multiplying CUTEX original fluxes by the Flux Correction Factor $FCF_{CUTEX(70)} = 0.77$. However, according to ROMAGAL, there are two separate effects that introduce uncertainties to the fluxes returned by CUTEX: (i) the background emission and (ii) the high velocity (i.e. 60 $arcsec/sec$) at which the Hi-GAL 1 maps were scanned. At this scanning speed, the on-board co-addition in groups of several frames results in an elongation of the PSF in all Herschel bands (but specially in the PACS bands[18]) that show significant departures from a circularly symmetric morphology. As we explained in Sect. 3.3.2.2, CUTEX assumes the sources' brightness profiles to be Gaussian and uses this assumption to calculate the sources' fluxes by fitting a 2D Gaussian to the sources' brigthness profiles. However, because of the distortion that the PSF suffers, these approximation is no longer valid and leads to incorrect fluxes. In order to determine the flux uncertainties introduced by the PSF distortion, the ROMAGAL group carried out a series of tests in which they used a Hi-GAL image of a point-like primary calibrator, Arcturus, observed at a scanning velocity of 60 $arcsec/sec$. They then measured the source's flux in each Herschel band with CUTEX and compared these results with the expected values as derived from theoretical models (Müller et al. 2014). The previous tests allowed the ROMAGAL group to establish a series of Flux Correction Factors (FCF), presented in July 2013, that, when multiplied by the flux returned by CUTEX, correct the error introduced by the PSF distortion. These are: $FCF_{CUTEX(70\mu m)} = 1.367$, $FCF_{CUTEX(160\mu m)} = 1.153$, $FCF_{CUTEX(250\mu m)} = 1.294$,$FCF_{CUTEX(350\mu m)} = 1.138$ and $FCF_{CUTEX(500\mu m)} = 1.181$. Since the Flux Correction Factors we presented do not take into account such distortion, we concluded that ROMAGAL's values are preferable to ours.

[18]This asymmetry in the PSF affects specially the PACS bands because of the greater amount of data that needs to be compressed.

3.6 Summary and Conclusions

The purpose of this chapter was to find an algorithm able to successfully perform source and flux extraction in the Hi–GAL maps. In order to accomplish such goals we selected a total of five algorithms: DAOPHOT, SExtractor, the Wiener Filter, the Timeline Source Fitter and CUTEX and we run them through the 70 μm, 160 μm, 250 μm, 350 μm and 500 μm Hi–GAL 1 maps centred in b=0° and l=290° to determine whether they were, or were not, suitable for the extraction and source extraction of the Hi-GAL sources. The first three routines were chosen for being amongst the most widely "pre-Herschel" routines used within the astrophysics community and the latter two were selected for having been recently developed with the arrival of Herschel and for having proved to deliver accurate photometry on Herschel maps. While DAOPHOT, SExtractor, the Wiener Filter and CUTEX perform both source and flux extraction, TSF only carries out photometry and can only be used in the 250 μm, 350 μm and 500 μm Hi-GAL maps.
After examining the results we concluded that:

- DAOPHOT's use of a unique threshold is inappropriate for the source extraction of sources in the Hi-GAL maps and leads to the detection of a great number of false positives, located within the map's brightest regions, along the ISM filamentary structures present on the map or in the map's edges. On the other hand, DAOPHOT's use of a unique source and sky apertures is inadequate for the flux extraction in the Hi-GAL maps and leads to incorrect fluxes.

- SExtractor's use of a Bayesian source filtering and photometric technique, in which only models with uniform background are considered, is inappropriate for the source and flux extraction of sources in the Hi-GAL 1 maps and leads to the detection of an even greater number of false positives than that found with DAOPHOT and to obtaining incorrect fluxes.

- The Wiener Filter Fourier Transform deconvolution technique successfully removes most of the background emission present in the Hi-GAL map except for some interstellar filaments. However, to achieve that the program makes use of a global threshold, which leads to the sources being also filtered in the process and to obtaining incorrect fluxes.

- The CUTEX differentiation method and source finding strategy successfully separates the sources from the background emission and the interstellar filaments. Moreover, the CUTEX use of an adjustable Gaussian leads to obtaining highly accurate fluxes.

- The Timeline Source Fitter use of Signal Timeline Data leads to fluxes of an accuracy comparable to that of CUTEX fluxes.

In light of the previous findings, DAOPHOT, SExtractor and the Wiener Filter were discarded as not being suitable and only TSF and CUTEX were regarded as adequate. In order to determine the source-extracting performance of CUTEX and compare the flux-extracting performance of TSF and CUTEX we next conducted a series of tests. These tests consisted on the extraction of 121 identical synthetic sources that were injected into the original 70 μm, 160 μm, 250 μm, 350 μm and 500 μm $l = 290°$, $b = 0°$ Hi-GAL maps. The flux of these sources was changed in each test to be 0.1, 0.2, 0.5, 1, 2, 5, 10, 20, 50, 100 and 200 Jy. We then determined the number of synthetic sources extracted by TSF and CUTEX and compared the algorithms' output and input source flux densities.
Through these tests we were able to establish:

1. The CUTEX *Source Extraction Limit*, i.e. the minimum level, in each band, for which CUTEX was able to extract the 100% of the injected source sample.

2. The TSF and CUTEX *Source Flux Fitting Limit*, i.e. the flux level, in each band, for which the number of positive sample fluxes returned by TSF and CUTEX was maximised while the number of sample null and negative fluxes was minimised.

3. The TSF and CUTEX *Source Flux Accuracy Limit*, i.e. the flux level, in each band, below which the sample fluxes returned by TSF and CUTEX were unreliable.

4. The statistical outliers present in the TSF and CUTEX returned flux distributions.

5. The flux uncertainties associated with the TSF and CUTEX returned fluxes.

6. The Flux Correction Factors for the TSF and CUTEX returned fluxes.

Listed in Table 3.16 and 3.17 is a summary of the results obtained for TSF and CUTEX.

Table 3.16: Summary of the results obtained when testing the TSF and CUTEX performance on source and flux extracting a total of 121 synthetic sources artificially injected on the 70 μm, 160 μm, 250 μm, 350 μm and 500 μm Hi–GAL maps centred in the l=290°, b=0° Galactic region. Included in the table are: the Source Extraction Limits, the Source Flux Fitting Limits and the Source Flux Accuracy Limits that we derived. Also included are the Flux Correction Factors derived by us (S) and ROMAGAL (R).

Source Extraction Limits					
	70 μm	**160 μm**	**250 μm**	**350 μm**	**500 μm**
CUTEX	0.5 Jy	1 Jy	0.1 Jy	0.1 Jy	2 Jy
Source Flux Fitting Limits					
	70 μm	**160 μm**	**250 μm**	**350 μm**	**500 μm**
TSF	–	–	1 Jy	1 Jy	1 Jy
CUTEX	1 Jy	2 Jy	0.1 Jy	0.2 Jy	2 Jy
Source Flux Accuracy Limits					
	70 μm	**160 μm**	**250 μm**	**350 μm**	**500 μm**
TSF	–	–	1 Jy	1 Jy	1 Jy
CUTEX	0.1 Jy	1 Jy	1 Jy	1 Jy	1 Jy
Flux Correction Factors					
	70 μm	**160 μm**	**250 μm**	**350 μm**	**500 μm**
TSF^{S}	–	–	1.18	1.21	1.13
CUTEX^{S}	0.77	–	–	–	–
CUTEX^{R}	1.367	1.153	1.294	1.138	1.181

Table 3.17: Mean percentages of sample sources whose TSF and CUTEX returned flux was found to be lying within $|1\sigma|$, $|2\sigma|$, $|3\sigma|$, $\pm$ 1σ, $\pm$ 2σ and $\pm$ 3σ of the samples' μ.

TSF						**CUTEX**					
TOTAL=98.99						**TOTAL=97.53**					
$\|1\sigma\|$		$\|2\sigma\|$		$\|3\sigma\|$		$\|1\sigma\|$		$\|2\sigma\|$		$\|3\sigma\|$	
72.47		21.50		5.02		79.12		13.75		4.66	
-3σ	-2σ	-1σ	1σ	2σ	3σ	-3σ	-2σ	-1σ	1σ	2σ	3σ
1.97	11.16	36.87	35.59	10.34	3.05	2.01	6.83	40.19	38.93	6.92	2.65

From the results listed in Table 3.16 and Table 3.17, we concluded that:

- In the 70 μm, 160 μm, 250 μm, 350 μm and 500 μm bands, the CUTEX source extraction is most efficient when extracting sources with fluxes equal or larger than 0.5 Jy, 1 Jy, 0.1 Jy, 0.1 Jy and 2 Jy, respectively.

- The CUTEX 70 μm, 160 μm and 500 μm output sourcelists are only complete within the [0.5 Jy, 200 Jy], [1 Jy, 200 Jy] and [2 Jy, 200 Jy] flux ranges respectively while the CUTEX 250 μm and 350 μm output sourcelists are complete within the [0.1 Jy, 200 Jy] flux range.

- All the fluxes extracted by TSF in the 250 μm, 350 μm and 500 μm bands are systematically underestimated but can be corrected if multiplied by the Flux Correction Factor: $FCF_{TSF(250)} = 1.18$, $FCF_{TSF(350)} = 1.21$ and $FCF_{TSF(500)} = 1.13$. On the other hand, all the fluxes extracted by CUTEX in the 70 μm band are systematically overestimated but can be corrected if multiplied by: $FCF_{CUTEX(70)} = 0.77$. For the other bands no general flux correction could be applied despite some of the returned fluxes being overestimated.

- For the 160 μm, 250 μm, 350 μm and 500 μm bands the flux reliability of the (corrected) fluxes returned by TSF and CUTEX is: (i) low for <1 Jy sources, (ii) moderate for 1 Jy sources (160 μm and 250 μm bands) and 2 Jy sources (350 μm and 500 μm bands) and (iii) high for >1 Jy sources (160 μm and 250 μm bands) and >2 Jy sources (350 μm and 500 μm bands). On the other hand, for the 70 μm band, the flux reliability of the (corrected) fluxes returned by CUTEX is: (i) moderate for <0.1 Jy sources and (ii) high for >0.1 Jy sources.

- The amount of TSF-extracted fluxes with uncertainties lying within $|1\sigma|$ ($|2\sigma|+|3\sigma|$) of the injected flux value was found to be slightly lower (greater) than that of CUTEX-extracted fluxes. Therefore, CUTEX fluxes are slightly more accurate than those returned by TSF.

The lower accuracy of the fluxes returned by TSF, added to the fact that TSF does not perform source extraction and only performs flux extraction in three of the five Herschel bands, led us to the conclusion that between DAOPHOT, SExtractor, the Wiener Filter, TSF and CUTEX, the latter is the best algorithm for the source and flux extraction of the sources in the Hi-GAL maps.

The results that we found for CUTEX were then compared to the results obtained by the ROMAGAL team in a series of tests they carried out to characterise the CUTEX performance when source and flux extracting.

The first tests that ROMAGAL conducted consisted in the injection of artificial sources on real Hi-GAL 1 maps, which were then extracted with CUTEX in order to establish the number of sources successfully recovered and to compare the fluxes of the extracted sources with the injected flux level. These tests are very similar to those we conducted, being the only differences: (i) the number of fields in which the tests were carried out - 1 in our case and 30 in ROMAGAL's, (ii) the number of sources injected - 121 in our case and 1,000 in ROMAGAL's and (iii) the shape and the flux of the sources injected - while our sources were given a 2D Gaussian circular shape and a fixed FWHM, ROMAGAL's sources were given a variable elliptical shape and FWHM.

In the second tests that ROMAGAL conducted, the team used a Hi-GAL image of a point-like primary calibrator, Arcturus, observed at a scanning velocity of 60 $arcsec/sec$ and measured the source's flux in each Herschel band with CUTEX. These fluxes were then compared with the expected values as derived from theoretical models (Müller et al. 2014). Through these tests, the ROMAGAL team was able to establish:

(i) The minimum flux levels at which the CUTEX extracted sourcelists had a completeness of 90% in each of the 30 Hi-GAL fields tested and for each Herschel band.

These flux levels are equivalent to the Source Extraction Limits (SELs) we derived. However, whereas our values were derived only for the $l = 290°$ Hi-GAL 1 field and then extrapolated to the rest of the fields, ROMAGAL's table of SELs has specific values for each one of the 30 Hi-GAL 1 fields. In light of these results, we concluded that ROMAGAL's SEL table constitutes a more complete, but posterior, version of our values.

(ii) The average flux uncertainty values found for the 1,000 sources extracted in each of the 30 Hi-GAL fields tested and for each Herschel band.

These flux uncertainties are different from those we derived. While we studied the effect of the $l = 290°$ field background emission in sources with different flux levels, ROMAGAL studied how the background emission affected the fluxes CUTEX attributed to each field's sources, regardless of the sources' flux level.

Since the results we obtained established that CUTEX flux uncertainties depend very strongly on the sources' flux, we concluded that, for the $l = 290°$ field, ROMAGAL's flux uncertainties are not as accurate as ours. Moreover, given that the background conditions present in the $l = 290°$ field are representative of those found in the majority of the Hi-GAL 1 fields, we concluded that the results obtained for the $l = 290°$ field can be extended to the majority of Hi-GAL 1 fields.

(iii) A series of Flux Correction Factors (FCF) that, when multiplied by the flux returned by CUTEX, correct the error introduced by the PSF distortion.

This distortion is a result of the high velocity (i.e. 60 $arcsec/sec$) at which the Hi-GAL 1 maps were scanned. Since the FCF we presented do not take into account such distortion, we concluded that ROMAGAL's FCF, which are listed in Table 3.16, are preferable to ours.

Chapter 4

Building a Point Source Catalogue for Hi-GAL 1

"To be able to see the entire lifecycle of material in the Galaxy in a single real image, exactly as shown in theory, from diffuse to dense clouds and on until the final phases of stellar evolution was a truly remarkable experience."

Sergio Molinari

4.1 Introduction

The aim of this chapter is to build a Point Source Catalogue containing the positions and flux densities of the sources detected in the Hi-GAL 1 Survey.
In the following sections I:

(i) introduce the series of requirements this catalogue must fulfil and describe the procedure followed in its creation,

(ii) cross-match our catalogue with Point Source Catalogues of other surveys in order to identify the sources contained in our catalogue, expand their photometric range and correct possible astrometric offsets and

(iii) discuss the catalogue's source and flux reliability, distribution, completeness and photometric coverage.

4.2 Point Source Catalogues

A *Point Source Catalogue* (PSC) is a catalogue that includes the position and the fluxes, amongst other parameters, of sources that are not extended but point-like. For every IR space mission undertaken since IRAS was launched in 1983, a PSC has been generated, the following being the most relevant to our work:

- The *IRAS catalogue of point sources*

  This catalogue contains the positions and photometry in the four IRAS IR bands, (hereafter referred to as *I1*, *I2*, *I3* and *I4* bands), centred at 12 μm, 25 μm, 60 μm and 100 μm respectively, for a total of 245,889 sources detected with IRAS.

- The *WISE All-Sky Source Catalogue* (Cutri and et al. 2012)

  This catalogue contains the positions and photometry in the four WISE Survey Camera MIR bands, (hereafter referred to as *W1*, *W2*, *W3* and *W4* bands), centred at 3.4 μm, 4.6 μm, 12 μm, and 22 μm respectively, for a total of 563,921,584 point-like and resolved objects detected on the Atlas Intensity images.

- The *complete MSX6C IR Point Source Catalogue* (Egan et al. 2003)

  This catalogue contains the positions and photometry in the six MSX SPIRIT III MIR bands, (hereafter referred to as *B1*, *B2*, *A*, *C*, *D* and *E* bands), centred at 4.29 μm, 4.35 μm, 8.28 μm, 12.13 μm, 14.65 μm and 21.34 μm respectively, for a total of 431,711 sources detected with MSX.

- The *2MASS All Sky Survey Point Source Catalogue* (Skrutskie et al. 2006)

  This catalogue contains the positions and photometry in the three 2MASS NIR bands, (hereafter referred to as *J*, *H* and *K* bands), centred at 1.25 μm, 1.65 μm and 2.17 μm respectively, for a total of 470,992,970 objects.

- The *GLIMPSE Source Catalogue* (I + II + 3D) (Benjamin et al. 2003)

  This catalogue contains the positions and photometry in the four Spitzer bands, (hereafter referred to as *G1*, *G2*, *G3* and *G4* bands), centred at 3.6 μm, 4.5 μm, 5.8 μm and 8.0 μm respectively, for a total of 104,240,613 sources detected in the GLIMPSE I ($|l| = 10° - 65°$, $|b| \leq 1°$), II [1] ($|l| \leq 10°$, $|b| \leq 1° - 2°$) and 3D [2].

[1] The GLIMPSE II coverage excludes the Galactic Centre region within $|l| \leq 1°$ and $|b| \leq 0.75°$. In this catalogue version, the *GLIMPSE II Highly reliable Catalogue* and *Archive* records are merged.

[2] The GLIMPSE 3D adds vertical extensions up to $|b| = 3° - 4.2°$.

- The *AKARI/IRC and AKARI/FIS All-Sky Survey Point Source Catalogues*

  On the one hand, the *AKARI/IRC All-Sky Survey PSC* contains the positions and photometry in the two IRC (Onaka et al. 2007) bands, (hereafter referred to as *A1* and *A2* bands), centred at 9 μm and 18 μm respectively, for a total of 870,973 point-like sources. On the other hand, the *AKARI/FIS All-Sky Survey PSC* contains the positions and photometry in the four FIS bands (Kawada et al. 2007), (hereafter referred to as *A3*, *A4*, *A5* and *A6* bands), centred at 65 μm, 90 μm, 100 μm and 160 μm respectively, for a total of 427,071 sources.

From here onwards we will refer to the previous catalogues as the *Survey Catalogues*. In the case of Herschel, at the beginning of this PhD study (October 2010) there was no PSC catalogue available. Thus, we had to build one ourselves; a process we have described from Chapter 2 to this current Chapter 4. We started by choosing our preferred pipeline to process the Hi-GAL 1 maps (see Chapter 2), we then selected a suitable algorithm to perform source and flux extraction on the Hi-GAL 1 maps (see Chapter 3) and finally, we created our Hi-GAL 1 PSC, hereafter referred to as SMA Hi-GAL 1 PSC. However, in 2012, long after we compiled our SMA Hi-GAL 1 PSC, the ROMAGAL group published their own Hi-GAL 1 PSC, hereafter referred as ROMAGAL Hi-GAL 1 PSC. Facing this situation, we decided to perform a comparison between the ROMAGAL and the SMA Hi-GAL 1 PSC catalogues in order to determine the differences between them. As a result, in the following sections, we not only explain each step taken in the creation of our catalogue, but also comment on the different methodology followed by the ROMAGAL group on the creation of their catalogue. The ultimate goal of this comparison was to establish whether we should use our SMA Hi-GAL 1 PSC or the ROMAGAL Hi-GAL 1 PSC.

4.3 Hi-GAL 1 Point Source Catalogue

4.3.1 Source and flux extraction of the Hi-GAL 1 sources

In order to extract the positions and fluxes of the sources contained in the 70 μm, 160 μm, 250 μm, 350 μm and 500 μm maps of all the 63 fields contained in the Hi–GAL 1 Survey we made use of CUTEX, which was found to be the most suitable algorithm to perform source and flux extraction on the Hi–GAL maps. For the complete 63 fields, we used the same CUTEX source detection and flux extraction methods we presented in Sect. 3.3.2.2.

4.3.2 Hi-GAL 1 band catalogues

Having run CUTEX through each of the total 63 Hi-GAL 1 70 μm maps, we then proceeded to create a band catalogue, referred to as *SMA Hi-GAL 1 70 μm band catalogue*, that contained the positions (RA and dec, in degrees) and fluxes (in Jy) of all the sources included in the 63 individual CUTEX output sourcelists. This process was repeated for the other bands in order to obtain the *SMA Hi-GAL 1 160 μm*, *250 μm*, *350 μm* and *500 μm band catalogues*.

As we mentioned at the beginning of this Chapter 4, long after we created our Hi-GAL 1 band catalogues, the ROMAGAL group presented their own catalogues, which we called *the ROMAGAL Hi-GAL 1 band catalogues*. When comparing the two versions of the catalogues, it was found that:

(i) The number of sources included in our band catalogues was different than that included in their band catalogues.

(ii) The fluxes listed for a source included in both our and their band catalogues were also different.

In order to understand these differences and to reach a conclusion on which of the catalogue versions should we be using, we performed an analysis of the two catalogue versions, which we present in the following section.

4.3.2.1 Comparison between the SMA and ROMAGAL Hi-GAL 1 band catalogues

(i) *Differences on the number of sources included in the SMA and ROMAGAL Hi-GAL 1 band catalogues*

Listed in Table 4.1 are the number of sources (n) included in the 70 μm, 160 μm, 250 μm, 350 μm and 500 μm SMA and ROMAGAL Hi-GAL 1 band catalogues. Here, we can see that $n_{SMA} < n_{ROMAGAL}$ for the 160 μm, 250 μm, 350 μm and 500 μm Hi-GAL 1 band catalogues while $n_{SMA} > n_{ROMAGAL}$ for the 70 μm band Hi-GAL 1 band catalogue. In order to find the cause of these differences we compared the sourcelist ROMAGAL extracted from the 70 μm l=290°, b=0° Hi-GAL 1 map to the sourcelist we extracted from the same map.

Table 4.1: Number of sources (n) included in the 70 μm, 160 μm, 250 μm, 350 μm and 500 μm SMA (n_{SMA}) and ROMAGAL ($n_{ROMAGAL}$) Hi-GAL 1 band catalogues.

Hi-GAL 1 band catalogue	n_{SMA}	$n_{ROMAGAL}$
70 μm	171,114	120,579
160 μm	175,169	291,858
250 μm	118,414	280,143
350 μm	98,165	161,946
500 μm	63,081	85,811

Shown in Fig. 4.1 is the 70 μm l=290° Hi-GAL map in which we over plotted the sources extracted by us (blue crosses) and by ROMAGAL (green circles). Indicated with a blue (green) frame is the area in which we (ROMAGAL) performed source extraction.
From the inspection of Fig. 4.1 we determined that:

1. *The map area in which ROMAGAL performed the source extraction is larger than that chosen by us and it is lying either outside or on top of the edges of our maps.*

   This fact results in some of the ROMAGAL sources being located outside our maps' boundaries, which indicates that the ROMAGAL group used a different set of Hi-GAL 1 maps than ours. Since the set of maps used by ROMAGAL is posterior to ours, these maps will be further processed than those we used.

   Shown in Fig. 4.2 are the 70 μm l=290°, b=0° Hi-GAL 1 map that we used (left panel) and the 70 μm l=290°, b=0° Hi-GAL 1 map used by ROMAGAL (right panel). Here, we can see that, indeed, the ROMAGAL maps are slightly larger than ours and that the quality of the map edges and the overall map has been improved with respect to ours.

   The previous results explain why those sources lying in ROMAGAL maps' edges are not included in our band catalogues. However, this explanation does not apply to the large amount of ROMAGAL sources that lie in the maps' common inner part (i.e. within the blue frame) and for which no counterparts were found in our band catalogues.

Figure 4.1: Image of the 70 μm l=290°, b=0° Hi-GAL 1 map showing the different sources we extracted (blue crosses) and the sources ROMAGAL extracted (green circles) as well as the different area in which we (in blue) and ROMAGAL (in green) performed the source extraction. Here, we can see that the map area in which ROMAGAL performed the source extraction is greater than that chosen by us and that ROMAGAL's selected area is lying either outside or on top of the edges of our maps. This fact results in some of the ROMAGAL sources being located outside of our maps' boundaries, which indicates that the ROMAGAL group used a different and further processed set of Hi-GAL 1 maps than ours. In this image, the contrast of the original map has been modified so that all the features described in the text can be seen with the maximum clarity.

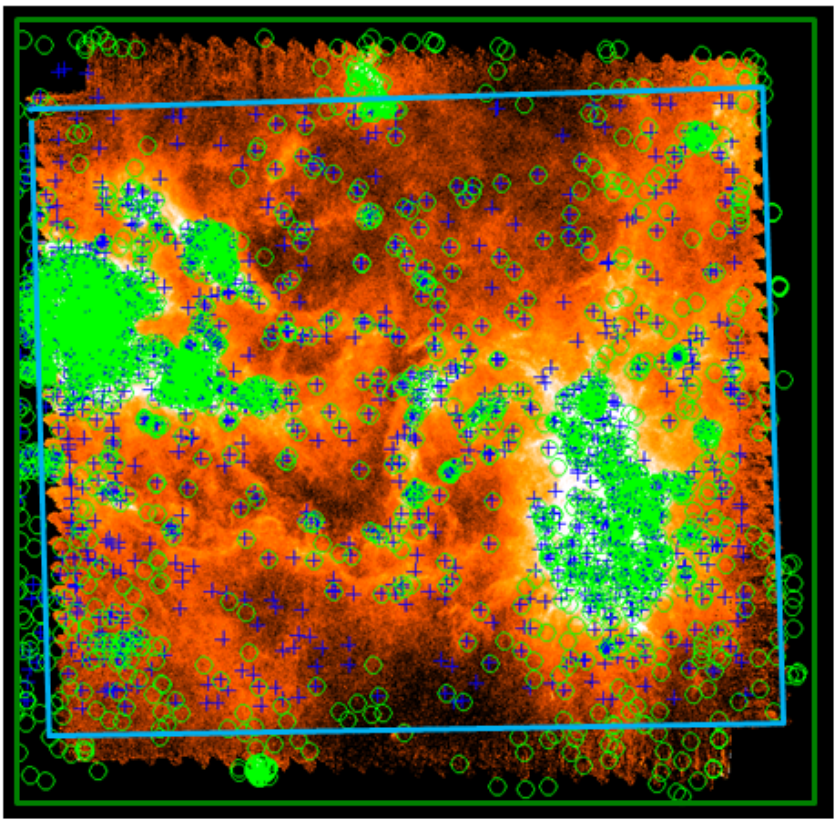

Figure 4.2: Image of the 70 μm l=290°, b=0° Hi-GAL 1 map used by us (left panel) and ROMAGAL (right panel) for the extraction of the sources contained in the 70 μm SMA and ROMAGAL Hi-GAL 1 band catalogues. Here, we can see that the maps used by ROMAGAL are slightly larger than ours and that the quality of the maps' edges is better for the ROMAGAL maps.

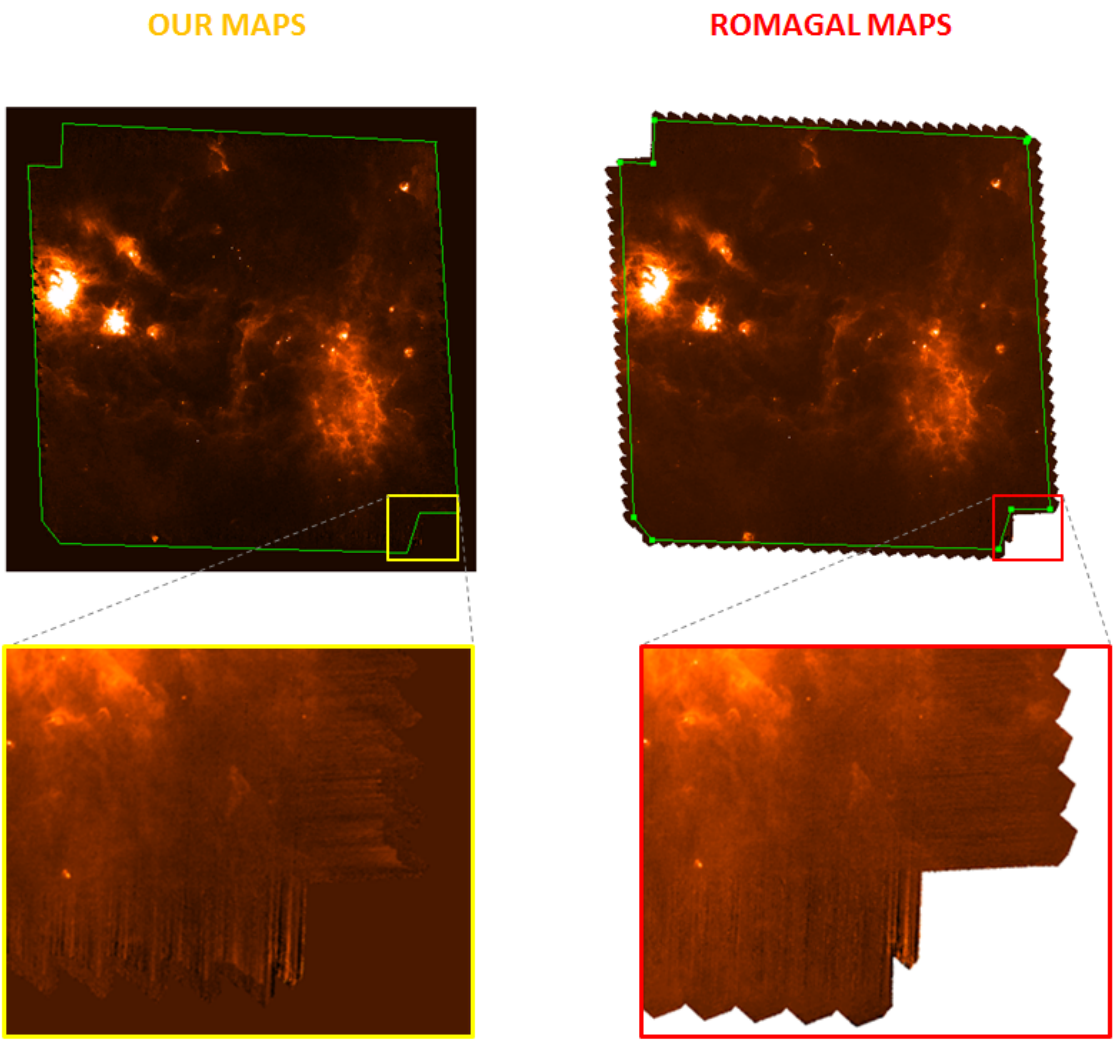

2. *Within the area common to the ROMAGAL and our maps, we detect more (less) sources in the 70 μm band (160 μm, 250 μm, 350 μm and 500 μm bands).*

   This fact is a direct consequence of the different thresholds that ROMAGAL and us used in the source extraction. Whereas we selected: thr=1.8, 2.5, 3.5, 3.2 and 3 for the 70 μm, 160 μm, 250 μm, 350 μm and 500 μm bands respectively, the ROMAGAL team used thr=2 for all the Herschel bands (see Molinari et al. 2015). Thus, while for the 70 μm band our threshold was set to be lower (i.e. more sensitive) than ROMAGAL's, for the remaining bands our chosen thresholds are higher (i.e. less sensitive) than ROMAGAL's. As a result, our 70 μm band catalogue has more source detections than the ROMAGAL 70 μm band catalogue whereas our 160 μm, 250 μm, 350 μm and 500 μm band catalogues have less source detections than the corresponding ROMAGAL band catalogues.

   Although the difference on the threshold values used for the source extraction is the main cause for the different number of entries in ROMAGAL and our catalogues, there is another cause that significantly affects the source extraction: the use of different maps. In order to prove the previous statement we carried out the following test. First, we created two new maps that included only the inner map area that coincides in the l=290° 70 μm Hi-GAL 1 maps used by us and ROMAGAL. Next, we run CUTEX through these two new maps using the same exact CUTEX configuration (i.e. we use the same values for the thr and for the rest of the CUTEX source extraction and flux detection keywords). We then compared the number of sources extracted in the two different maps. The process was repeated for two different threshold values: thr=1.8 and thr=10. The first value (thr=1.8) was chosen for being the same value that we used in our maps whereas the second value (thr=10) was chosen for being high. The use of a high thr presented the advantage that it only detected a few hundreds of map sources, which facilitated the sources' visual inspection. The results show that, despite using the same CUTEX configuration, the ROMAGAL map sourcelist contains, in general, more entries than that for our map. When using thr=1.8, we found a difference of 107 sources whereas when using thr=10, we found a difference of only 2 sources. Thus, the greater the value of the thr, the less significant the difference between the number of entries contained in the two maps' sourcelist.

Next, we cross-matched the sourcelists extracted from the two maps allowing, between the matches, a maximum distance of 3.2" (i.e. the pixel size in the 70 μm band). When cross-matching the thr=1.8 sourcelist, we found that: (i) 58% of the sources were common in both sourcelists, (ii) 23% of the sources were detected only in the ROMAGAL map and (iii) 19% of the sources were detected only in our map[3]. The previous process was repeated for the thr=10 sourcelists. In this case, we found that: (i) 88% of the sources were common in both sourcelists, (ii) 6% of the sources were detected only in the ROMAGAL map and (iii) 5% of the sources were detected only in our map. These results prove that the use of different maps leads to a difference in the number of entries contained in the output sourcelists and also in the sources extracted. They also establish that the lower the thr value used, the greater the differences in the number of entries and the fewer common sources there are.

The previous findings led us to the conclusion that the different number of sources in the SMA and ROMAGAL Hi-GAL 1 band catalogues was due to: (i) ROMAGAL's use of different maps than ours and (ii) ROMAGAL's use of a threshold of lower (higher) sensitivity than ours in the 70 μm band (160 μm, 250 μm, 350 μm and 500 μm bands).

(ii) *Differences between the fluxes listed for the sources common to the SMA and the ROMAGAL Hi-GAL 1 band catalogues*

When comparing the fluxes listed for the sources common to the SMA and the ROMAGAL Hi-GAL 1 band catalogues, we found that the ROMAGAL fluxes were deviant from ours. The difference in the sources' fluxes was found to be due to two things:

1. *The different Flux Correction Factors (FCF) used by ROMAGAL and us*

   As we explained in Sect. 3.5.3 and 3.5.7, the FCF that ROMAGAL applied to the CUTEX extracted fluxes are different than those we applied. While our FCF correct only the flux uncertainties introduced by the strong background emission present in the Hi-GAL 1 maps, ROMAGAL's FCF correct also the flux uncertainties introduced by the distortion that the PSF suffers in all Herschel bands while scanning at high velocity.

[3]The previous percentages were established considering the total amount of map sources to be the sum of all the detected sources.

2. *The different maps used by ROMAGAL and us*

   If the FCF were the only cause for the different fluxes found in ROMAGAL's and our band catalogues, the ratio between the ROMAGAL and our fluxes for a specific band should be the same for all the sources found in common. However, this was not the case, and so, we investigated the possibility that our results were also due to the use of different maps.

   In order to prove the previous hypothesis we used the thr=1.8 sourcelists that we obtained in the previous section. These sourcelists contained the fluxes of the sources extracted with CUTEX in the common central area of the l=290° 70 μm Hi-GAL 1 maps used by us and ROMAGAL and were generated having set CUTEX threshold to be equal to 1.8.

   The thr=1.8 sourcelists were then cross-matched allowing, between the matches, a maximum distance of 3.2" (i.e. the pixel size in the 70 μm band) and with the matches found, we calculated the absolute difference between the fluxes (ΔF) extracted from the ROMAGAL and our map.

   We then determine the fraction of sources for which the flux difference was found to be: (a) $\Delta F < 0.2\ Jy$, (b) $0.2\ Jy < \Delta F < 2\ Jy$, (c) $2\ Jy < \Delta F < 10\ Jy$ and (d) $\Delta F > 10\ Jy$. These percentages were found to be (a) ∼65%, (b) ∼28%, (c) ∼6% and (d) ∼2%, respectively.

   These results prove that the use of different maps leads to a difference in the flux of the extracted sources, which is smaller than 0.2 Jy for the majority of the sources (∼65%) and within [0.2,2] Jy for a considerable amount of sources (∼28%). The results also show that for ∼2% of the sources the flux difference can be greater than 10 Jy and that there are some extreme cases (∼0.3%) for which the flux difference was found to be of hundreds of Jy. No connection was found between the sources' ΔF values and the sources' matching distance, position or background conditions.

The previous findings agree with the differences we found between the fluxes listed in the ROMAGAL and our Hi-GAL 1 band catalogues and led us to the conclusion that the difference found between the fluxes in the two band catalogues was due to: (i) ROMAGAL's use of different maps than ours and (ii) ROMAGAL's use of different Flux Correction Factors.

4.3.2.2 Final choice of Hi-GAL 1 band catalogues

In the previous Sect. 4.3.2.1 we established that the different number of sources and fluxes contained in the SMA and ROMAGAL Hi-GAL 1 band catalogues was mainly due to ROMAGAL's use of different maps, thresholds and Flux Correction Factors (FCF). The previous results confirm that despite the differences, both the ROMAGAL and the SMA band catalogues are equally valid, with the only exception being that our extracted fluxes should be corrected with the FCF presented by ROMAGAL instead of our own - since their FCF also consider the flux uncertainties introduced by the PSF distortion.
Nevertheless, because the ROMAGAL band catalogue sources were extracted from a set of maps further processed, of better quality and slightly larger than ours, we decided to use the ROMAGAL band catalogues instead of ours. This decision was also made to guarantee that the work presented in the following chapters was carried out using the most updated catalogues' version. Thus, from this moment onwards we proceeded to work exclusively with the Hi-GAL 1 ROMAGAL band catalogues.
In the following section, we present a study of the catalogues' flux distribution and flux reliability in which we will prove that by removing a small fraction of the catalogues' sources, it is possible to significantly increase their flux reliability and accuracy.

4.3.2.3 Catalogues' flux distribution and flux reliability

Shown in Fig. 4.3 are the percentages of sources contained in the 70 μm, 160 μm, 250 μm, 350 μm and 500 μm ROMAGAL Hi-GAL 1 band catalogues whose flux is: (i) < 1 Jy, (ii) in the [1,2) Jy range, (iii) in the [2,5) Jy range, (iv) in the [5,10) Jy range and (v) ≥ 10 Jy. These percentages are listed in Table 4.2 and establish that:

- The majority of the sources (60%) included in the 70 μm ROMAGAL Hi-GAL 1 band catalogue are brighter than 2 Jy. There is a large percentage of the sources (27%) that are fainter than 1 Jy and there is a considerable percentage of the sources (14%) that have flux values lying within the [1,2) Jy range.

- The majority of the sources ($\sim$75%) included in the 160 μm, 250 μm, 350 μm and 500 μm ROMAGAL Hi-GAL 1 band catalogues are brighter than 2 Jy. There is a considerable percentage of the sources ($\sim$16%) that have flux values lying within the [1,2) Jy range and there is a low percentage of the sources ($\sim$9%) that are fainter than 1 Jy.

Figure 4.3: Flux distributions of the sources contained in the 70 μm, 160 μm, 250 μm, 350 μm and 500 μm ROMAGAL Hi-GAL 1 band catalogues.

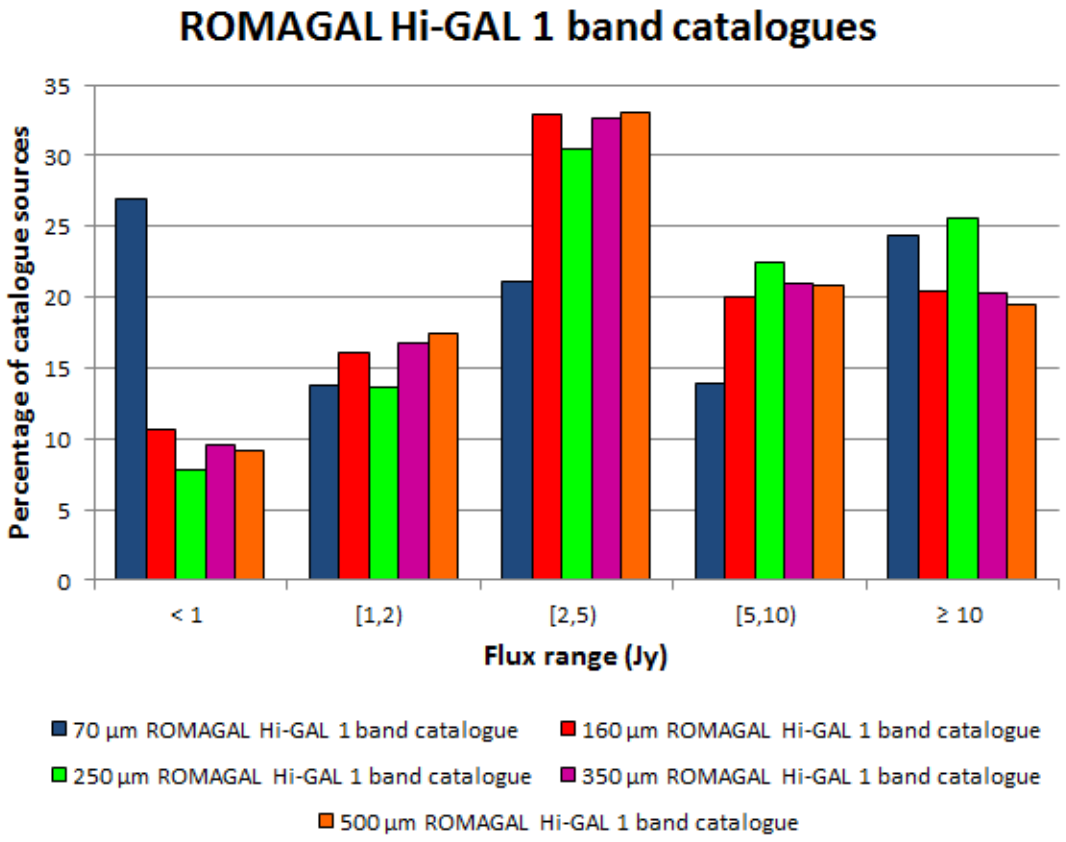

Table 4.2: Percentage of sources included in the 70 μm, 160 μm, 250 μm, 350 μm and 500 μm ROMAGAL Hi-GAL 1 band catalogues whose flux is: (i) $<$ 1 Jy, (ii) in the [1,2) Jy range, (iii) in the [2,5) Jy range, (iv) in the [5,10) Jy range and (v) $\geq$ 10 Jy.

ROMAGAL Hi-GAL 1 band catalogues	**Flux range**				
	<1 Jy	**[1,2) Jy**	**[2,5) Jy**	**[5,10) Jy**	**≥10 Jy**
70 μm	26.9	13.8	21.1	13.9	24.3
160 μm	10.6	16.1	32.9	20.0	20.4
250 μm	7.8	13.7	30.4	22.5	25.6
350 μm	9.5	16.8	32.7	20.9	20.3
500 μm	9.1	17.5	33.1	20.8	19.5

Figure 4.4: S/N distributions of the sources contained in the 70 μm, 160 μm, 250 μm, 350 μm and 500 μm ROMAGAL Hi-GAL 1 band catalogues.

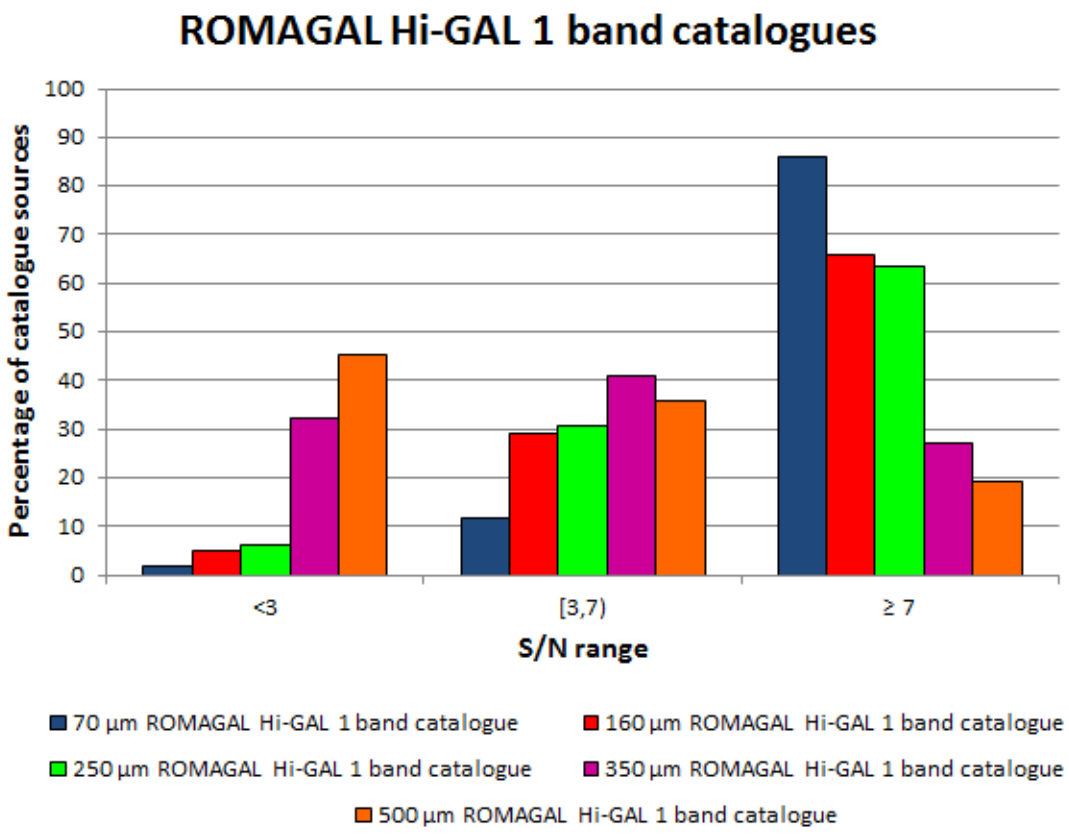

Table 4.3: Percentage of sources included in the 70 μm, 160 μm, 250 μm, 350 μm and 500 μm ROMAGAL Hi-GAL 1 band catalogues for which: (i) S/N $<$ 3, (ii) 3 $\leq$ S/N $\leq$ 7 and (iii) S/N $>$ 7.

ROMAGAL Hi-GAL 1 band catalogues	**S/N range**		
	$<$3	**[3,7)**	**$\geq$7**
70 μm	2.0	11.8	86.2
160 μm	5.1	29.0	65.9
250 μm	6.1	30.6	63.3
350 μm	32.1	40.8	27.1
500 μm	45.1	35.8	19.2

Shown in Fig. 4.4 are the percentages of sources contained in the 70 μm, 160 μm, 250 μm, 350 μm and 500 μm ROMAGAL Hi-GAL 1 band catalogues whose S/N is: (i) < 3, (ii) in the [3,7) range, (iii) ≥ 7 and whose flux reliability is: (i) low, (ii) moderate and (iii) high, respectively. These percentages are listed in Table 4.3 and establish that:

- The majority of the sources (86%) included in the 70 μm ROMAGAL Hi-GAL 1 band catalogue have S/N ≥ 7, i.e. they have a high flux reliability. There is a considerable percentage of the sources (12%) that have $3 \leq$ S/N < 7, i.e. they have a moderate flux reliability. There is also a low percentage of the sources (2%) that have S/N < 3, i.e. they have a low flux reliability. Thus, in general, the fluxes listed in the 70 μm Hi-GAL 1 band catalogues have a high reliability.

- The majority of the sources ($\sim$65%) included in the 160 μm and 250 μm ROMAGAL Hi-GAL 1 band catalogues have S/N ≥ 7, i.e. they have a high flux reliability. There is a high percentage of the sources ($\sim$30%) that have $3 \leq$ S/N < 7, i.e. they have a moderate flux reliability. There is also a low percentage of the sources ($\sim$6%) that have S/N < 3, i.e. they have a low flux reliability. Therefore, in general, the fluxes listed in the 160 μm and 250 μm Hi-GAL 1 band catalogues have a moderate reliability.

- There is a high percentage ($\sim$39%) of the sources included in the 350 μm and 500 μm ROMAGAL Hi-GAL 1 band catalogues that have S/N < 3, i.e. they have a low flux reliability. There is also a high percentage of the sources ($\sim$38%) that have $3 \leq$ S/N < 7, i.e. they have a moderate flux reliability. In addition, there is a considerable percentage of the sources ($\sim$26%) that have S/N ≥ 7, i.e. they have a high flux reliability. Thus, in general, the fluxes listed in the 350 μm and 500 μm ROMAGAL Hi-GAL 1 band catalogues have a low to moderate reliability.

Shown in Fig. 4.5 and 4.6 are the percentages of S/N < 3, S/N=[3,7) and S/N ≥ 7 sources contained in the 70 μm, 160 μm, 250 μm, 350 μm and 500 μm ROMAGAL Hi-GAL 1 band catalogues whose flux is: (i) < 1 Jy, (ii) in the [1,2) Jy range, (iii) in the [2,5) Jy range, (iv) in the [5,10) Jy range and (v) ≥ 10 Jy. These percentages are listed in Table 4.4 and 4.5 and establish that:

- In the 70 μm, 160 μm and 250 μm ROMAGAL Hi-GAL 1 band catalogues, the majority of the S/N < 3 sources ($\sim$89%) are < 1 Jy sources.

- On the other hand, the majority of the $3 \leq S/N < 7$ sources (∼95%) are fainter than 1 Jy (for the 70 μm band) or fainter than 5 Jy (for the 160 μm and 250 μm bands). Finally, the majority of the $S/N > 7$ sources (∼87%) are $\geq$ 2 Jy sources.

- In the 350 μm and 500 μm ROMAGAL Hi-GAL 1 band catalogues, the majority of the $S/N < 3$ sources (∼92%) are $<$ 5 Jy sources. On the other hand, the majority of the $3 \leq S/N < 7$ sources (∼81%) are [2, 10) Jy sources. Finally, the majority of the $S/N > 7$ sources (∼94%) are $\geq$ 5 Jy sources.

The previous results confirm that, as we established in Sect. 3.5.6, for the 70 μm, 160 μm and 250 μm bands: (i) CUTEX <1 Jy fluxes generally have $S/N < 3$ and so, in general, they have a low reliability while (ii) CUTEX $\geq$ 2 Jy fluxes generally have $S/N \geq 7$ and therefore, in general, they have a high reliability.

These results also establish that, contrary to what was concluded in Sect. 3.5.6, for the 350 μm and 500 μm bands, the reliability of the CUTEX fluxes is: (i) low for sources fainter than 5 Jy (instead of 1 Jy) and (ii) high for sources equal or brighter than 5 Jy (instead of 2 Jy). The worsening of these limits can be understood taking into account that back in Sect. 3.5.6 the CUTEX flux reliability limits were established for a total of 121 artificial sources whereas here, we are dealing with $\sim 10^5$ real sources.

Next, in order to increase the flux reliability of the 70 μm, 160 μm, 250 μm, 350 μm and 500 μm ROMAGAL Hi-GAL 1 band catalogues and in the light of the previous findings, we decided to remove from the catalogues all the sources with low flux reliability, i.e. all the sources with $S/N < 3$.

As indicated in Table 4.3, only 2% of the sources contained in the 70 μm ROMAGAL Hi-GAL 1 band catalogue were found to have $S/N < 3$ and thus, the removal of these sources (2,455 sources) did not represent a significant loss. In the case of the 160 μm and 250 μm ROMAGAL Hi-GAL 1 band catalogues, around 5% and 6% of the catalogues' sources were found to have $S/N < 3$ (see Table 4.3) and thus, the removal of these sources (14,902 and 17,077 sources respectively) represented a moderate loss. Given that in the 70 μm, 160 μm and 250 μm ROMAGAL Hi-GAL 1 band catalogues, the majority of the $S/N < 3$ sources were found to be <1 Jy sources (see Table 4.4 and 4.5), the removal of the $S/N < 3$ sources led to a moderate decrease in the number of <1 Jy sources contained in our 70 μm, 160 μm and 250 μm Hi-GAL 1 band catalogues.

Figure 4.5: Flux distributions of the S/N < 3, S/N=[3,7) and S/N ≥ 7 sources contained in the 70 μm and 160 μm ROMAGAL Hi-GAL 1 band catalogues.

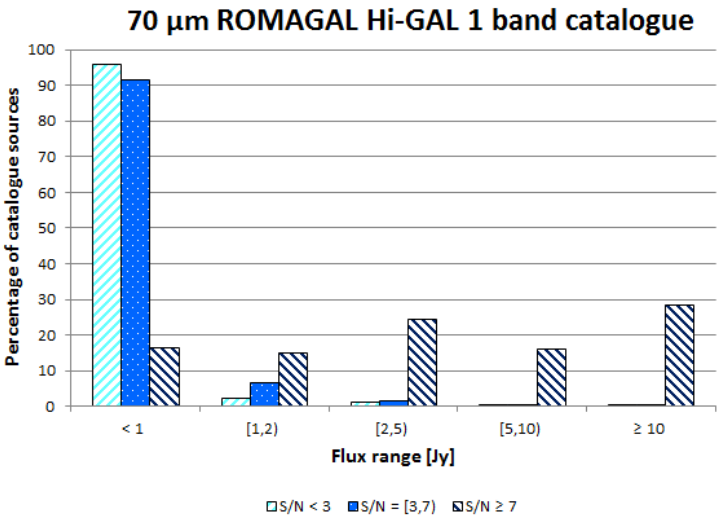

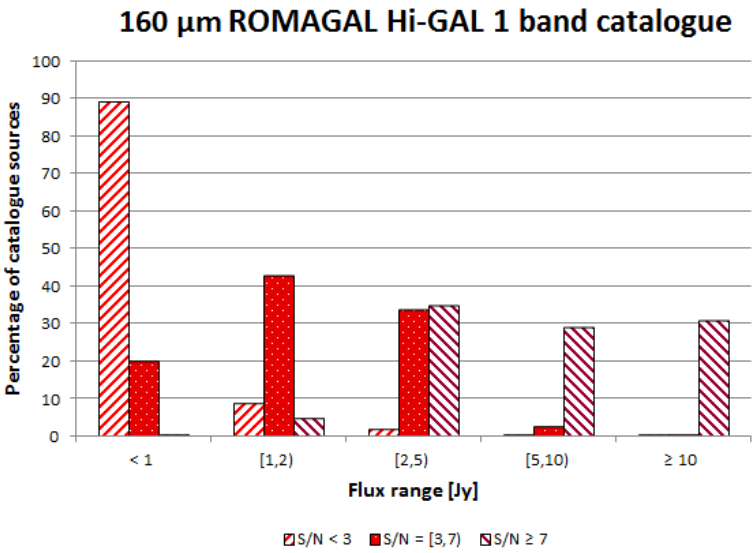

Figure 4.6: Flux distributions of the S/N < 3, S/N=[3,7) and S/N ≥ 7 sources contained in the 250 μm, 350 μm and 500 μm ROMAGAL Hi-GAL 1 band catalogues.

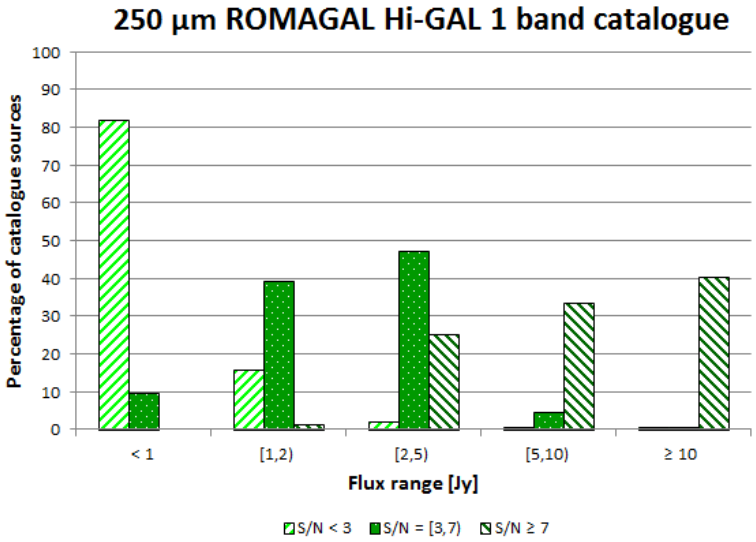

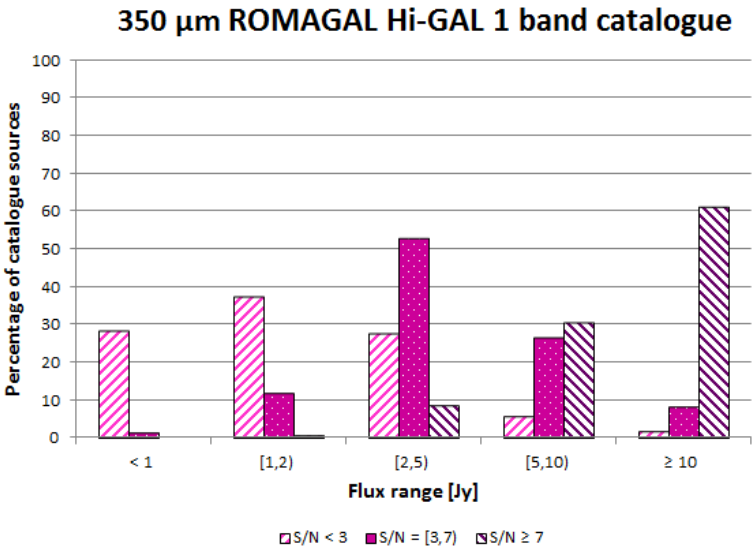

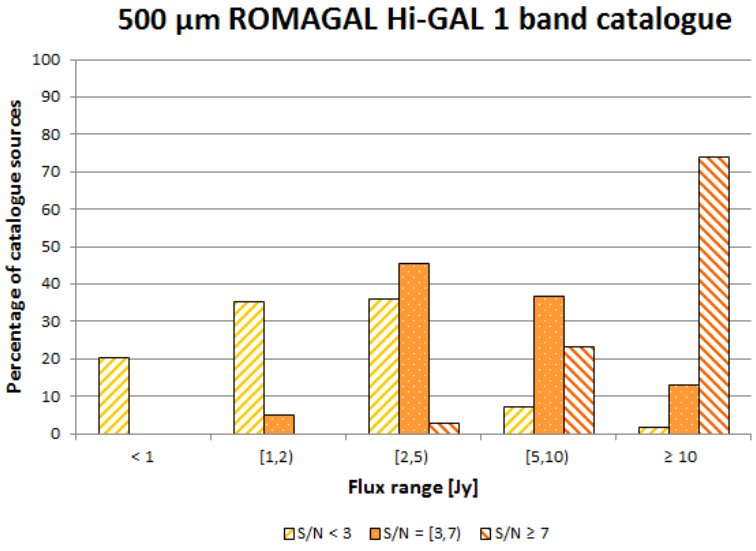

Table 4.4: Percentage of S/N < 3, $3 \leq$ S/N ≤ 7 and S/N > 7 sources included in the 70 μm and 160 μm ROMAGAL Hi-GAL 1 band catalogues whose flux is: (i) < 1 Jy, (ii) in the [1,2) Jy range, (iii) in the [2,5) Jy range, (iv) in the [5,10) Jy range and (v) ≥ 10 Jy.

70 μm ROMAGAL Hi-GAL 1 band catalogue

S/N range	**Flux range**				
	<1 Jy	**[1,2) Jy**	**[2,5) Jy**	**[5,10) Jy**	**≥10 Jy**
S/N < 3	96.0	2.3	1.3	0.2	0.2
S/N = [3,7)	91.5	6.6	1.5	0.3	0.1
S/N ≥ 7	16.5	15.0	24.3	16.0	28.2

160 μm ROMAGAL Hi-GAL 1 band catalogue

S/N range	**Flux range**				
	<1 Jy	**[1,2) Jy**	**[2,5) Jy**	**[5,10) Jy**	**≥10 Jy**
S/N < 3	89.2	8.6	1.9	0.3	0.1
S/N = [3,7)	20.0	43.0	34.0	2.6	0.4
S/N ≥ 7	0.5	4.8	34.8	29.1	30.8

Table 4.5: Percentage of S/N < 3, $3 \leq$ S/N ≤ 7 and S/N > 7 sources included in the 250 μm, 350 μm and 500 μm ROMAGAL Hi-GAL 1 band catalogues whose flux is: (i) < 1 Jy, (ii) in the [1,2) Jy range, (iii) in the [2,5) Jy range, (iv) in the [5,10) Jy range and (v) ≥ 10 Jy.

250 μm ROMAGAL Hi-GAL 1 band catalogue

S/N range	**Flux range**				
	<1 Jy	**[1,2) Jy**	**[2,5) Jy**	**[5,10) Jy**	**≥10 Jy**
S/N < 3	81.9	15.8	1.8	0.3	0.1
S/N = [3,7)	9.4	39.0	47.0	4.3	0.3
S/N ≥ 7	0.0	1.2	25.0	33.4	40.3

350 μm ROMAGAL Hi-GAL 1 band catalogue

S/N range	**Flux range**				
	<1 Jy	**[1,2) Jy**	**[2,5) Jy**	**[5,10) Jy**	**≥10 Jy**
S/N < 3	28.4	37.4	27.4	5.4	1.4
S/N = [3,7)	1.0	11.6	52.9	26.6	8.0
S/N ≥ 7	0.0	0.2	8.3	30.4	61.1

500 μm ROMAGAL Hi-GAL 1 band catalogue

S/N range	**Flux range**				
	<1 Jy	**[1,2) Jy**	**[2,5) Jy**	**[5,10) Jy**	**≥10 Jy**
S/N < 3	20.1	35.2	36.1	7.1	1.6
S/N = [3,7)	0.2	4.7	45.4	36.7	12.9
S/N ≥ 7	0.0	0.0	2.8	23.3	73.9

Table 4.6: Number of sources contained in the final 70 μm, 160 μm, 250 μm, 350 μm and 500 μm ROMAGAL Hi-GAL 1 band catalogues, after the removal of the S/N < 3 sources, which have a moderate and a high flux reliability.

Flux reliability	**Flux quality flag (q_Flux)**	**Number of sources included in the modified ROMAGAL Hi-GAL 1 band catalogues**				
		70 μm	**160 μm**	**250 μm**	**350 μm**	**500 μm**
Moderate	2	14,214	84,578	85,821	66,128	30,692
High	3	103,910	192,378	177,245	43,876	16,434
Total		118,124	276,956	263,066	110,004	47,126

In the case of the 350 μm and 500 μm ROMAGAL Hi-GAL 1 band catalogues, around 32% and 45% of the catalogues' sources were found to have S/N < 3 (see Table 4.3) and thus, the removal of these sources (51,942 and 38,685 sources respectively) led to a substantial decrease. Given that in the 350 μm and 500 μm ROMAGAL Hi-GAL 1 band catalogues, the majority the S/N < 3 sources were found to be < 5 Jy sources (see Table 4.5), the removal of the S/N < 3 sources led to a considerable loss in the number of < 5 Jy sources included in our 350 μm and 500 μm Hi-GAL 1 band catalogues.

Listed in Table 4.6 are the total number of entries in the final 70 μm, 160 μm, 250 μm, 350 μm and 500 μm ROMAGAL Hi-GAL 1 band catalogues after the removal of the S/N < 3 sources. Also listed are the number of sources with a moderate and a high flux reliability. These are indicated with the flux quality flags *q_Flux=2* and *q_Flux=3*, respectively (see Sect. 3.5.6).

The final 70 μm, 160 μm, 250 μm, 350 μm and 500 μm ROMAGAL Hi-GAL 1 band catalogues obtained after the removal of the S/N < 3 sources, referred hereafter as "*Hi-GAL 1 band catalogues*", are included in the CD attached and contain:

- The identification (*ID*) assigned to the sources by ROMAGAL. This is in the form of *HIGALPalllllllsbbbbb*, where: *a* is the instrument array - B=blue, R=red, S=PSW, M=PMW, L=PLW, *lllllll* is the Galactic longitude of the centre of the map with four significant decimals, *s* is the sign of the Galactic latitude (+ for positive, - for negative) and *bbbbb* is the Galactic latitude with four significant decimals.

- The sources' position (*RA*, *dec* and *l*, *b* in degrees), corrected fluxes (*F* in Jy) and flux uncertainties (*EF*, in Jy), Signal-to-Noise (S/N) and flux quality flag (q_Flux).

4.3.3 Hi-GAL 1 band-merged catalogue

Next, the Hi-GAL 1 band catalogues were combined to create the *SMA Hi-GAL 1 band-merged catalogue*. When creating this catalogue, it was decided to:

- Follow the recommendation of the ROMAGAL group of including only sources whose 2^{nd} derivative was 2 times higher than the threshold and therefore had a high S/N ratio and rejecting any source detected in any band which is formed of less than two contiguous map pixels.

- Include only the sources detected in the 70 μm Hi-GAL 1 band catalogue for which we then found counterparts in the 160 μm, 250 μm, 350 μm and 500 μm Hi-GAL 1 band catalogues. This cross-match was done in TOPCAT allowing a maximum angular separation of 1.7 arcsec between the positions of two matching sources. The value of this maximum separation was chosen to be equal to the smallest beam size from all the Hi-GAL, 2MASS, WISE, GLIMPSE, MSX, AKARI and IRAS bands (see Table 4.7).

Therefore, the SMA Hi-GAL 1 band-merged catalogue contains:

- The identification (*ID*) assigned to the source by ROMAGAL in each band catalogue.

- The position (*RA*, *dec* and l, b in degrees), the fluxes (F in Jy) and the flux uncertainties (*EF*, in Jy) of the 119,359 sources included in the Hi-GAL 1 70 μm band catalogue (see Table 4.6) and of the 160 μm, 250 μm, 350 μm and 500 μm band counterparts found for the 70 μm sources.

- The distance (d in arcsec) between the position of the 70 μm sources and the counterparts found in the other bands.

The previous actions were taken in order to prevent false detections from being included in our catalogue. Our decision of only including in our catalogue the sources detected in the 70 μm band was based on the fact that, amongst the Herschel bands, the 70 μm band has the smallest beam size (see Table 4.7) and therefore, this band is the most reliable band for finding sources within crowded fields and for studying the sources' IR dust properties.

Table 4.7: Full Width at Half Maximum (FWHM) for all the Hi-GAL, 2MASS, WISE, GLIMPSE, MSX, AKARI and IRAS bands.

Survey	Band	λ (μm)	FWHM
HiGAL	blue	70	5.2”
	red	160	12”
	PSW	250	18”
	PMW	350	25”
	PLW	500	37”
2MASS	J	1.25	2.8”
	H	1.65	2.7”
	K	2.17	2.8”
WISE	W1	3.4	6.1”
	W2	4.6	6.4”
	W3	12	6.5”
	W4	22	12”
GLIMPSE	G1	3.6	1.7”
	G2	4.5	1.7”
	G3	5.8	1.9”
	G4	8	2”
MSX	B1	4.29	4.2”
	B2	4.35	4.2”
	A	8.28	6.8”
	C	12.13	11.1”
	D	14.65	13.5”
	E	21.34	18.2”
AKARI/IRC	A1	9	5.5”
	A2	18	5.7”
AKARI/FIS	A3	65	37”
	A4	90	39”
	A5	140	58”
	A6	160	61”
IRAS	I1	12	0.8’
	I2	25	0.8’
	I3	60	1.4’
	I4	100	2.9’

Table 4.8: Number of sources included in our SMA and the ROMAGAL Hi-GAL 1 band-merged catalogues in the 70 μm, 160 μm, 250 μm, 350 μm and 500 μm bands.

SMA Hi-GAL 1 band-merged catalogue				
70 μm	**160 μm**	**250 μm**	**350 μm**	**500 μm**
118,124	10,306	2,534	1,029	289
Total=118,124 sources				

ROMAGAL Hi-GAL 1 band-merged catalogue				
70 μm	**160 μm**	**250 μm**	**350 μm**	**500 μm**
122,971	292,051	280,258	161,855	85,880
Total=519,403 sources				

Our SMA Hi-GAL 1 band-merged catalogue is very different from the ROMAGAL Hi-GAL 1 band-merged catalogue. Unlike us, ROMAGAL included all the sources detected in their Hi-GAL 1 band catalogues. The sources detected in one band were considered to be independent sources unless a match was found in any other band. These matches were found as follows. First, they matched the Hi-GAL 1 ROMAGAL 500 μm band catalogue with the Hi-GAL 1 ROMAGAL 350 μm band catalogue, allowing a maximum separation between the positions of two matching sources equal to the FWHM of the largest wavelength, that is, Herschel's 500 μm FWHM (37"). The position assigned to the matched sources was then chosen to be that registered at the shorter wavelength, that is the 350 μm band. If multiple associations were found, the closest source was kept while the remainder were considered as independent sources. Finally, both the matched sources and the unmatched sources were added to a sourcelist which was then cross-matched with the next wavelengths down to 70 μm, using the same criteria (Elia et al. 2010).

Listed in Table 4.8 are the sources included in the SMA and ROMAGAL Hi-GAL 1 band-merged catalogue for each band. Here, we can see that as expected: (i) in the 70 μm band our SMA Hi-GAL band-merged catalogue has a similar number of sources than ROMAGAL's and (ii) in the 160 μm, 250 μm, 350 μm, and 500 μm bands our SMA Hi-GAL 1 band-merged catalogue has much fewer sources than ROMAGAL's.

4.3.3.1 Catalogue's completeness

The results shown in Table 4.8 indicate that our SMA Hi-GAL 1 band-merged catalogue contains 96%, 4%, 0.9%, 0.6%, 0.3% of the sources included in the ROMAGAL Hi-GAL 1 band-merged catalogue in the 70 μm, 160 μm, 250 μm, 350 μm and 500 μm bands, respectively.

Thus, in the 70 μm band, our SMA Hi-GAL 1 band-merged catalogue is almost as complete as ROMAGAL's while in the 160 μm, 250 μm, 350 μm and 500 μm bands, the ROMAGAL Hi-GAL band-merged catalogue is much more complete than ours.

4.3.3.2 Catalogue's flux distribution

Shown in Fig. 4.7 and 4.8 are the number of 70 μm, 160 μm, 250 μm, 350 μm and 500 μm sources contained in the SMA and ROMAGAL Hi-GAL 1 band-merged catalogues whose flux is: (i) $<$ 1 Jy, (ii) in the [1,2) Jy range, (iii) in the [2,5) Jy range, (iv) in the [5,10) Jy range and (v) $\geq$ 10 Jy. These numbers are listed in Table 4.2 and establish that:

- In the 70 μm band, our SMA Hi-GAL 1 band-merged catalogue contains 200 more $<$1 Jy sources and $\sim 5 * 10^3$ fewer $\geq$1 Jy sources than the ROMAGAL Hi-GAL 1 band-merged catalogue.
- In the 160 μm, 250 μm, 350 μm and 500 μm bands, as expected, our SMA Hi-GAL 1 band-merged catalogue contains, in general, much fewer sources than the ROMAGAL Hi-GAL 1 band-merged catalogue. While the sources contained in our catalogue are mainly brighter than 2 Jy, for the ROMAGAL catalogue many of the sources are fainter than 2 Jy.

4.3.3.3 Catalogue's flux reliability

Shown in Fig. 4.9 and 4.10 are the S/N distributions of the 70 μm, 160 μm, 250 μm, 350 μm and 500 μm sources included in the SMA and ROMAGAL Hi-GAL 1 band-merged catalogues. Here, we show the number of 70 μm, 160 μm, 250 μm, 350 μm and 500 μm sources contained in the SMA and ROMAGAL Hi-GAL 1 band catalogues whose S/N is: (i) $<$ 3, (ii) in the [3,7) range, (iii) $\geq$ 7. These numbers are listed in Table 4.10 and allow us to determine and compare the reliability of the fluxes listed in the SMA and ROMAGAL Hi-GAL 1 band-merged catalogues.

Through the inspection of Fig. 4.9 and 4.10 and Table 4.10, we established that:

- Our SMA Hi-GAL 1 band-merged catalogue does not contain S/N < 3 sources in any of the bands while the ROMAGAL Hi-GAL 1 band-merged catalogue does.
- In the 70 μm band, our SMA Hi-GAL 1 band-merged catalogue contains $\sim 15 * 10^3$ fewer $3 \leq$ S/N < 7 sources and $\sim 19 * 10^3$ more S/N ≥ 7 sources than the ROMAGAL Hi-GAL 1 band-merged catalogue. The total number of S/N ≥ 3 sources is greater in our catalogue (118,124 sources) than in ROMAGAL's (114,545 sources).
- In the 160 μm, 250 μm, 350 μm and 500 μm bands, as expected, our SMA Hi-GAL 1 band-merged catalogue contains, in general, much fewer sources than the ROMAGAL Hi-GAL 1 band-merged catalogue and thus the number of S/N ≥ 3 sources is much greater in ROMAGAL's catalogue.

In light of these results, we concluded that in the 70 μm band, the flux reliability of our SMA Hi-GAL 1 band-merged catalogue sources is greater than that of the ROMAGAL Hi-GAL 1 band-merged catalogue sources. With respect to the other bands, given the superior completeness of the ROMAGAL catalogue, it was not possible to draw any conclusion other than the fact that our catalogue contains no sources with low flux reliability while ROMAGAL's does.

Figure 4.7: Flux distributions of the 70 μm and 160 μm sources contained in the SMA and ROMAGAL Hi-GAL 1 band-merged catalogues.

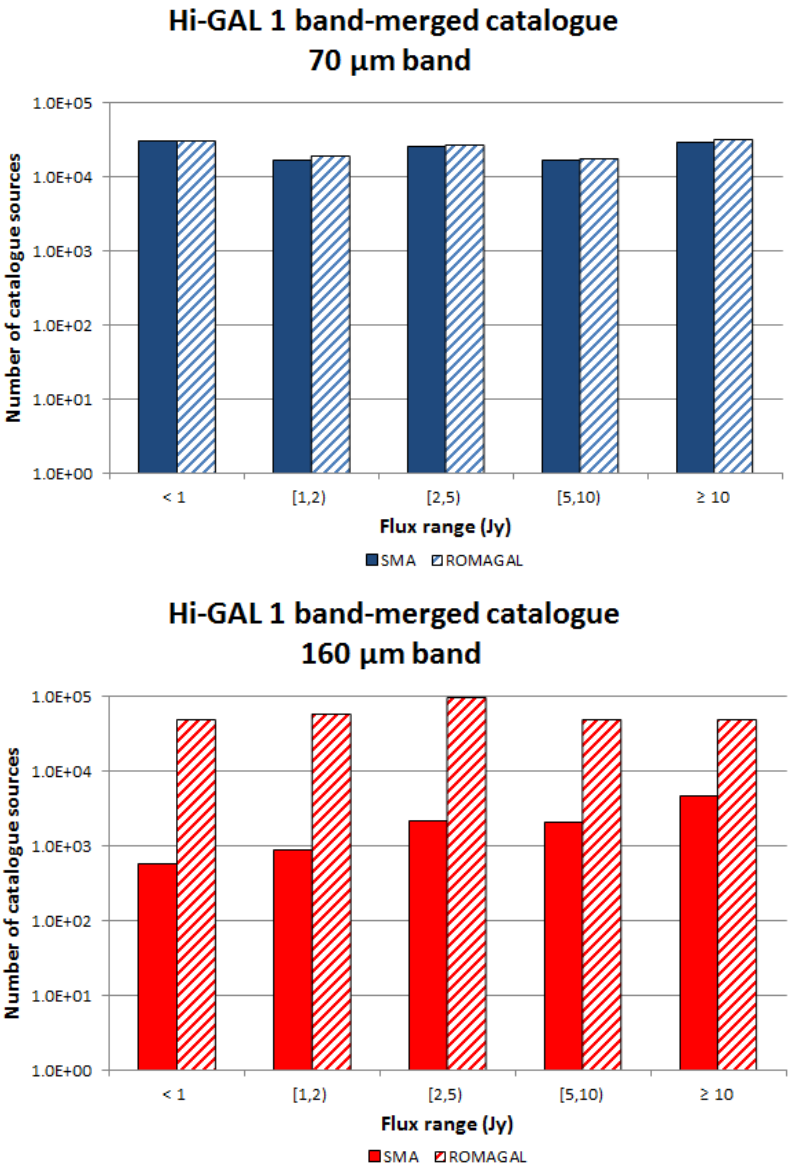

Figure 4.8: Flux distributions of the 250 μm, 350 μm and 500 μm sources contained in the SMA and ROMAGAL Hi-GAL 1 band-merged catalogues.

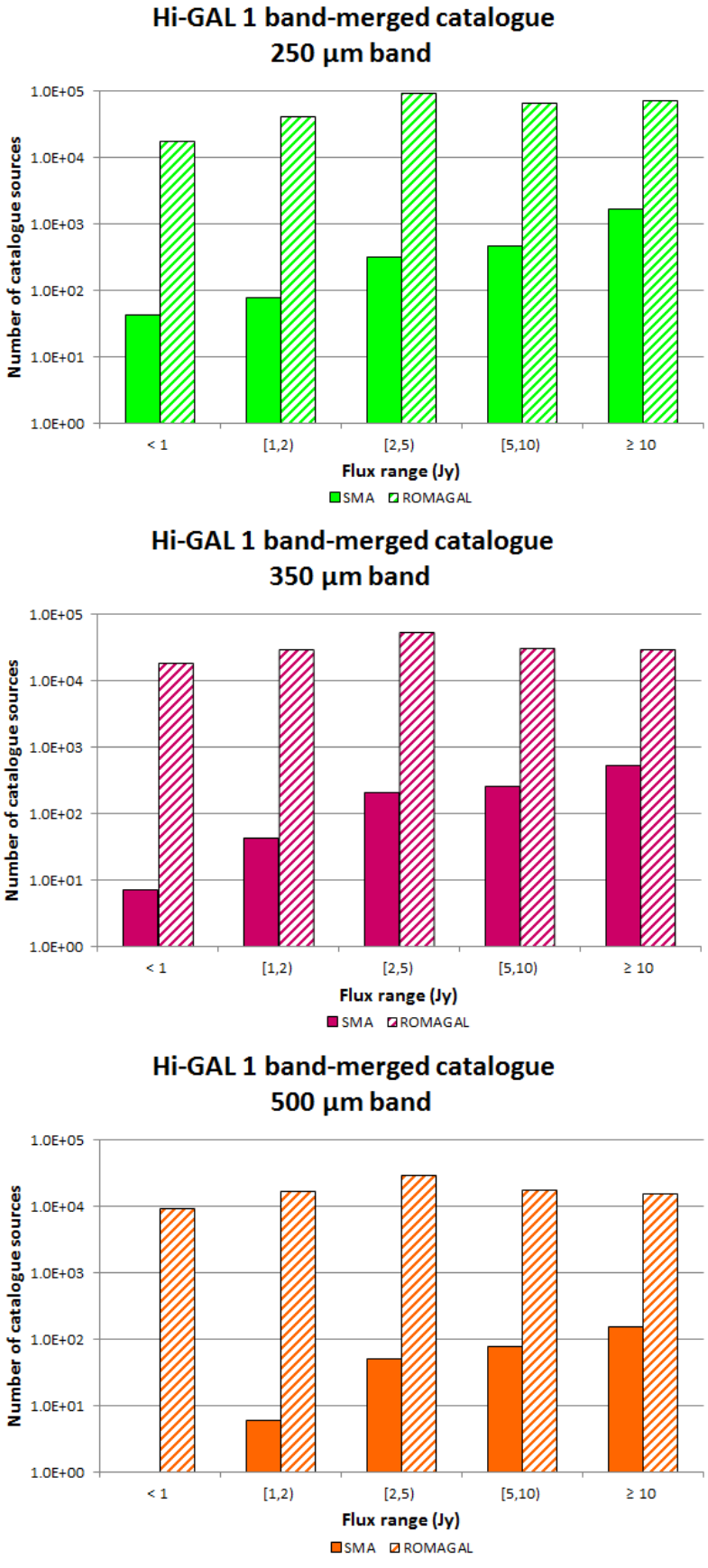

Table 4.9: Number of 70 μm, 160 μm, 250 μm, 350 μm and 500 μm sources included in the SMA and ROMAGAL Hi-GAL 1 band-merged catalogues whose flux is: (i) $<$ 1 Jy, (ii) in the [1,2) Jy range, (iii) in the [2,5) Jy range, (iv) in the [5,10) Jy range and (v) $\geq$ 10 Jy.

SMA Hi-GAL 1 band-merged catalogue	**Flux range**				
	$<$1 Jy	**[1,2) Jy**	**[2,5) Jy**	**[5,10) Jy**	**$\geq$10 Jy**
70 μm	30,140	16,504	25,429	16,720	29,331
160 μm	567	868	2,144	2,071	4,656
250 μm	43	78	310	458	1,645
350 μm	7	42	203	258	519
500 μm	0	6	50	78	155

ROMAGAL Hi-GAL 1 band-merged catalogue	**Flux range**				
	$<$1 Jy	**[1,2) Jy**	**[2,5) Jy**	**[5,10) Jy**	**$\geq$10 Jy**
70 μm	29,940	18,475	25,953	17,224	31,379
160 μm	47,461	57,346	93,046	47,589	46,609
250 μm	17,315	39,910	88,841	63,358	70,834
350 μm	18,434	29,639	53,064	31,453	29,265
500 μm	9,045	16,374	28,948	16,739	14,774

Figure 4.9: S/N distributions of the 70 μm and 160 μm sources contained in the SMA and ROMAGAL Hi-GAL 1 band-merged catalogues.

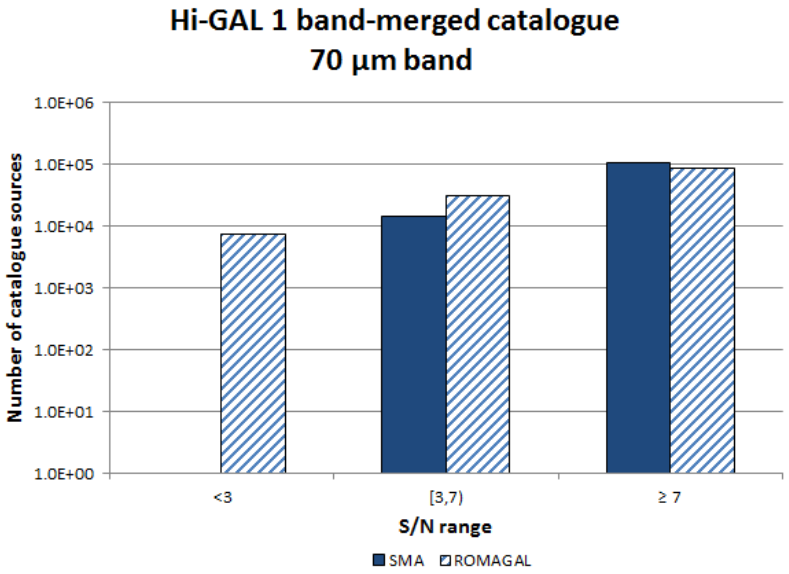

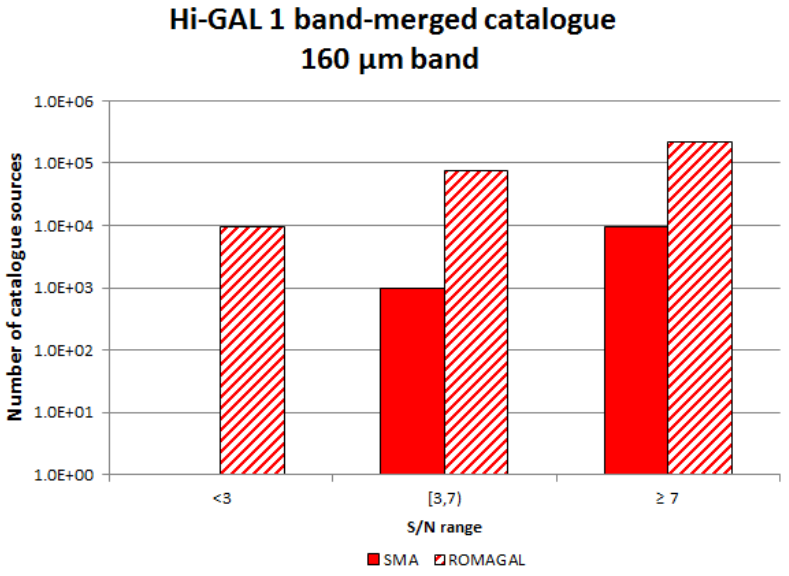

Figure 4.10: S/N distributions of the 250 μm, 350 μm and 500 μm sources contained in the SMA and ROMAGAL Hi-GAL 1 band-merged catalogues.

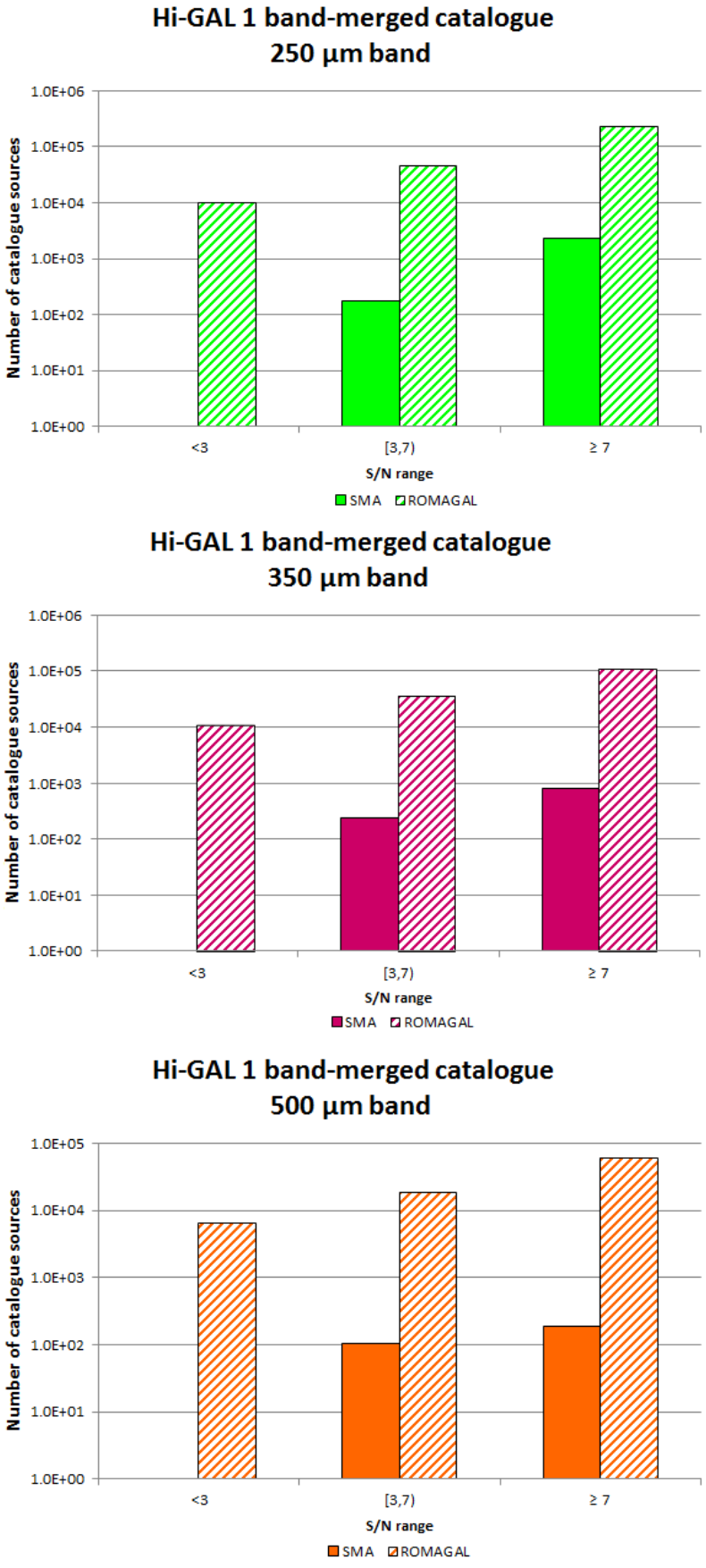

Table 4.10: Number of 70 μm, 160 μm, 250 μm, 350 μm and 500 μm sources included in the SMA and ROMAGAL Hi-GAL 1 band-merged catalogues for which: (i) S/N $<$ 3, (ii) 3 $\leq$ S/N $\leq$ 7 and (iii) S/N $>$ 7.

SMA Hi-GAL 1 band-merged catalogue	**S/N range**		
	<3	**[3,7)**	**≥7**
70 μm	0	14,234	103,890
160 μm	0	1,000	9,306
250 μm	0	174	2,360
350 μm	0	235	794
500 μm	0	103	186

ROMAGAL Hi-GAL 1 band-merged catalogue	**S/N range**		
	<3	**[3,7)**	**≥7**
70 μm	7,200	29,564	84,981
160 μm	9,414	72,435	209,664
250 μm	9,997	45,132	223,657
350 μm	10,910	35,721	113,110
500 μm	6,299	18,437	59,013

4.3.3.4 Catalogue's source reliability

Shown in Fig. 4.11 are the number of sources contained in the SMA Hi-GAL 1 band-merged catalogues for which we found 1 (or more) counterparts in the Survey Catalogues, lying within a maximum angular separation of 1.7 arcsec. These numbers are listed in Table 4.11 and establish that:

- We found 1 (or more) counterparts in the Survey Catalogues for a total of 33,456 sources (28%) included in our SMA Hi-GAL 1 band-merged catalogue. Thus, the source reliability[4] of our catalogue is of 28%.
- We found 1 (or more) counterparts in the Survey Catalogues for a total of 87,001 sources (17%) included in the ROMAGAL Hi-GAL 1 band-merged catalogue. Thus, the source reliability[4] of their catalogue is of 17%.

Because the ROMAGAL Hi-GAL 1 band-merged catalogue has in general many more sources than our SMA Hi-GAL 1 band-merged catalogue except for the 70 μm band, the comparison between the level of reliability of the catalogues' sources can only be made in this band. Shown in Fig. 4.12 and listed in Table 4.12 are the number of sources contained in the 70 μm band in the SMA and ROMAGAL Hi-GAL 1 band-merged catalogues for which we found 1 (or more) counterparts in the Survey Catalogues, lying within a maximum angular separation of 1.7 arcsec. These results establish that:

- We found 1 (or more) counterparts in the Survey Catalogues for a total of 4,145 sources (3%) included in the 70 μm band in the ROMAGAL Hi-GAL 1 band-merged catalogue. Thus, in the 70 μm band, the source reliability[4] of the ROMAGAL Hi-GAL 1 band-merged catalogue is of 3%, which is much lower than that found for our SMA Hi-GAL 1 band-merged catalogue (28%).

For those SMA Hi-GAL 1 band-merged catalogue sources for which a counterpart was found in the Survey Catalogues, we included in our catalogue: (i) the source identification (*ID*) assigned in the Survey Catalogue, (ii) the position (*RA*, *dec*, in degrees), (iii) the fluxes (*F*, in Jy) and the flux uncertainties (*EF*, in Jy) measured in each band, (iv) the distance (*d*, in arcsec) between the position of our catalogue source and the counterpart found and (v) a label indicating whether or not (Y/N) a counterpart was found in at least one of the Survey Catalogues, lying within a maximum angular separation of 1.7 arcsec.

[4]This is having chosen a maximum distance of 1.7 arcsec between the matches.

Figure 4.11: Number of sources contained in the SMA (filled bars) and the ROMAGAL (striped bars) Hi-GAL 1 band-merged catalogues for which we found 1 (or more) counterparts in the Survey Catalogues, lying within a maximum angular separation of 1.7 arcsec.

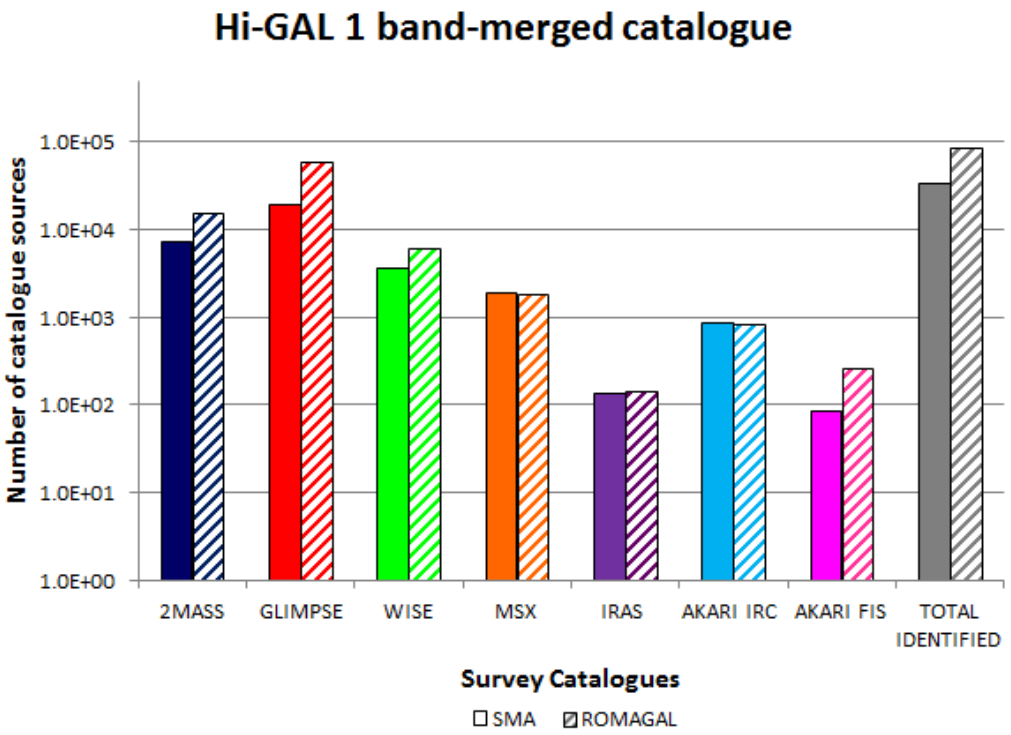

Table 4.11: Number of sources contained in the SMA (n_{SMA}) and the ROMAGAL ($n_{ROMAGAL}$) Hi-GAL 1 band-merged catalogues for which we found 1 (or more) counterparts in the Survey Catalogues, lying within a maximum angular separation of 1.7 arcsec.

Survey Catalogue	n_{SMA}	$n_{ROMAGAL}$
2MASS	7,398	16,070
GLIMPSE	19,456	61,409
WISE	3,654	6,351
MSX	1,864	1,896
AKARI IRC	866	860
IRAS	133	150
AKARI FIS	85	265
TOTAL	33,456	87,001

Figure 4.12: Number of sources contained in the 70 μm band in the SMA (filled bars) and the ROMAGAL (striped bars) Hi-GAL 1 band-merged catalogues for which we found 1 (or more) counterparts in the Survey Catalogues, lying within a maximum angular separation of 1.7 arcsec.

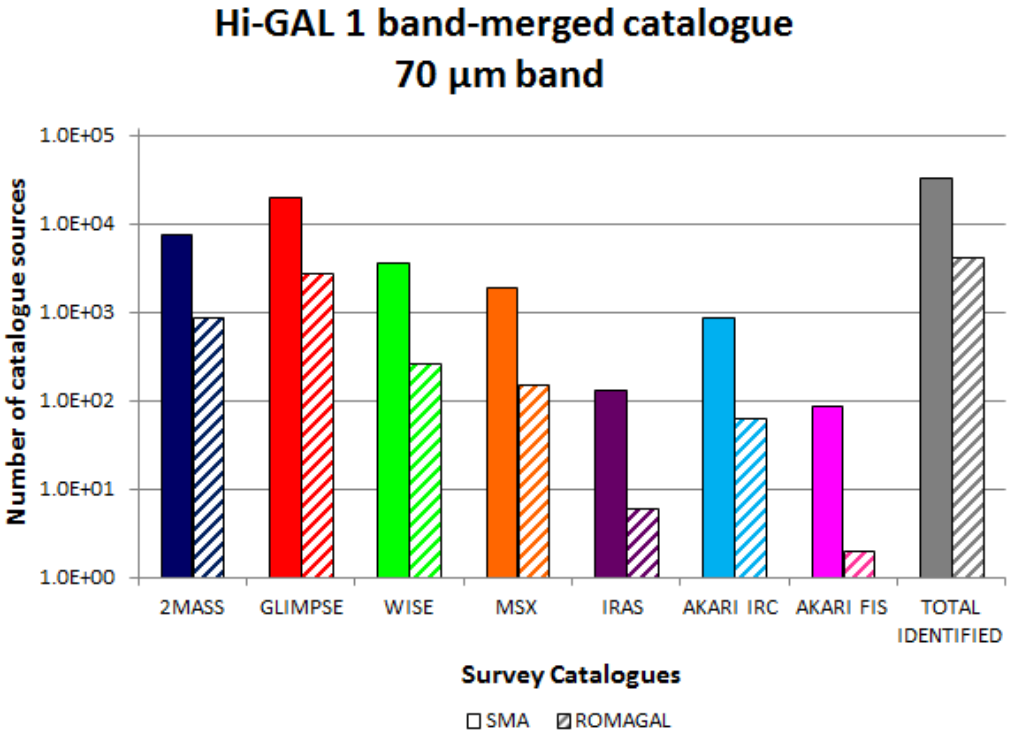

Table 4.12: Number of sources contained in the 70 μm band in the SMA (n_{SMA}) and the ROMAGAL ($n^{70\ \mu m}_{ROMAGAL}$) Hi-GAL 1 band-merged catalogues for which we found 1 (or more) counterparts in the Survey Catalogues, lying within a maximum angular separation of 1.7 arcsec.

Survey Catalogue	n_{SMA}	$n^{70\ \mu m}_{ROMAGAL}$
2MASS	7,398	884
GLIMPSE	19,456	2,778
WISE	3,654	265
MSX	1,864	148
AKARI IRC	866	62
IRAS	133	6
AKARI FIS	85	2
TOTAL	33,456	4,145

Figure 4.13: Percentages of SMA Hi-GAL 1 band-merged catalogue sources for which photometric data are available in all Herschel H1 (70 μm), H2 (160 μm), H3 (250 μm), H4 (350 μm) and H5 (500 μm) bands, 2MASS J (1.25 μm), H (1.65 μm) and K (2.17 μm) bands, WISE W1 (3.4 μm), W2 (4.6 μm), W3 (12 μm) and W4 (22 μm) bands, GLIMPSE G1 (3.6 μm), G2 (4.5 μm), G3 (5.8 μm) and G4 (8 μm) bands, MSX B1 (4.29 μm), B2 (4.35 μm), A (8.28 μm), C (12.13 μm), D (14.65 μm) and E (21.34 μm) bands, IRAS I1 (12 μm), I2 (25 μm), I3 (60 μm) and I4 (100 μm) bands and AKARI A1 (9 μm), A2 (18 μm), A3 (65 μm), A4 (90 μm), A5 (140 μm) and A6 (160 μm) bands.

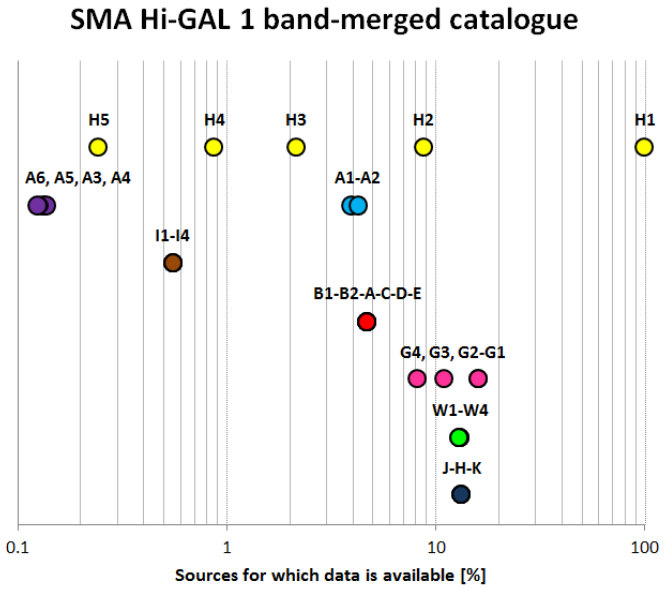

4.3.3.5 Catalogue's photometric coverage

The previous cross-match between the SMA Hi-GAL 1 band-merged catalogue and the Survey Catalogues allowed us to increase the wavelength range for which our catalogue had fluxes available.

Shown in Fig. 4.13 are the percentages of SMA Hi-GAL 1 band-merged catalogue sources for which photometric data are available in all Herschel, 2MASS, WISE, GLIMPSE, MSX, IRAS and AKARI bands. Here, we can see that our catalogue is:

(i) ∼100% complete for the Herschel 70 μm band,

(ii) ∼16% complete for the GLIMPSE 3.6 μm and 4.5 μm bands,

(iii) ∼13% complete for all the 2MASS and WISE bands,

(iv) ∼11% complete for the GLIMPSE 5.8 μm band and

(v) $<$ 10% complete for the remaining bands.

4.3.3.6 Astrometric Corrections

The cross-match between the SMA Hi-GAL 1 band-merged catalogue and the 2MASS, GLIMPSE and MSX PSCs allowed us also to compare the Herschel sources' positions with the 2MASS, Spitzer and MSX sources' positions.

Since the beam size (i.e. FWHM) of the PACS and SPIRE instruments is greater than that of the 2MASS, Spitzer and MSX instruments (see Table 4.7), the accuracy of the positions included in these catalogues is higher than that of the positions included in our SMA Hi-GAL 1 band-merged catalogue. For those sources for which we found a more accurate position in the 2MASS, GLIMPSE or MSX PSCs than that registered by Herschel 70 μm band, we decided to include in our catalogue: (i) the most accurate (*macc*) source position available (*macc_RA*, *macc_dec*) and (ii) the Survey Catalogue (*macc_Cat*) from which this position was taken. On the other hand, for those sources for which Herschel 70 μm band positions were the most accurate positions available, the *macc_RA*, *macc_dec* positions correspond to the Herschel 70 μm band positions and the *macc_Cat* catalogue is our SMA Hi-GAL 1 band-merged catalogue. This modified SMA Hi-GAL 1 band-merged catalogue constitutes our final *SMA Hi-GAL 1 PSC* and is hereafter referred to as *Hi-GAL 1 PSC*. The Hi-GAL 1 PSC can be found in the CD attached and contains:

- The identification (*ID*) assigned to the source by ROMAGAL in each band catalogue.
- The most accurate position available for the source (*macc_RA*, *macc_dec* in degrees) and the catalogue from which this position was taken (*macc_Cat*).
- The identification (*ID*), the position (*RA*, *dec* and l, b in degrees), the fluxes (F in Jy) and the flux uncertainties (*EF*, in Jy) of the 118,124 sources included in the SMA Hi-GAL 1 70 μm band catalogue.
- The identification (*ID*), the position (*RA*, *dec* in degrees), the fluxes (F in Jy) and the flux uncertainties (*EF*, in Jy) of the counterparts found in the 160 μm, 250 μm, 350 μm and 500 μm SMA Hi-GAL 1 band catalogues and the Survey Catalogues.
- The separation (d in arcsec) between the positions of the 70 μm SMA Hi-GAL band catalogue sources and the counterparts found in the 160 μm, 250 μm, 350 μm and 500 μm SMA Hi-GAL 1 band catalogues and in the Survey Catalogues.
- A label indicating whether or not (Y/N) a source counterpart was found in at least one of the Survey Catalogues, lying within a maximum angular separation of 1.7 arcsec.
- The sources' Signal-to-Noise (S/N) and the flux quality flag (q_Flux).

4.3.3.7 Source distributions

Shown in Fig. 4.14 is the distribution of the sources contained in the Hi-GAL 1 PSC catalogue, along the Galactic plane region covered by Hi-GAL 1 (i.e. the $l = [0°, 66°]$ and $l = [290°, 358°]$, $|b| < 1°$ region). Here, we can see that the number of detected sources increases towards the Galactic Centre. We observe that the different number of sources detected at each Galactic longitude can be attributed to the structure of the Galaxy and the distinct number of Galactic arms across the telescope's line of sight (see Fig. 4.15 and 4.16). For instance, we can see that the regions around the Galactic Centre ($l = 0°$, in purple), for which the telescope's line of sight crosses the Galactic Bulge, the Perseus Arm, the Outer Arm, the Scutum-Centaurus Arm and the Carina Sagittarius Arm, are extremely populated. In contrast, the regions towards the edge of the Galaxy ($l = 61°$, in orange), for which the telescope's line of sight crosses only the Perseus and the Outer Arms, are hardly populated in comparison.

In reality, the contrast between the number of sources located in the inner (say $l = 0°$) and outer (say $l = 336°$) parts of the Galaxy should be dramatically greater. However, due to the extremely bright emission detected in the Galactic Bulge, only a small percentage of the Galactic Centre sources can be detected by CUTEX. In general, the stronger the background emission present in the Hi-GAL 1 maps and the more populated a Galactic region is, the harder it is for CUTEX to find point sources in this region.

The greater number of sources detected in the $l = 336°$ region (in dark blue) with respect to that found in the $l = 310°$ and $l = 321°$ regions (in yellow) can be explained by the larger number of star forming regions present in the $l = 336°$ region - while in the $l = 336°$ region Avedisova 2002 found up to 21 star forming regions, in the $l = 310°$ and $l = 321°$ regions Avedisova 2002 found up to 12 star forming regions.

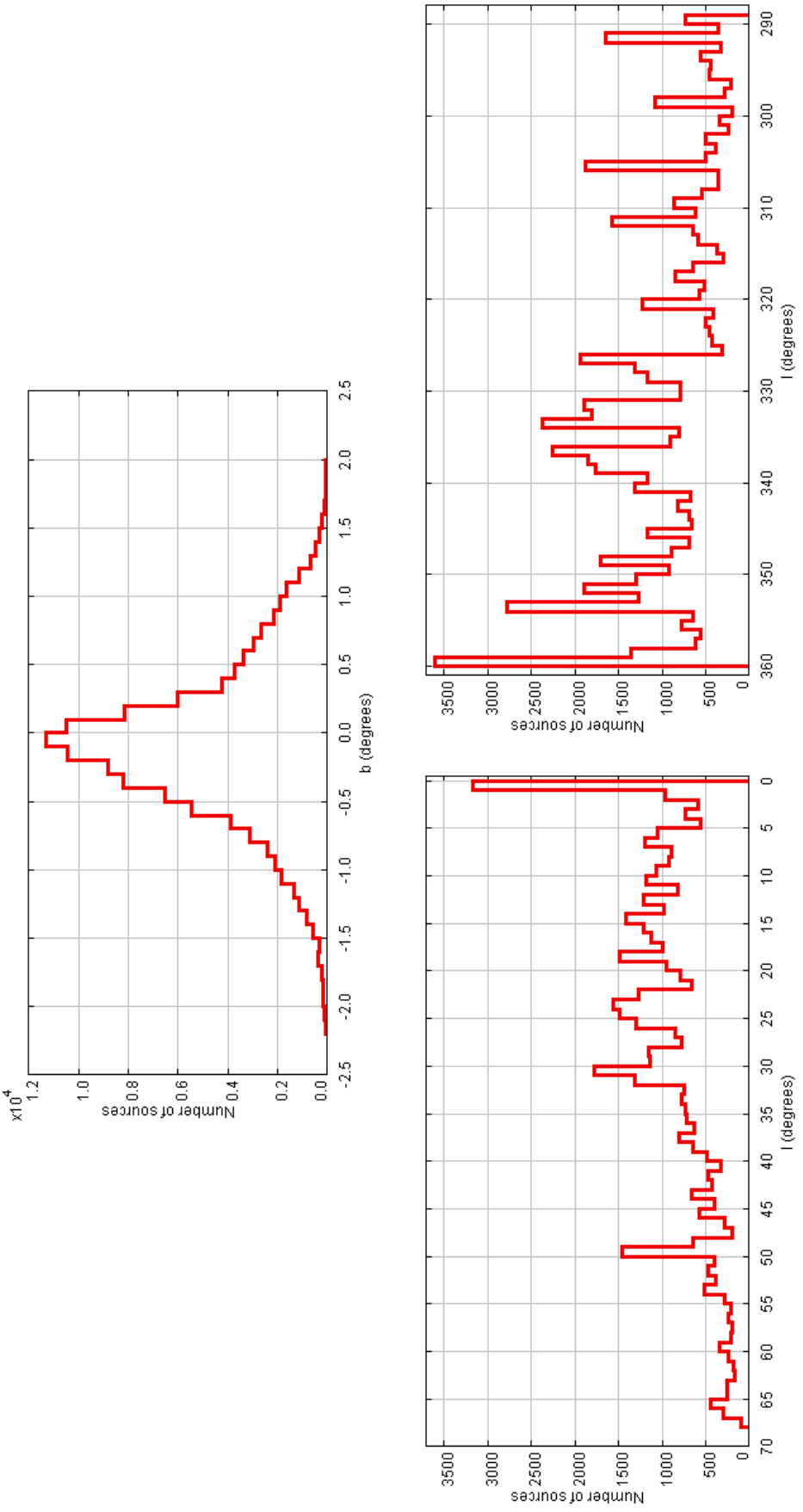

Figure 4.14: Distributions of the sources contained in the Hi-GAL 1 PSC catalogue along the Galactic plane region covered by the Hi-GAL 1 Survey.

Figure 4.15: Galactic arms across the telescope's line of sight in each tile covered in the Hi-GAL 1 Survey.

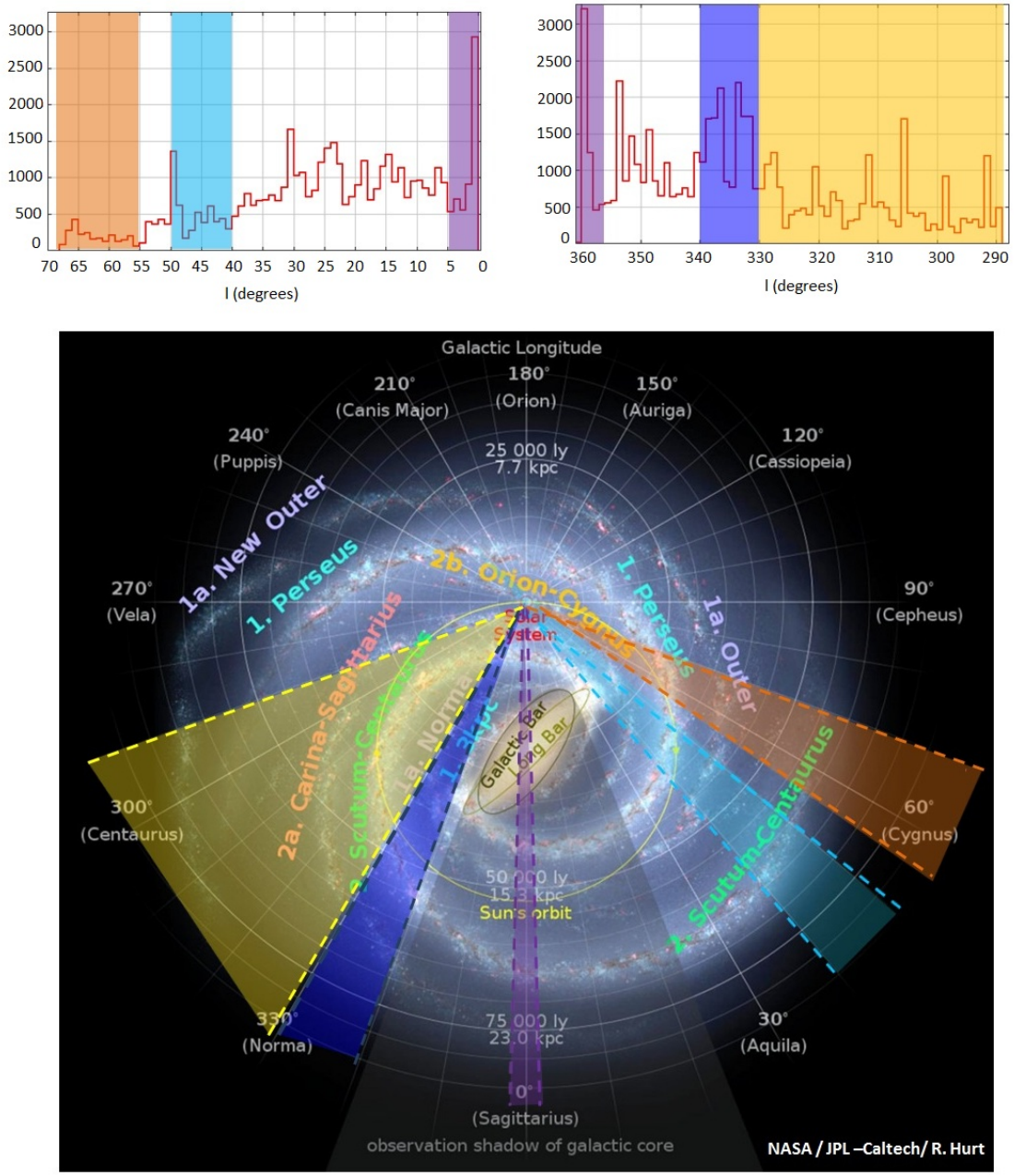

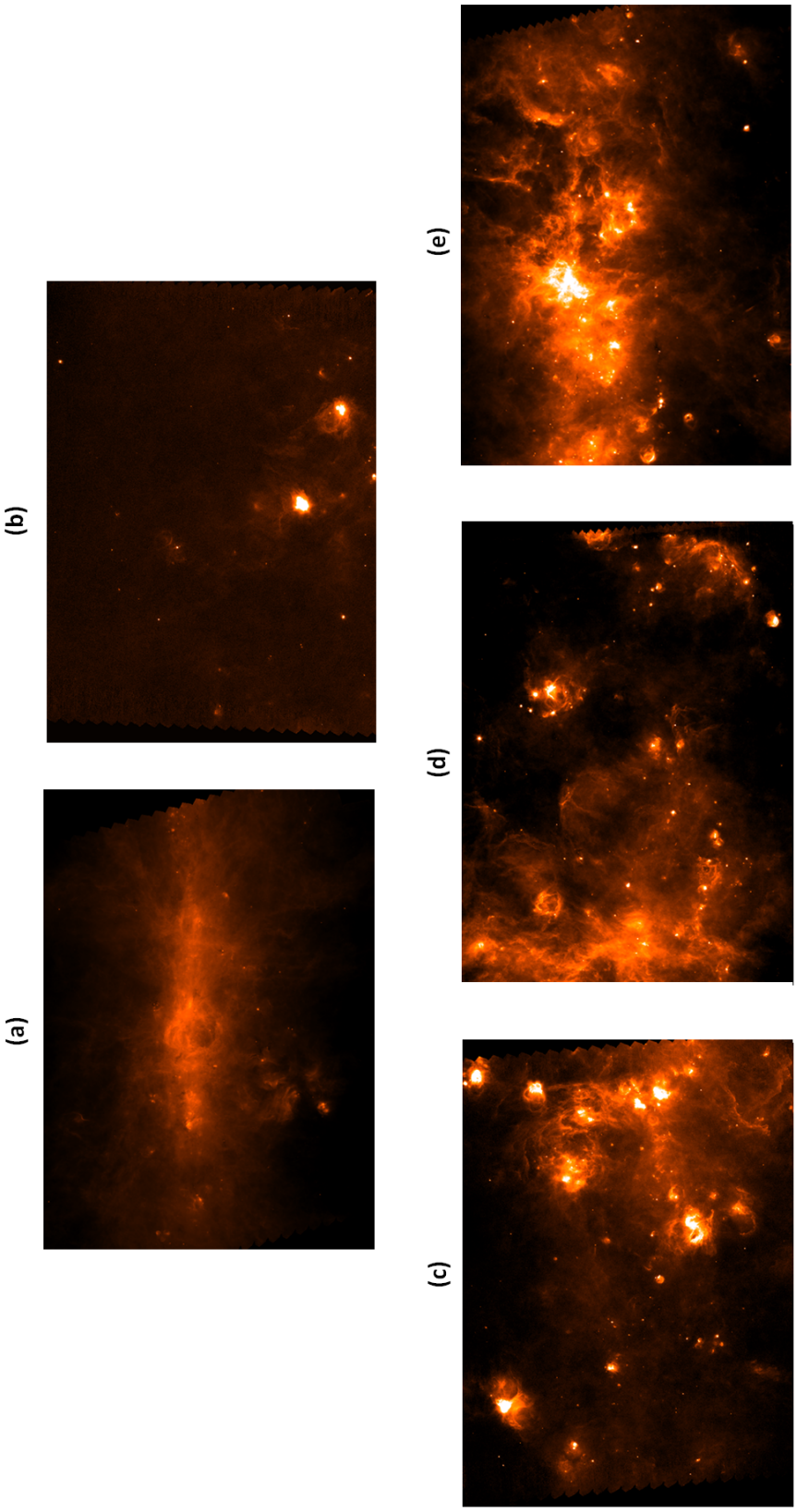

Figure 4.16: Images of the 70 μm Hi-GAL 1 maps centred on the $|b| < 1°$ and (a) $l = 0°$, (b) $l = 61°$, (c) $l = 310°$, (d) $l = 321°$ and (e) $l = 336°$ Galactic regions.

4.4 Summary and Conclusions

The purpose of this chapter was to build a reliable Point Source Catalogue (PSC) containing the positions and flux densities of the sources detected in the total 63 fields included in the Hi-GAL 1 Survey. In order to accomplish such goal we first ran CUTEX through the Hi-GAL 1 maps and created the SMA Hi-GAL 1 70 μm, 160 μm, 250 μm, 350 μm and 500 μm band catalogues, which contained the position and fluxes measured in the 70 μm, 160 μm, 250 μm, 350 μm and 500 μm of all the sources included in the 63 individual CUTEX output sourcelists. The SMA Hi-GAL 1 band catalogues were then compared to the band catalogues created by ROMAGAL. Through this comparison we learnt that:

(i) The SMA and ROMAGAL Hi-GAL 1 band catalogues included different number of sources. This was attributed to the ROMAGAL use of different maps than ours and the ROMAGAL use of a threshold of lower (higher) sensitivity than ours in the 70 μm band (160 μm, 250 μm, 350 μm and 500 μm bands).

(ii) The fluxes listed for a source included in both our and their catalogue were also different. This was found to be due to the ROMAGAL use of different maps than ours and the ROMAGAL use of distinct Flux Correction Factors. While our FCF only consider the flux errors introduced by the highly variable background emission present in the Hi-GAL 1 maps, ROMAGAL's FCF also take into account the flux errors introduced by the distortion the PSF suffers when using the Herschel fast parallel scanning mode.

(iii) The ROMAGAL band catalogue sources were extracted from a set of maps further processed, of better quality and slightly larger than ours.

In light of the previous findings, we decided to use the ROMAGAL band catalogues instead of ours. This decision was also made to guarantee that the work presented in the following chapters was carried out using the most updated catalogues' version.
After the inspection of the source and S/N distributions of the sources included in the ROMAGAL band catalogues it was decided to remove all those sources with a low flux reliability, i.e. sources with $S/N < 3$ in order to increase the flux reliability of the original ROMAGAL band catalogues. In the case of the 70 μm ROMAGAL Hi-GAL 1 band catalogue, the removal of these sources did not constitute a significant loss because only 2% of the catalogue sources were found to have $S/N < 3$.

In the case of the 160 μm, 250 μm, 350 μm and 500 μm ROMAGAL Hi-GAL 1 band catalogues, the removal of these sources led to a substantial decrease in the number of catalogue sources since 5%, 6%, 32% and 45% of the sources included in the 160 μm, 250 μm, 350 μm and 500 μm ROMAGAL Hi-GAL 1 band catalogues were found to have $S/N < 3$.

Next, the modified ROMAGAL Hi-GAL 1 band catalogues were combined to create the *SMA Hi-GAL 1 band-merged catalogue*, which included only the sources detected in the 70 μm modified ROMAGAL Hi-GAL 1 band catalogue as well as the corresponding counterparts found lying at a maximum distance of 1.7 arcsec in the modified ROMAGAL 160 μm, 250 μm, 350 μm and 500 μm Hi-GAL 1 band catalogues. The SMA Hi-GAL 1 band-merged catalogue was then compared to the band-merged catalogue created by ROMAGAL. Through this comparison we learnt that:

(i) The ROMAGAL band-merged catalogue was built following a completely different method and therefore, contains different number of sources in each band.

(ii) Our SMA Hi-GAL 1 band-merged catalogue includes 96%, 4%, 0.9%, 0.6% and 0.3% of the sources included in the ROMAGAL Hi-GAL 1 band-merged catalogue in the 70 μm, 160 μm, 250 μm, 350 μm and 500 μm bands, respectively. Thus, in the 70 μm band, the completeness of our catalogue is similar to that of the ROMAGAL Hi-GAL 1 band-merged catalogue while, in the 160 μm, 250 μm, 350 μm and 500 μm bands, the ROMAGAL Hi-GAL 1 band-merged catalogue is much more complete.

(iii) In the 70 μm band, our SMA Hi-GAL 1 band-merged catalogue contains 200 more $<$1 Jy sources and $\sim 5 * 10^3$ fewer $\geq$1 Jy sources than the ROMAGAL Hi-GAL 1 band-merged catalogue. While the majority of the sources contained in our catalogue are > 2 Jy sources, in the ROMAGAL catalogue there are many < 2 Jy sources.

(iv) In the 70 μm band, our SMA Hi-GAL 1 band-merged catalogue contains $\sim 15 * 10^3$ fewer $3 \leq$ S/N < 7 sources and $\sim 19 * 10^3$ more S/N ≥ 7 sources than the ROMAGAL Hi-GAL 1 band-merged catalogue. The total number of S/N ≥ 3 sources is greater in our catalogue than in ROMAGAL's. These results established that, in the 70 μm band, the flux reliability of our SMA Hi-GAL 1 band-merged catalogue sources is greater than that of the ROMAGAL Hi-GAL 1 band-merged catalogue sources.

(v) In the 160 μm, 250 μm, 350 μm and 500 μm bands, as expected, our SMA Hi-GAL 1 band-merged catalogue contains much fewer sources than the ROMAGAL Hi-GAL 1 band-merged catalogue and thus the number of S/N $\geq$ 3 sources is much greater in ROMAGAL's catalogues.

(vi) In the 70 μm band, 28% of the SMA Hi-GAL 1 band-merged catalogue sources were found to have a counterpart in the Survey Catalogues lying within a maximum angular distance of 1.7 arcsec whereas, in the case of the ROMAGAL Hi-GAL 1 band-merged catalogue, only 3% of the catalogue sources included in the 70 μm band were found to have a counterpart. These results established that the source reliability of our catalogue, in the 70 μm band, is greater than that of ROMAGAL's.

In light of these results, we concluded that, in the 70 μm band, the source and flux reliability of our SMA Hi-GAL 1 band-merged catalogue is greater than that of the ROMAGAL catalogue and that the completeness of our catalogue is similar to that of ROMAGAL's. On the contrary, in the 160 μm, 250 μm, 350 μm and 500 μm bands, the completeness of our catalogue is significantly inferior than that of ROMAGAL's.

The cross-match between the SMA Hi-GAL 1 band-merged catalogue and the Survey Catalogues allowed us to increase the wavelength range for which our catalogue had fluxes available. The resulting catalogue was determined to be: (i) $\sim$100% complete for the Herschel 70 μm band, (ii) $\sim$16% complete for the GLIMPSE 3.6 μm and 4.5 μm bands, (iii) $\sim$13% complete for all the 2MASS and WISE bands, (iv) $\sim$11% complete for the GLIMPSE 5.8 μm band and (v) $<$ 10% complete for the remaining bands.

Moreover, the cross-match between the SMA Hi-GAL 1 band-merged catalogue and the 2MASS, GLIMPSE and MSX PSCs allowed us also to include in our catalogue the most accurate position available for the source within the 2MASS, GLIMPSE and MSX PSCs. The resulting SMA Hi-GAL 1 band-merged catalogue, with the additional photometric measurements and the corrected source position, was established as our final *Hi-GAL 1 PSC*. Finally, we examined the spatial distribution along the Galactic plane (in longitude and latitude) of the sources included in the Hi-GAL 1 PSC and concluded that it is possible to establish a connection between the sources' density distribution and the structure of our Galaxy.

Chapter 5

Selection of the Hi-GAL 1 C-rich and O-rich AGB candidates

"Herschel has taught us so much ... we simply didn't know before."

Alvaro Giménez

5.1 Introduction

The aim of this chapter is two-fold. First, we want to find colour criteria that allow us to separate the AGB stars from the other stellar types contained in our Hi-GAL 1 PSC, such as YSOs, HII regions and PNe. Secondly, we want to find colour criteria that allow us to classify the AGB stars identified in the Hi-GAL 1 PSC into C-rich and O-rich AGB stars. In the following sections I:

(i) explain the derivation process of the colour criteria and compare their efficiency to that of other colour criteria derived in previous studies and

(ii) describe the building of the catalogues of Hi-GAL 1 PSC AGB, C-rich and O-rich AGB star candidates and discuss the catalogues' reliability and source distribution.

5.2 Source Spectral Energy Distribution and colour

The *Spectral Energy Distribution* (SED) of a source is defined as a plot in which the source measured flux densities F_{λ_i} (or F_{ν_i}) are plotted against the different wavelengths λ_i (or frequencies ν_i) these measures were taken at.

The shape of a source SED is dependent on the source temperature, structure, its chemical composition and the physical processes to which it is subjected. Since sources sharing the same stage of evolution should have analogous structural, chemical and physical properties, their SEDs should present similarities. In particular, the difference in *apparent magnitude* (m) between two wavelengths (λ_i and λ_j, where $i < j$), known as the sources' *colour*, will be comparable. Thus, the colour of a source provides us with a simple method to readily identify and classify different source types.

The apparent magnitude of a source is given by:

$$m_\lambda = -2.5 \times log_{10} F_\nu \tag{5.1}$$

Therefore, the colour of a source is given by:

$$\begin{aligned}[\lambda_i] - [\lambda_j] = [m_{\nu_i}] - [m_{\nu_j}] &= (-2.5 \times log_{10} F_{\nu_i}) - \left(-2.5 \times log_{10} F_{\nu_j}\right) \\ &= 2.5 \times log\left(\frac{F_{\nu_j}}{F_{\nu i}}\right)\end{aligned} \tag{5.2}$$

The number of colours available (c) for a source is given by:

$$c = \frac{[n\,(n-1)]}{2} \tag{5.3}$$

where n is the number of wavelengths for which there are photometric data available.

5.3 Colour-colour diagrams

A *colour-colour diagram* is defined as a plot in which two different source colours are plotted against each other. Shown in Fig. 5.1 is a hypothetical example of a colour-colour diagram in which the $colour_1$ colour is plotted against the $colour_2$ colour.

Figure 5.1: Plot showing a hypothetical colour-colour diagram ($Colour_1$ vs. $Colour_2$) in which reference sources of two different stellar types ($Type_1$ and $Type_2$) lay in different colour-colour regions ($Region_1$ and $Region_2$). In this hypothetical case, since $Region_1$ and $Region_2$ are clearly separated from each other, there would be no overlap between the $Colour_1$ and $Colour_2$ colour cuts (CC) of each stellar type.

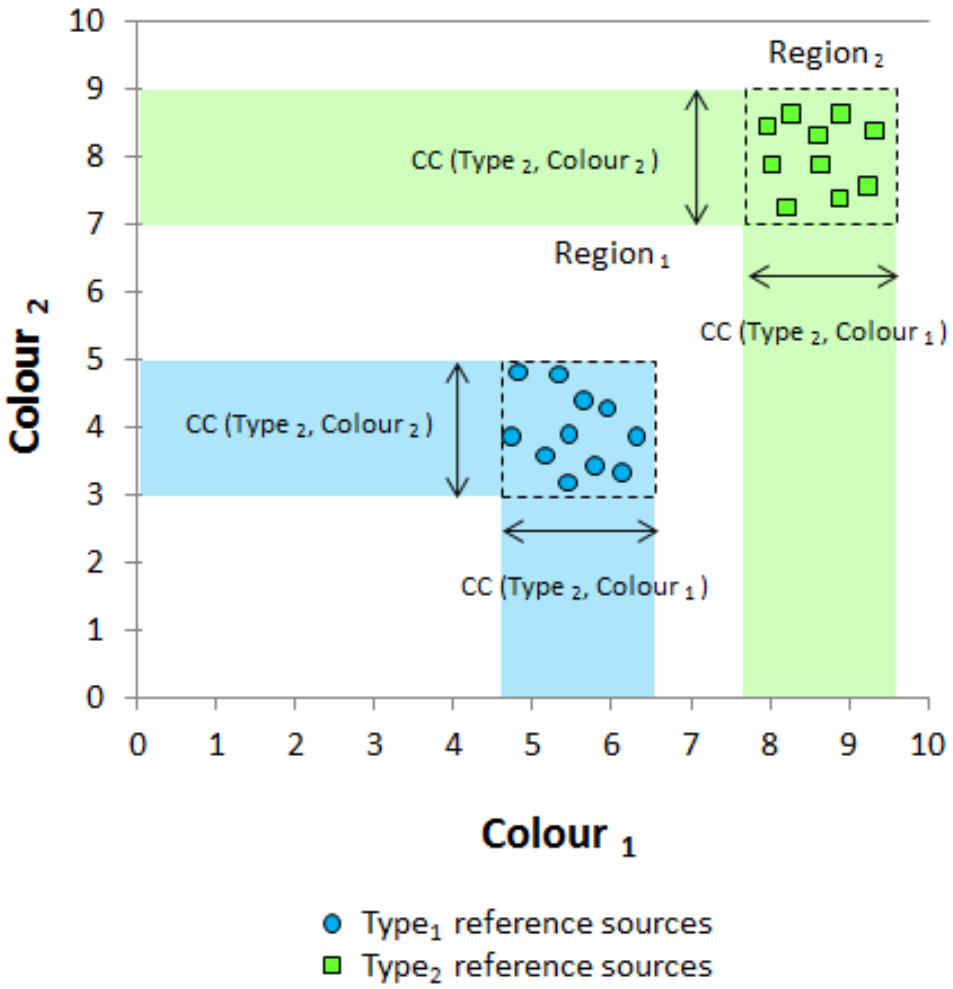

5.4 Stellar population separation

The usefulness of colour-colour diagrams relies on the fact that they can be employed to separate the different stellar types contained in a source catalogue using the following method. Firstly, a list of sources of known stellar types ($Type_1, Type_2$,...) is selected. These are referred to as "known" sources and will be used as reference sources. Secondly, all flux measurements (F_{ν_1}, F_{ν_2}, F_{ν_3},...) available for each of the reference sources are compiled. Then, a colour-colour diagram is built for every pair of colours available.

In each of these colour-colour diagrams, the $Type_1$ and $Type_2$ reference sources will occupy a certain region, say $Region_1$ and $Region_2$, delimited by a certain range of colour values known as $Type_1$ and $Type_2$ *colour cuts* (CC) (see Fig. 5.1). In general, the more distinct the $Type_1$ and $Type_2$ stellar types, the further away the $Region_1$ and $Region_2$ will be and the less overlap there will be between the $Type_1$ and $Type_2$ colour cuts.

Once the colour cuts for sources of different stellar types have been defined, they can be used to infer the stellar type of unknown sources. For instance, if an unknown source has the same colour values as those found for the $Type_1$ ($Type_2$) reference sources, such unknown source will be considered to be also of $Type_1$ ($Type_2$).

In the hypothetical example shown in Fig. 5.1, the $Region_1$ and $Region_2$ are clearly separated from each other and therefore, there is no overlap between the colour cuts of each stellar type. However, in the majority of real cases, the $Region_1$ and $Region_2$ will be partially superimposed and therefore, the colour cuts defined for the $Type_1$ reference sources will be somewhat similar to those defined for the $Type_2$ reference sources. As a result, an unknown source with colour values characteristic of both stellar types could either be a $Type_1$ or a $Type_2$ source. In order to establish the probability of an unknown source to be mistakenly classified as a $Type_1$ or a $Type_2$ source, one can use: (i) the percentage of reference sources successfully classified by the colour cut (*verification rate*) and (ii) the percentage of reference sources erroneously classified by the colour cut (*contamination rate*) as indicators. The lower the colour cut's contamination rate and the greater its verification rate, the more efficient the colour cut is said to be. On the other hand, the more reference sources the colour cut has been tested upon, the more reliable the subsequent classification of unknown sources is.

5.5 Previous studies on stellar population separation

The colour-colour separation method has been widely used in the past to identify the different stellar types contained in the IRAS, MSX6C, GLIMPSE, AKARI, WISE and 2MASS PSCs. For instance:

- van der Veen and Habing (1988) used the colour-colour diagram in Fig. 5.2 to identify O-rich AGB stars (OH/IR-stars and Mira-stars), C-rich AGB stars and PNe from a sample of 8,864 IRAS PSC sources.

- Lumsden et al. (2002) employed the colour-colour diagram in Fig. 5.3 to study the colour separation between HII regions, (massive) YSOs and the evolved C and O-rich mass-losing stars found in a subset of 14,897 MSX6C PSC sources.

- Ita et al. (2010) used the colour-colour diagrams in Fig. 5.4 to separate the known YSOs, PNe, C, S, M, post-AGB and OH/IR-stars contained in a sub-sample (58,793 sources) of the totality of the AKARI-IRC PSC sources.

- Ishihara et al. (2011) used the colour-colour diagrams in Fig. 5.5 to separate the known YSOs, PNe, C, S, M, post-AGB and OH/IR-stars contained in a subset (614,204 sources) of the AKARI-IRC PSC sources.

- Anderson et al. (2012b) used for the first time the Hi-GAL fluxes measured for a sample of Galactic HII regions (126 sources) and PNe (43 sources) to derive a series of colour cuts that efficiently separated HII regions from PNe.

  The results obtained by Anderson et al. (2012b) are listed in Table 5.6. From these results, we can see that the fluxes detected in the Herschel 70 μm and 160 μm bands, (together with the WISE 12 μm and 22 μm bands, the MIPSGAL 24 μm band and the GLIMPSE 8 μm band), are crucial to distinguish between HII regions and PNe.

Figure 5.2: [12] − [25] vs. [25] − [60] colour-colour diagram, from van der Veen and Habing (1988), showing a total of 10 different colour regions, each one found to contain IRAS PSC evolved stars with different IR characteristics (e.g. number densities, variability average and Low Resolution Spectra classification) summarised in the table. Objects from regions IIIb, IV and V are believed to form an evolutionary sequence from the AGB star phase to the PNe-phase. The full line indicates the black body curve while the dashed line shows the evolutionary track that Mira-stars (concentrated on the lower left side) are found to follow on their evolution towards OH/IR-stars (on the upper right side). This is a continuous sequence in mass-loss rates ranging from 10^{-7} $M_{\odot}/yr$ (Mira-stars) to more than 10^{-4} $M_{\odot}/yr$ (OH/IR-stars) (Bedijn 1987). This sequence can be expressed by $[25]-[60] = -2.5 + 0.5 \times e^{1.5*([12]-[25])}$ for $-1.1 < [12]-[25] < 1.3$. The transition between Mira and OH/IR-stars is found to take place around $[12]-[25] = 0.2$.

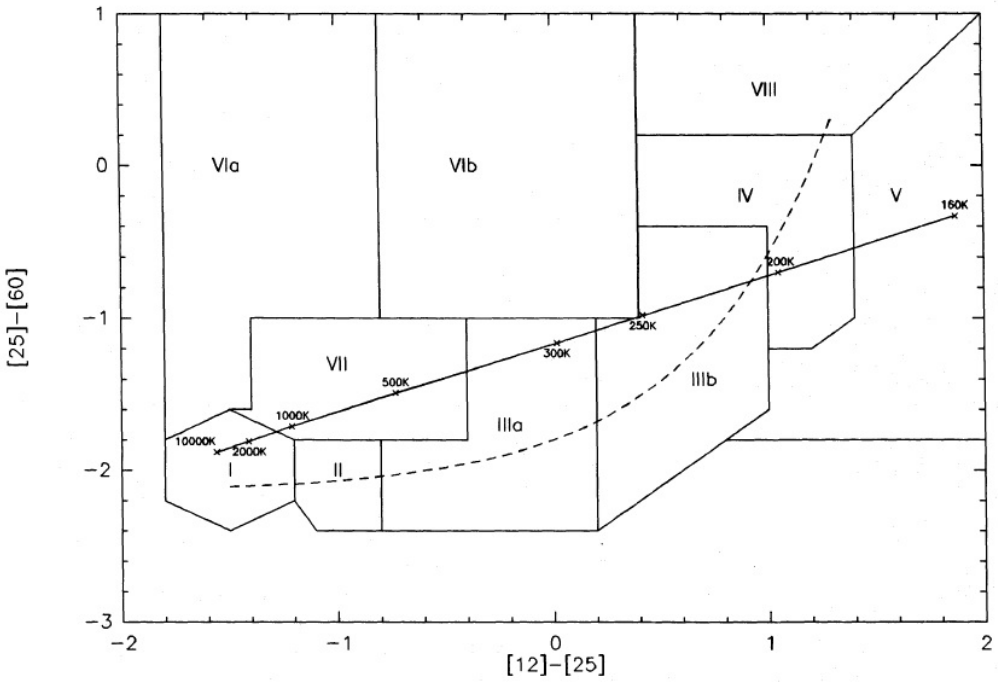

Region	Characteristic type of object	Region	Characteristic type of object
I	Oxygen-rich non-variable stars without circumstellar shells	VIa	Non-variable stars with relatively cold dust at large distances; a significant part of the stars is carbon-rich
II	Variable stars with "young" O-rich circumstellar shells		
IIIa	Variable stars with more evolved O-rich circumstellar shells	VIb	Variable stars with relatively hot dust close to the star and relatively cold dust at large distances; some of the objects have proven to be oxygen-rich
IIIb	Variable stars with thick O-rich circumstellar shells		
IV	Variable stars with very thick O-rich circumstellar shells	VII	Variable stars with more evolved C-rich circumstellar shells
V	Planetary nebulae and non-variable stars with very cool circumstellar shells	VIII	Different sort of objects

Figure 5.3: [*Top*] Colour-colour diagrams, from Lumsden et al. (2002), showing the colour distribution of the known young star types found in their subset of 14,897 MSX PSC sources. Young stellar types include Herbig Ae/Be stars (×), massive YSOs (+), methanol maser sources without radio emission (•) and compact HII regions (○).
[*Centre*] Same colour-colour diagrams, now showing the colour distribution of the known evolved star types including C-stars (•), OH/IR-stars (+) and PNe (∗). Comparison of the right-hand top and bottom panels shows that the majority of PNe can be separated from the HII regions and MYSOs.
[*Bottom*] Same colour-colour diagrams, this time for C-stars (•), silicate emission objects (+), silicate absorption objects (×) and those having PAH emission without any ionized gas emission (∗) classified under Kwok (1994) IRAS LRS (i.e. Low Resolution Spectra). Comparison of the location of the C- and O-rich sources shows that there is a clear separation between the two types.

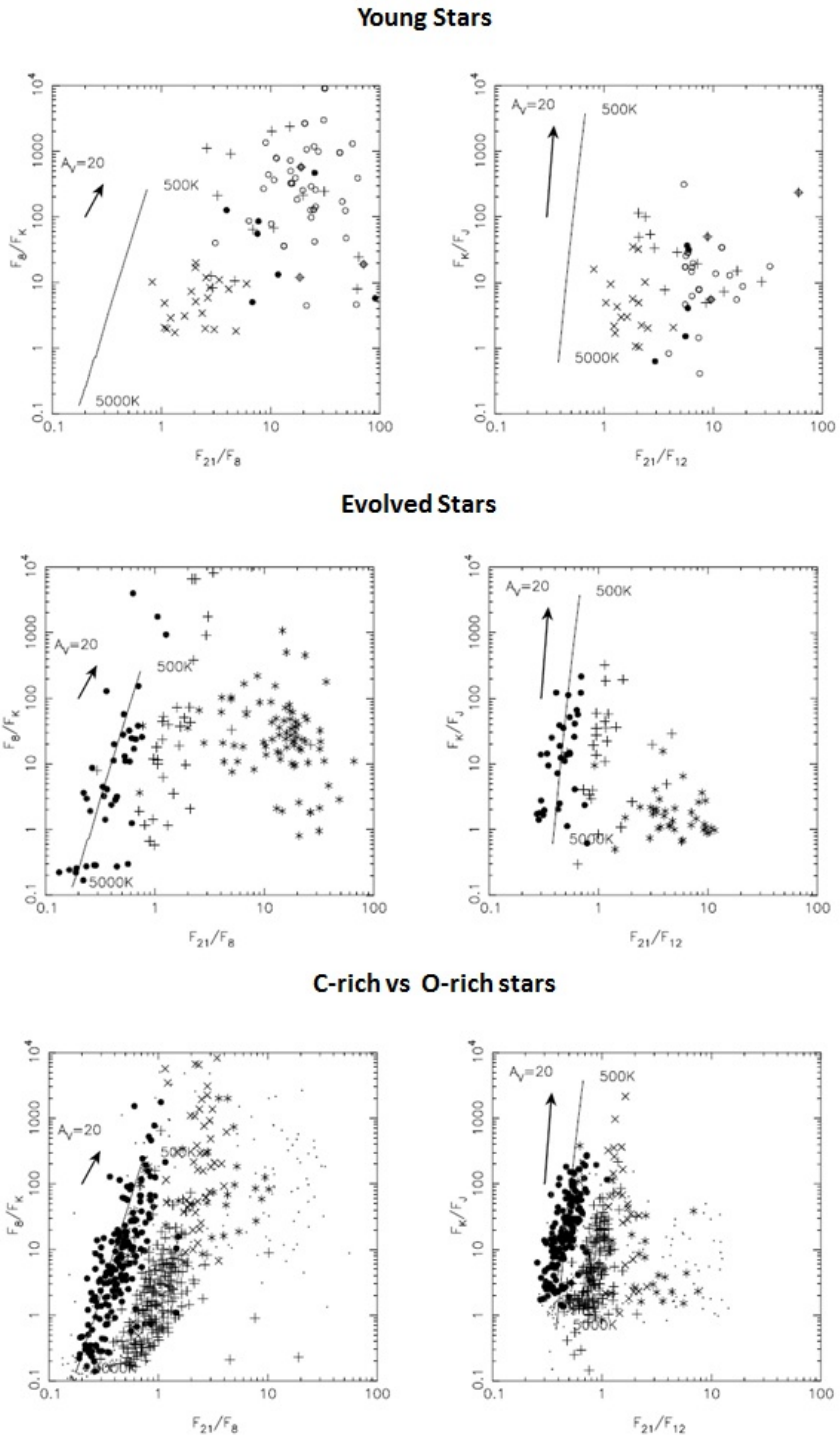

Figure 5.4: In the $[S9W] - [L18W]$ vs. $[J] - [L18W]$ colour-colour diagrams shown below, Ita et al. (2010) defined six regions, from A to E, depicted in the frames below, to make an approximate object classification for a total of 58,793 AKARI-IRC PSC sources. Symbols indicate different types of known objects as described in the legend: *Carbon, MIII, MI, S, PMS, YSOs, OH/IR, PAGB, PNe, WR,* and *Be* represent C-stars, M-type giants, M-type supergiants, S-type stars, Pre-Main Sequence stars, Young Stellar Objects, OH/IR-stars, post-AGB stars, Planetary Nebulae, Wolf-Rayet stars, and Be-stars. The grey dots (with error bars) show the colours of objects without known identifications. The representative object types in the different regions are:
(A) Red C-stars.
(B) OH/IR-stars and some YSOs.
(C) M-type giants, SG and S-type stars, as well as bluer C-stars (in the blue part) and PMS stars (in the red part)
(D) Be-stars, M-type giants, and S-stars.
(E) PMS stars, PNe, and PAGB stars.
(F) PNe and PAGB stars.

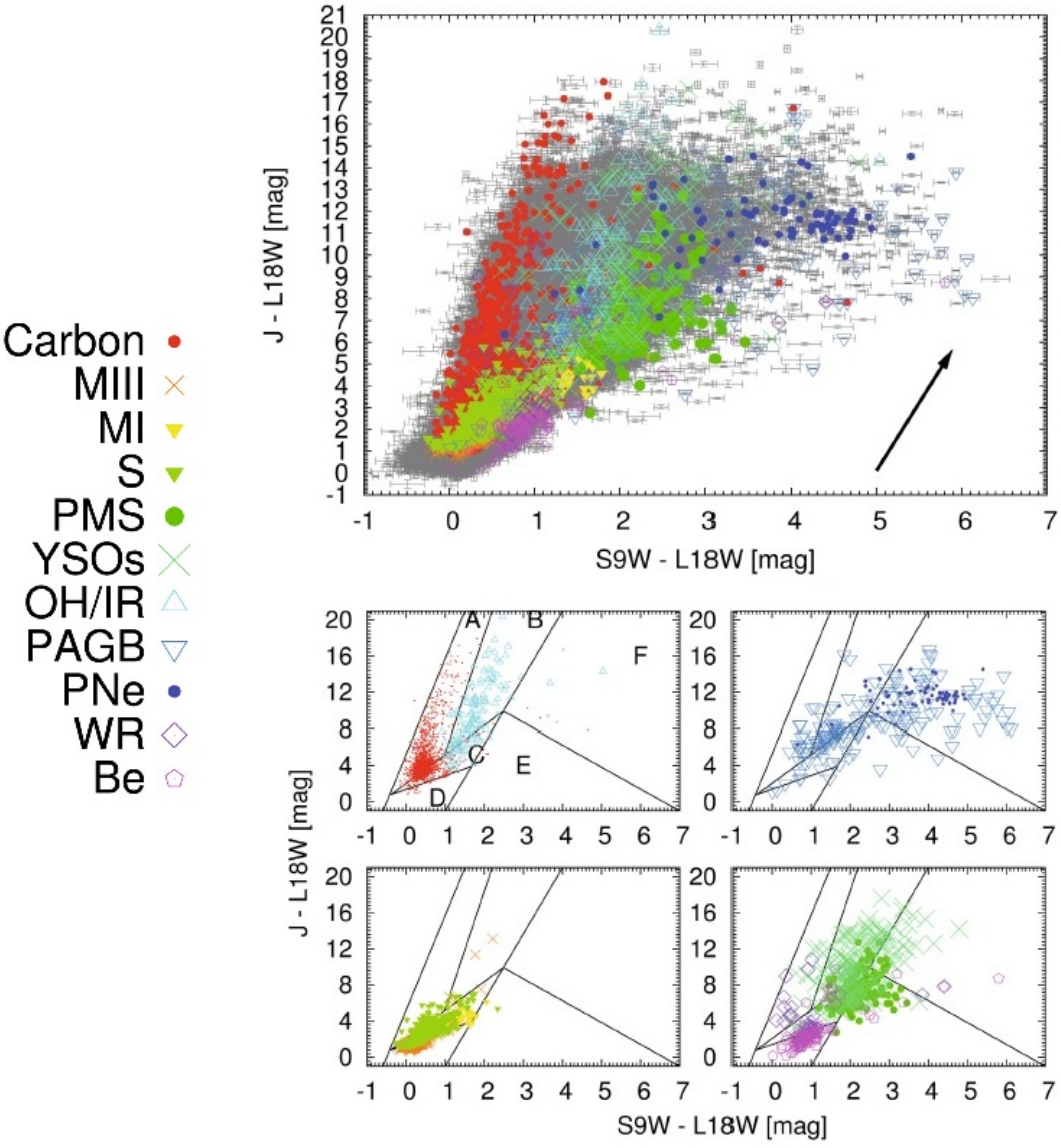

Figure 5.5: Shown in the $[K] - [9]$ vs. $[J] - [K]$, $[9] - [18]$ vs. $[K] - [9]$ and $[9] - [18]$ vs. $[J] - [K]$ colour-colour diagrams are the distributions of the reference sources (identified in SIMBAD) used by Ishihara et al. (2011).
Panel (a) shows C-rich AGB stars (red, group E), AGB stars (black) and OH/IR-stars (blue) (group F).
Panel (b) shows T-Tauri (brown) and YSOs (green) (group A).
Panel (c) shows Be-stars (including Wolf-Rayet stars, brown) and emission-line stars (green) (group B).
Panel (d) shows normal stars including OM giants and dwarfs (green; group C).
Panel (e) shows S-stars (green, group D), and post-AGB stars and PNe (brown, group G) and
panel (f) shows normal and starburst galaxies (green) and Seyferts (brown) (group H).
The contours show 20%, 50%, and 80% of the peak density value.

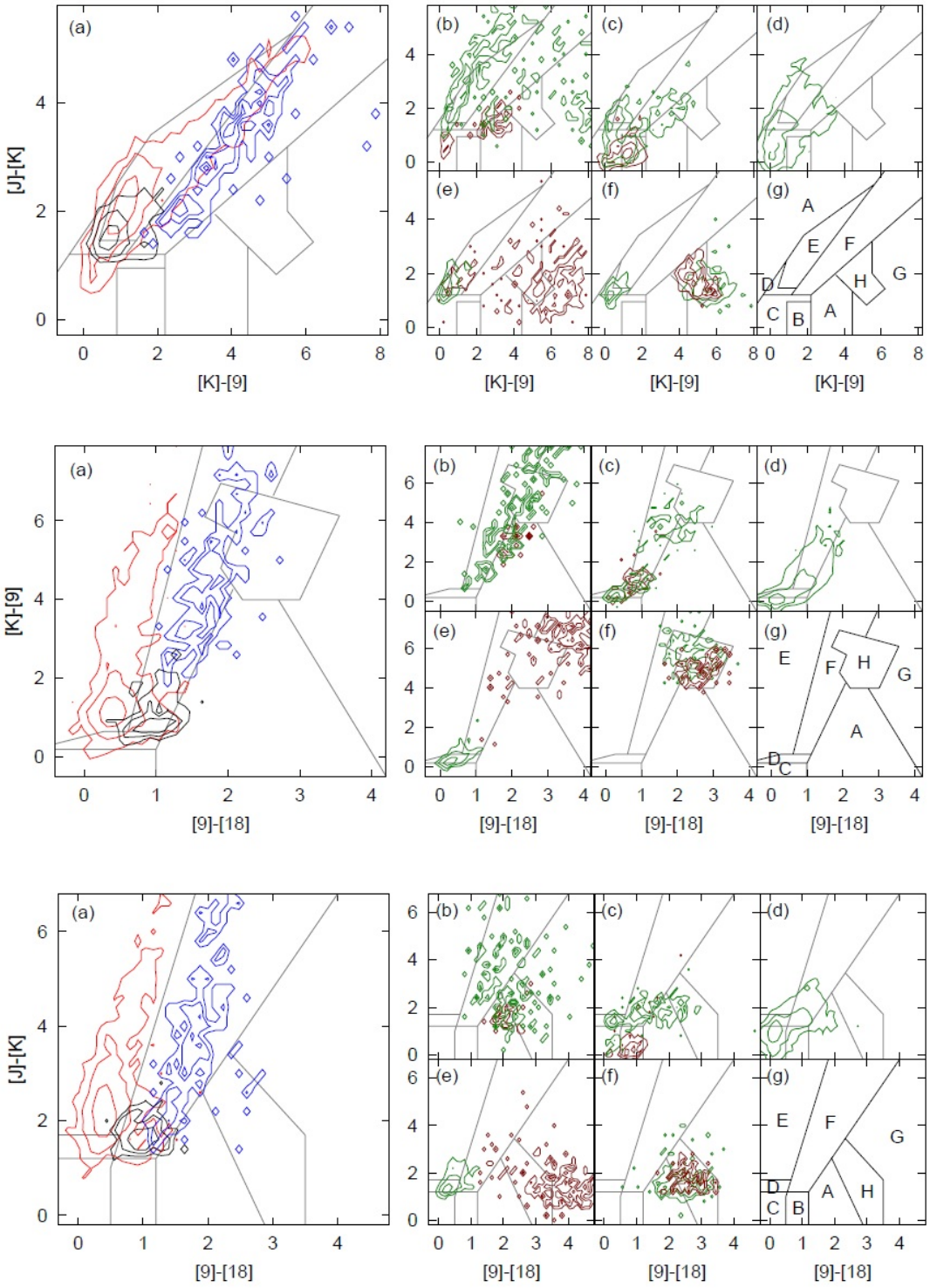

Figure 5.6: Table showing the statistics for the colour cuts that Anderson et al. (2012b) used to best discriminate between their sample of 126 HII regions and 43 PNe. Shown are the colours, the proposed discriminating colour cutoff values, the percentage of HII regions and PNe satisfying the colour cutoff, the colour average value with the corresponding standard deviation and the number of HII regions and PNe that were used in the calculations. According to these results, the four most robust discriminating colours are: $[F12/F8] < 0.3$, $[F160/F12] > 1.3$, $[F160/F24] > 0.8$ and $[F160/F22] > 0.8$ where the brackets indicate the log of the flux ratio.

Color	Cutoff	%H II	%PNe	Avg. (H II)	Avg. (PNe)	#H II	#PNe
$[F_{12}/F_8]$	< 0.3	98	18	-0.09 ± 0.11	0.57 ± 0.29	96	38
$[F_{22}/F_8]$	< 1.0	92	20	0.59 ± 0.31	1.23 ± 0.34	110	39
$[F_{24}/F_8]$	< 1.0	93	21	0.55 ± 0.29	1.23 ± 0.31	86	37
$[F_{70}/F_{12}]$	> 1.3	96	20	1.92 ± 0.36	1.01 ± 0.40	96	40
$[F_{70}/F_{22}]$	> 0.8	98	26	1.25 ± 0.22	0.39 ± 0.51	110	42
$[F_{70}/F_{24}]$	> 0.8	100	26	1.26 ± 0.21	0.42 ± 0.47	86	41
$[F_{160}/F_{12}]$	> 1.3	100	10	2.06 ± 0.38	0.80 ± 0.49	96	30
$[F_{160}/F_{22}]$	> 0.8	100	12	1.38 ± 0.26	0.16 ± 0.64	110	31
$[F_{160}/F_{24}]$	> 0.8	100	10	1.40 ± 0.25	0.22 ± 0.55	86	29
$[F_{160}/F_{70}]$	> -0.2	97	25	0.10 ± 0.17	-0.32 ± 0.24	126	31

5.6 Population separation for the Hi-GAL 1 PSC sources

Next, we followed the example of Anderson et al. (2012b) and used the Hi-GAL 1 fluxes, in combination with the fluxes in other survey bands, in an attempt to derive colour cuts, involving at least one of the 70 μm and 160 μm Herschel bands, that allow us to separate a sample of reference AGB stars from a sample of reference HII regions, YSOs and PNe located within the Hi-GAL 1 Galactic Plane surveyed region.

5.6.1 Reference sample

Our reference sample was formed of a total of 537 Galactic sources and included 205 YSOs, 178 HII regions, 95 AGB stars and 59 PNe. The reference sources were selected: (i) for being included in our Hi-GAL 1 PSC and in one, or several, of the Survey Catalogues, (ii) for being point-like sources and (iii) for having their stellar type confirmed through robust stellar identification methods carried out in previous studies. These methods include (i) SED fitting and the detection of (ii) optically thick CSM shells, (iii) IR excess emission from dusty CSM disks and envelopes, (v) luminosity variability, (vi) radio emission and the (vii) inspection of the source's spectroscopic data.
Listed in Tables 5.2-5.4 are the names and authors of the catalogues the selected reference sources were found to belong to. Also included is the number of reference sources belonging to each catalogue. The fluxes of the reference sources are those listed in our Hi-GAL 1 PSC - while the 70 μm - 500 μm Herschel fluxes were obtained with CUTEX, the fluxes for the remaining bands were taken from the Survey Catalogues' counterparts found lying within a maximum angular distance of 1.7 arcsec. The positions of the reference sources correspond to the most accurate positions (*macc_RA*, *macc_dec*) listed in the Hi-GAL 1 PSC. The complete list of reference sources can be found in the CD accompanying this thesis. There are four tables, one for each stellar type, which include:

- The sources' identification (*ID*), the position (*RA*,*dec* and *l*, *b* in degrees), the fluxes (*F* in Jy) and the flux uncertainties (*EF* in Jy), the Signal-to-Noise (S/N) and the flux quality flag (q_Flux), as listed in the Hi-GAL 1 PSC.

- The most accurate position available for the source (*macc_RA*, *macc_dec* in degrees), as listed in the Hi-GAL 1 PSC, the sources' stellar type (*Type*) and the name of the catalogue (*Ref_Cat*) the sources belong to.

Table 5.1: List of catalogues containing our reference YSOs.

YSO Reference Catalogues		
Catalogue name	**Author**	**n sources included**
Radio observations of MYSO candidates	Urquhart et al. (2007b)	75
13 CO observations of YSO in South Galactic plane		
Catalogue of bright YSO candidates in ISOGAL	Felli et al. (2002)	38
YSOs in Vul OB1 association	Billot et al. (2010)	35
RMS survey: 6cm observations of YSOs	Urquhart et al. (2009)	30
Embedded YSO candidates in W51	Kang et al. (2009)	13
YSO candidates in M17 SWex	Povich and Whitney (2010)	9
YSOs in the central 400pc of the Galaxy	Yusef-Zadeh et al. (2009)	4
Transitional YSOs candidates	Magnier et al. (1999)	1

Table 5.2: List of catalogues containing our reference HII regions.

HII region Reference Catalogues		
Catalogue name	**Author**	**n sources included**
The WISE catalog of Galactic HII regions	Anderson et al. (2014)	52
The Red MSX Source Survey: massive protostars	Lumsden et al. (2013)	33
Red MSX Survey (RMS): Bolometric fluxes of YSOs	Mottram et al. (2011)	31
Ultracompact HII regions studies II	Walsh et al. (1998)	11
A $C_{S(2-1)}$ survey of UC HII regions	Bronfman et al. (1996)	11
Infrared fluxes of HII regions and PNe	Anderson et al. (2012b)	9
RMS compact HII regions distances	Urquhart et al. (2012)	8
Maser and outflows in UC HII regions	Codella et al. (2004)	5
ATLASGAL. Properties of compact HII regions	Urquhart et al. (2013)	3
Ultracompact HII regions radio images	Kurtz et al. (1994)	3
Galactic radio compact HII regions at 1.4 GHz	Giveon et al. (2005)	3
SCUBA ultracompact HII regions	Thompson et al. (2006)	2
HRDS III. HII region kinematic distances	Anderson et al. (2012a)	2
The HII Region Discovery Survey (HRDS). II.	Anderson et al. (2011)	1
Velocities of HII regions	Kolpak et al. (2003)	1
VLA observations of ultracompact HII regions	Molinari et al. (1998)	1
H_2CO and Hα observations of UC HII	Araya et al. (2002)	1
The RMS survey: water masers of YSOs	Urquhart et al. (2009)	1

Table 5.3: List of catalogues containing our reference AGB stars.

AGB star Reference Catalogues		
Catalogue name	**Author**	**n sources included**
OH-Selected AGB and post-AGB objects I	Sevenster (2002)	42
Infrared two-colour diagrams for AGB stars using AKARI, MSX, IRAS and near-infrared data	Suh and Kwon (2011)	40
High mass-loss AGB stars in the Galactic Buldge	Ojha et al. (2007)	14
Mass-loss rates of Galactic AGB stars	Le Bertre et al. (2003a)	7
Infrared photometry of mass losing AGB stars	Guandalini and Busso (2008)	5
The Red MSX Source Survey: massive protostars	Lumsden et al. (2013)	6
GLMP sample of Galactic OH/IR stars	Jiménez-Esteban et al. (2006)	2
JHKL' photometry of selected AGB stars		
Evolved stars in the MSX survey	Ortiz et al. (2005)	1
Near-IR spectra of extremely red AGB stars	Wright et al. (2009)	1

Table 5.4: List of catalogues containing our reference PNe.

PN Reference Catalogues		
Catalogue name	**Author**	**n sources included**
The Red MSX Source Survey: massive protostars	Lumsden et al. (2013)	30
Candidate Planetary Nebulae in IPHAS catalog	Viironen et al. (2009)	12
MASH Catalogues of Planetary Nebulae	Parker et al. (2006)	7
Planetary nebulae near the Galactic center	Jacoby and Van de Steene (2004)	6
Optical coordinates of southern PNe	Kimeswenger (2001)	3
Accurate coordinates of Planetary Nebulae	Kohoutek and Kühl (2002)	1
Binary PNe towards the Galactic buldge	Miszalski et al. (2009)	1
Infrared fluxes of HII regions and PNe	Anderson et al. (2011)	1

5.6.2 Colour cuts to separate AGB stars, YSOs, PNe and HII regions

Next, we used all the fluxes (F_{ν_1}, F_{ν_2}, F_{ν_3},...) available for the reference AGB stars, YSOs, PNe and HII regions to calculate their colours ($[\lambda_1]-[\lambda_2]$, $[\lambda_1]-[\lambda_3]$, $[\lambda_2]-[\lambda_3]$,...) and studied each colour distribution in order to determine if there was one or more colour cuts, involving the Herschel 70 μm or 160 μm bands, with which it was possible to separate the reference AGB stars from the reference YSOs, PNe and HII regions. The importance of selecting only colour cuts involving the 70 μm or 160 μm bands relies on the fact that these bands trace the emission of the dust around AGB stars. Moreover, in order to guarantee the efficiency and reliability of the colour cuts, we decided to only consider those colour cuts which: (i) could be tested upon $\geq$ 70% of our reference AGB stars and $\geq$ 70% of our reference YSOs, PNe and HII regions and had (ii) the maximum verification rate and (iii) the minimum contamination rate. Shown in Fig. 5.7 and 5.8 are the percentages of the reference YSOs, AGB stars, PNe and HII regions for which we had fluxes in the Herschel, 2MASS, WISE, GLIMPSE, MSX, IRAS and AKARI bands. Here, we can see that for the Herschel 160 μm, 250 μm, 350 μm and 500 μm bands and for all the GLIMPSE, IRAS and AKARI-FIS bands, the percentage of reference AGB stars available is $<$ 70%. Thus, those colour cuts that involved these bands were not considered. Shown in Fig. 5.9 and 5.10 are the colour distributions and colour cuts that were found to separate most efficiently the reference AGB stars from the reference YSOs, PNe and HII regions and to satisfy the previous three conditions. These are:

AGB stars vs. YSOs	**AGB stars vs. HII regions**		**AGB stars vs. PNe**
$[70/4.6] < -0.1$	$[70/1.65] < 3.5$	$[70/12] < 0.1$	$[70/4.6] < 0.5$
$[70/12] < -0.1$	$[70/2.17] < 2.6$	$[70/22] < -0.2$	$[70/12] < 0$
	$[70/4.6] < 0.5$		

Listed in Table 5.5 are: (i) the percentages of reference AGB stars, YSOs, PNe and HII regions that satisfy each of the previous colour cuts, (ii) the number of sources and (iii) the fraction of the total reference sample upon which the colour cut was used. Shown in Fig. 5.11-5.14 are the colour-colour diagrams, involving the colours listed above, in which we can separate the reference AGB stars from the reference YSOs, PNe and HII regions. Also indicated are the colour cuts suggested. From Fig. 5.9 we can see that there is a considerable fraction of the reference YSOs and AGB stars that have similar [70/4.6] and [70/12] colours. In Chapter 6 we identify these YSOs as being of class I and II.

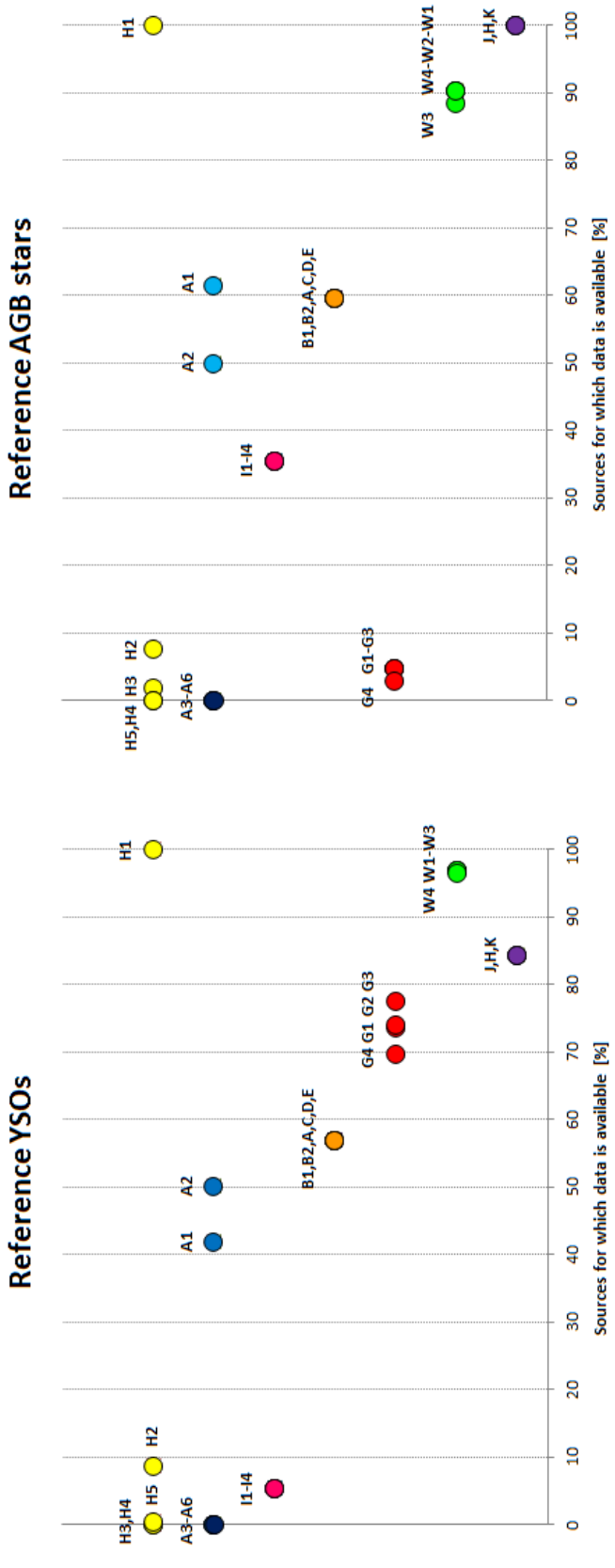

Figure 5.7: Percentages of reference YSOs and AGB stars for which photometric data are available in all Herschel H1 (70 μm), H2 (160 μm), H3 (250 μm), H4 (350 μm) and H5 (500 μm) bands, 2MASS J (1.25 μm), H (1.65 μm) and K (2.17 μm) bands, WISE W1 (3.4 μm), W2 (4.6 μm), W3 (12 μm) and W4 (22 μm) bands, GLIMPSE G1 (3.6 μm), G2 (4.5 μm), G3 (5.8 μm) and G4 (8 μm) bands, MSX B1 (4.29 μm), B2 (4.35 μm), A (8.28 μm), C (12.13 μm), D (14.65 μm) and E (21.34 μm) bands, IRAS I1 (12 μm), I2 (25 μm), I3 (60 μm) and I4 (100 μm) bands and AKARI A1 (9 μm), A2 (18 μm), A3 (65 μm), A4 (90 μm), A5 (140 μm) and A6 (160 μm) bands.

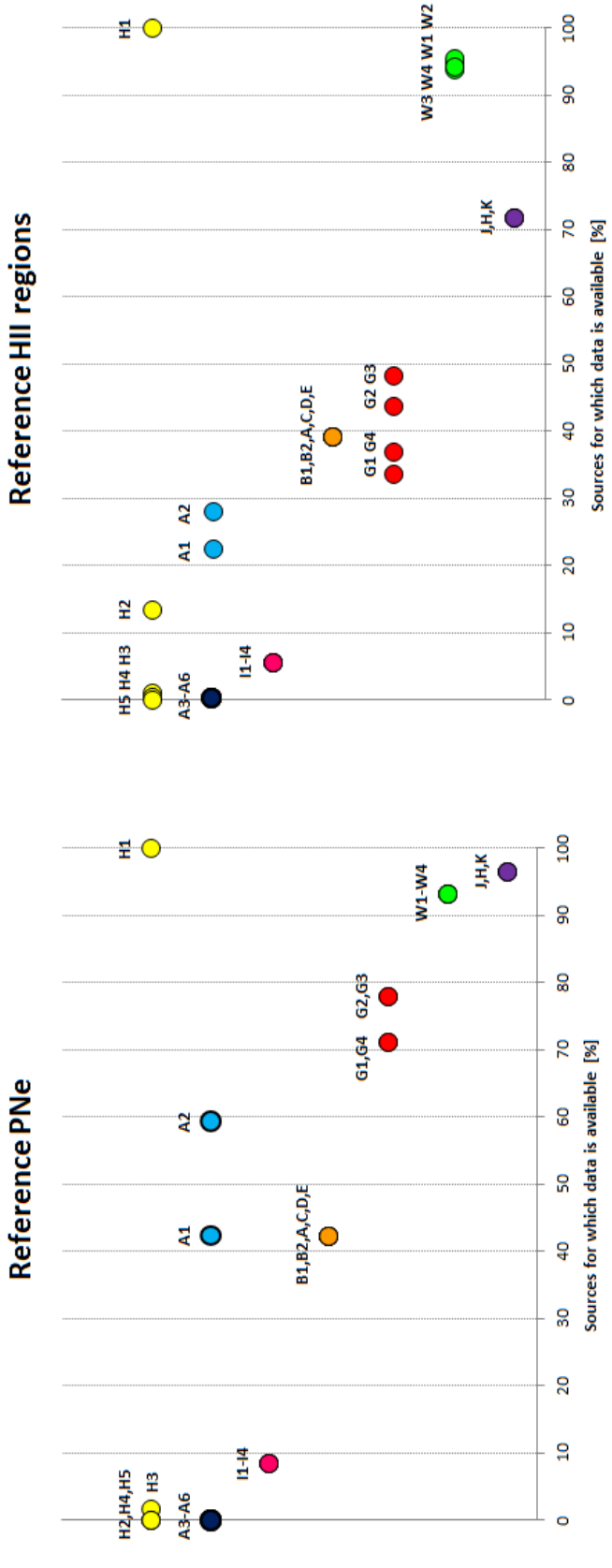

Figure 5.8: Percentages of reference PNe and HII regions for which photometric data is available in all Herschel H1 (70 μm), H2 (160 μm), H3 (250 μm), H4 (350 μm) and H5 (500 μm) bands, 2MASS J (1.25 μm), H (1.65 μm) and K (2.17 μm) bands, WISE W1 (3.4 μm), W2 (4.6 μm), W3 (12 μm) and W4 (22 μm) bands, GLIMPSE G1 (3.6 μm), G2 (4.5 μm), G3 (5.8 μm) and G4 (8 μm) bands, MSX B1 (4.29 μm), B2 (4.35 μm), A (8.28 μm), C (12.13 μm), D (14.65 μm) and E (21.34 μm) bands, IRAS I1 (12 μm), I2 (25 μm), I3 (60 μm) and I4 (100 μm) bands and AKARI A1 (9 μm), A2 (18 μm), A3 (65 μm), A4 (90 μm), A5 (140 μm) and A6 (160 μm) bands.

Figure 5.9: Colour distributions in which we can most efficiently separate the reference AGB stars (in red) from the reference YSOs (in green) and PNe (in orange). Indicated in grey are the colour cuts suggested. These colour distributions verify that: (i) they involve the 70 μm Herschel band, (ii) they can be tested upon $\geq$ 70% of our reference AGB stars and $\geq$ 70% of our reference HII regions, YSOs and PNe and (iii) they have the maximum verification rate and minimum contamination rate.

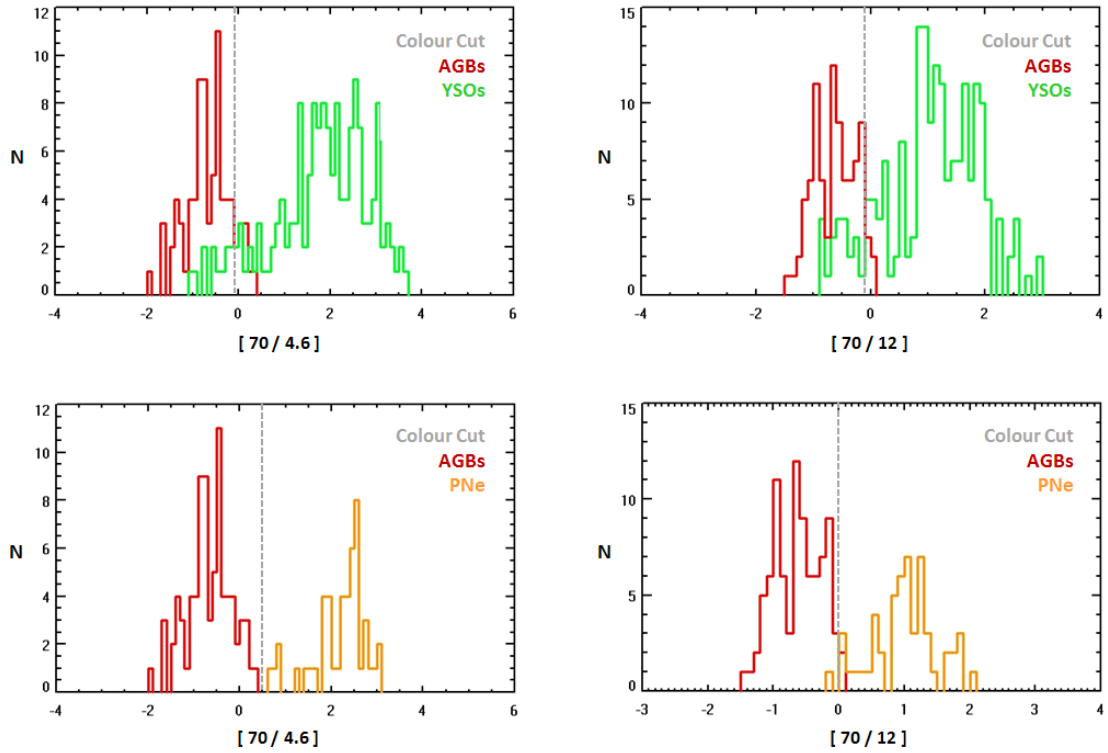

Figure 5.10: Colour distributions in which we can most efficiently separate the reference AGB stars (in red) from the reference HII regions (in blue). Indicated in grey are the colour cuts suggested. These colour distributions verify that: (i) they involve the 70 μm Herschel band, (ii) they can be tested upon $\geq$ 70% of our reference AGB stars and $\geq$ 70% of our reference HII regions and (iii) they have the maximum verification rate and minimum contamination rate.

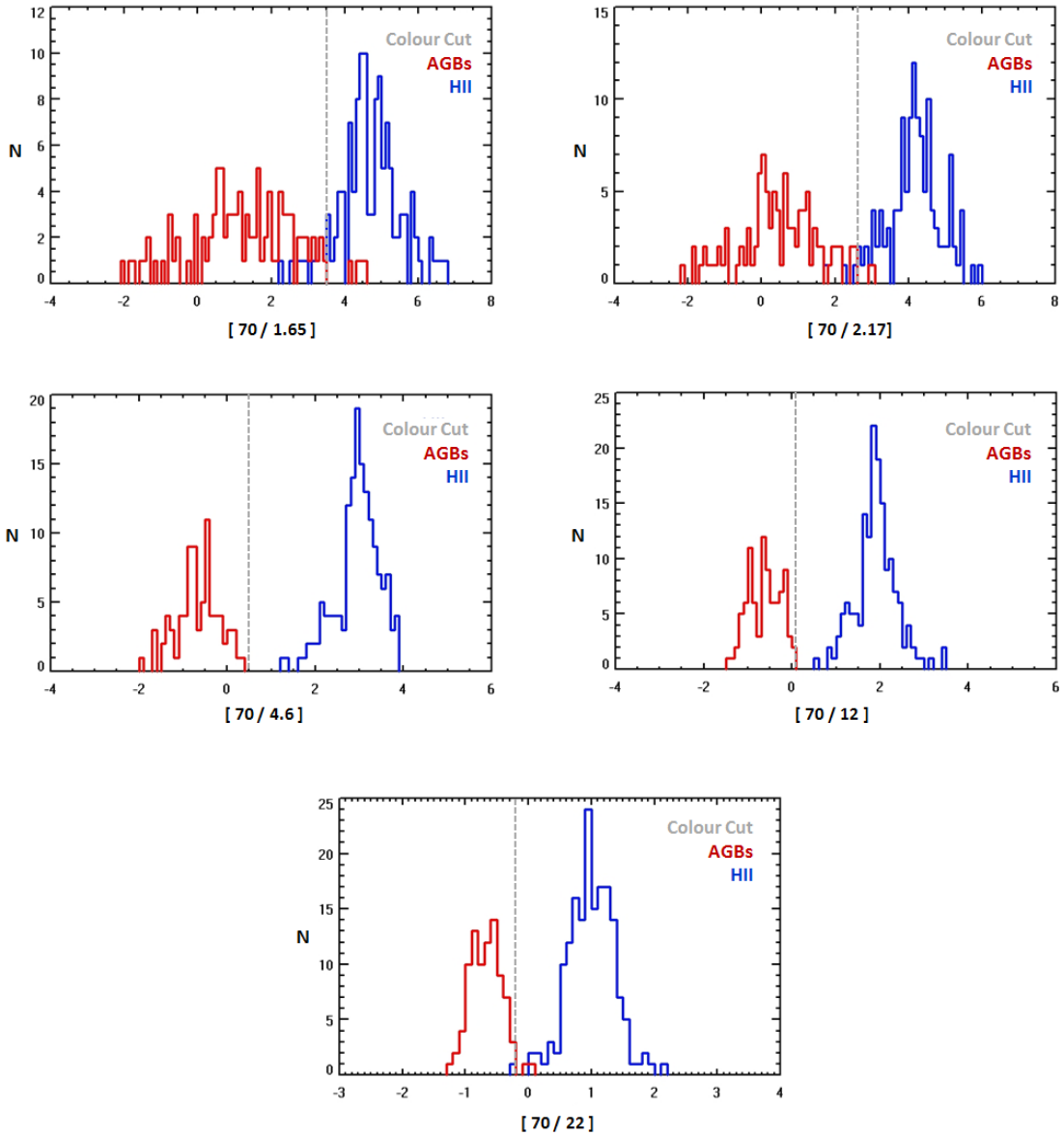

Table 5.5: Colour cuts that separate most efficiently the reference AGB stars from the reference YSOs, PNe and HII regions. These colour cuts verify that: (i) they involve the 70 μm Herschel band, (ii) they can be tested upon $\geq$ 70% of our reference AGB stars and $\geq$ 70% of our reference HII regions, YSOs and PNe and (iii) they have the maximum verification rate and minimum contamination rate.

Colour Cut	**%(AGB stars)**	**%(YSOs)**	**Sample AGB stars**		**Sample YSOs**	
			#	%	#	%
$[70/4.6] < -0.1$	87	7	82	86	161	79
$[70/12] < -0.1$	94	11	89	94	195	95

Colour Cut	**%(AGB stars)**	**%(PNe)**	**Sample AGB stars**		**Sample PNe**	
			#	%	#	%
$[70/4.6] < 0.5$	99	2	82	86	50	85
$[70/12] < 0$	98	2	89	94	54	92

Colour Cut	**%(AGB stars)**	**%(HII regions)**	**Sample AGB stars**		**Sample HII regions**	
			#	%	#	%
$[70/1.65] < 3.5$	96	8	95	100	126	71
$[70/2.17] < 2.6$	98	2	95	100	128	72
$[70/4.6] < 0.5$	99	1	82	86	154	87
$[70/12] < 0.1$	100	1	89	94	159	89
$[70/22] < -0.2$	98	1	87	92	168	94

Figure 5.11: Colour-colour diagrams in which we can separate the reference AGB stars (in red) from the reference YSOs (in green), PNe (in orange) and HII regions (in blue). Indicated in grey are the colour cuts suggested.

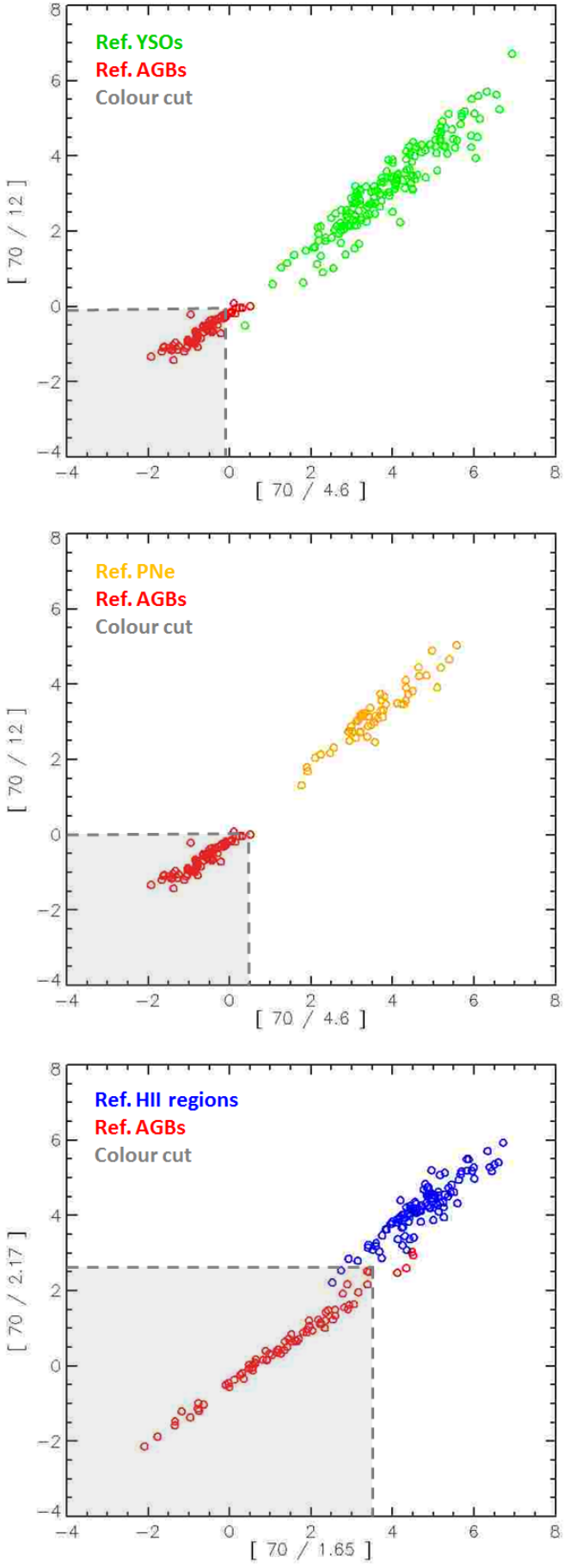

Figure 5.12: Other colour-colour diagrams in which we can separate the reference AGB stars (in red) from the reference HII regions (in blue). Indicated in grey are the colour cuts suggested.

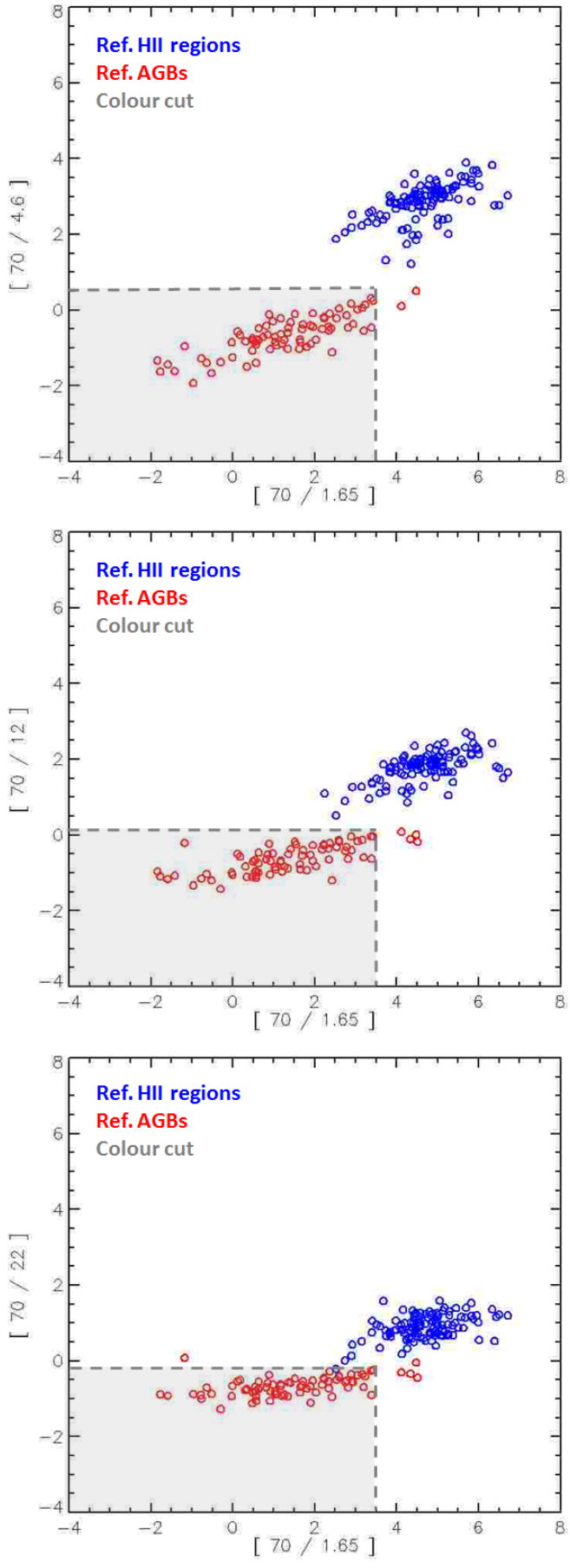

Figure 5.13: More colour-colour diagrams in which we can separate the reference AGB stars (in red) from the reference HII regions (in blue). Indicated in grey are the colour cuts suggested.

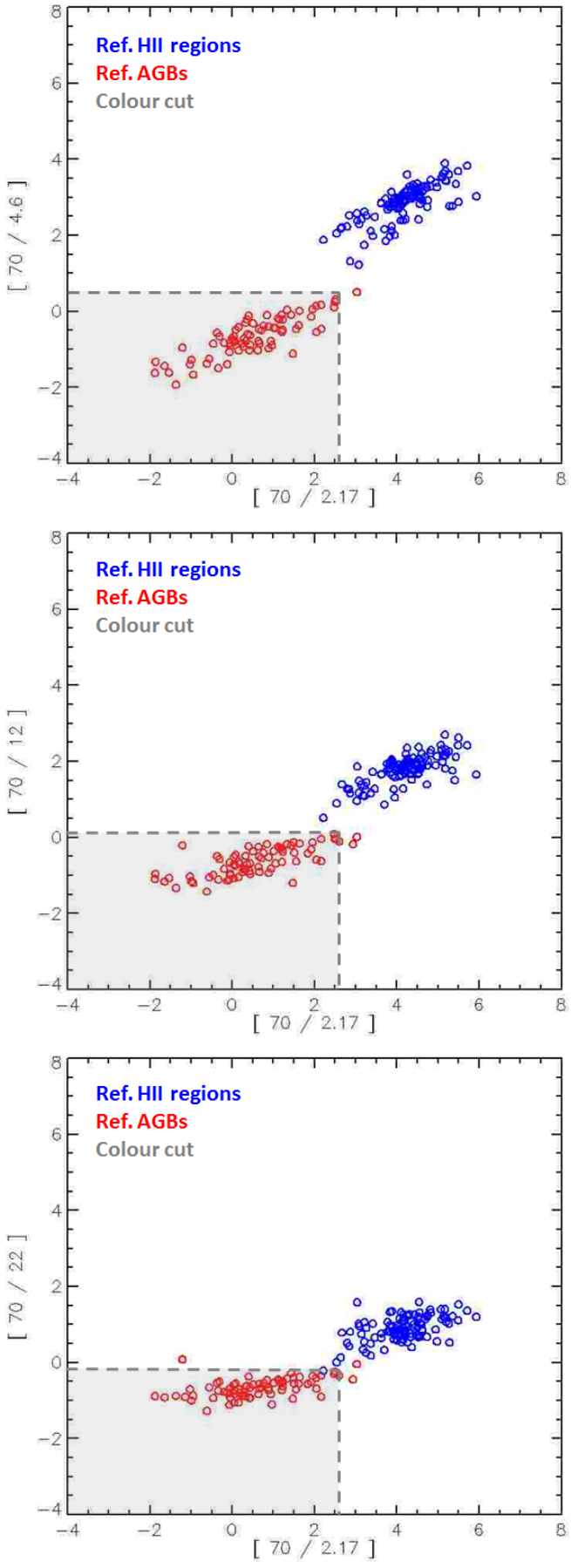

Figure 5.14: Some more colour-colour diagrams in which we can separate the reference AGB stars (in red) from the reference HII regions (in blue). Indicated in grey are the colour cuts suggested.

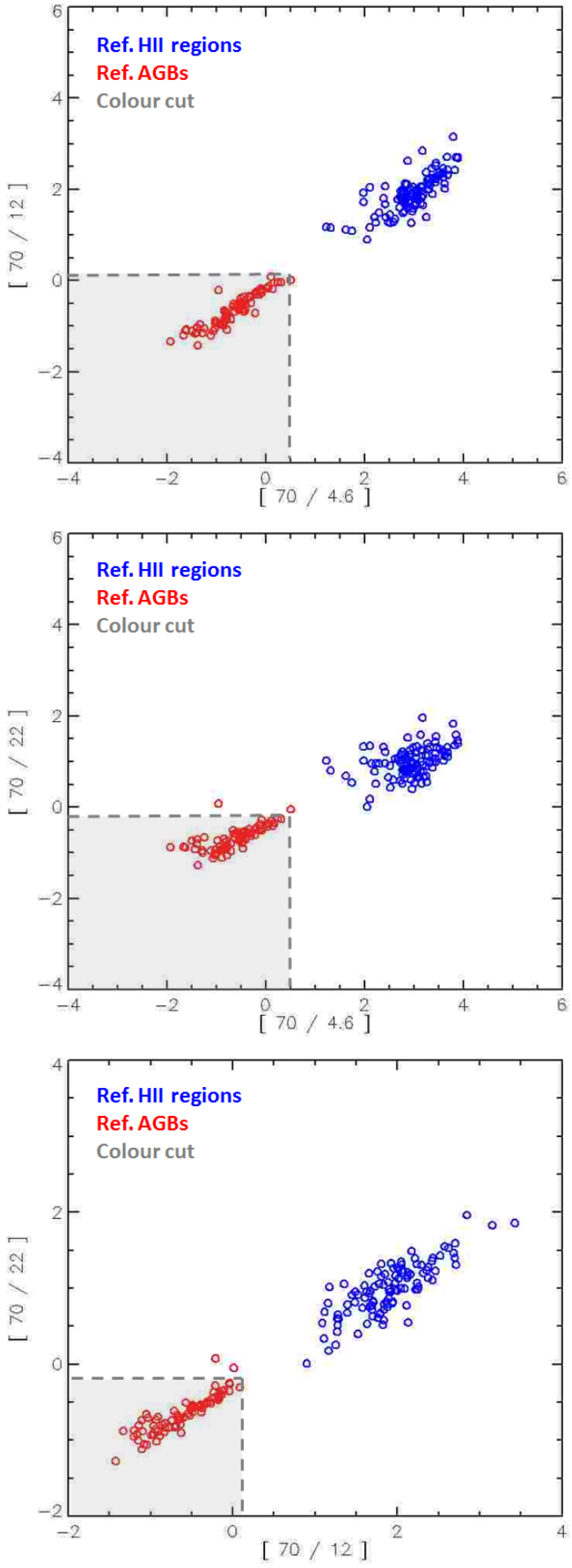

The colour distributions shown in Fig. 5.15 and 5.16 are included as examples of discarded colours which, despite providing a relatively good separation between the reference AGB stars and the reference YSOs, PNe and HII regions, they did not fulfil the conditions described in Sect. 5.6.2, and therefore they were not included in our final selection of colour cuts.

In the cases of (a) and (b), the contamination between the reference AGB stars and the reference YSOs and PNe was found to be not minimal while in the cases of (c)-(f), the percentage of reference AGB stars or/and PNe and HII regions used for the distributions was <70%. Cases (e), (f) and (g)-(m) are colour cuts that do not involve the Herschel 70 μm or 160 μm bands but are as efficient as those listed in Table 5.5.

Listed in Table 5.6 are our suggested colour cuts for the previous colour distributions together with: (i) the percentage and number of sources that satisfy such colour cuts and (ii) the fraction of the total reference sample upon which the colour cuts were tested.

From the colour distributions shown in Fig. 5.9-5.16 we can see that all the colour cuts found to separate AGB stars from YSOs, PNe and HII regions involve the WISE bands and/or the 70 μm band. This result confirms that the WISE and the Herschel 70 μm bands are highly effective in distinguishing AGB stars from YSOs, PNe and HII regions and that these bands play a decisive role in the identification of AGB stars. Moreover, since only the Hi-GAL Survey data contains such accurate 70 μm fluxes, this result confirms that the Hi-GAL Survey data is crucial for the detection of AGB stars.

Figure 5.15: Other interesting colour distributions. The reference AGB stars, YSOs, PNe and HII regions are indicated in red, green, orange and blue respectively while the colour cuts suggested are indicated in grey. These colour distributions were discarded as they: (i) do not involve the 70 μm Herschel band and/or (ii) they cannot be tested upon $\geq$ 70% of our reference AGB stars and/or $\geq$ 70% of our reference YSOs, PNe and HII regions and/or (iii) they do not have the maximum verification rate and/or minimum contamination rate.

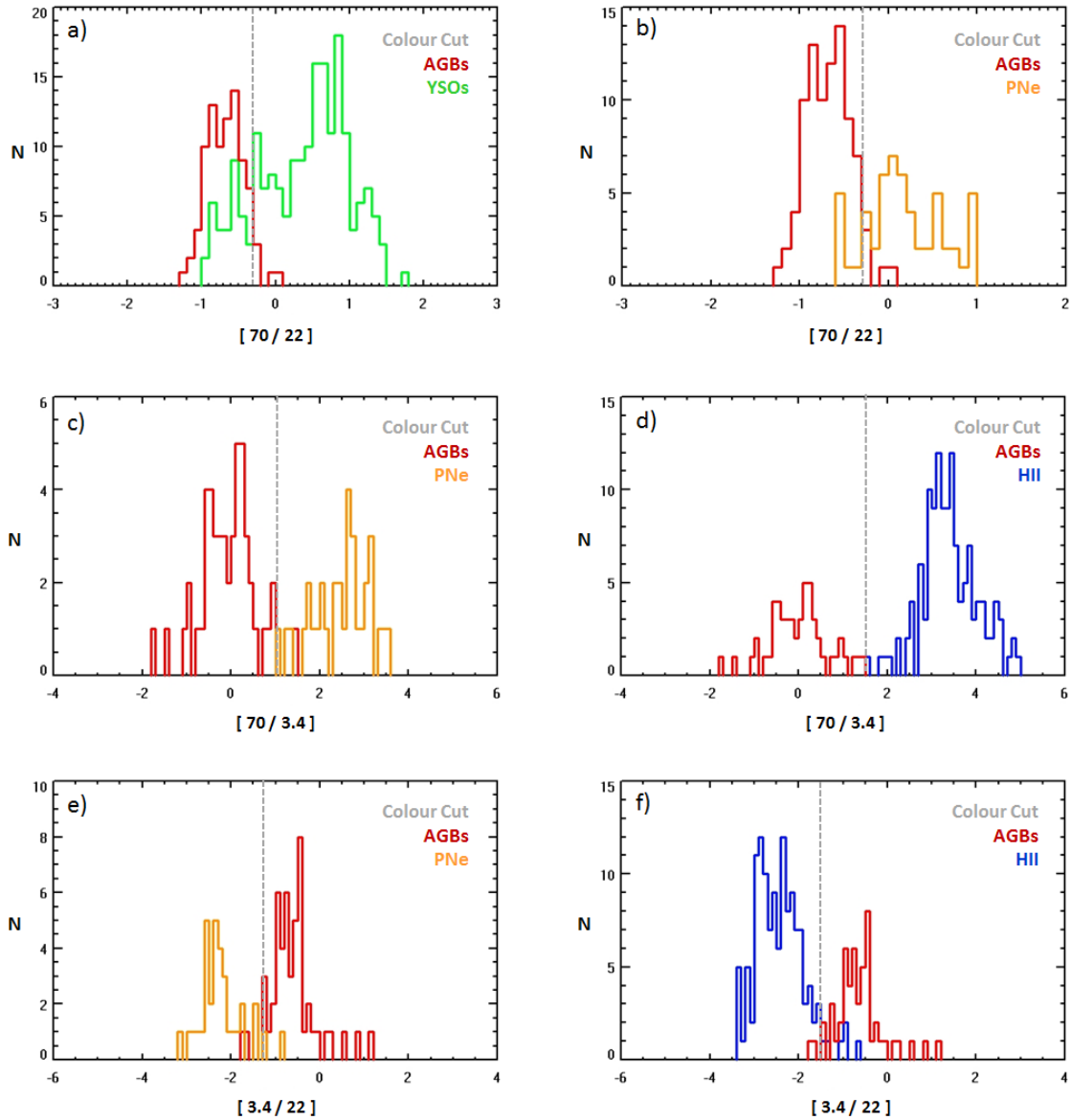

Figure 5.16: More interesting colour distributions. The reference AGB stars, YSOs, PNe and HII regions are indicated in red, green, orange and blue respectively while the colour cuts suggested are indicated in grey. These colour distributions were discarded as they: (i) do not involve the 70 μm Herschel band and/or (ii) they cannot be tested upon $\geq$ 70% of our reference AGB stars and/or $\geq$ 70% of our reference YSOs, PNe and HII regions and/or (iii) they do not have the maximum verification rate and/or minimum contamination rate.

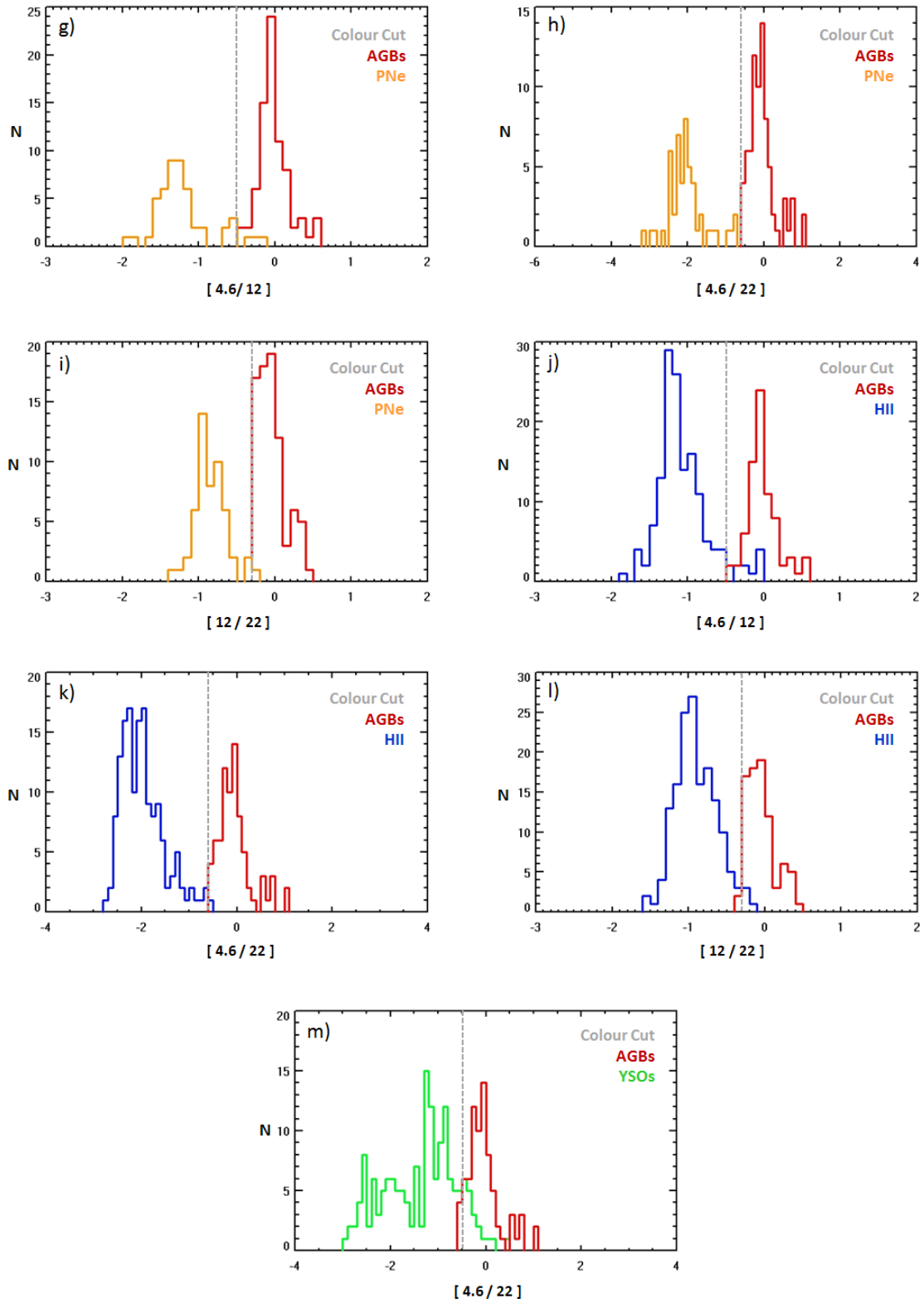

Table 5.6: The colour cuts listed below were also found to provide a relatively good separation between our reference AGB stars and reference YSOs, PNe and HII regions. However, these colour cuts were discarded as they: (i) do not involve the 70 μm Herschel band and/or (ii) they cannot be tested upon $\geq$ 70% of our reference AGB stars and/or $\geq$ 70% of our reference YSOs, PNe and HII regions and/or (iii) they do not have the maximum verification rate and/or minimum contamination rate.

Colour Cut	**%(AGB stars)**	**%(YSOs)**	**Sample AGB stars**		**Sample YSOs**	
			#	%	#	%
$[70/22] < -0.3$	94	17	87	92	197	96
$[4.6/22] > -0.5$	95	13	77	81	160	78

Colour Cut	**%(AGB stars)**	**%(PNe)**	**Sample AGB stars**		**Sample PNe**	
			#	%	#	%
$[70/3.4] < 1$	93	3	53	56	33	56
$[70/22] < -0.3$	94	13	87	92	55	93
$[3.4/22] > -1.3$	92	6	52	55	33	56
$[4.6/12] > -0.5$	100	6	78	82	50	85
$[4.6/22] > -0.6$	100	2	77	81	50	85
$[12/22] > -0.3$	98	4	83	87	54	92

Colour Cut	**%(AGB stars)**	**%(HII regions)**	**Sample AGB stars**		**Sample HII regions**	
			#	%	#	%
$[70/3.4] < 1.5$	100	1	53	56	131	74
$[3.4/22] > -1.5$	96	5	52	55	129	72
$[4.6/12] > -0.5$	100	6	78	82	145	81
$[4.6/22] > -0.6$	100	1	77	81	153	86
$[12/22] > -0.3$	98	3	83	87	158	89

5.6.2.1 Revision of the colour cuts derived in previous studies

In this section, we determine whether our reference 205 YSOs, 178 HII regions, 95 AGB stars and 59 PNe verify the colour cuts presented by Ita et al. (2010), Ishihara et al. (2011) and Anderson et al. (2012b) (see Sect. 5.5).

- Ita et al. (2010)

  Shown in the top panel of Fig. 5.17 is the $[9]-[18]$ vs. $[J]-[18]$ colour-colour diagram that Ita et al. (2010) used to define the three regions indicated in the diagram: (i) C - stars, (ii) OH/IR-stars and YSOs and (iii) PNe. Shown in the bottom panel of Fig. 5.17 are the colour-colour regions that our reference YSOs, AGB stars and PNe occupy in the previous colour-colour diagram. Here, we can see that: (i) all our reference AGB stars lie within the C-stars and OH/IR-stars regions, (ii) the majority (88%) of our reference PNe lie within the PNe region and (iii) there is a large amount of reference YSOs (49%) that do not verify Ita's YSO colour cuts. Thus, the colour cuts defined by Ita et al. (2010) provide a good separation only to our reference AGB stars and PNe and not to our reference YSOs.

- Ishihara et al. (2011)

  Shown in the top panel of Fig. 5.18, 5.19 and 5.20 are the $[K]-[9]$ vs. $[J]-[K]$, $[9]-[18]$ vs. $[K]-[9]$ and $[9]-[18]$ vs. $[J]-[K]$ colour-colour diagrams that Ishihara et al. (2011) used to define the five regions indicated in the diagrams: (i) C-rich AGB stars, (ii) O-rich AGB stars, (iii) S-stars, (iv) YSOs and (v) PNe and post-AGB stars. Shown in the bottom panels of Fig. 5.18, 5.19 and 5.20 are the colour-colour regions that our reference YSOs, AGB stars and PNe occupy in the previous colour-colour diagrams. Here, we can see that the majority ($\sim$88%) of our reference AGB stars and PNe are correctly classified by the colour-colour regions defined by Ishihara et al. (2011) in the $[9]-[18]$ vs. $[J]-[K]$ and $[K]-[9]$ vs. $[J]-[K]$ colour-colour diagrams, respectively. Also, we can see that if we extrapolate the limits of Ishihara's colour-colour regions to the whole area occupied by our reference PNe in the $[9]-[18]$ vs. $[K]-[9]$ and $[9]-[18]$ vs. $[J]-[K]$ colour-colour diagrams, then the majority ($\sim$88%) of our reference PNe lie within the PNe region. Finally, we can see that our reference YSOs do not verify Ishihara's YSO colour cuts. Thus, the colour cuts defined by Ishihara et al. (2011) in the $[K]-[9]$ vs. $[J]-[K]$ and

$[9]-[18]$ vs. $[K]-[9]$ colour-colour diagrams provide a good separation only to our reference PNe whereas the colour cuts defined by Ishihara et al. (2011) in the $[9]-[18]$ vs. $[J]-[K]$ colour-colour diagram provide a good separation to both our reference AGB stars and PNe.

- Anderson et al. (2012b)

  Shown in Fig. 5.21 are the [12/8], [22/8], [70/12] and [70/22] colour distributions of the colour cuts that Anderson et al. (2012b) used to best discriminate between a sample of 126 HII regions and 43 PNe (see Table 5.6). Here, we can see that Anderson's suggested $[70/12] > 1.3$ colour cut provides a good separation between our reference PNe and HII regions whereas the $[12/8] < 0.3$ and $[22/8] < 1.0$ colour cuts do not. In the case of the [70/22] colour distribution we can see that our reference HII regions and PNe can be separated. However, for our sample, such separation occurs at [70/22]=0.5 instead of at [70/22]=0.8 as suggested by Anderson et al. (2012b). Therefore, our suggested colour cut would be $[70/22] > 0.5$ instead of Anderson's $[70/22] > 0.8$. As a result, we conclude that, as found in Anderson et al. (2012b), the [70/12] and [70/22] colour distributions provide a good separation between our reference PNe and HII regions.

The previous results establish that:

(i) The colour cuts defined by Ita et al. (2010) in the $[9]-[18]$ vs. $[J]-[18]$ colour-colour diagram provide a good separation to our reference AGB stars and PNe but not to our reference YSOs.

(ii) The colour cuts defined by Ishihara et al. (2011) in the $[K]-[9]$ vs. $[J]-[K]$, $[9]-[18]$ vs. $[K]-[9]$ and $[9]-[18]$ vs. $[J]-[K]$ colour-colour diagrams are verified, in general, by our reference AGB stars and PNe but not by our reference YSOs.

(iii) The $[70/12] > 1.3$ colour cut defined by Anderson et al. (2012b) successfully discriminates our reference PNe from our reference HII regions. The [70/22] colour distribution was also found to provide a good separation, but we obtained better results for $[70/22] > 0.5$ than for Anderson's $[70/22] > 0.8$ suggested colour cut.

(iv) Our colour criteria are different and more efficient on separating our reference AGB stars, YSOs, PNe and HII regions than those established by Ita et al. (2010) and Ishihara et al. (2011) and Anderson et al. (2012b).)

Figure 5.17: Shown in the top panel is the [9] − [18] vs. [J] − [18] colour-colour diagram that Ita et al. (2010) used to define the three regions indicated in the diagram: (i) C-stars (in blue), (ii) OH/IR-stars (in red) and YSOs (in green) and (iii) PNe (in orange), within the colour-colour region used by Ita et al. 2010. Shown in the bottom panel are the colour-colour regions that our reference AGB stars (in red), YSOs (in green) and PNe (in yellow) occupy in the colour-colour diagram shown in the top panel.

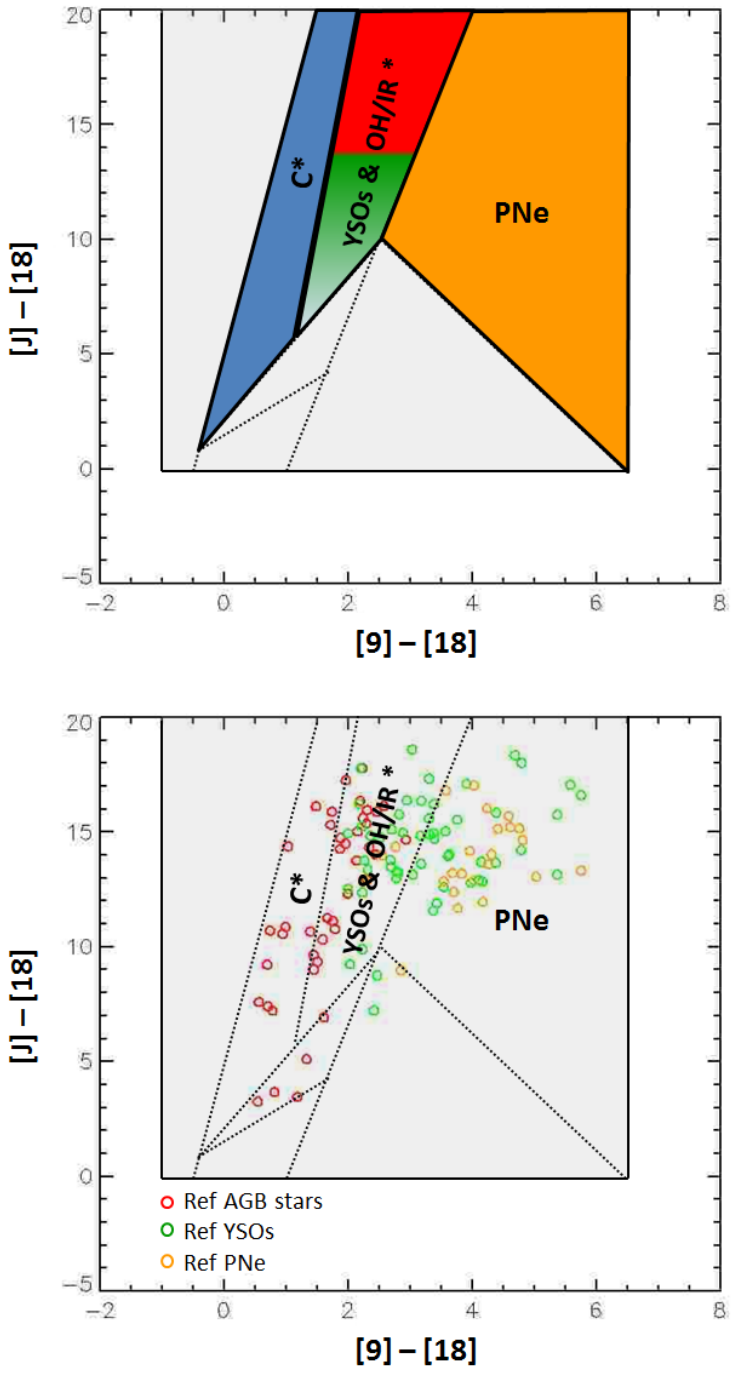

Figure 5.18: Shown in the top panel is the $[K] - [9]$ vs. $[J] - [K]$ colour-colour diagram that Ishihara et al. (2011) used to define the five regions indicated in the diagram: (i) C-rich AGB stars (in blue), (ii) O-rich AGB stars (in red), (iii) S-stars (in purple), (iv) YSOs (in green) and (v) post-AGB stars and PNe (in orange), within the colour-colour region used by Ishihara et al. (2011). Shown in the bottom panel are the colour-colour regions that our reference AGB stars (in red), YSOs (in green) and PNe (in yellow) occupy in the colour-colour diagram shown in the top panel.

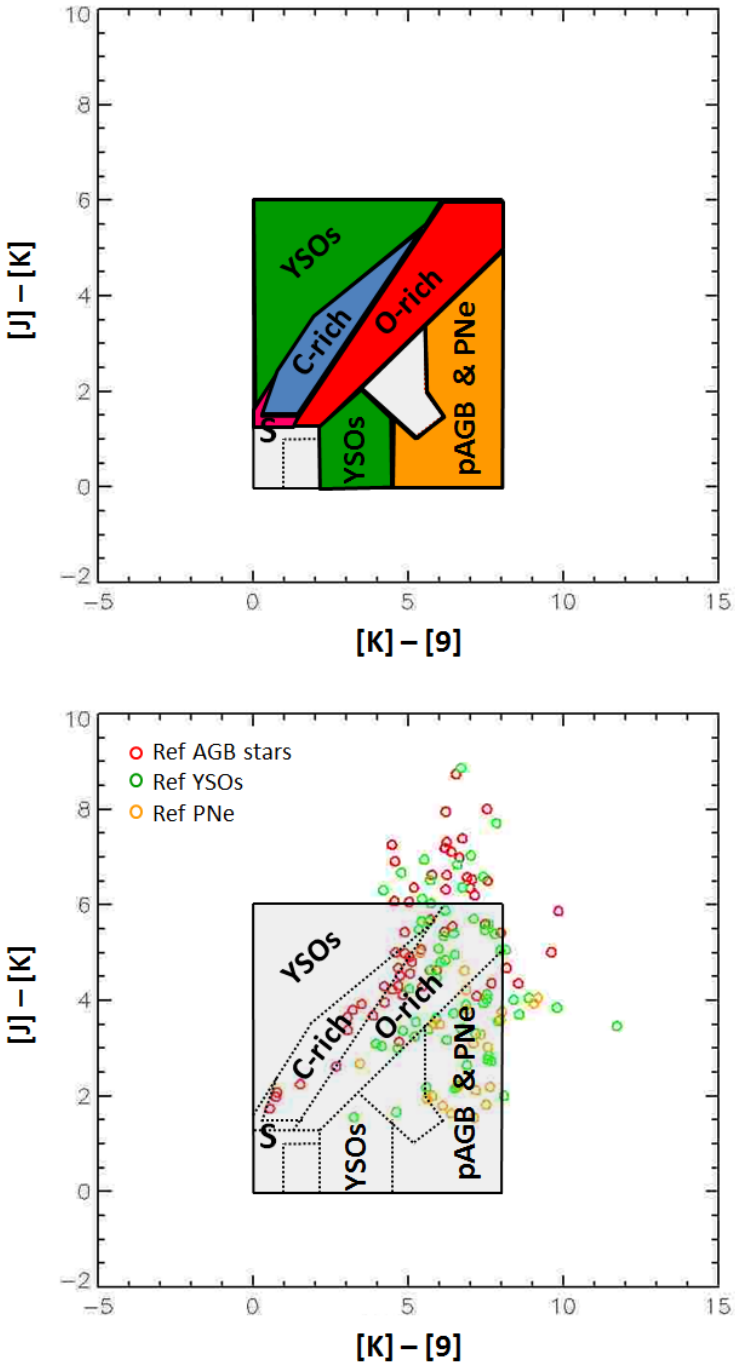

Figure 5.19: Shown in the top panel is the [9] − [18] vs. [K] − [9] colour-colour diagram that Ishihara et al. (2011) used to define the five regions indicated in the diagram: (i) C-rich AGB stars (in blue), (ii) O-rich AGB stars (in red), (iii) S-stars (in purple), (iv) YSOs (in green) and (v) post-AGB stars and PNe (in orange), within the colour-colour region used by Ishihara et al. (2011). Shown in the bottom panel are the colour-colour regions that our reference AGB stars (in red), YSOs (in green) and PNe (in yellow) occupy in the colour-colour diagram shown in the top panel.

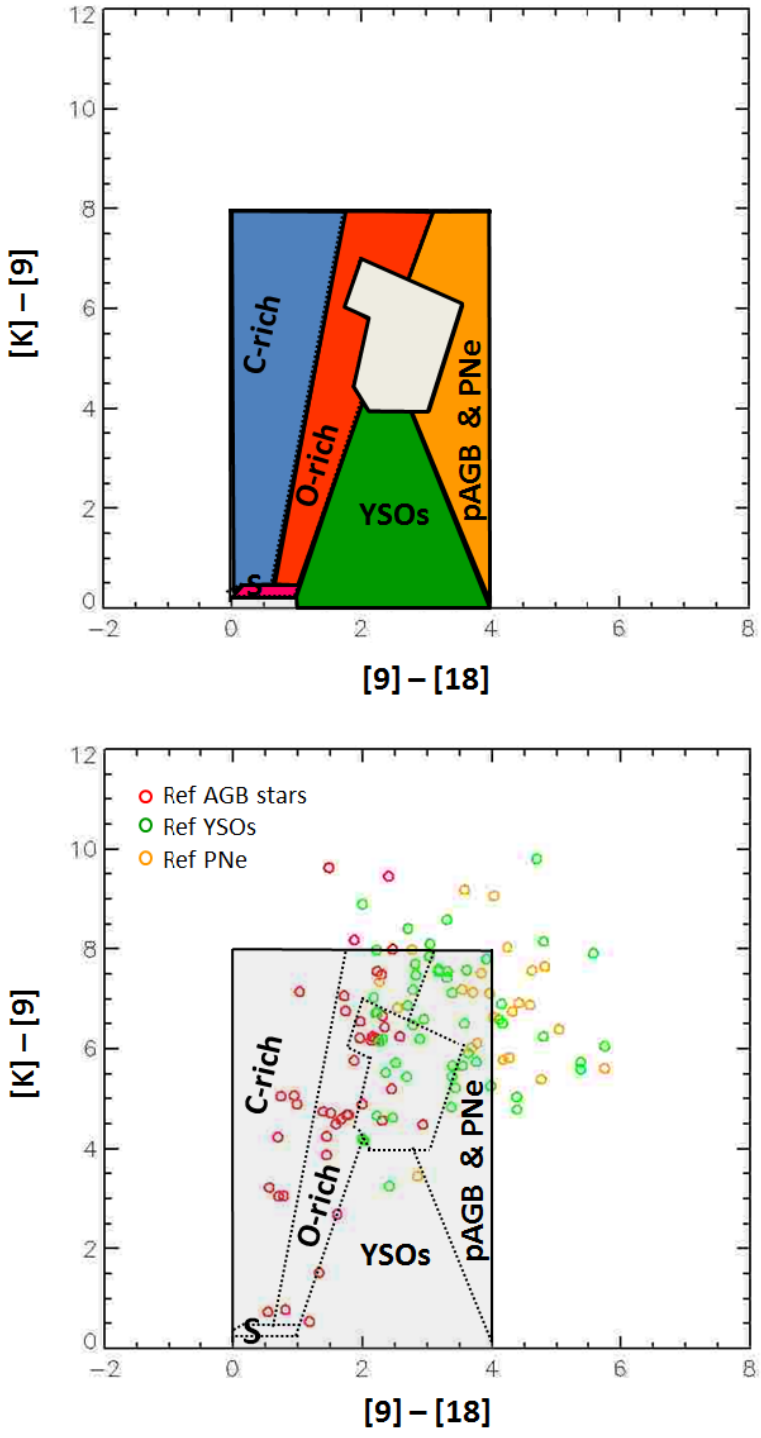

Figure 5.20: Shown in the top panel is the [9] − [18] vs. [J] − [K] colour-colour diagram that Ishihara et al. (2011) used to define the five regions indicated in the diagram: (i) C-rich AGB stars (in blue), (ii) O-rich AGB stars (in red), (iii) S-stars (in purple), (iv) YSOs (in green) and (v) post-AGB stars and PNe (in orange), within the colour-colour region used by Ishihara et al. (2011). Shown in the bottom panel are the colour-colour regions that our reference AGB stars (in red), YSOs (in green) and PNe (in yellow) occupy in the colour-colour diagram shown in the top panel.

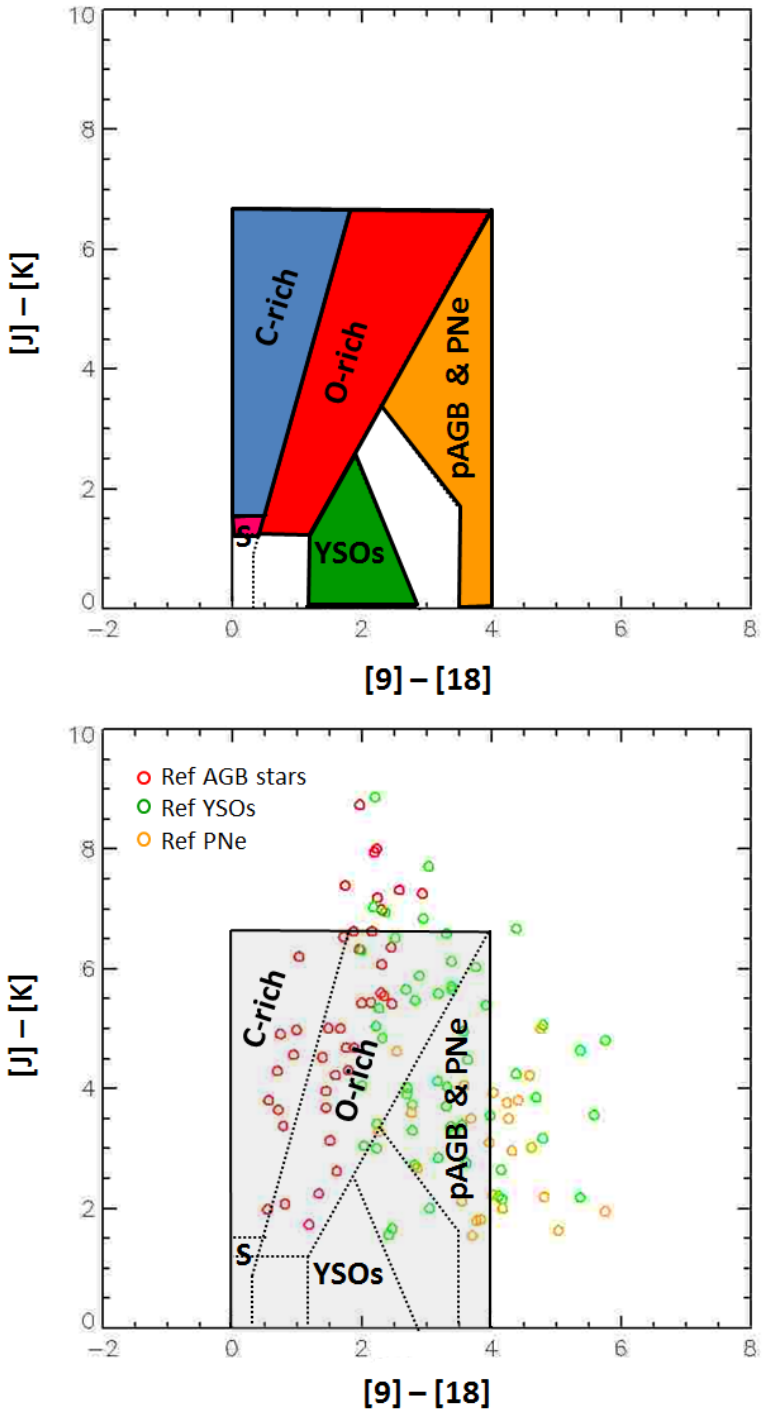

Figure 5.21: Shown below are the colour distributions of our reference PNe (in orange) and HII regions (in blue). Indicated with a grey dashed line are the colour cuts that Anderson et al. (2012b) found to best discriminate between a sample of 126 HII regions and 43 PNe (see Table 5.6).

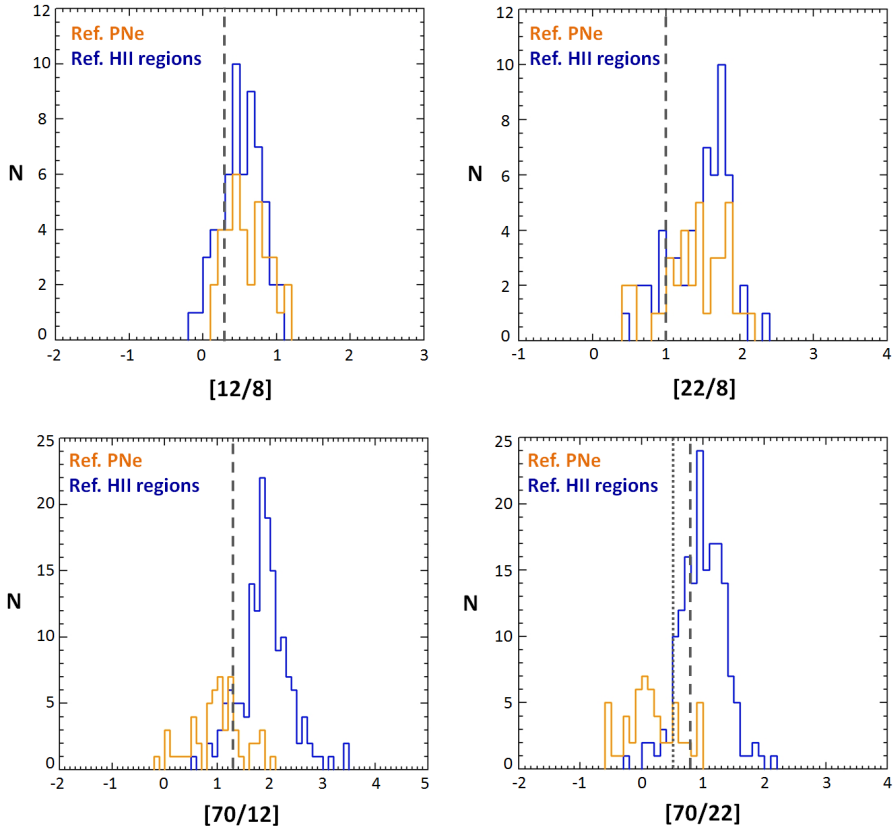

5.7 The Hi-GAL 1 PSC AGB catalogue

In Sect. 5.6.2 we found colour cuts to separate 95 reference AGB stars from 205, 178 and 59 reference YSOs, HII regions and PNe, respectively. The efficiency of these colour cuts was established by considering a sample containing the reference AGB stars and either the reference YSOs or the reference PNe or the reference HII regions. However, in a given catalogue, for instance, our Hi-GAL 1 PSC, the AGB stars are not only mixed with, say YSOs, but also with PNe and HII regions (plus other stellar types). Therefore, to establish how efficient the previous colour cuts would be in selecting AGB stars from the Hi-GAL 1 PSC, we had to consider a sample containing all the reference AGB stars, HII regions, YSOs and PNe. Each colour cut was then applied to the sample and from those sources satisfying the colour cut (n_{Total}) we established how many of them were AGB stars ($n_{AGBstars}$), YSOs (n_{YSOs}), PNe (n_{PNe}) and HII regions (n_{HII}) (see Table 5.7).

Table 5.7: Number of reference AGB stars, YSOs, PNe and HII regions that verify the colour cuts in Table 5.5.

Colour Cut	$n_{AGBstars}$	n_{YSOs}	n_{PNe}	n_{HII}	n_{Total}
$[70/4.6] < -0.1$	71	0	0	0	71
$[70/12] < -0.1$	84	1	0	0	85
$[70/1.65] < 3.5$	95	158	50	10	313
$[70/2.17] < 2.6$	95	192	54	3	344
$[70/4.6] < 0.5$	81	0	0	0	81
$[70/12] < 0.1$	89	1	0	0	90
$[70/22] < -0.2$	85	1	1	0	87
$[70/12] < 0$	87	1	0	0	88

Here, we can see that: (i) the verification rate of the $[70/4.6] < 0.5$, $[70/12] < 0.1$ and $[70/22] < -0.2$ colour cuts is greater than that of the $[70/4.6] < -0.1$, $[70/12] < -0.1$ and $[70/12] < 0$ colour cuts and that (ii) the total[1] contamination rate of the $[70/1.65] < 3.5$ and $[70/2.17] < 2.6$ colour cuts is much greater than that of the other colour cuts - for which the total contamination rate ranges from 0 to 2 sources. As a result, the $[70/4.6] < 0.5$, $[70/12] < 0.1$ and $[70/22] < -0.2$ colour cuts provide a more reliable AGB classification than the rest.

[1] i.e. counting the YSOs, PNe and HII regions found all together.

Table 5.8: Final selection of colour cuts used to separate AGB stars in the Hi-GAL 1 PSC.

Selected colour cuts		
$[70/4.6] < 0.5$	$[70/12] < 0.1$	$[70/22] < -0.2$

In light of these results, it was decided that all the Hi-GAL 1 PSC sources satisfying any of the colour cuts listed in Table 5.8 would be considered as AGB star candidates. The more colour cuts a source satisfied, the more reliable its classification will be. Listed in Table 5.9 are the number of Hi-GAL 1 PSC sources verifying the $[70/4.6] < 0.5$, $[70/12] < 0.1$ and $[70/22] < -0.2$ colour cuts and the number of sources verifying 1, 2 or all 3 colour cuts.

Table 5.9: Number of Hi-GAL 1 PSC sources verifying the colour cuts in Table 5.8

Colour Cut	**n(Hi-GAL 1 PSC sources)**
$[70/4.6] < 0.5$	4,607
$[70/12] < 0.1$	4,510
$[70/22] < -0.2$	4,489
One colour cut	4,928
Two colour cuts	4,511
Three colour cuts	4,167

From the results in Table 5.9 we can see that the colour cuts from Table 5.8 classified a total of 4,928 sources as Hi-GAL 1 PSC AGB star candidates. Included amongst these sources were 46, 1 and 11 reference YSOs, HII regions and PNe that the colour cuts mis-classified as AGB stars. These sources were manually rejected from the AGB star candidate sample. The few reference AGB stars that the colour cuts mis-classified as non-AGB stars (12 sources) were also manually re-injected to the AGB candidate sample. The new sample of 4,882 sources was then carefully inspected in order to ensure that all the Hi-GAL 1 PSC AGB star candidates were point-like AGB stars. We first examined the sources' size and established a criteria to identify and reject extended sources. We then inspected the sources' SED and discarded those sources that had SEDs with a shape atypical for an AGB star. Finally, we cross-matched our sample with the SIMBAD database and rejected those sources classified in SIMBAD as non-AGB stellar types. A detailed description of the processes listed above is given in the following sections 5.7.1-5.7.3 and the final Hi-GAL 1 PSC AGB catalogue is presented in Sect. 5.7.4.

5.7.1 Source size restrictions

In this section we inspect the sizes and images of the 4,882 Hi-GAL 1 PSC AGB star candidates in order to establish a criteria that allows us to identify and reject any Hi-GAL 1 PSC AGB star candidate that does not appear as point source.

Shown in Fig. 5.22 is the distribution of the ratio (FWHM_{ratio}) between the sources' major axis FWHM (FWHM_{Major}) and minor axis FWHM (FWHM_{Minor}) whose value was taken as the major and minor value between the CUTEX output FWHM_X and FWHM_Y variables (see Sect. 3.3.2.2). The figure shows the sources' FWHM_{ratio} as measured in the Herschel 70 μm band. From all the Herschel bands, the 70 μm band has the smaller beam size and therefore, the resolution of the sources' images will be greater and so will be the accuracy of the FWHM_{Major} and FWHM_{Minor} parameters. Moreover, for the 70 μm band there is a greater amount of data available. From Fig. 5.22, we can see that: (i) the majority of the sources (81%) verify that $\mathrm{FWHM}_{ratio} \leq 1.3$, (ii) a small percentage (12%) satisfy that $1.3 < \mathrm{FWHM}_{ratio} < 1.5$ and (iii) only a few sources (7%) have $\mathrm{FWHM}_{ratio} \geq 1.5$.

Figure 5.22: Distribution of the ratio between the Hi-GAL 1 PSC AGB star candidates' 70 μm major axis FWHM (FWHM_{Major}) and minor axis FWHM (FWHM_{Minor}).

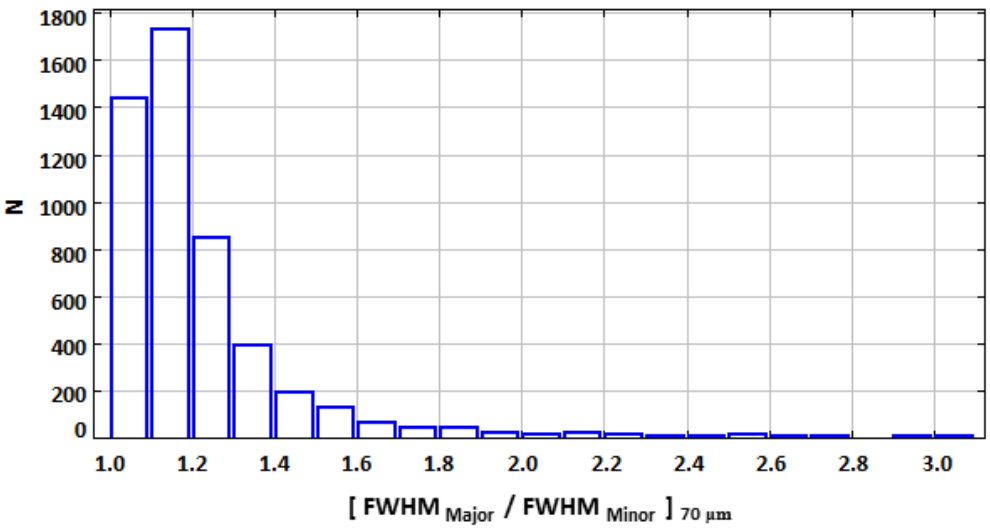

Shown in Fig. 5.23 are the images of a set of Hi-GAL 1 PSC AGB star candidates for which $\mathrm{FWHM}_{ratio} = (1.0, 1.1, 1.2, 1.3, 1.4, 1.5)$. Here, we can see that:

(i) sources with $\mathrm{FWHM}_{ratio} = (1.0, 1.1, 1.2)$ are essentially point-like,

(ii) sources with $\mathrm{FWHM}_{ratio} = 1.3$ are only slightly elliptical and

(iii) sources with $\mathrm{FWHM}_{ratio} = (1.4, 1.5)$ are clearly extended.

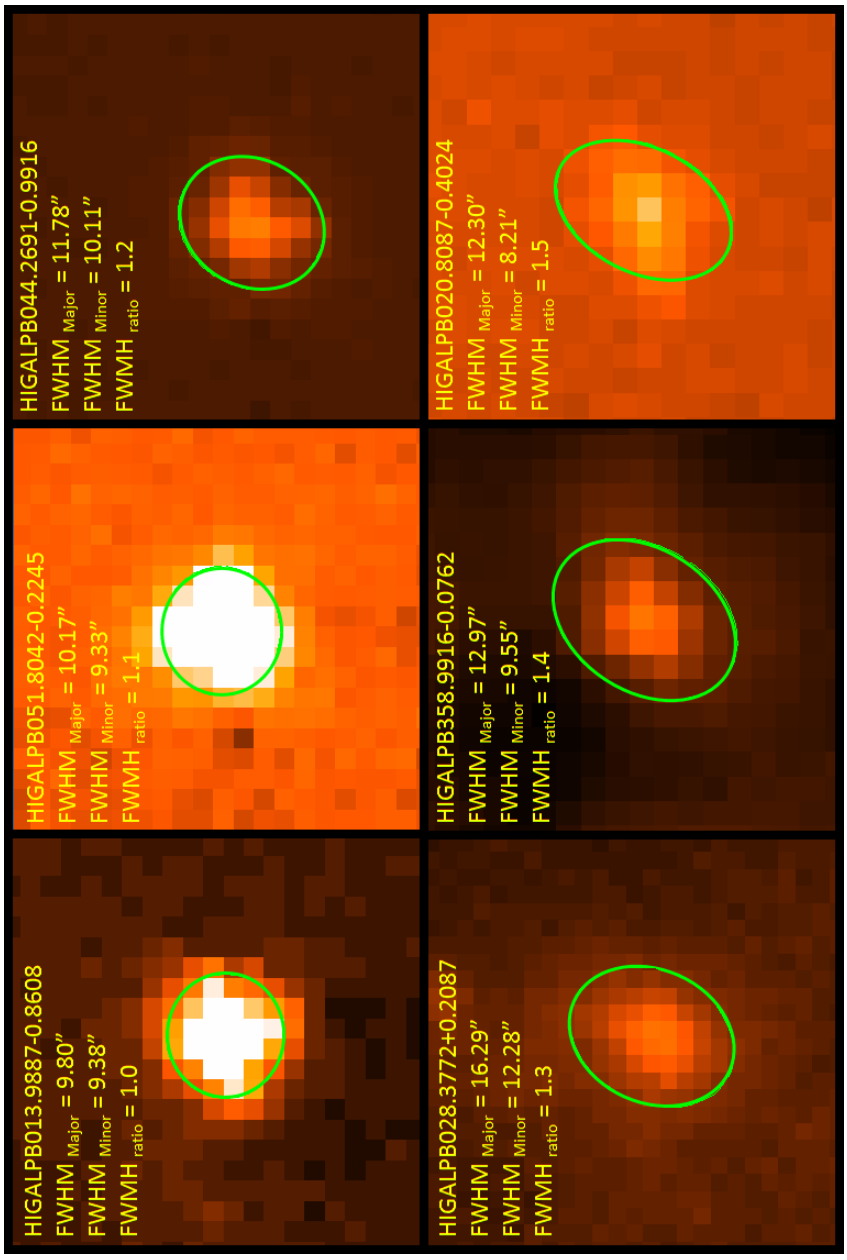

Figure 5.23: The images below show a series of Hi-GAL 1 PSC AGB star candidates for which the ratio between the candidates' 70 μm major axis FWHM ($FWHM_{Major}$) and minor axis FWHM ($FWHM_{Minor}$) is $\mathrm{FWHM}_{ratio} = (1.0, 1.1, 1.2, 1.3, 1.4, 1.5)$.

In light of the results presented in Fig. 5.22 and 5.23, we decided to eliminate all those sources that verify that $\mathrm{FWHM}_{ratio} > 1.3$ in order to ensure that no extended sources were included amongst the Hi-GAL 1 PSC AGB star candidates. This criteria was established taking into account that a more conservative limit such as $\mathrm{FWHM}_{ratio} > 1.2$ would result in the loss of 800 AGB star candidates which, as shown in Fig. 5.23 could be considered to be almost point-like. After applying the previous source size limit, the number of sources contained in the Hi-GAL 1 PSC AGB star candidate sample reduced from 4,882 sources to a total of 3,962 sources.

5.7.2 Source SED examination

Next, we examined the Spectral Energy Distributions (SEDs[2]) of the 3,962 Hi-GAL 1 PSC AGB star candidates in order to identify and reject those sources whose SED did not appear to be typical of an AGB. After visual inspection, the sources' SEDs were classified into one of the following groups:

- The *good* SEDs - This group included the SEDs that (i) had a shape typical of that of an AGB star and (ii) were well defined (see Fig. 5.24 for examples).
- The *bad* SEDs - This group included the SEDs that were confusing (see Fig. 5.24 for examples).
- The *ugly* SEDs - This group included the SEDs that might belong to: (i) blended sources and/or (ii) YSOs (class I/II) mis-classified as AGB stars (see Fig. 5.24 for examples).

  Blended sources can be identified for having an inverted "w"-shaped SED (complete or uncomplete) whereas YSOs (class I/II) can be identified for having two distinct SED components: one in the NIR that indicates the presence of a young hot star and another in the FIR that indicates the presence of a surrounding cold dust cloud/torus (see Sect. 1.5.4.5 for a detailed description of the YSO typical SEDs).

Those Hi-GAL 1 PSC AGB star candidates identified as having *bad* or *ugly* SEDs (575 sources) were then rejected from the sample, which reduced from 3,962 sources to a total of 3,385 sources.

[2]The SED of a source is a plot in which all the flux densities (F_{ν_i}) available for the source are plotted against the different wavelengths (λ_i) these measurements were taken at.

Figure 5.24: Examples of SEDs that were classified as *"good"*, *"bad"* and *"ugly"* SEDs

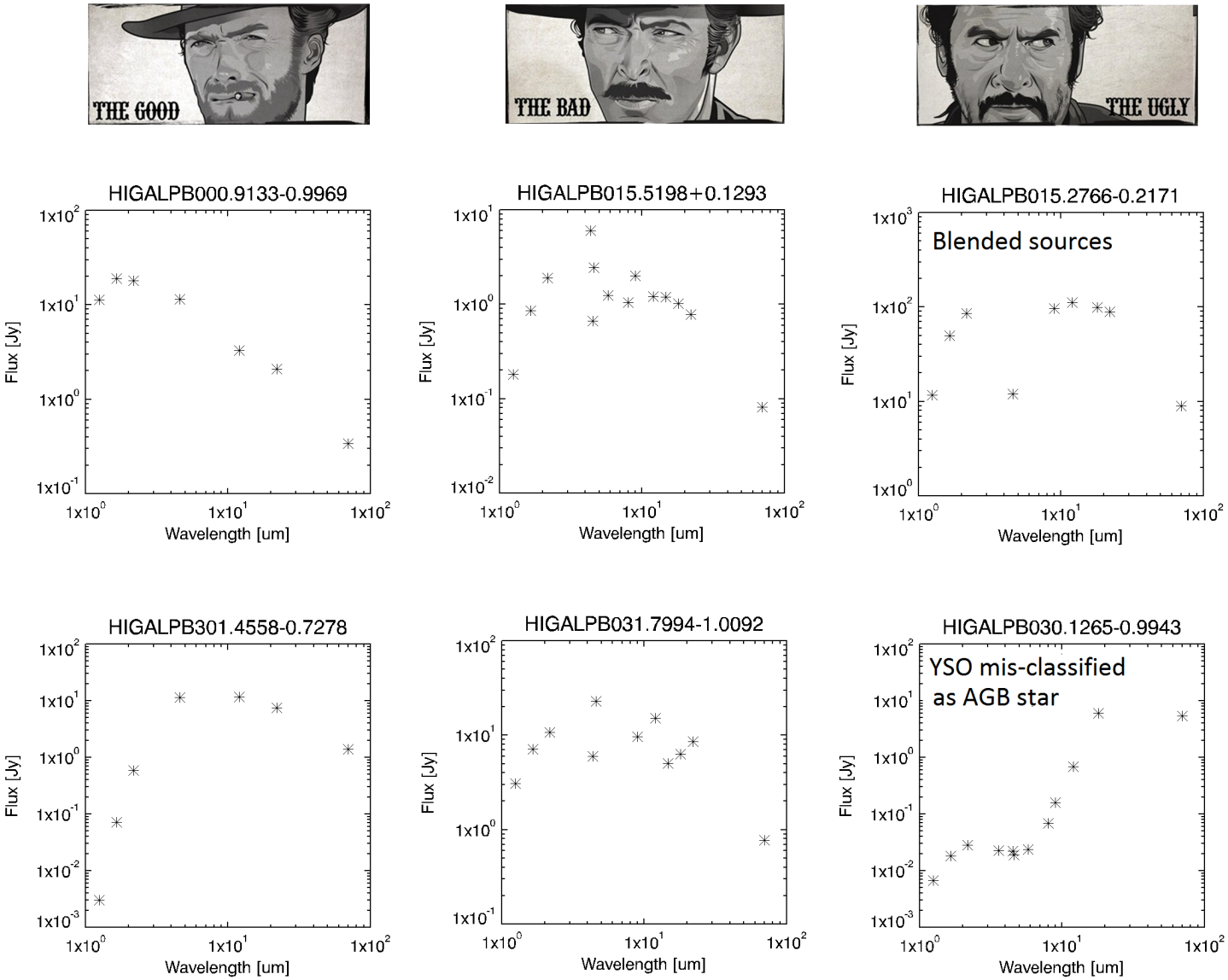

5.7.3 SIMBAD cross-match

Finally, we cross-matched the sample of 3,385 Hi-GAL 1 PSC AGB star candidates with the SIMBAD database in order to identify and reject those sources that are classified in SIMBAD as non-AGB stellar types. The cross-match between the two samples was done allowing a maximum angular separation of 1.7 arcsec in the cross-match and it returned a total of 1,668 matches. Shown in Table 5.10 and in Fig. 5.25 are a list and a colour-colour diagram with the different stellar classes found in SIMBAD for these 1,668 matches. Here, we can see that in the SIMBAD database:

- 103[3], 11[3] and 0 sources are classified as YSOs, PNe and HII regions.
- 224[3] sources are classified as AGB stars.
- 1,081 and 144 sources are classified as *Stars* and *IR sources*.
- 82 (23) sources are classified as other stellar types related (not related) to AGB stars.

Next, we proceeded to reject from the catalogue the 219 Hi-GAL 1 PSC AGB star candidates (7%) that were classified in SIMBAD as YSOs, PNe and stellar types related or not related to AGB stars. Prior to their removal we investigated what method was used to determine the sources' class in order to establish whether such method was robust enough to consider the sources' class as reliable. After inspection, we concluded that:

- The majority of YSOs (93%) were classified by Mottram et al. (2007) (82%, 84 sources) and Felli et al. (2002) (11%, 11 sources). On the one hand, the sources from Mottram et al. (2007) are part of a larger sample of 2,000 MYSO candidates from the MSX PSC that were colour-selected using the colour criteria established by Lumsden et al. (2002). The stellar class of these objects was then verified with a series of ground-based mid-IR follow-up observations that are part of the RMS survey and which allowed the removal of contaminant objects such as UCHII regions, PNe and evolved stars. On the other hand, the sources from Felli et al. (2002) are part of a larger sample of 715 YSO candidates from the ISOGAL PSC, which were selected with the $[15] \leq 4.5$, $[7]-[15] \geq 1.8$ colour criteria. This criteria were established by Felli et al. (2002) using ISOGAL observations and VLA radio continuum observations and allow the separation between the bright YSOs and Post-MS stars detected with ISOCAM.

[3]These values include also sources classified as candidates.

- The stellar class of the PNe was determined by a series of different methods. These include the use of: (i) AAO/UKST Hα-survey spectroscopic observations (Miszalski et al. 2008), (ii) HRDS (Miszalski et al. 2008), VLA and RMS survey observations (Urquhart et al. 2009), (iii) hydrogen radio recombination line emission (Anderson et al. 2011, Anderson et al. 2012a), (iv) CO emission (Urquhart et al. 2007b) and (v) radio continuum emission (Urquhart et al. 2007a).

- For the majority of the sources classified as other stellar types related and not related to AGB stars, we found that although these sources have different bibliographic references assigned, it is not possible to retrieve the name of the publication where the sources' stellar class was taken from.

The previous findings established that the methods used for the identification of the YSOs and PNe were robust and that the sources' stellar class was reliable enough to proceed with the elimination process of these sources. In the case of the sources classified as other stellar types related and not related to AGB stars, since it was not possible to verify the sources' identification methods, we decided to eliminate them as a precaution.

5.7.4 Final catalogue

The resulting catalogue contains a total of 3,166 sources and constitutes our catalogue of Hi-GAL 1 PSC AGB star candidates (see Fig. 5.26).
Included in the catalogue are:

- The sources' identification (*ID*), the position (*RA*, *dec* and *l*, *b* in degrees), the fluxes (*F* in Jy), the flux uncertainties (*EF* in Jy), the Signal-to-Noise (S/N), the flux quality flag (q_Flux) and the most accurate position available for the source (*macc_RA*, *macc_dec* in degrees), as listed in the Hi-GAL 1 PSC.

- A label (*Ref_Source*) indicating whether the source has (Y) or has not (N) been used as a reference AGB star and the name of the catalogue (*Ref_Cat*) where the sources were selected from. Also included are a label (*Reliability*) indicating the number of colour cuts (1, 2 or 3) listed in Table 5.8 verified by the source and a label (*SIMBAD type*) indicating the sources' stellar type assigned in the SIMBAD database.

Because of its length, this catalogue is excluded from this thesis and included in the CD attached.

Table 5.10: Complete list of SIMBAD stellar types found for the 1,668 Hi-GAL 1 PSC sources.

AGB stars	
SIMBAD stellar type	**Number of sources**
AGB star	4
Candidate AGB star	83
OH/IR-star	59
Mira-star	22
C-star	40
S-star	8
Candidate S-star	8
Stellar types related to AGB stars	
SIMBAD stellar type	**Number of sources**
Red Super Giant star	7
Post-AGB star	7
Candidate Red Giant Branch star	1
Candidate Red Super Giant star	3
Variable star	21
Semi-regular Variable star	9
Pulsating Variable star	6
Irregular Variable star	1
Masers	27
YSOs	
SIMBAD stellar type	**Number of sources**
YSO	37
Candidate YSO	66
HII regions	
SIMBAD stellar type	**Number of sources**
HII region	0
PNe	
SIMBAD stellar type	**Number of sources**
PN	5
Candidate PN	6
Other stellar types	
SIMBAD stellar type	**Number of sources**
Star	1,081
IR source	144
Other	23

Figure 5.25: [70/4.6] vs. [70/12] colour-colour diagram showing the process in which SIMBAD identifications were used to further classify the Hi-GAL 1 PSC sources in AGB star candidates or non AGB star candidates. Panel (a) shows the Hi-GAL 1 PSC sources (in black), which were classified by SIMBAD as any type of AGB (in red), YSOs (in green), PNe (in magenta), Stars (in yellow), IR sources (in blue) and other stellar types related (in pink) or unrelated (in purple) to AGB stars. Panel (b) shows in detail the sources from each SIMBAD stellar type that were classified as AGB stars by the colour cuts (in magenta dashed line).

(a)

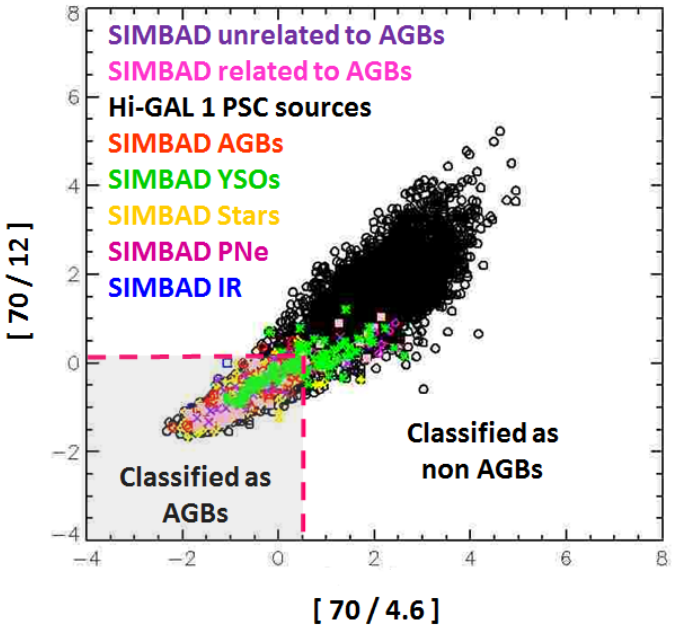

(b)

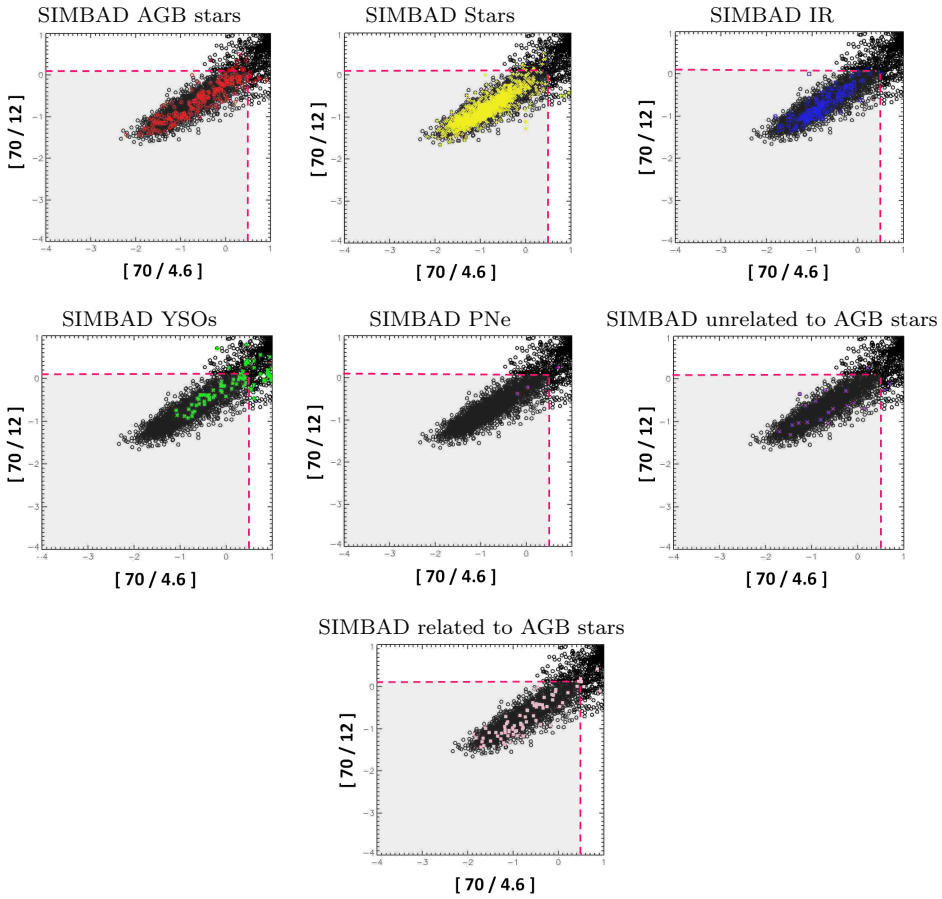

Figure 5.26: [70/4.6] vs. [70/12] colour-colour diagram showing the different types of AGB stars included in the final catalogue of Hi-GAL 1 PSC AGB star candidates. Panel (a) shows the complete sample of AGB star candidates (in grey) and the AGB star candidates that were classified by SIMBAD as: AGB stars (in red), AGB star candidates (in pink), S-stars (in dark green), S-star candidates (light green), OH/IR-stars (in blue), C-stars (in cyan), Mira-stars (in orange), Stars (in magenta) and IR sources (in purple). Panel (b) shows in detail the Hi-GAL 1 PSC AGB star candidates from each stellar type identified in SIMBAD.

(a)

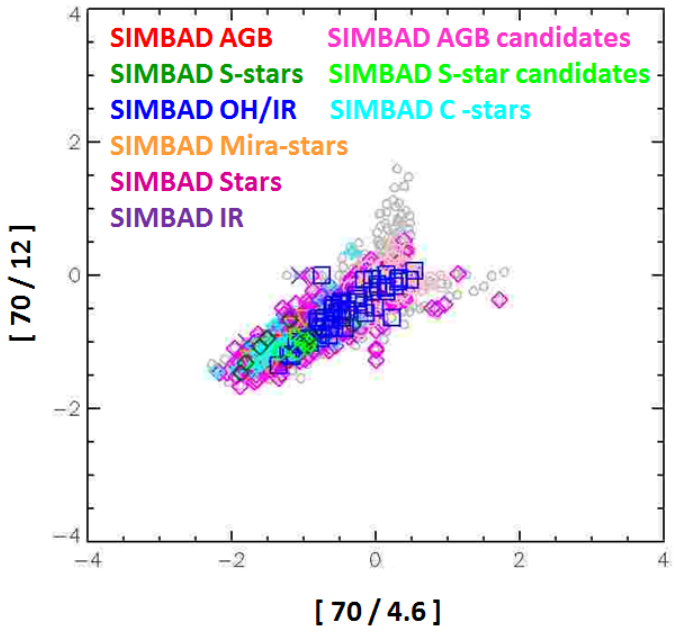

(b)

SIMBAD AGB stars and candidate AGB stars

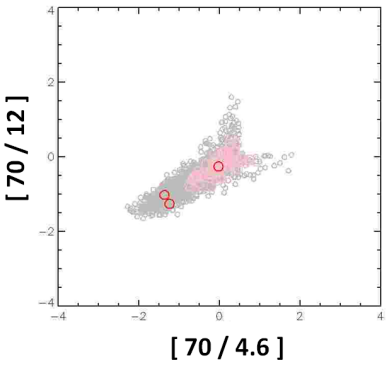

SIMBAD S-stars and candidate S-stars

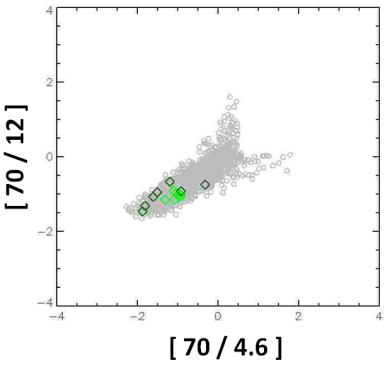

SIMBAD OH/IR, Mira and C-stars

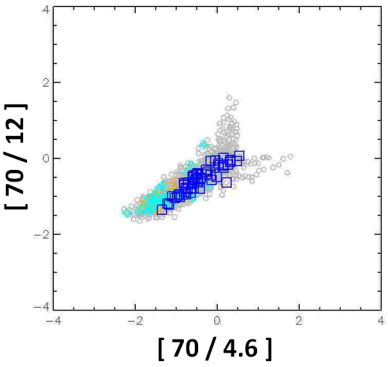

SIMBAD IR sources and Stars

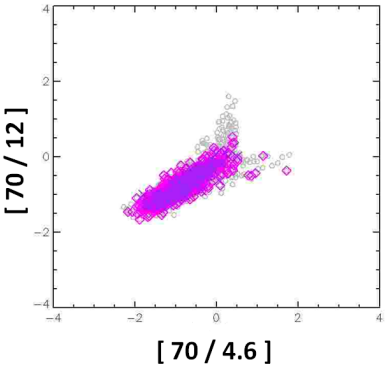

5.8 Population separation for the Hi-GAL 1 PSC AGB stars

Next, we compiled a reference sample of OH/IR-stars and C-stars in an attempt to derive colour cuts that enable us to separate these two stellar types.

5.8.1 Reference sample

Our reference sample was formed of a total of 157 Galactic sources: 101 OH/IR-stars (Oxygen-rich AGB stars) and 56 C-stars (Carbon-rich AGB stars). Included in the reference sample are 43 and 36 Hi-GAL 1 PSC AGB star candidates that were identified in SIMBAD as OH/IR and C-stars, respectively (see Table 5.10 in Sect. 5.7). Also included are a total of 58 OH/IR-stars and 20 C-stars that were extracted from the catalogues listed in Table 5.11 and 5.12.

From Table 5.11 we can see that 91% of our OH/IR-star sample is taken from Sevenster (2002) (56%, 32 sources) and Suh and Kwon (2011) (35%, 20 sources). On the one hand, the sources from Sevenster (2002) are part of a larger sample of 766 sources that includes Mira-stars, OH/IR-stars, post-AGB stars and PNe, which were found in a VLA/ATCA combined survey, in the 1612 MHz OH maser line, of the $5^\circ \leq l \leq 45^\circ$ and $|b| \leq 3^\circ$ Galactic plane region. On the other hand, the sources from Suh and Kwon (2011) are part of a larger sample of 2,193 O-rich stars, listed in the IRAS PSC, whose class was identified in previous works using different class identification methods. These methods included the use of: (i) IRAS Low Resolution Spectrograph and ISO Short Wavelength Spectrometer data, (ii) IRTS Near Infrared Spectrometer NIR data and (iii) radio OH and SiO maser data.

Moreover, from Table 5.12 we can see that 80% of our C-star sample is taken from Chen and Yang (2012) (16 sources). These sources are part of a larger sample of 974 Galactic IR C-stars collected from literature and identified by different methods. These methods included the use of: (i) IRAS Low Resolution Spectrograph and ISO Short Wavelength Spectrometer data, (ii) the SiC emission feature at 11.2 μm, (iii) $[K]-[L]$ vs. $[12]-[25]$ colour–colour diagrams, (iv) $[F12/F25] < 3$ and $[F25/F60] > 2.75$ colour cuts and (v) the $HCN + C_2H_2$ absorption feature at 3.1 μm.

Since the previous classification methods are robust, we established our reference sources' stellar class to be reliable.

Table 5.11: List of catalogues containing our reference OH/IR-stars.

OH/IR-star Reference Catalogues		
Catalogue name	**Author**	**n sources included**
OH-selected AGB and post-AGB objects. I.	Sevenster (2002)	32
Infrared two-colour diagrams for AGB stars	Suh and Kwon (2011)	20
The Red MSX Source Survey: massive protostars	Lumsden et al. (2013)	3
Mass-loss rates of Galactic AGB stars	Le Bertre et al. (2003a)	1
Radio Observations of OH/IR stars close to Galactic Center	Lindqvist et al. (1992)	1

Table 5.12: List of catalogues containing our reference C-stars.

C-star Reference Catalogues		
Catalogue name	**Author**	**n sources included**
A catalog of Galactic infrared carbon stars	Chen and Yang (2012)	16
Mass-loss rates of Galactic AGB stars	Le Bertre et al. (2003a)	3
General Catalog of Galactic Carbon Stars, 3d Ed.	Alksnis et al. (2001)	1

All the reference sources verified that they: (i) were included in our Hi-GAL 1 PSC AGB star catalogue, (ii) had q_Flux=2 or q_Flux=3 flux reliability flags (see Sect. 3.5.6) and (iii) had at least one counterpart in the Survey Catalogues (see Sect. 4.2).
The complete list of reference OH/IR and C-stars can be found in the CD accompanying this thesis. There are two tables, one for each stellar type, which include:

- The sources' identification (*ID*), the position (*RA*, *dec* and *l*, *b* in degrees), the fluxes (*F* in Jy), the flux uncertainties (*EF* in Jy), the Signal-to-Noise (S/N) and the flux quality flag (q_Flux), as listed in the Hi-GAL 1 PSC.
- The most accurate position available for the source (*macc_RA*, *macc_dec* in degrees), as listed in the Hi-GAL 1 PSC.
- The sources' stellar type (*Type*).
- The name of the catalogue (*Ref_Cat*) where the sources were selected from.

5.8.2 Colour cuts to separate OH/IR and C-stars

The previous reference sample was used to find colour cuts that separated the reference OH/IR-stars from the reference C-stars. In order to guarantee these colours to be reliable and efficient we only selected those colour cuts that: (i) were testable upon $\geq$ 70% of the reference sample and had (ii) the maximum verification rate and (iii) the minimum contamination rate (see Sect. 5.6.2).

Shown in Fig. 5.27 are the colour distributions and colour cuts that were found to verify the previous three conditions while Fig. 5.29 and 5.30 show the colour-colour diagrams involving such colours. Here, we can see how the suggested colour cuts provide a good separation between the reference OH/IR and C-stars. Shown in Fig. 5.28 are some examples of colours cuts that were only testable upon <70% of the reference sample. Despite being efficient, these latter colour cuts are less reliable than those in Table 5.13 and therefore, they were not included in our final selection of colour cuts.

Listed in Table 5.13 and 5.14 are our suggested colour cuts for the previous colour distributions together with: (i) the percentage and number of sources that satisfy such colour cuts and (ii) the fraction of the total reference sample upon which the colour cuts were tested.

From Table 5.13 and 5.14 we can see that all the colour cuts found to most efficiently separate the OH/IR-stars from the C-stars involve wavelengths around 10 μm and 20 μm. We can also see that the two colour cuts involving the Herschel 70 μm are the least efficient. These results can be explained by the fact that the MSX 8.28 μm band, the AKARI 9 μm and 18 μm bands and the WISE 12 μm and 22 μm bands cover the silicate features that O-rich AGB stars present around 10 μm and 20 μm and the carbonaceous features that C-rich AGB stars present around 11 μm. Hence, these bands are highly effective in distinguishing C-stars (Carbon-rich AGB stars) from OH/IR-stars (Oxygen-rich AGB stars).

Figure 5.27: Colour distributions in which we can separate the reference OH/IR-stars (in green) from the reference C-stars (in orange). Indicated in grey are the colour cuts suggested.

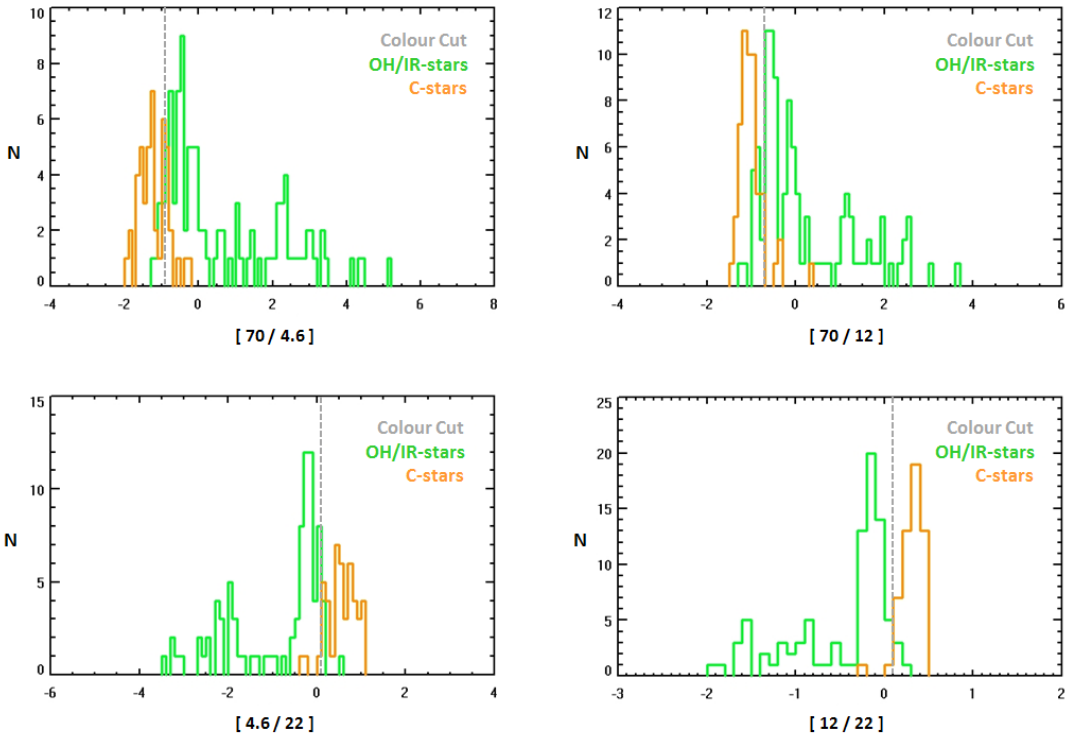

Table 5.13: Colour cuts that separate the reference OH/IR-stars from the reference C-stars.

Colour Cut	**%(OH/IR-stars)**	**%(C-stars)**	**Sample OH/IR-stars**		**Sample C-stars**	
			#	%	#	%
$[70/4.6] > -0.8$	88	11	93	92	46	82
$[70/12] > -0.7$	86	7	97	96	54	96
$[4.6/22] < 0.1$	94	7	87	77	46	82
$[12/22] < 0.1$	96	4	89	79	54	96

Figure 5.28: Other interesting flux distributions. The reference OH/IR and C-stars are indicated in green and orange respectively while the colour cuts suggested are indicated in grey.

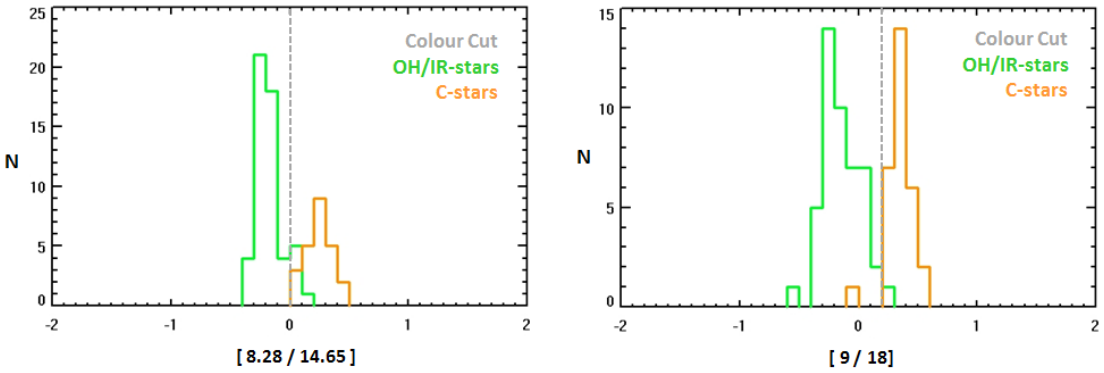

Table 5.14: The colour cuts listed below were also found to successfully separate the reference OH/IR-stars from the reference C-stars but they are less reliable than those listed in Table 5.13 because they were only testable upon <70% of the reference sample.

Colour Cut	**%(OH/IR-stars)**	**%(C-stars)**	**Sample OH/IR-stars**		**Sample C-stars**	
			#	%	#	%
$[8.28/14.65] < 0$	89	4	53	53	24	43
$[9/18] < 0.2$	98	3	47	47	30	54

Figure 5.29: Colour-colour diagrams in which we can separate the reference OH/IR-stars (in green) from the reference C-stars (in orange). Indicated in grey are the colour cuts suggested.

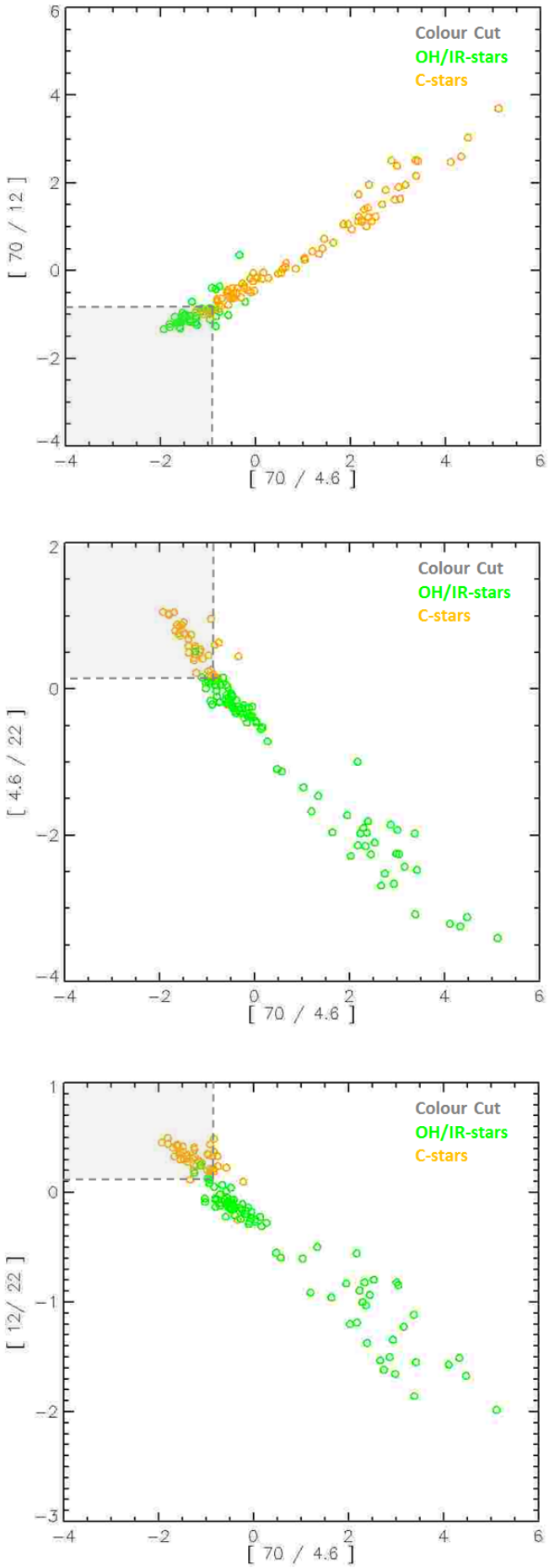

Figure 5.30: Additional colour-colour diagrams in which we can separate the reference OH/IR-stars (in green) from the reference C-stars (in orange). Indicated in grey are the colour cuts suggested.

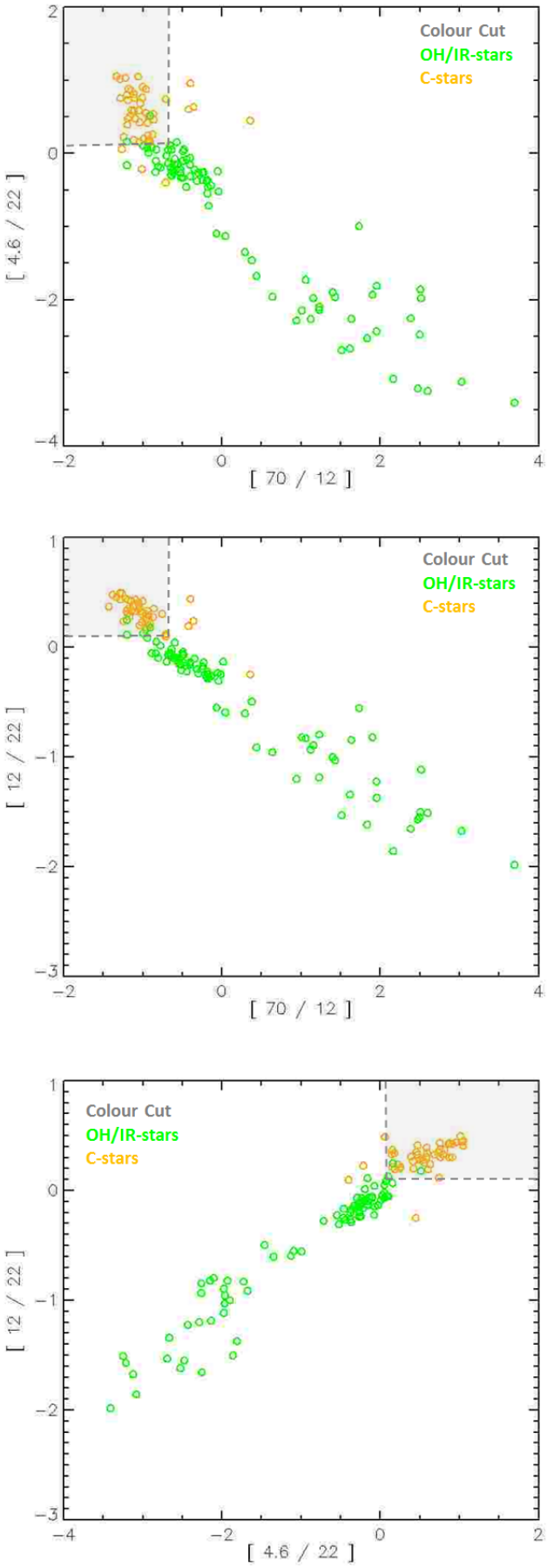

5.8.2.1 Revision of the colour cuts derived in previous studies

In this section, we determine whether our reference 101 OH/IR-stars (Oxygen-rich AGB stars) and 56 C-stars (Carbon-rich AGB stars) verify the colour cuts presented by Ita et al. (2010) and Ishihara et al. (2011) (see Sect. 5.5).

- Ita et al. (2010)

  Shown in the top panel of Fig. 5.31 is the $[9]-[18]$ vs. $[J]-[18]$ colour-colour diagram that Ita et al. (2010) used to define the three regions indicated in the diagram: (i) C-stars, (ii) YSOs and OH/IR-stars and (iii) PNe. Shown in the bottom panel of Fig. 5.31 are the colour-colour regions that our reference OH/IR and C-stars occupy in the previous colour-colour diagram. Here, we can see that: (i) the majority (93%) of our reference C-stars lie within the C-stars regions and (ii) there is a large amount of reference OH/IR-stars (42%) that do not verify Ita's OH/IR-star colour cuts. Thus, the colour cuts defined by Ita et al. (2010) provide a good separation only to our reference C-stars.

- Ishihara et al. (2011)

  Shown in the top panel of Fig. 5.32, 5.33 and 5.34 are the $[K]-[9]$ vs. $[J]-[K]$, $[9]-[18]$ vs. $[K]-[9]$ and $[9]-[18]$ vs. $[J]-[K]$ colour-colour diagrams that Ishihara et al. (2011) used to define the five regions indicated in the diagrams: (i) C-rich AGB stars, (ii) O-rich AGB stars, (iii) S-stars, (iv) YSOs and (v) PNe and post-AGB stars. Shown in the bottom panels of Fig. 5.32, 5.33 and 5.34 are the colour-colour regions that our reference OH/IR and C-stars occupy in the previous colour-colour diagrams. Here, we can see that in the $[K]-[9]$ vs. $[J]-[K]$, $[9]-[18]$ vs. $[K]-[9]$ and $[9]-[18]$ vs. $[J]-[K]$ colour-colour diagrams: (i) the majority (79%, 93% and 90%) of our reference C-stars lie within the C-stars region and (ii) there is a considerable amount of reference OH/IR-stars (53%, 47% and 35%) that do not verify Ishihara's OH/IR-star colour cuts. In light of these results, we concluded that the colour cuts defined by Ishihara et al. (2011) provide a good separation only to our reference C-stars.

The previous results establish that our colour criteria are different and more efficient on separating our reference OH/IR and C-stars than those established by Ita et al. (2010) and Ishihara et al. (2011) since their colour cuts are verified only by our reference C-stars.

Figure 5.31: Shown in the top panel is the [9] − [18] vs. [J] − [18] colour-colour diagram that Ita et al. (2010) used to define the three regions indicated in the diagram: (i) C-stars (in blue), (ii) OH/IR-stars (in red) and YSOs (in green) and (iii) PNe (in orange), within the colour-colour region used by Ita et al. 2010. Shown in the bottom panel are the colour-colour regions that our reference OH/IR-stars (in red) and C-stars (in blue) occupy in the colour-colour diagram shown in the top panel.

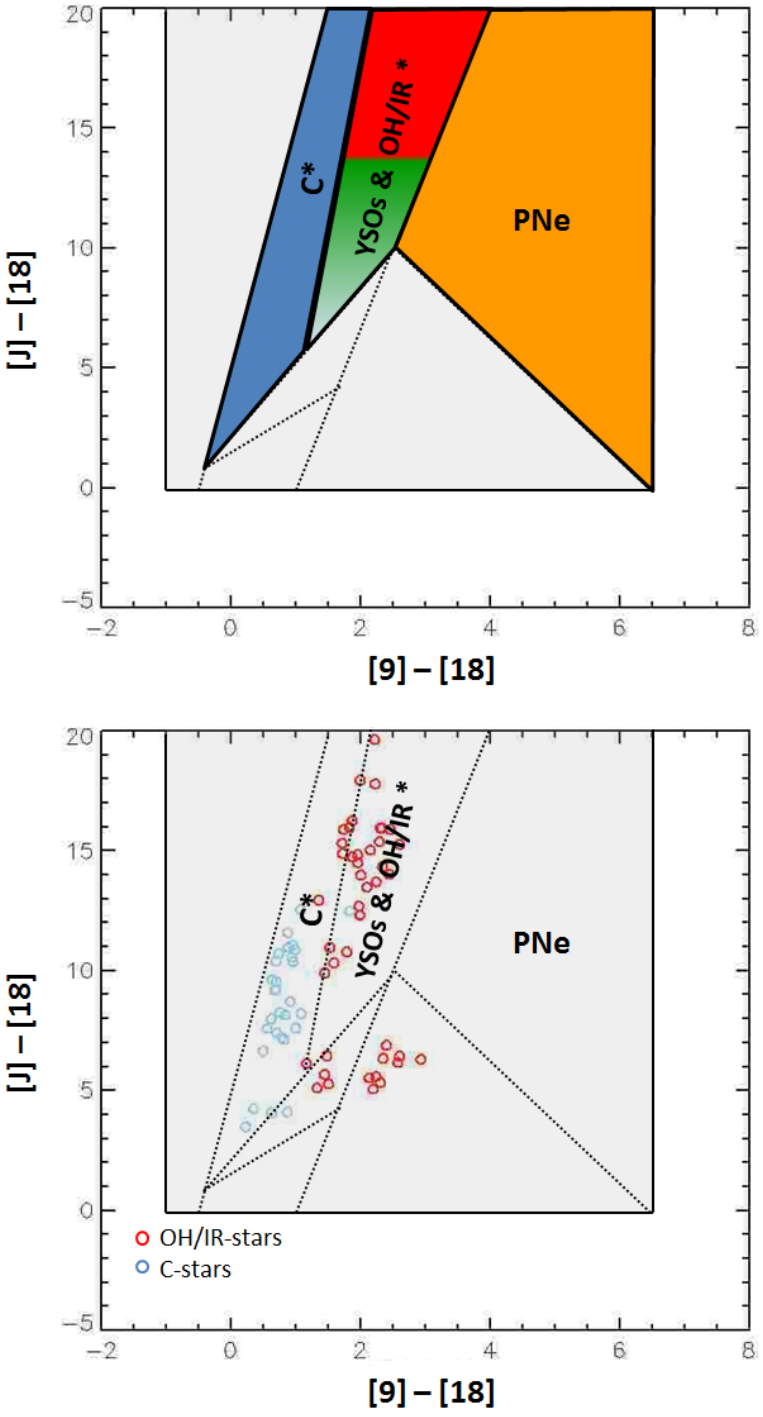

Figure 5.32: Shown in the top panel is the $[K] - [9]$ vs. $[J] - [K]$ colour-colour diagram that Ishihara et al. (2011) used to define the five regions indicated in the diagram: (i) C-rich AGB stars (in blue), (ii) O-rich AGB stars (in red), (iii) S-stars (in purple), (iv) YSOs (in green) and (v) PNe and post-AGB stars (in orange), within the colour-colour region used by Ishihara et al. (2011). Shown in the bottom panel are the colour-colour regions that our reference OH/IR-stars (in red) and C-stars (in blue) occupy in the colour-colour diagram shown in the top panel.

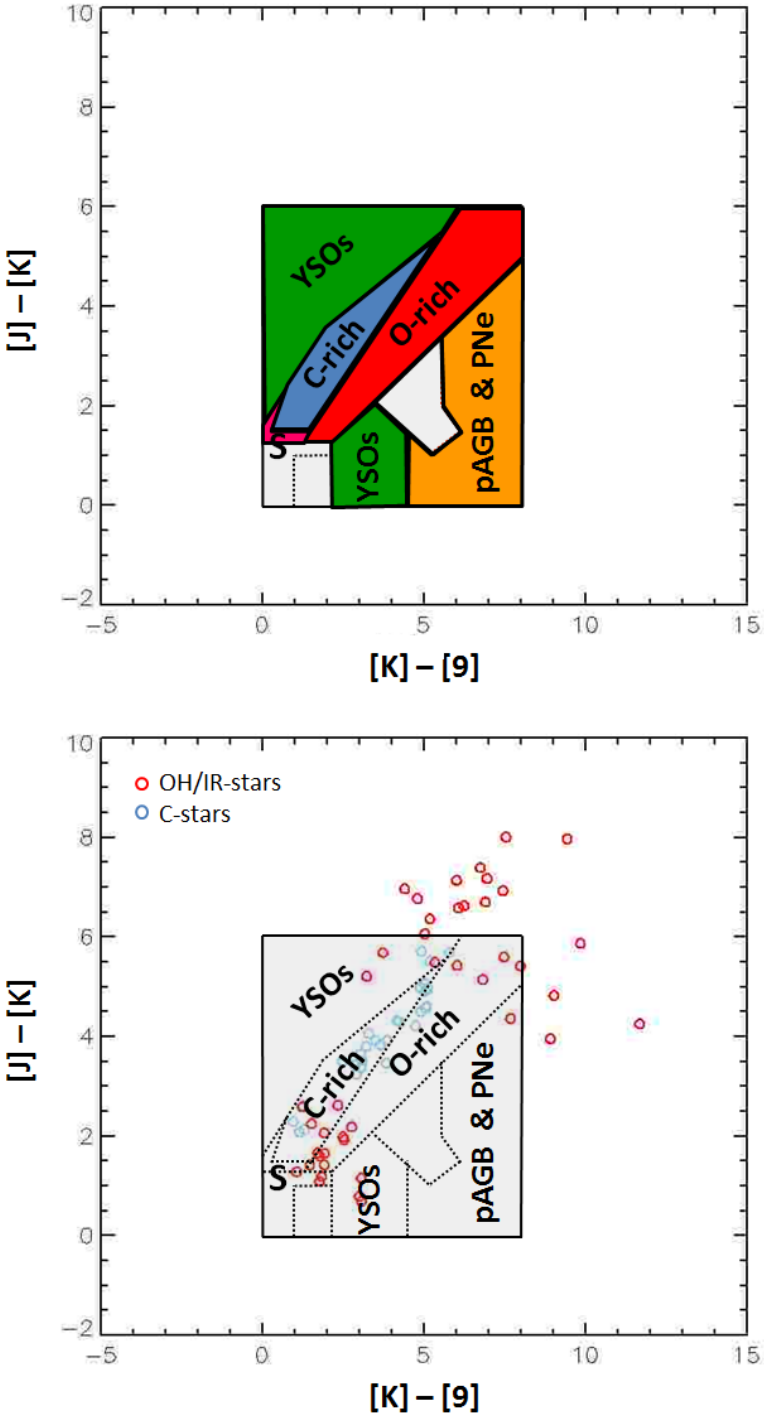

Figure 5.33: Shown in the top panel is the $[9]-[18]$ vs. $[K]-[9]$ colour-colour diagram that Ishihara et al. (2011) used to define the five regions indicated in the diagram: (i) C-rich AGB stars (in blue), (ii) O-rich AGB stars (in red), (iii) S-stars (in purple), (iv) YSOs (in green) and (v) PNe and post-AGB stars (in orange), within the colour-colour region used by Ishihara et al. (2011). Shown in the bottom panel are the colour-colour regions that our reference OH/IR-stars (in red) and C-stars (in blue) occupy in the colour-colour diagram shown in the top panel.

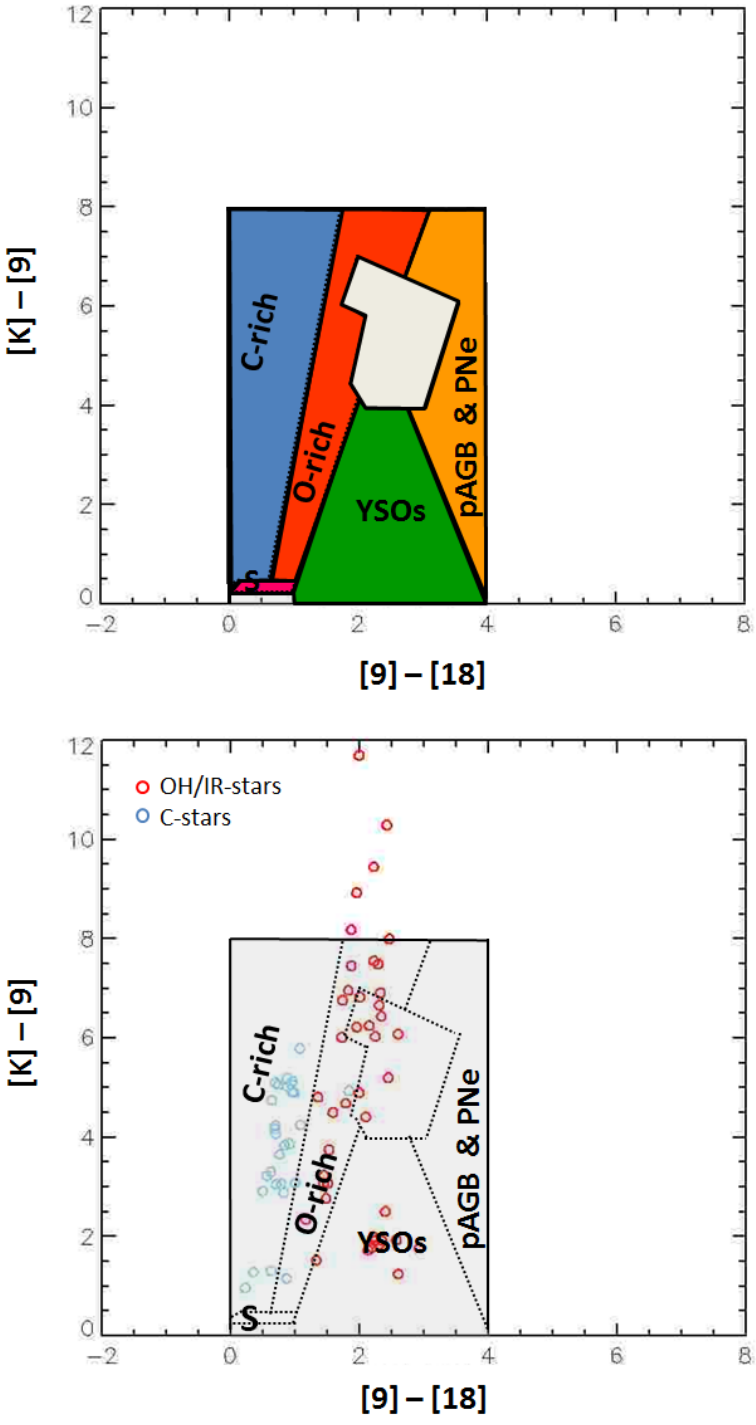

Figure 5.34: Shown in the top panel is the $[9]-[18]$ vs. $[J]-[K]$ colour-colour diagram that Ishihara et al. (2011) used to define the five regions indicated in the diagram: (i) C-rich AGB stars (in blue), (ii) O-rich AGB stars (in red), (iii) S-stars (in purple), (iv) YSOs (in green) and (v) PNe and post-AGB stars (in orange), within the colour-colour region used by Ishihara et al. (2011). Shown in the bottom panel are the colour-colour regions that our reference OH/IR-stars (in red) and C-stars (in blue) occupy in the colour-colour diagram shown in the top panel.

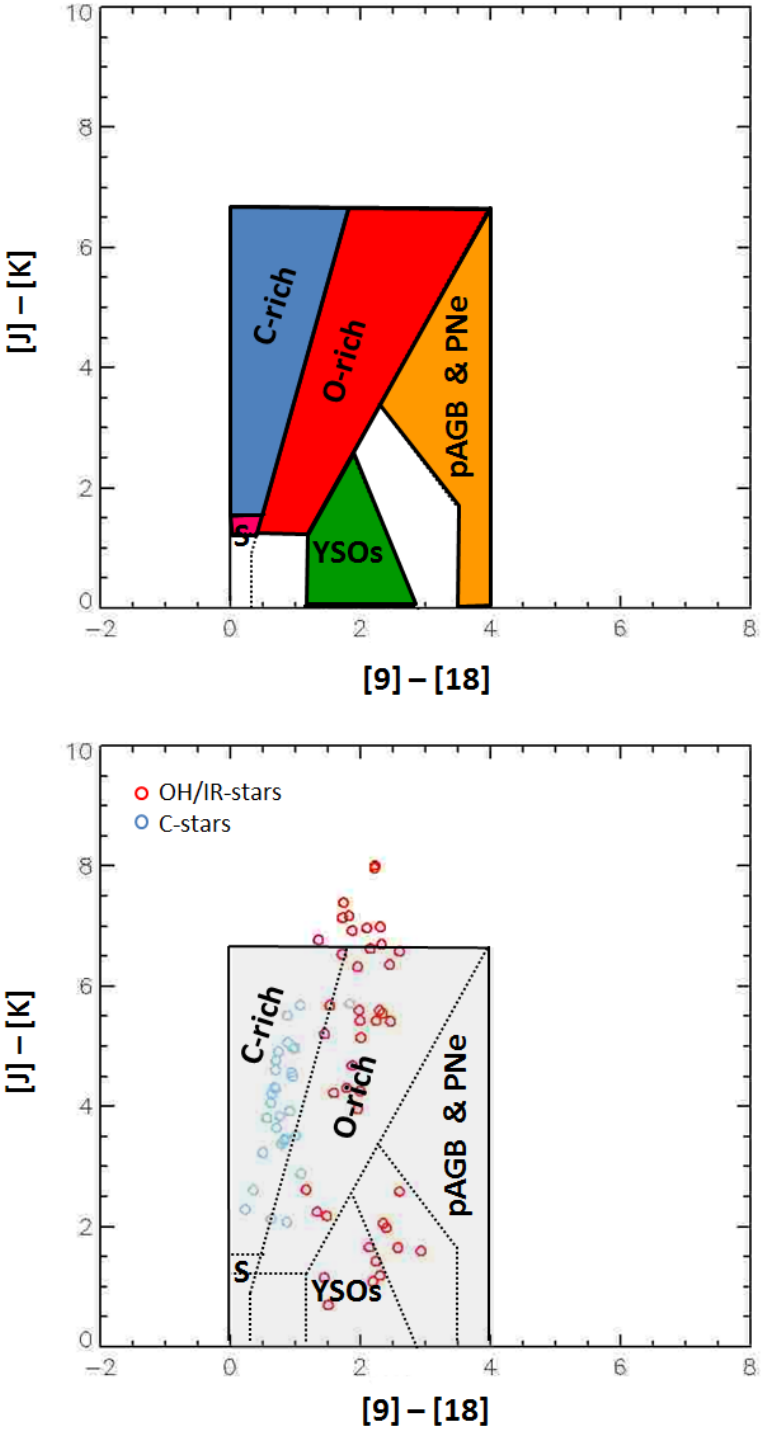

5.9 The Hi-GAL 1 PSC C-rich and O-rich AGB catalogues

From Table 5.13 we can see that of the four colour cuts that allowed us to separate the reference OH/IR-stars (O-rich AGB stars) from the reference C-stars (C-rich AGB stars), the $[4.6/22] < 0.1$ and $[12/22] < 0.1$ colour cuts have the maximum verification rates and the minimum contamination rates. In light of these results, it was decided that all the Hi-GAL 1 PSC AGB star candidates verifying both (none) of the colour cuts listed in Table 5.15 would be considered as O-rich (C-rich) AGB star candidates.

Table 5.15: Final selection of colour cuts used to classify the Hi-GAL 1 PSC AGB star candidates into C-rich and O-rich.

Selected colour cuts	
$[4.6/22] < 0.1$	$[12/22] < 0.1$

Listed in Table 5.16 are the number of Hi-GAL 1 PSC AGB star candidates verifying the $[4.6/22] < 0.1$ and $[12/22] < 0.1$ colour cuts as well as the number of sources verifying both and none of the colour cuts.

Table 5.16: Number of Hi-GAL 1 PSC AGB star candidates verifying the colour cuts in Table 5.15.

Colour Cut	**n(Hi-GAL 1 PSC AGB star candidates)**
$[4.6/22] < 0.1$	1,749
$[12/22] < 0.1$	2,132
Both	1,636
None	901

Here, we can see that the colour cuts from Table 5.15 classified 1,636 and 901 Hi-GAL 1 PSC AGB star candidates as being O-rich and C-rich, respectively. Included amongst the O-rich AGB star candidate sample were the few reference C-stars that the colour cuts mis-classified as O-rich. These sources were manually re-injected back to the C-rich AGB candidate sample. On the other hand, the few reference OH/IR-stars that the colour cuts mis-classified as non-O-rich were manually re-incorporated to the O-rich AGB star candidate sample. The previous operation was repeated for the case of the C-rich AGB star candidate sample. After the previous process, the final number of Hi-GAL PSC AGB star candidates classified as O-rich and C-rich was 1,652 and 917 sources, respectively.

Next, we visually inspected the SEDs of the 917 sources previously classified as C-rich in order to identify, (if existent), any O-rich AGB stars that were mis-classified as C-rich by the colour cuts in Table 5.15. O-rich AGB stars, as opposed to C-rich AGB stars, have a very distinctive silicate absorption feature at 10 μm and thus, they are easy to identify. After inspection, we concluded that a total of 76 sources were mis-classified by the colour cuts as C-rich despite having spectral features that identify them as O-rich AGB stars. These sources were excluded from the sample of C-rich AGB stars and added to the sample of O-rich AGB stars.

We then inspected the SEDs of the 1,652 sources previously classified as O-rich in order to identify, (if existent), any C-rich AGB stars that were mis-classified as O-rich by the colour cuts in Table 5.15. In this case, the mis-classification is due to the fact that some of the C-rich AGB star SEDs have two temperature components (see Sect. 6.6 in Chapter 6). This results on a decrease on the source flux that is misinterpreted as the absorption line characteristic from O-rich AGB stars. After inspection, we concluded that a total of 7 sources were mis-classified by the colour cuts as O-rich. These sources were excluded from the sample of O-rich AGB stars and added to the sample of C-rich AGB stars.

The final lists of 1,721 O-rich and 848 C-rich Hi-GAL 1 PSC AGB star candidates can be found in the CD accompanying this thesis. Included in these lists are:

- The sources' identification (*ID*), the position (*RA*, *dec* and *l*, *b* in degrees), the fluxes (*F* in Jy), the flux uncertainties (*EF* in Jy), the Signal-to-Noise (S/N) and the flux quality flag (q_Flux), as listed in the Hi-GAL 1 PSC.

- The most accurate position available for the source (*macc_RA*, *macc_dec* in degrees), as listed in the Hi-GAL 1 PSC.

- A label indicating if the source has been used as a reference C-star or OH/IR-star (*Ref_C-rich* / *Ref_O-rich*) or if instead, the source has been classified as a C or O-rich AGB star by our colour criteria (*C-rich* / *O-rich*).

Our catalogues of Hi-GAL 1 PSC O-rich and C-rich AGB star candidates are, to date, the largest catalogues of Galactic O-rich and C-rich AGB stars within the Hi-GAL 1 Galactic region. The most recent catalogues of Galactic C-rich and O-rich AGB stars are those of Suh and Kwon 2011, which include 3,003 O-rich AGB stars and 1,168 C-rich AGB stars detected by IRAS within the $b = (-85°, 86°)$ and $l = (0°, 360°)$ Galactic region.

However, if we only consider the Hi-GAL 1 region, i.e. $b = (-2°, 2°)$, $l = (0°, 68°)$ and $l = (289°, 360°)$, then the number of entries contained in the Suh catalogue reduces to 1,208 O-rich AGB stars and 187 C-rich AGB stars. Thus, in the Hi-GAL 1 Galactic region, our catalogues contain 513 more O-rich AGB stars and 661 more C-rich AGB stars than Suh's catalogues, i.e. our Hi-GAL 1 PSC O and C-rich AGB star catalogues contain 1.4 times as many O-rich AGB stars and 4.5 times as many C-rich AGB stars as the catalogues from Suh and Kwon (2009).

When considering the amount of C and O-rich AGB stars contained in our catalogue, one should also have in mind that, as we explained in Sect. 5.7, our catalogue of Hi-GAL 1 PSC AGB star candidates contains only those Hi-GAL 1 PSC sources satisfying any of the colour cuts listed in Table 5.8: $[70/4.6] < 0.5$, $[70/12] < 0.1$ and $[70/22] < -0.2$. From the total of 118,124 sources included in the Hi-GAL 1 PSC only 15,322 sources (∼13%) had fluxes available in the 70 μm, 4.6 μm, 12 μm and 22 μm bands. From these 15,322 sources, 3,166 sources (∼21%) were classified as AGB star candidates and from these 3,166 sources, a total of 1,721 sources (∼54%) were classified as O-rich AGB stars and 848 sources (∼27%) were classified as C-rich AGB stars. Thus, based on these percentages, we can estimate that if we had the photometric data corresponding to the 4.6 μm, 12 μm and 22 μm WISE bands for all the Hi-GAL 1 PSC sources, we would be able to detect up to ∼24,400 possible AGB stars from which ∼13,300 would be O-rich AGB stars and ∼6,500 would be C-rich AGB stars. That is ∼8 times the number of AGB star candidates, O-rich AGB stars and C-rich AGB stars currently contained in our catalogues. In the future, the source extraction of all Hi-GAL 1 catalogue sources from the WISE maps will allow us to expand the number of (C-rich and O-rich) AGB stars contained in our catalogues and to confirm the number of total entries here estimated as an upper limit.

5.9.1 Source distributions

Shown in Fig. 5.35 and 5.36 are the distributions of the Hi-GAL 1 PSC C and O-rich AGB stars and the ratio between the number of Hi-GAL 1 PSC C and O-rich AGB stars ($\frac{N_{C-rich}}{N_{O-rich}}$ ratio) along the Galactic plane region covered by the Hi-GAL 1 Survey.

From Fig. 5.35 we can see that, in the case of the Hi-GAL 1 PSC O-rich AGB stars, the number of detected stars increases towards the Galactic Centre.

In the case of the Hi-GAL 1 PSC C-rich AGB stars, we find that in the $b = [-1°, 1°]$, $l = [35°, 0°]$ and $l = (360°, 325°]$ Galactic regions, these stars are distributed evenly along the Galactic longitude and latitude. On the contrary, we detect an increase in the number of C-rich AGB stars in the $b = (-2°, -1°]$, $b = (2°, 1°]$, $l = (70°, 45°]$ and $l = (285°, 315°]$ Galactic regions.

Moreover, from Fig 5.36 we can see that, in general, the $\frac{N_{C-rich}}{N_{O-rich}}$ ratio increases with increasing galactocentric distance. As established by Wood (1981), Jura and Kleinmann (1990), Marigo et al. (1999) (and many other authors), the previous results can be attributed to the fact that the efficiency of the ^{12}C dredge-up and the formation of C-rich stars increases with decreasing metallicity. Given that the metallicity in our Galaxy decreases towards the Galactic outer parts, the number of C-rich stars present in our Galaxy decreases towards the Galactic Centre whereas the number of O-rich stars increases inwardly. As a result, the $\frac{N_{C-rich}}{N_{O-rich}}$ ratio increases outwardly.

5.9.2 Catalogue reliability

Based on the results obtained in Sect. 5.7 and 5.9 we estimate:

- $\leqslant$87% of the sources contained in the catalogue of Hi-GAL 1 PSC AGB star candidates to be possible AGB stars[4].
- $\geqslant$54% and $\geqslant$27% of the sources contained in the catalogue of Hi-GAL 1 PSC AGB star candidates to be O-rich and C-rich, respectively.
- $\leqslant$5% of the sources contained in the catalogue of Hi-GAL 1 PSC AGB star candidates to be evolved stars related to AGB stars and $\sim$8% to be to be either PNe, HII regions, YSOs or any other stellar types not related to AGB stars.

As a result, we estimate the reliability of our catalogue to be of order $\sim$87%.

[4]This percentage is obtained considering SIMBAD's identified AGB stars, Mira-, C-, S- and OH/IR-stars, Stars and IR sources as valid candidates.

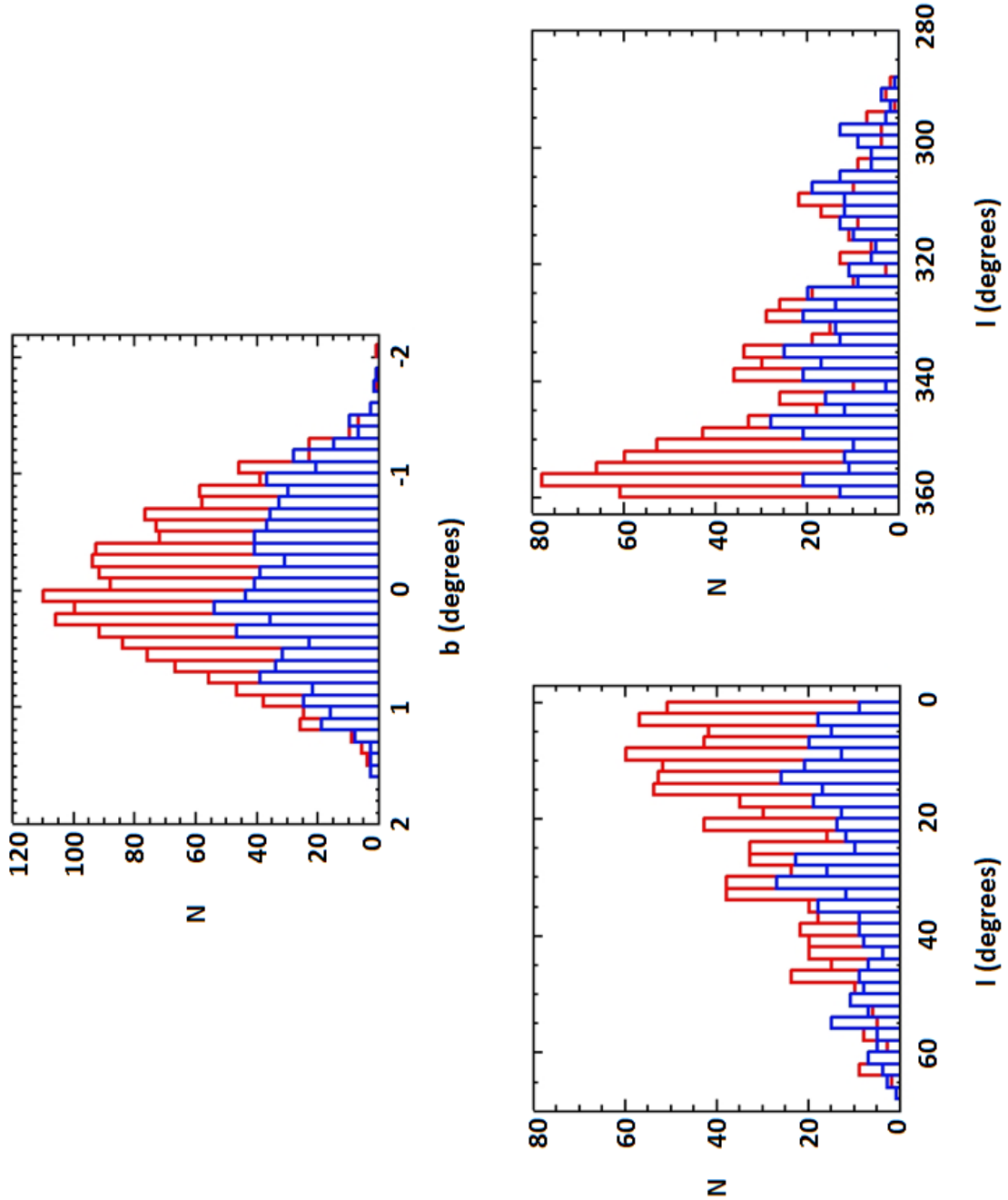

Figure 5.35: Distribution of the sources contained in the catalogues of Hi-GAL 1 PSC C-rich (in blue) and O-rich (in red) AGB star candidates along the Galactic plane region covered by the Hi-GAL 1 Survey.

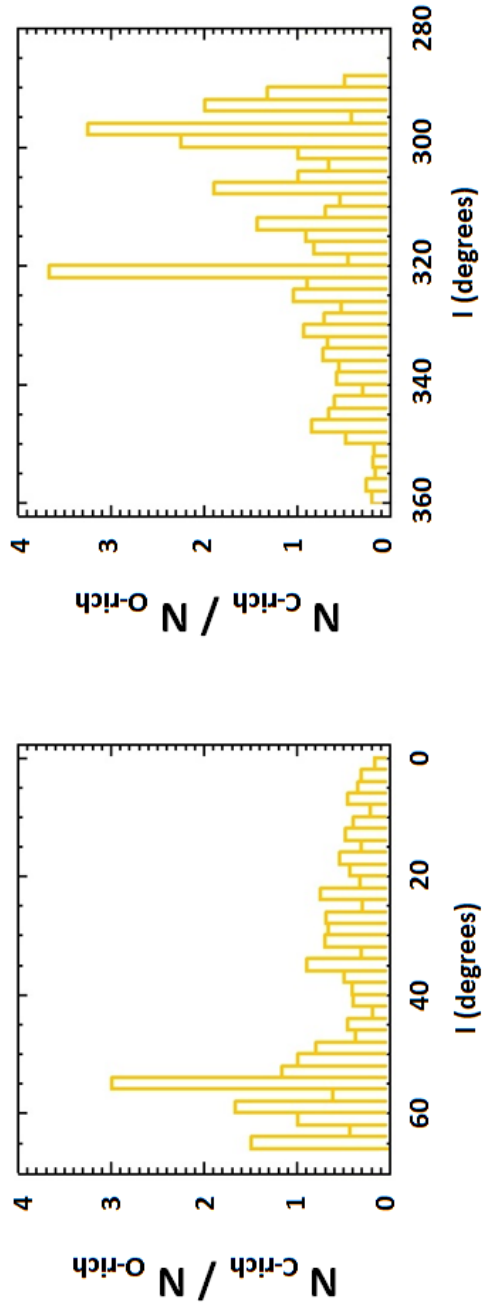

Figure 5.36: Ratio between the number of Hi-GAL 1 PSC C-rich and O-rich AGB star candidates detected along the Galactic plane region covered by the Hi-GAL 1 Survey.

5.10 Summary and Conclusions

The purpose of this chapter was: (i) to find colour cuts that allowed us to separate AGB stars from other stellar types contained in our Hi-GAL 1 PSC, such as YSOs, HII regions and PNe and (ii) to use these colour cuts to build a catalogue of Hi-GAL 1 PSC AGB star candidates. In order to accomplish this goal, we first compiled a reference sample formed of a total of 537 Galactic sources: 205 YSOs, 178 HII regions, 95 AGB stars and 59 PNe verify, which were included in our Hi-GAL 1 PSC and for which at least one counterpart was found in the Survey Catalogues (see Sect. 4.2). The reference sources were selected: (i) for being included in our Hi-GAL 1 PSC and in one, or several, of the Survey Catalogues, (ii) for being point-like sources and (iii) for having their stellar type confirmed through robust stellar identification methods carried out in previous studies. The fluxes of these sources are those listed in our Hi-GAL 1 PSC - while the 70 μm - 500 μm Herschel fluxes were obtained with CUTEX, the fluxes for the remaining bands were taken from the Survey Catalogues' counterparts found lying within a maximum angular distance of 1.7 arcsec. On the other hand, the positions of the reference sources correspond to the most accurate positions (*macc_RA*, *macc_dec*) listed in the Hi-GAL 1 PSC.

Next, for each colour available, we examined the colour distributions of the reference AGB stars and the reference HII regions, YSOs and PNe in order to determine if it was possible to separate the reference AGB stars by means of colour cuts. These colour cuts were imposed to involve either the Herschel 70 μm or 160 μm bands since these bands trace the emission of the dust around AGB stars. Moreover, in order to guarantee the efficiency and reliability of the colour cuts, we decided only to consider those colour cuts which: (i) could be tested upon $\geq 70\%$ of our reference AGB stars and $\geq 70\%$ of our reference YSOs, PNe and HII regions and had (ii) the maximum verification rate and (iii) the minimum contamination rate. The table below shows the colours cuts that were found to satisfy the previous conditions and to provide a good separation between the reference AGB stars and the reference YSOs, HII regions and PNe.

AGBs vs. YSOs	**AGBs vs. HII regions**		**AGBs vs. PNe**
$[70/4.6] < -0.1$	$[70/1.65] < 3.5$	$[70/12] < 0.1$	$[70/4.6] < 0.5$
$[70/12] < -0.1$	$[70/2.17] < 2.6$	$[70/22] < -0.2$	$[70/12] < 0$
	$[70/4.6] < 0.5$		

In addition, we found that the colour cuts listed in the table below also provided a relatively good separation between the reference AGB stars and the reference YSOs, HII regions and PNe. However, these colour cuts did not fulfil the three efficiency and reliability conditions we imposed, and were therefore excluded from our final selection of colour cuts.

AGBs vs. YSOs	**AGBs vs. HII regions**		**AGBs vs. PNe**	
$[70/22] < -0.3$	$[70/3.4] < 1.5$	$[3.4/22] > -1.5$	$[70/3.4] < 1$	$[70/22] < -0.3$
$[4.6/22] > -0.5$	$[4.6/12] > -0.5$	$[4.6/22] > -0.6$	$[3.4/22] > -1.3$	$[4.6/12] > -0.5$
	$[4.6/22] > -0.6$	$[12/22] > -0.3$	$[12/22] > -0.3$	

Since all the colour cuts that were found to separate AGB stars from YSOs, PNe and HII regions involved the 70 μm wavelength, we concluded that the Herschel 70 μm band is highly effective in distinguishing AGB stars from other stellar types and that this band plays a decisive role on the detection of AGB stars. Moreover, since only the Hi-GAL Survey data contains such accurate 70 μm fluxes, we concluded that the Hi-GAL Survey data is crucial for the detection of AGB stars.

Finally, we showed that the colour cuts defined by Ita et al. (2010) and Ishihara et al. (2011) are verified, in general, by our reference AGB stars and PNe but not by our reference YSOs. We also confirmed that the $[70/12] > 1.3$ colour cut defined by Anderson et al. (2012b) successfully discriminates our reference PNe from our reference HII regions. The $[70/22]$ colour distribution was also found to provide a good separation but we found better results for $[70/22] > 0.5$ than for Anderson's $[70/22] > 0.8$ suggested colour cut. In light of these results, we concluded that our colour criteria are different and more efficient on separating our reference AGB stars, YSOs, PNe and HII regions than those established by Ita et al. (2010), Ishihara et al. (2011) and Anderson et al. (2012b).

We then used the colour cuts previously derived to identify possible AGB star candidates amongst our Hi-GAL 1 PSC. Given that the statistics on the colour cuts showed that the $[70/4.6] < 0.5$, $[70/12] < 0.1$ and $[70/22] < -0.2$ colour cuts provide a more reliable AGB classification than the other colour cuts, it was decided that all Hi-GAL 1 PSC sources satisfying any of the previous colour cuts would be considered as an AGB star candidate. In total, we identified 4,928 Hi-GAL 1 PSC sources as potential AGB star candidates. However, since the colour cuts are not 100% efficient, a few reference YSOs, PNe and HII regions were mis-classified as AGB stars while a few reference AGB stars were mis-classified as non AGB stars.

After manually excluding from the sample the mis-classified YSOs, PNe and HII regions and manually re-injecting the mis-classified AGB stars, the number of possible AGB star candidates identified in the Hi-GAL 1 PSC decreased to 4,882 sources.

Next, we eliminated all those sources with $\mathrm{FWHM}_{ratio} > 1.3$ in order to ensure that no extended sources were included amongst the Hi-GAL 1 PSC AGB star candidates. We then inspected the sources' SEDs and discarded those sources that had SEDs that were confusing or that had a shape atypical for an AGB star. After applying the previous source size limit and SED selection, the number of sources contained in the Hi-GAL 1 PSC AGB star candidate sample reduced from 4,882 sources to a total of 3,385 sources.

Finally, we cross-matched our sample with the SIMBAD database and rejected those sources classified in SIMBAD as non-AGB stellar types. The cross-match between the two samples was done allowing a maximum angular separation of 1.7 arcsec in the cross-match and it returned a total of 1,668 matches. From these: (i) 11 and 103 sources were identified as PNe and YSOs, (ii) 224 sources were classified as AGB stars, (iii) 1,081 and 144 sources were identified as *Stars* and *IR sources* and (iv) 82 and 23 sources were classified as other stellar types related and not related to AGB stars.

Having confirmed the sources' class to be reliable, we then proceeded to reject from the catalogue the 219 Hi-GAL 1 PSC AGB star candidates (7%) that were classified in SIMBAD as PNe, YSOs and stellar types related or not related to AGB stars. The resulting catalogue contains a total of 3,166 sources and constitutes our catalogue of Hi-GAL 1 PSC AGB star candidates and its reliability is estimated to be of order $\sim$87%.

Next, we compiled a reference sample of 101 OH/IR-stars (Oxygen-rich AGB stars) and 56 C-stars (Carbon-rich AGB stars). Included in this reference sample were 43 and 36 Hi-GAL 1 PSC AGB star candidates that were identified in SIMBAD as OH/IR and C-stars respectively as well as 58 OH/IR-stars and 20 C-stars that were extracted from additional OH/IR and C-star catalogues.

Having confirmed the sources' class to be reliable, we then proceeded to study the colour distributions of these two stellar types in an attempt to derive colour cuts that enabled us to separate them. As before, in order to guarantee the reliability and efficiency of these colour cuts we only considered those colour cuts which: (i) could be tested upon $\geq$ 70% of our reference OH/IR and C-stars and had (ii) the maximum verification rate and (iii) the minimum contamination rate. In total, we found three colours cuts that provided a good separation between the reference OH/IR and C-stars and that satisfied

the previous conditions. These are: $[70/4.6] > -0.8$, $[70/12] > -0.7$, $[4.6/22] < 0.1$ and $[12/22] < 0.1$. In addition to these colour cuts, we found that the $[8.28/14.65] < 0$ and $[9/18] < 0.2$ colour cuts provided also a relatively good separation between the reference OH/IR and C-stars. However, these colour cuts were excluded from our final selection of colour cuts as they were only testable upon <70% of the reference sample. From these results, we concluded that the MSX 8.28 μm band, the AKARI 9 μm and 18 μm bands and the WISE 12 μm and 22 μm bands are highly effective in distinguishing C-stars (C-rich AGB stars) from OH/IR-stars (O-rich AGB stars) since they cover the silicate features that O-rich AGB stars present around 10 μm and 20 μm and the carbonaceous features that C-rich AGB stars present around 11 μm.

Finally, we showed that while the majority of our reference C-stars verify the colour cuts defined by Ita et al. (2010) and Ishihara et al. (2011), only half of our reference OH/IR-stars are successfully discriminated by their colour cuts. The previous results establish that our colour criteria are different and more efficient on separating our reference OH/IR and C-stars than those determined by Ita et al. (2010) and Ishihara et al. (2011).

Next, we used the colour cuts previously derived to classify our catalogue of Hi-GAL 1 PSC AGB star candidates into C-rich and O-rich AGB stars. Given that the statistics on the colour cuts showed that the $[4.6/22] < 0.1$ and $[12/22] < 0.1$ colour cuts had the maximum verification rates and the minimum contamination rates, it was decided to consider all the sources verifying both (none) of these colour cuts as O-rich AGB stars (C-rich AGB stars). In total, we identified 1,636 and 901 Hi-GAL 1 PSC AGB star candidates sources as O and C-rich AGB stars, respectively. However, once again, since our colour cuts are not 100% efficient, a few reference OH/IR-stars were mis-classified as C-rich AGB stars and a few C-stars were mis-classified as O-rich AGB stars. After manually correcting such mis-classifications, the number of Hi-GAL 1 PSC AGB star candidates classified as O-rich and C-rich AGB stars decreased to 1,652 and 917 sources, respectively.

We then visually inspected the sources' SEDs and concluded that a total of 76 (7) sources were mis-classified by the colour cuts as C-rich (O-rich) AGB stars. These 76 (7) sources were excluded from the sample of C-rich (O-rich) AGB stars and added to the sample of O-rich (C-rich) AGB stars. The resulting samples of 1,721 and 848 sources constitute our catalogues of O and C-rich Hi-GAL 1 PSC AGB star candidates, respectively. The number of total entries in these catalogues could be increased up to $\sim$8 times should we have the WISE fluxes for the totality of the sources included in the Hi-GAL 1 PSC.

The catalogues of Hi-GAL 1 PSC O and C-rich AGB star candidates are, to date, the largest catalogues of Galactic O and C-rich AGB stars. These catalogues contain 1.4 times and 4.5 times as many O and C-rich AGB stars as the catalogues from Suh and Kwon (2009).

Finally, we examined the spatial distribution of the Hi-GAL 1 PSC O and C-rich AGB star candidates along the Galactic plane region covered by the Hi-GAL 1 Survey. We established that while the number of Hi-GAL 1 PSC O-rich AGB stars increases towards the Galactic Centre, the Hi-GAL 1 PSC C-rich AGB stars are distributed relatively evenly along the Galactic latitude and longitude. Moreover, we established that the ratio between the number of Hi-GAL 1 PSC C and O-rich AGB stars increases with increasing galactocentric distance. The previous results agree with those obtained by Wood (1981), Jura and Kleinmann (1990), Marigo et al. (1999) and can be explained by the Galactic outwardly decreasing metallicity gradient.

Chapter 6

Properties of the Hi-GAL 1 C-rich and O-rich AGB candidates

"We are turning off the lights now."

Micha Schmidt

6.1 Introduction

The aim of this chapter is to use the Spectral Energy Distributions (SEDs) of the sources contained in the catalogues of Hi-GAL 1 PSC C-rich and O-rich AGB star candidates to obtain the stellar properties of a sub-sample of these sources.
In the following sections I:

(i) present the criteria employed to select the sub-sample sources,

(ii) calculate the bolometric flux and the distances of the sub-sample sources,

(iii) estimate the colour temperature of the sub-sample sources fitting their SEDs with a single or two-temperature black body function and

(iv) use the DUSTY radiative transfer code to model the SEDs and derive the mass-loss rate (amongst other stellar properties) of the sub-sample sources.

In the following sections we explain how the modelling of our AGB star candidates as black bodies (see Sect. 6.2) allowed the derivation of the bolometric flux (see Sect. 6.4), distance (see Sect. 6.5), colour temperature (see Sect. 6.6), mass-loss rate and other stellar parameters (see Sect. 6.7) of a sub-sample of the Hi-GAL 1 C-rich and O-rich AGB star candidates. Hereafter, we will refer to the Hi-GAL 1 C-rich and O-rich AGB star candidates as Hi-GAL 1 C-rich and O-rich AGB stars.

6.2 Modelling of stars as black bodies

A black body (bb) is defined as an idealized physical body that is a perfect absorber, i.e. it absorbs all incident electromagnetic radiation isotropically, i.e. regardless of frequency or angle of incidence. The bb reaches some equilibrium temperature (thermal equilibrium) and then re-emits the radiation (bb-radiation) at a rate equal to the rate in which the radiation was absorbed. The emission spectrum (Planck radiation curve) of a bb (see Fig. 6.1) is continuous and has an asymmetric bell shape, peaking at a specific wavelength (λ_{peak}), that is expressed by the *Planck's law* (see Eq. 6.1 or 6.2).

As a first approximation, the structure of a star can be modelled as an inner compact spherical hot dense nucleus (i.e. stellar core) surrounded by an outer, much more extended, cooler and tenuous spherical shell of gas (i.e. photosphere) from which light is radiating. The amount of energy radiated by the photosphere is dependent on the core's energy supply, which will vary with every change in the stellar core. Since core changes occur over long periods of time, the temperature of the photosphere can be approximated to be almost constant, i.e. in local thermal equilibrium (LTE) during such intervals. At the lower layers ("bottom") of the stellar photosphere, the majority of the radiated photons are re-absorbed by the surrounding gas close to where they were emitted while a negligible small fraction escapes into space. Given that the energy from within the star quickly replaces the energy carried away by the escaping photons, the bottom of the photosphere can be estimated to be a quasi perfect absorber (Gray 2005).

Under these assumptions the radiation emitted from a stellar photosphere can be approximated as bb radiation and thus, stellar SEDs can be modelled approximately by Planck functions [1].

[1] Strictly speaking, Planck radiation laws apply only at the bottom of a stellar photosphere where the optical depth to the surface is high enough to prevent the escape of the majority of photons and where the LTE assumption is valid (Gray 2005).

Figure 6.1: Emission spectra of a black body.

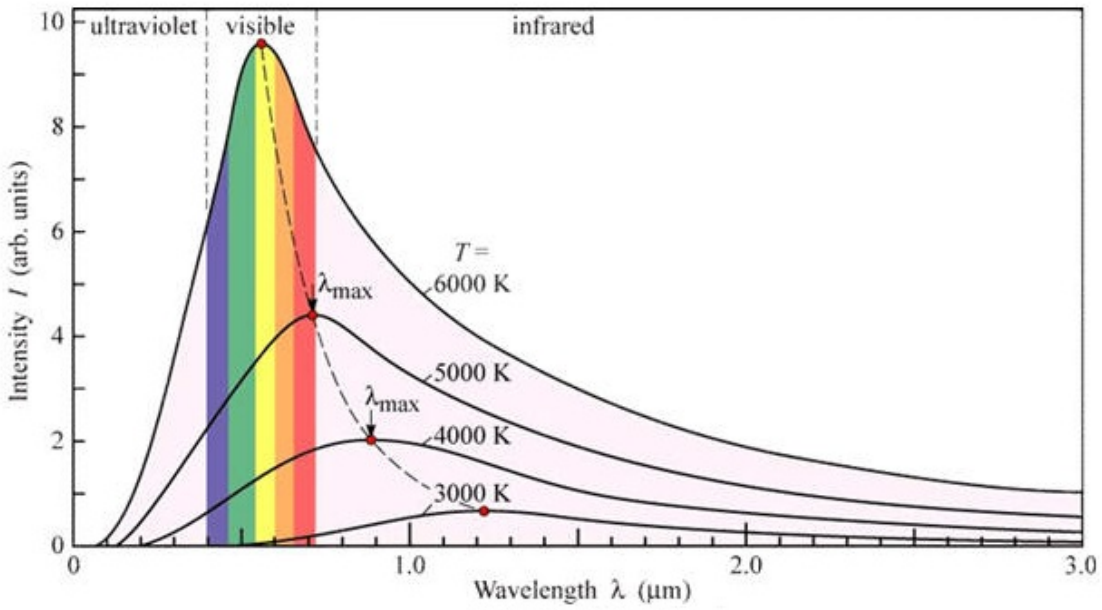

2 forms of the Planck law:

$$B_\lambda(T) = \frac{2hc^2}{\lambda^5}\frac{1}{e^{\frac{hc}{\lambda k_B T}} - 1}\ Wm^{-2}sr^{-1}m^{-1} \quad or \tag{6.1}$$

$$B_\nu(T) = \frac{2h\nu^3}{c^2}\frac{1}{e^{\frac{h\nu}{k_B T}} - 1}\ Wm^{-2}sr^{-1}Hz^{-1} \tag{6.2}$$

where:

$B_\lambda(T) \equiv$ Spectral radiance, which measures the amount of energy emitted per unit surface, per unit time, per unit solid angle and in the wavelength range between λ and $\lambda + \mathrm{d}\lambda$.

$B_\nu(T) \equiv$ Spectral radiance, which measures the amount of energy emitted per unit surface, per unit time, per unit solid angle and in the frequency range between ν and $\nu + \mathrm{d}\nu$.

T $\equiv$ bb temperature (or colour temperature) in K.

$k_B \equiv$ Boltzmann constant $= 1.38 \times 10^{-23}\ J\,K^{-1}$.

h $\equiv$ Planck constant $= 6.62 \times 10^{-34}\ J\,s$.

c $\equiv$ speed of light $= 2.998 \times 10^{8}\ m\,s^{-1}$.

6.3 Smoothing of the sources' SED

When modelling stellar SEDs with Planck functions, it is important to ensure that the shape of the SED to be fitted is smooth enough so that the fitting is correctly done. With this in mind, we proceeded to smooth the SEDs of our Hi-GAL 1 PSC O-rich and C-rich AGB star candidates.

The smoothing of the sources' SED was achieved by rejecting those SED fluxes that belonged to bands with large beam sizes. This decision was made taking into account that bands with large beam sizes will return less precise source positions and therefore, the fluxes measured in these bands will be less accurate.

In order to set a maximum beam size we revised the beam sizes of the Herschel bands from Table 4.7. Here, we can see that the PACS 70 μm band has a relatively small beam size (FWHM=5.2"), the PACS 160 μm band and the SPIRE 250 μm band have moderate beam sizes (FWHM=12" and 18" respectively) whereas the beam sizes of the SPIRE 350 μm and 500 μm bands are rather large (FWHM=25" and 37" respectively). While the PMW and PLW bands were discarded for having too large beam sizes, the PSW band was kept as it provides us with a measure (reliable enough) of the source flux in the FIR tail of the SED, which will allow us to determine if the source has an excess. As a result, we set the maximum beam size to be that of the PSW band (i.e. 18") and we excluded from our SEDs all those fluxes that were obtained with instruments whose band beam sizes were larger than 18".

Moreover, in order to further guarantee the accuracy of the fluxes listed in the SEDs, whenever there were two bands centred at a similar wavelength, we only included the flux measured in the band with smaller beam size. As a result, we:

- Selected the GLIMPSE 3.6 μm, 4.5 μm, 5.8 μm and 8 μm bands, the 2MASS 1.25 μm, 1.65 μm and 2.17 μm bands, the AKARI 9 μm and 18 μm bands, the WISE 12 μm and 22 μm bands, the MSX 14.65 μm band and the Herschel 70 μm, 160 μm and 250 μm bands for having beam sizes smaller or equal to 18".

- Discarded the MSX 21.34 μm band, the IRAS 12 μm, 25 μm, 60 μm and 100 μm bands and the AKARI 65 μm, 90 μm, 140 μm and 160 μm bands for having beam sizes larger than 18".

- Discarded the MSX 4.29 μm and 4.35 μm bands and the WISE 4.6 μm band since we included the GLIMPSE 4.5 μm band, which covers a similar wavelength with greater accuracy. Also discarded was the WISE 3.4 μm band since we included the GLIMPSE 3.6 μm band, which covers a similar wavelength with greater accuracy.

- Discarded the MSX 8.28 μm band since we included the GLIMPSE 8 μm band, which covers a similar wavelength with greater accuracy. Also discarded was the MSX 12.13 μm band since we included the WISE 12 μm band, which covers a similar wavelength with greater accuracy.

The resulting SEDs of our 1,721 and 848 Hi-GAL 1 O-rich and C-rich AGB star candidates were then visually inspected in order to detect and reject any SEDs that were left with too few points or were still not sufficiently smooth. After the process, a total of 279 O-rich and 87 C-rich AGB stars were rejected. From this point onwards, only the remaining 1,442 O-rich and 761 C-rich AGB stars were considered when calculating the stars' properties. Amongst the 1,442 O-rich AGB stars, there were 101 sources that were identified as being reference sources[2] whereas the remaining 1,341 were identified as being non reference sources. In the case of the C-rich AGB stars, a total of 55 and 706 sources were identified as being reference and non reference sources, respectively. In the following sections, the stellar properties of reference and non-reference sources are presented separately for comparison purposes.

[2]We refer as *reference* and *non reference* AGB star candidates to those sources which were and were not used as a reference to derive the colours cuts that separate C-rich from O-rich AGB stars (see Sect. 5.8.1).

6.4 Bolometric fluxes

6.4.1 Definition

The bolometric flux of a source (F_{bol}) can be defined as the flux received at Earth from the source, integrated over all frequencies and can be expressed as in Eq. 6.3. Thus, the F_{bol} of a source can be calculated through integration of the source SED over the observed frequency or wavelength range.

$$F_{bol} = \int_0^\infty B_\lambda(T)d\lambda \quad or \quad F_{bol} = \int_0^\infty B_\nu(T)d\nu \tag{6.3}$$

where:

$B_\nu(T),\ B_\lambda(T) \equiv$ bb spectral radiance, as defined by the Planck function.

Given that our F_ν fluxes were in Jy (i.e. $10^{-26}\ \frac{W}{m^2 Hz}$), previous to the integration we had to convert the fluxes from Jy units to $\frac{W}{m^2 \mu m}$ units. This was achieved by converting our F_ν into F_λ by means of Eq. 6.4.

$$F_\lambda = F_\nu \times \frac{c}{\lambda^2} \tag{6.4}$$

As a result:

$$F_\lambda = F_\nu\ Jy \times \frac{3 * 10^8\ \frac{m}{s}}{\lambda^2\ \mu m^2} = F_\nu\ 10^{-26}\ \frac{W}{m^2 Hz} \times \frac{3 * 10^{14}\ \frac{\mu m}{s}}{\lambda^2\ \mu m^2}$$

$$F_\lambda = F_\nu \times \frac{3 * 10^{-12}}{\lambda^2}\ \frac{W}{m^2 \mu m} \tag{6.5}$$

6.4.2 Results

Shown in Fig. 6.2 are the distributions of the bolometric fluxes F_{bol} derived for the 761 Hi-GAL 1 C-rich AGB stars (55 reference and 706 non reference) and the 1,442 Hi-GAL 1 O-rich AGB stars (101 reference and 1,341 non reference) whose SED was classified as *smooth* in Sect. 6.3.

Listed in Table 6.1 are the average bolometric fluxes ($< F_{bol} >$), in $W\,m^{-2}$, found for the reference (*Ref.*) and non reference (*Non ref.*) Hi-GAL 1 C-rich and O-rich AGB stars. Also included are the average bolometric fluxes derived for the whole sample (*Total*) of Hi-GAL 1 C-rich and O-rich AGB stars. These values were calculated by averaging the results obtained for the reference sources with those obtained for the non reference sources.

Table 6.1: Mean and STDEV of the bolometric fluxes F_{bol} (in $W\,m^{-2}$) found for the reference (*Ref.*), non reference (*Non ref.*) and total Hi-GAL 1 C-rich and O-rich AGB stars. Indicated within parenthesis is the number of sources considered in the calculation of the bolometric flux Mean and STDEV.

$< F_{bol} >$ **Hi-GAL 1 C-rich AGB stars** ($W\,m^{-2}$)		
Ref.	**Non ref.**	**Total**
3.57E-11 ± 3.43E-11 (55)	2.69E-11 ± 3.66E-11 (706)	2.75E-11 ± 3.65E-11 (761)

$< F_{bol} >$ **Hi-GAL 1 O-rich AGB stars** ($W\,m^{-2}$)		
Ref.	**Non ref.**	**Total**
1.22E-11 ± 2.01E-11 (101)	5.77E-12 ± 1.10E-11 (1,341)	6.23E-12 ± 1.20E-11 (1,442)

From these results, we can see that for the sample of Hi-GAL 1 C-rich AGB stars, the bolometric fluxes found are within the $F_{bol} = [1.20E-13,\ 3.90E-10]\ W\ m^{-2}$ range. On the other hand, for the Hi-GAL 1 O-rich AGB stars, the bolometric fluxes found are within the $F_{bol} = [2.26E-13,\ 2.69E-10]\,W\,m^{-2}$ range. Also, we can see that the average bolometric flux $< F_{bol} >$ found for the Hi-GAL 1 C-rich AGB stars is 4.4 times greater than that found for the Hi-GAL 1 O-rich AGB stars.

The higher bolometric flux of the Hi-GAL 1 C-rich AGB stars could be a consequence of these stars being closer to us - as we discussed in Sect. 5.9.1 there are relatively more C-rich stars in the outer parts of our Galaxy than in the inner parts. The bolometric fluxes derived in this section were added to the catalogues of Hi-GAL 1 PSC O-rich and C-rich AGB star candidates under a column labelled *F_bol* and are in units of $W\,m^{-2}$.

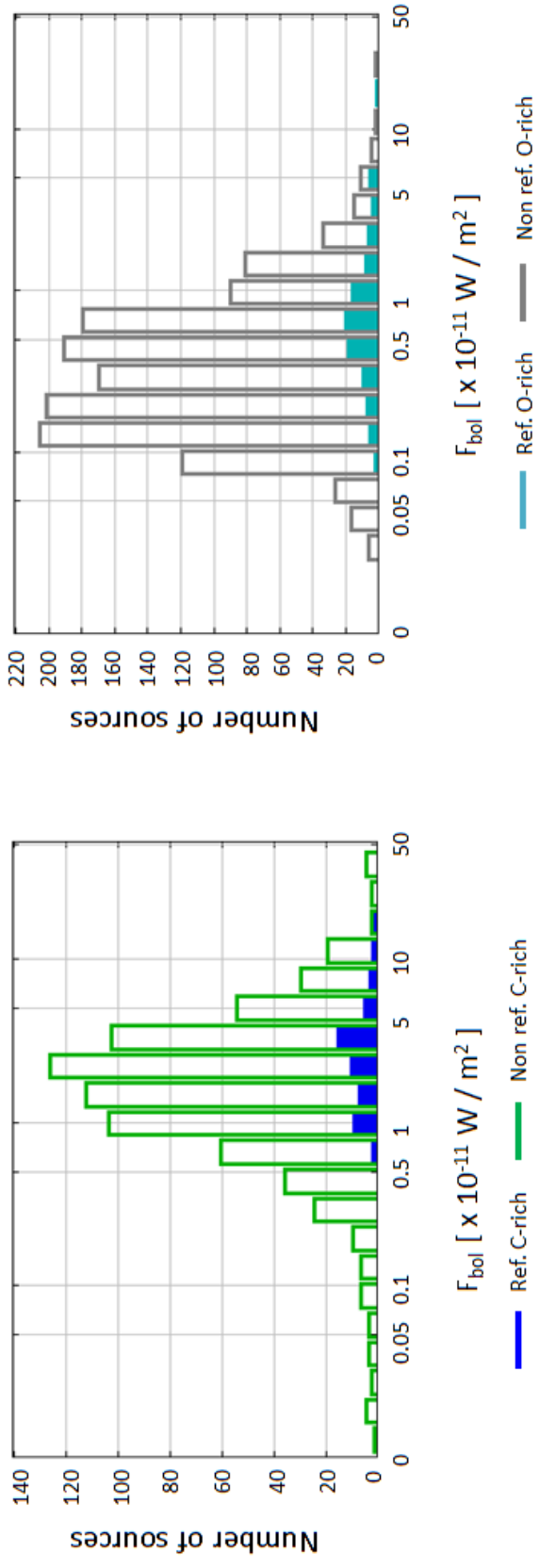

Figure 6.2: [Left panel] Distributions of the bolometric fluxes F_{bol}, in 10^{-11} W/m^2, found for the reference (in blue) and non reference (in green) Hi-GAL 1 C-rich AGB stars. [Right panel] Distributions of the bolometric fluxes, in 10^{-11} W/m^2, found for the reference (in cyan) and non reference (in grey) Hi-GAL 1 O-rich AGB stars.

6.5 Distances

6.5.1 Definition

The distance of a source can be estimated using the expression in Eq. 6.6 in which L_{bol} is the source's bolometric luminosity, F_{bol} is the source's bolometric flux and d is the distance from Earth to the source.

$$L_{bol} = 4\pi d^{\,2} F_{bol} \quad \longrightarrow \quad d = \sqrt{\frac{L_{bol}}{4\pi F_{bol}}} \tag{6.6}$$

6.5.2 Assumptions

From the Hertzsprung-Russell diagram in Fig. 1.13 we can see that the luminosity of AGB stars varies from $L_{min} \sim 10^3\ L_{\odot}$ (E-AGB phase) to $L_{max} \sim 5 * 10^4\ L_{\odot}$ (TP-AGB phase) during their lifetime. With this in mind, we proceeded to calculate the distances of the 761 Hi-GAL 1 C-rich AGB stars (55 reference and 706 non reference) and the 1,442 Hi-GAL 1 O-rich AGB stars (101 reference and 1,341 non reference), with smoothed SEDs, adopting for all the stars $L_{bol} = 10^4\ L_{\odot}$. This value is between L_{min} and L_{max} and is often considered in the literature as the typical bolometric luminosity of AGB stars. The assumption of all stars having the same L_{bol} is, however, very crude. In reality, since different AGB stars have different ages, they will have different L_{bol}. Moreover, the L_{bol} of an AGB star will also depend on whether the star is C-rich or O-rich. On the one hand, C-rich AGB stars are typically located, in the Hertzsprung-Russell diagram, where the 3^{rd} dregde-up occurs and so, the assumption of $L_{bol} = 10^4\ L_{\odot}$ is fairly suitable. On the other hand, O-rich AGB stars can have L_{bol} lower or higher than $10^4\ L_{\odot}$. This can be explained by the fact that a C-rich AGB star can become O-rich if the star undergoes sufficient thermal pulses so that the abundance of ^{16}O becomes greater than that of ^{12}C. Furthermore, C-rich AGB stars can also become O-rich during the Hot Bottom burning process (see Sect. 1.5.4.6). As a result, the choice of $L_{bol} = 10^4\ L_{\odot}$ is, in general, more inappropriate for O-rich AGB stars than for C-rich AGB stars. This in turn implies that, under this assumption, the distances obtained for the C-rich AGB stars could be more realistic than for the O-rich AGB stars. Despite the previous caveats, we decided to use the $L_{bol} = 10^4\ L_{\odot} = 3.83 * 10^{30}\ W$, in conjunction with the F_{bol} in W/m^2 calculated in Sect. 6.4 in order to: (i) obtain an estimation of the (nominal) distances of our Hi-GAL 1 C-rich and O-rich AGB stars and (ii) establish whether we see a difference between the sources' Galactic distribution.

6.5.3 Results

Shown in Fig. 6.3 are the distributions of the (nominal) distances (d, in kpc[3]) derived when adopting $L_{bol} = 10^4\ L_{\odot}$ for the 761 Hi-GAL 1 C-rich AGB stars (55 reference and 706 non reference) and the 1,442 Hi-GAL 1 O-rich AGB stars (101 reference and 1,341 non reference) whose SEDs was classified as *smooth* in Sect. 6.3.

Listed in Table 6.2 are the average distances ($< d >$), in *kpc*, found for the reference and non reference Hi-GAL 1 C-rich and O-rich AGB stars. Also included are the average distances derived for the whole sample of Hi-GAL 1 C-rich and O-rich AGB stars. These values were calculated by averaging the results obtained for the reference sources with those obtained for the non reference sources.

Shown in Fig. 6.4 and 6.5 are the space distributions projected on the Galactic plane of the reference and non reference Hi-GAL 1 C-rich and O-rich AGB stars. Also shown is a face–on image of the Milky Way, (which was used in Sect. 1.5.2 to indicate the Galactic coverage of Hi–GAL 1, Hi–GAL 2 and Hi–GAL 3 surveys), that we include here as a reference for the discussion of the distances found.

From Table 6.2 and Fig. 6.3-6.5 we can see that, with the exception of a few sources, the Hi-GAL 1 C-rich AGB stars were found to be located at shorter distances than the Hi-GAL 1 O-rich AGB stars. While the majority of C-rich AGB stars were found to lie within $d = [2,\ 6]\ kpc$, the O-rich AGB stars expand over the $d = [4,\ 16]\ kpc$ range.

From the previous results we can establish that:

(i) The (nominal) distances found for the majority of Hi-GAL 1 O-rich AGB stars are clearly incorrect.

This result could be due to the fact that the bolometric luminosities of these Hi-GAL 1 O-rich AGB stars are, in reality, much lower than the assumed value of $L_{bol} = 10^4\ L_{\odot}$. Another possibility is that the bolometric fluxes of these sources are, in reality, greater than those we obtained in Sect. 6.4. This would be true if these stars were further away from us and/or if they had large quantities of dust in their shells. In that case, the NIR fluxes in their SEDs would be strongly affected by extinction, which would lead to the underestimation of the sources' bolometric flux and the subsequent overestimation of the sources' distance.

[3] $1\ kpc = 3.086 * 10^{19}\ m$

(ii) The (nominal) distances found for the majority of Hi-GAL 1 C-rich AGB stars are more reasonable than those found for the Hi-GAL 1 O-rich AGB stars.

This result confirms that, as we mentioned in Sect. 6.5.2, the assumption of $L_{bol} = 10^4\ L_{\odot}$ is more appropriate for the Hi-GAL 1 C-rich AGB stars than for the Hi-GAL 1 O-rich AGB stars. Nevertheless, we reiterate that these distances are nominal and would change without the assumption of a common absolute luminosity for all the stars.

(iii) The number of Hi-GAL 1 C-rich AGB stars found across the Galactic longitudes can be related to the Galactic structure.

We observe that for those directions for which the line of sight crosses several Galactic arms or the Galactic Bulge, the number of detected stars is higher than for those directions for which only one arm is crossed (e.g. the Scutum-Centaurus Arm or the Perseus Arm).

The distances derived in this section were added to the catalogues of Hi-GAL 1 PSC O-rich and C-rich AGB star candidates under a column labelled d and are in units of kpc.

Figure 6.3: [Left panel] Distributions of the distances d (in kpc) found for the reference (in blue) and non reference (in green) Hi-GAL 1 C-rich AGB stars. [Right panel] Distributions of the distances d (in kpc) found for the reference (in cyan) and non reference (in grey) Hi-GAL 1 O-rich AGB stars.

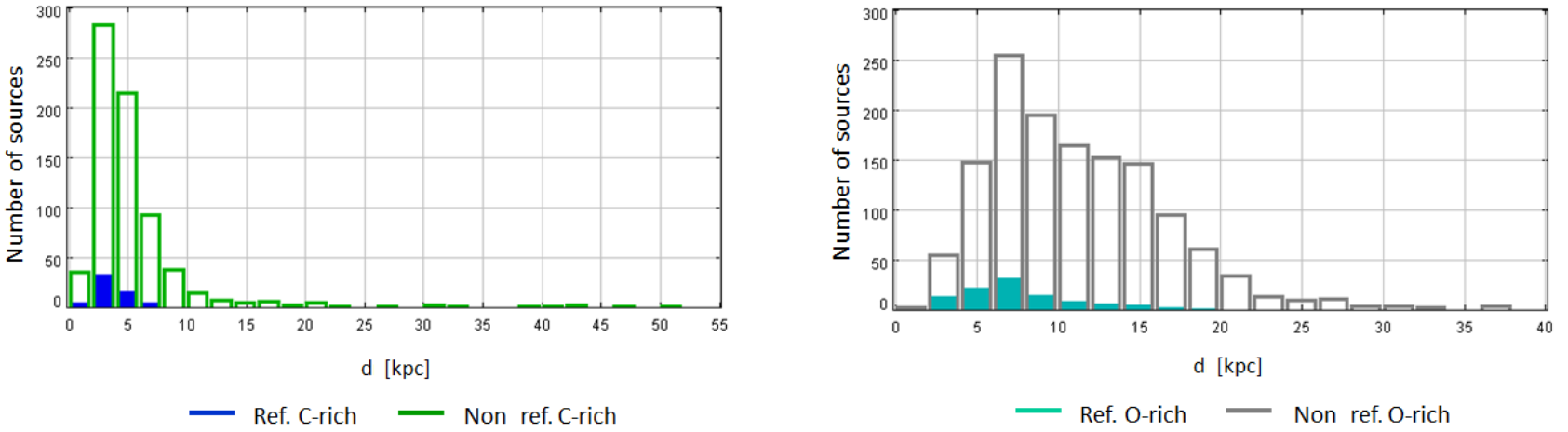

Table 6.2: Mean and STDEV of the distances d (in kpc) found for the reference, non reference and total Hi-GAL 1 C-rich and O-rich AGB stars. Indicated within parenthesis is the number of sources considered in the calculation of the Mean and STDEV of the distances.

< d > Hi-GAL 1 C-rich AGB stars (kpc)		
Ref.	**Non ref.**	**Total**
3.75 ± 1.39 (55)	5.46 ± 5.04 (706)	5.34 ± 4.89 (761)

< d > Hi-GAL 1 O-rich AGB stars (kpc)		
Ref.	**Non ref.**	**Total**
7.58 ± 3.61 (101)	11.14 ± 5.33 (1,341)	10.89 ± 5.31 (1,442)

Figure 6.4: [Right panel] Galactic distributions of the reference (in blue) and non reference (in green) Hi-GAL 1 C-rich AGB stars. [Left panel] Face–on image of the Milky Way in which we indicated the Galactic coverage of the Hi–GAL 1 (in purple), Hi–GAL 2 (in yellow) and Hi–GAL 3 (in red) surveys. This image is included as a reference to the right panel. The *GC* point indicates the Galactic Centre while the *Solar System (SS)* point and the yellow circle indicate the Sun's position and its orbit. The distance between the Sun and the Galactic Centre is estimated to be ∼7.7 kpc (Babusiaux and Gilmore 2005) and is indicated here as a reference.

Figure 6.5: [Right panel] Galactic distributions of the reference (in cyan) and non reference (in grey) Hi-GAL 1 O-rich AGB stars. [Left panel] Face–on image of the Milky Way in which we indicated the Galactic coverage of the Hi–GAL 1 (in purple), Hi–GAL 2 (in yellow) and Hi–GAL 3 (in red) surveys. This image is included as a reference to the right panel. The *GC* point indicates the Galactic Centre while the *Solar System (SS)* point and the yellow circle indicate the Sun's position and its orbit. The distance between the Sun and the Galactic Centre is estimated to be ∼7.7 kpc (Babusiaux and Gilmore 2005) and is indicated here as a reference.

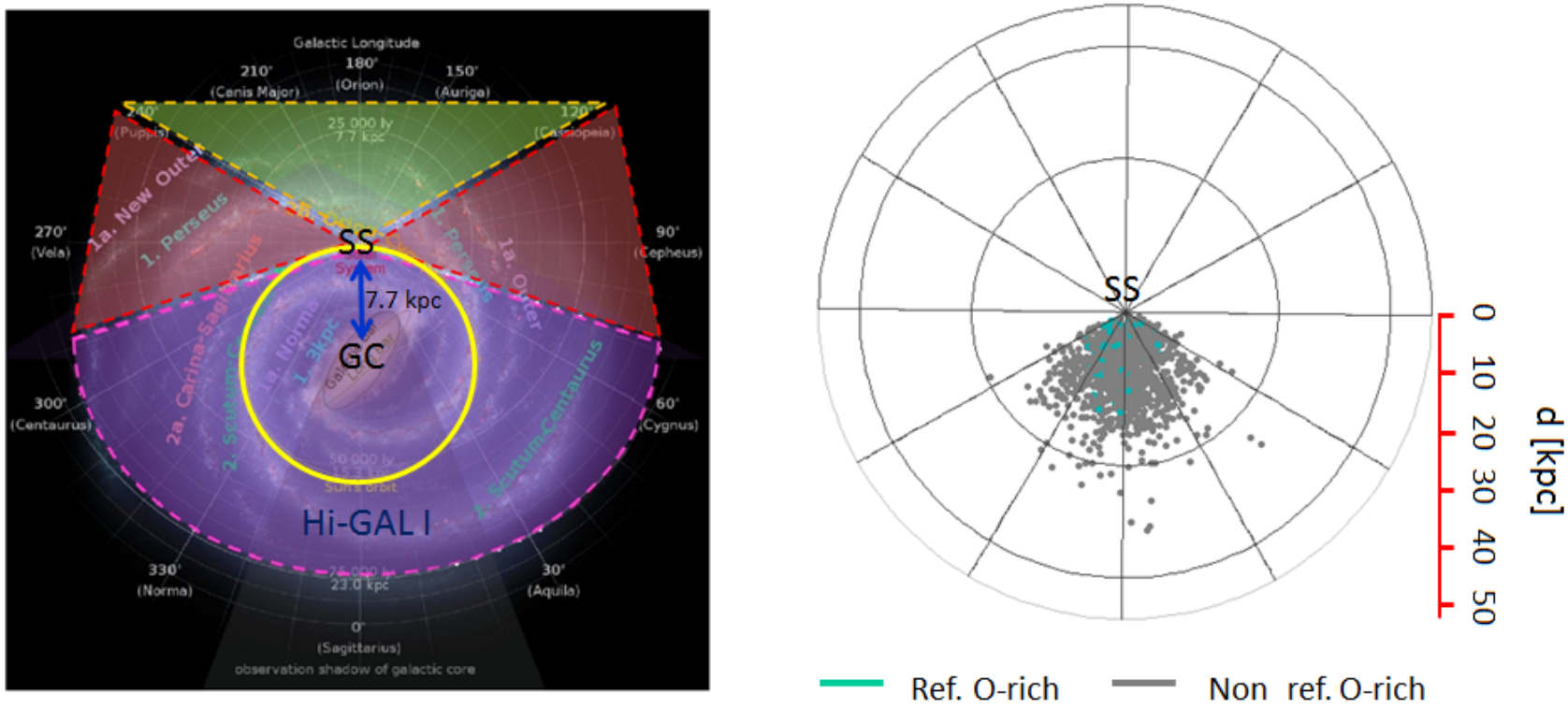

6.6 Colour temperatures

6.6.1 Definition

The colour temperature of a source Tc is defined as the apparent temperature of the source when measured as a whole system comprising the source's photosphere and the source's dusty shell. The value of this temperature can be taken as the temperature of the black body (bb) function that best describes the bb radiation curve of the source (i.e. SED). Thus, it is possible to estimate the colour temperature Tc of a source by fitting its SED with the Planck function of Eq. 6.1 with Tc set as a free parameter. With this in mind, we proceeded to fit one or two Planck functions to the SEDs of the 761 Hi-GAL 1 C-rich AGB stars (55 reference and 706 non reference) and the 1,442 Hi-GAL 1 O-rich AGB stars (101 reference and 1,341 non reference) whose SED was classified as *smooth* in Sect. 6.3. For those sources whose SED could be described by a single bb, the fit was done over the [1.25, 500] μm wavelength range in order to cover the fluxes measured in the 2MASS J band, centred at 1.25 μm, and the Herschel PLW band, centred at 500 μm. On the other hand, for those sources whose SEDs appeared to be described by two separate black bodies, one cold and one warm, the fit for the warm SED component was done over the NIR-MIR [1.25, 10] μm wavelength range whereas the fit for the cold SED component was done over the MIR-FIR (10, 500] μm wavelength range.

6.6.2 Results

Listed in Table 6.3 are the number of reference (*Ref.*), non reference (*Non ref.*) and total Hi-GAL 1 C-rich and O-rich AGB stars, with *smooth* SEDs (see Sect. 6.3), that were successfully fitted with 1 or 2 Planck functions. Here, we can see that:

- From all the 761 Hi-GAL 1 C-rich AGB stars whose SEDs was classified as *smooth*, only 567 stars (75%) were found to be successfully fitted with 1 (387 sources) or 2 (180 sources) Planck functions (see Fig. 6.6 for examples). Amongst the 387 Hi-GAL 1 C-rich AGB stars that were well fitted with 1 Planck function, 48 (339) sources were identified as being reference (non reference) sources. On the other hand, the 180 sources well fitted with 2 Planck functions were all established to be non reference.

- From all the 1,442 Hi-GAL 1 O-rich AGB stars whose SEDs was classified as *smooth*, only 817 stars (57%) were found to be successfully fitted with 1 Planck function (see Fig. 6.6 for examples). We found no cases of O-rich AGB stars that were well fitted with 2 Planck functions. Amongst the 817 Hi-GAL 1 O-rich AGB stars that were well fitted with 1 Planck function, 56 (761) sources were identified as being reference (non reference) sources.

Shown in Fig. 6.7 are the distributions of the colour temperatures found for the reference and non reference Hi-GAL 1 C-rich and O-rich AGB stars whose SEDs were successfully fitted with 1 or 2 Planck functions. Listed in Table 6.4 are the average colour temperatures ($< Tc >$), in K, found for these sources. Also included are the average colour temperatures derived for the whole sample of Hi-GAL 1 C-rich and O-rich AGB stars. These values were calculated by averaging the results obtained for the reference sources with those obtained for the non reference sources.

From these results, we can see that the average colour temperatures $< Tc >$ found for the reference and non reference Hi-GAL 1 C-rich AGB stars that were fitted with one Planck function ($< Tc >^{C-rich}_{Ref.} = 1,092\ K$ and $< Tc >^{C-rich}_{Non\ ref.} = 1,296\ K$ respectively) are slightly greater than the average colour temperatures found for the reference and non reference Hi-GAL 1 O-rich AGB stars ($< Tc >^{O-rich}_{Ref.} = 729\ K$ and $< Tc >^{O-rich}_{Non\ ref.} = 818\ K$ respectively).

The higher colour temperatures found for the Hi-GAL 1 C-rich AGB stars could be due to the Hi-GAL 1 O-rich AGB stars suffering from more extinction in the NIR. This fact could be a consequence of the Hi-GAL 1 O-rich AGB stars being further from us - as we discussed in Sect. 5.9.1 there are relatively more O-rich stars in the inner parts of our Galaxy than in the outer parts. The higher dust quantities present along the line of sight of the Hi-GAL 1 O-rich AGB stars would result in the SEDs of these stars being shifted towards longer wavelengths, which would in turn result in the lowering of the colour temperatures derived from the SED bb-fitting.

The colour temperature/s obtained in this section were added to the catalogues of Hi-GAL 1 PSC O-rich and C-rich AGB star candidates. For those sources fitted with 1 Planck function we added a column labelled Tc_1, which lists the sources' Tc_1 in K. For those sources fitted with 2 Planck functions a second column labelled Tc_2 was also added, which lists the sources' Tc_2 in K.

Figure 6.6: Examples of C-rich AGB star candidates that were successfully fitted with 1 (first column) and 2 (second column) Planck functions (PF) and examples of O-rich AGB star candidates that were successfully fitted with 1 Planck function (third column).

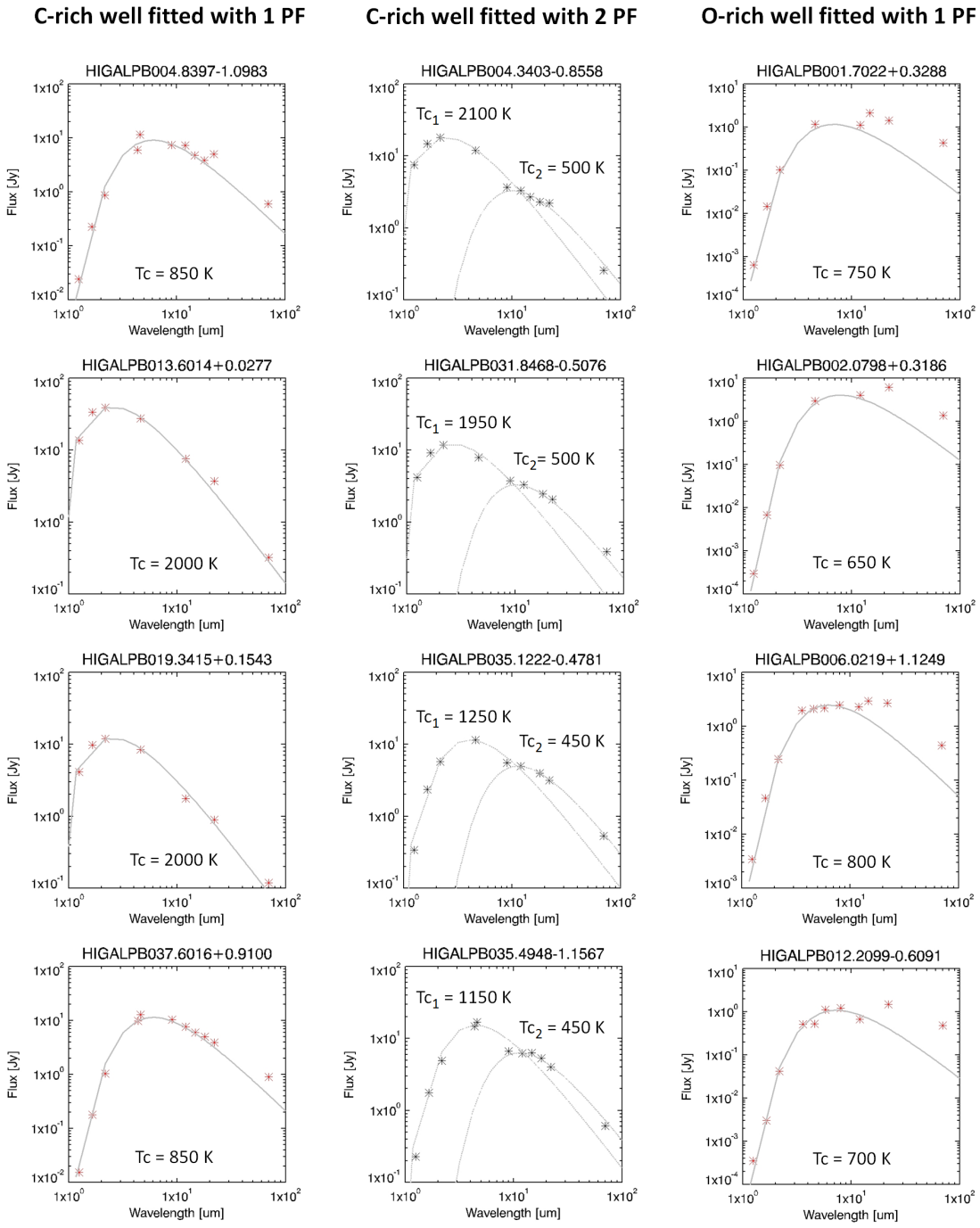

Figure 6.7: Distributions of the colour temperatures Tc found for the reference and non reference Hi-GAL 1 C-rich and O-rich AGB stars fitted with one and two Planck functions.

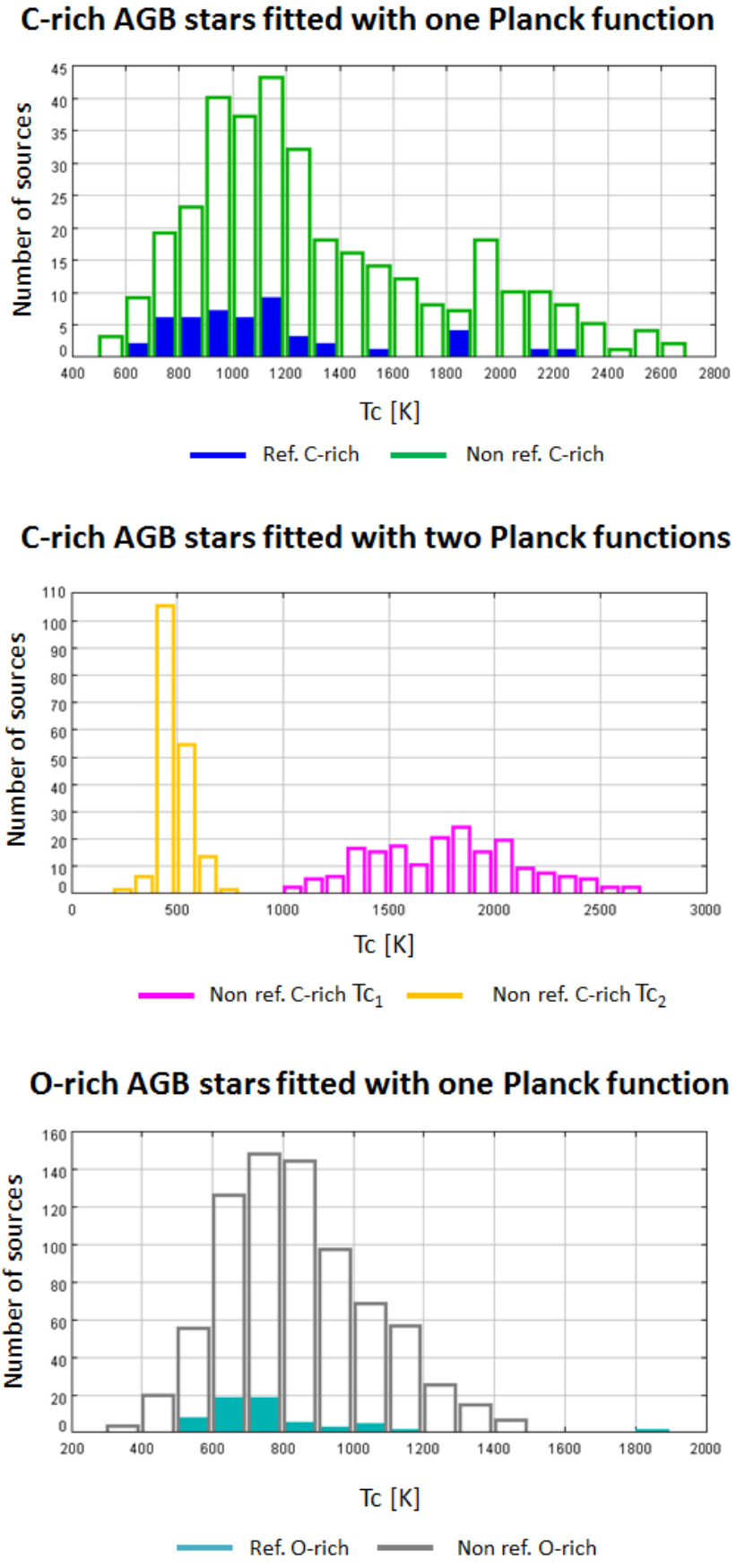

Table 6.3: Number of reference (*Ref.*), non reference (*Non ref.*) and total Hi-GAL 1 C-rich and O-rich AGB stars that were successfully fitted with 1 or 2 Planck functions (*PF*).

	C-rich AGB stars		**O-rich AGB stars**	
Fitted with	**1 PF**	**2 PF**	**1 PF**	**2 PF**
Ref.	48	0	56	0
Non ref.	339	180	761	0
Total	387	180	817	0

Table 6.4: Mean and STDEV of the colour temperatures Tc found for the reference, non reference and total Hi-GAL 1 C-rich and O-rich AGB stars fitted with one and two Planck functions. Indicated within parenthesis is the number of sources considered in the calculation of the Mean and STDEV of the colour temperatures.

	Fitted with 1 Planck function	**Fitted with 2 Planck functions**	
	$<$ **Tc** $>$ **(K)**	$<$ **Tc**$_1$ $>$ **(K)**	$<$ **Tc**$_2$ $>$ **(K)**
Ref. C-rich	1092 ± 378 (48)	–	–
Non ref. C-rich	1296 ± 472 (339)	1759 ± 348 (180)	468 ± 69 (180)
Total C-rich	1271 ± 466 (387)	1759 ± 348 (180)	468 ± 69 (180)
Ref. O-rich	729 ± 205 (56)	–	–
Non ref. O-rich	818 ± 207 (761)	–	–
Total O-rich	812 ± 208 (817)	–	–

6.7 Mass-loss rates and other stellar properties

In this section we explain the process through which we derived the mass-loss rate (amongst other stellar properties) of a total of 265 Hi-GAL 1 C-rich AGB stars and 465 Hi-GAL 1 O-rich AGB stars making use of the *DUSTY* code (Ivezic and Elitzur 1994, Ivezic and Elitzur 1997). First, we give a general description of the code (see Sect. 6.7.1.1) together with an overview of the physical principles upon which the code's solutions are based (see Sect. 6.7.1.2 and Appendices B and C) and a list of the inputs required by the program and the outputs it generates (see Sect. 6.7.1.3 and 6.7.1.4). Next, we present and discuss the results obtained for the modelled AGB stars (see Sect. 6.7.2).
The information presented in Sect. 6.7.1.1 - 6.7.1.4 has been extracted from Ivezic and Elitzur (1994) and Ivezic and Elitzur (1997), which we refer the readers to for a more detailed description of the code, its methodology, the input parameters and the obtaining of the output parameters.

6.7.1 DUSTY

6.7.1.1 General description

DUSTY is a *FORTRAN 77* code developed at the University of Kentucky by Ivezic, Nenkova and Elitzur. This code provides a solution for the radiative transfer equation (see Appendix C.1) in a dusty environment. It allows us to study the stellar properties of a cool star positioned at the centre of the density distribution of a dusty shell of inner boundary r_1 and outer boundary r_{out}. These properties include the source's colour temperature distribution, inner radiation field, wind structure and mass-loss rate.

6.7.1.2 Solution method

The DUSTY solution method for the calculation of the source's colour temperature distribution and inner radiation field is based on a self-consistent equation for the radiative transfer, including dust emission, absorption and scattering (see Appendix C.2 and C.3). On the other hand, the source's wind structure and mass-loss rate are computed by solving the hydrodynamic equation of motion, which includes the dust drift and the star's gravitation attraction, as a set coupled to radiative transfer (see Appendix D).

6.7.1.3 Inputs

DUSTY requires a series of input physical parameters to be introduced by the user. These include characteristics of the external radiation, properties of the dust grains and the density distribution of the dust shell. Below we describe the code's inputs and present our choice of parameters. Here, only those methods selected by us are discussed thoroughly. For a complete list of all the methods that are available in DUSTY, we refer the reader to the User manual for DUSTY (Ivezic et al. 1999).

- External radiation

  The user must select an external radiation model that adequately describes the external radiation that arrives to the dust shell inner boundary and that is coming from the central embedded point source. One can choose to describe the emergent spectra of the point source as: (i) a single black body (bb), (ii) a combination of up to 10 bb (each described by a Planck function of a given temperature) or (iii) a broken power law. The user must introduce the number of bb to use, the temperature of each bb and the stellar spectrum in the form of a λ (in μm) and F_λ (in arbitrary units) two-columns list. In our case, we described the emergent spectra of our C-rich and O-rich Hi-GAL 1 AGB stars as a bb with a temperature of T = 3,500 K. This temperature constitutes an upper limit derived by Bloecker (1995) from theoretical calculations of evolution models of low and intermediate-mass stars. The lower limit of this temperature is given by $T \sim 2,000\ K$, which corresponds to the minimum temperature necessary to ignite nuclear fusion in the AGB stellar core. From hereafter, we refer to this temperature as T_{bb}.

- Dust properties

  The user must choose a dust grain size and dust chemical model that adequately describes the dust properties of the dust shell.

  Although DUSTY supports only single-type grains, the program allows the user to set the grain composition to be made of a mixture of grain types. The user must indicate the fractional number abundances that the grains have. One can choose from a total of six grain types that are available in DUSTY. These are: (i) warm and (ii) cold silicates from Ossenkopf et al. (1992) (*Sil-Ow* and *Sil-Oc*), (iii) silicates and (iv) graphite grains from Draine and Lee (1984) (*Sil-DL* and *grf-DL*), (v) amorphous

carbon from Hanner (1988) (*amC-Hn*) and (vi) SiC by Pegourie (1988) (*SiC-Pg*). Alternatively, one can introduce self-defined extra grain types. In our case, we chose the Hi-GAL 1 O-rich AGB stars' dust grains to be composed mainly of warm silicates (i.e. *Sil-Ow*=1.00) and the Hi-GAL 1 C-rich AGB stars' dust grains to be composed mainly of amorphous carbon (i.e. *amC-Hn*=1.00).

- Grain size distribution

  The user must establish a suitable dust grain size distribution for the dust shell. One can choose either: (i) a standard MRN distribution (Mathis et al. 1977, see Eq. 6.7), (ii) a modified MRN distribution (Eq. 6.7 but with different cutoffs and power index) or (iii) a KMH distribution (Kim et al. 1994, see Eq. 6.8).

  $$n(a) \propto a^{-q} \text{ for } a_{min} \leq a \leq a_{max}\,,$$
  $$\text{where } q = 3.5\,,\, a_{min} = 0.005\,\mu m \text{ and } a_{max} = 0.25\,\mu m. \tag{6.7}$$

  $$n(a) \propto a^{-q}\, e^{-a/a_0} \text{ for } a \geq a_{min} \tag{6.8}$$

  In our case, we used a modified MRN distribution with q = 3.5, $a_{min} = 0.005\ \mu m$ and $a_{max} = 1\ \mu m$.

- Dust temperature on the inner boundary

  The user must select an adequate dust temperature T_1 (in K) on the shell inner boundary r_1, which will uniquely determine the external flux F_{e1} entering the dust shell (see Sect. 6.7.1.4).

  In our case, we chose $T_1 = 1000\ K$, which is the typical temperature of dust condensation measured in the laboratory by Tielens (2005).

- Shell thickness

  The user must specify the dust shell thickness $Y = r_{out}/r_1$, where r_{out} and r_1 are the shell outer and inner boundaries respectively. The value of r_{out} conditions the dust temperature at the outer boundary T_{out}, which should be somewhere between ∼20 K (Ziurys 2006) and a few hundred K (Zhang et al. 2009).

  In our case, we chose Y=1000 as it was proved to return adequate T_{out} values.

- Optical depth

  Finally, the user must establish the grid of optical depths τ, at a specified wavelength, to be used by DUSTY in the computation of the models. The user can choose this grid to be spaced either linearly or logarithmically and must introduce two values for the minimum (τ_{min}) and maximum (τ_{max}) optical depths as well as the number of models the user wishes to generate [4]. The user must also enter the wavelength λ_0 (in μm) pertaining to the optical depth τ_0.

  In our case, we selected a logarithmic grid and created 40 different models ranging from $\tau_{min} = 0.01$ to $\tau_{max} = 100$ and chose the fiducial wavelength to be equal to $\lambda_0 = 0.55\ \mu m$.

6.7.1.4 Outputs

In a typical run, DUSTY generates many outputs, the most important being the following:

- f_{Tot}

  This is the spectral shape of the output spectra of the central embedded point source after being processed by the dust shell. For every model run and generated in DUSTY, the program generates a table that contains a list of wavelengths (λ, in μm) and the corresponding emergent fluxes (λF_λ, in $W\ m^{-2}$) allowing the user to plot the emergent spectra in an external program such as IDL.

  In order to compare the DUSTY emergent spectra to the SED of our Hi-GAL 1 AGB stars it is necessary to first, convert the λF_λ fluxes returned from DUSTY to F_ν in Jy[5]. Next, the user has to scale the output emergent spectra to the SED of the source being analysed. This scaling is achieved by simply multiplying the emergent converted fluxes by whichever value provides a good fitting. This value can be roughly [6] described as a joint single constant that is a function of d^2 and L, where d is the star's distance and L is its luminosity.

  Finally, the user has to choose whichever model fits the best the SED of the source being analysed and consider the corresponding model outputs as the source's physical parameters.

[4] The number of models generated by DUSTY is equal to the number of optical depths introduced by the user.

[5] $1\ Jy = 10^{-26}\ W\ m^{-2}\ Hz^{-1}$

[6] The explanation and formalism of this scaling factor is provided in Appendix C.3.

- F_1

  This parameter, hereafter referred to as $Fbol_{in}$, is defined as the bolometric flux (in $W\ m^{-2}$) at the inner radius and is fully determined by the scale chosen in the previous step.

- r_1

  This parameter, hereafter referred to as r_{in}, is the dust shell inner radius (in cm) where the dust temperature is T_1. This radius scales in proportion to $L^{1/2}$, where L is the source's luminosity. The tabulated value corresponds to $L = 10^4 L_{\odot}$.

- r_1/r_c

  This parameter, hereafter referred to as r_{in}/r_{source}, is the ratio between the dust shell inner radius r_{in} and the radius of the central source r_c, hereafter referred to as r_{source}. This quantity scales in proportion to $(T_{bb}/T_{in})^2$ where $T_{bb} = 3,500\ K$.

- $T_d(Y)$

  This parameter, hereafter referred to as T_{out}, gives the dust temperature (in K) at the outer edge of the dust shell.

- $\dot{M}$

  This is the mass-loss rate (in $M_{\odot}\ yr^{-1}$) and it scales in proportion to $L^{3/4}(r_{gd}\rho_s)^{1/2}$ where r_{gd} is the gas-to-dust ratio and ρ_s is the density of the dust solid material. This quantity has $\sim$30% inherent uncertainty.

- V_e

  This parameter, hereafter referred to as v, is defined as the terminal outflow velocity (in $km\ s^{-1}$), scales in proportion to $L^{1/4}(r_{gd}\rho_s)^{-1/2}$ and is subject to the same inherent uncertainty as $\dot{M}$.

- M_{lim}

  Finally, this parameter, termed $M>$ in DUSTY, constitutes an upper limit on the stellar mass M (in $M_{\odot}$) and scales in proportion to $L/(r_{gd}\rho_s)$.

Figure 6.8: C-rich and O-rich AGB star models generated with DUSTY.

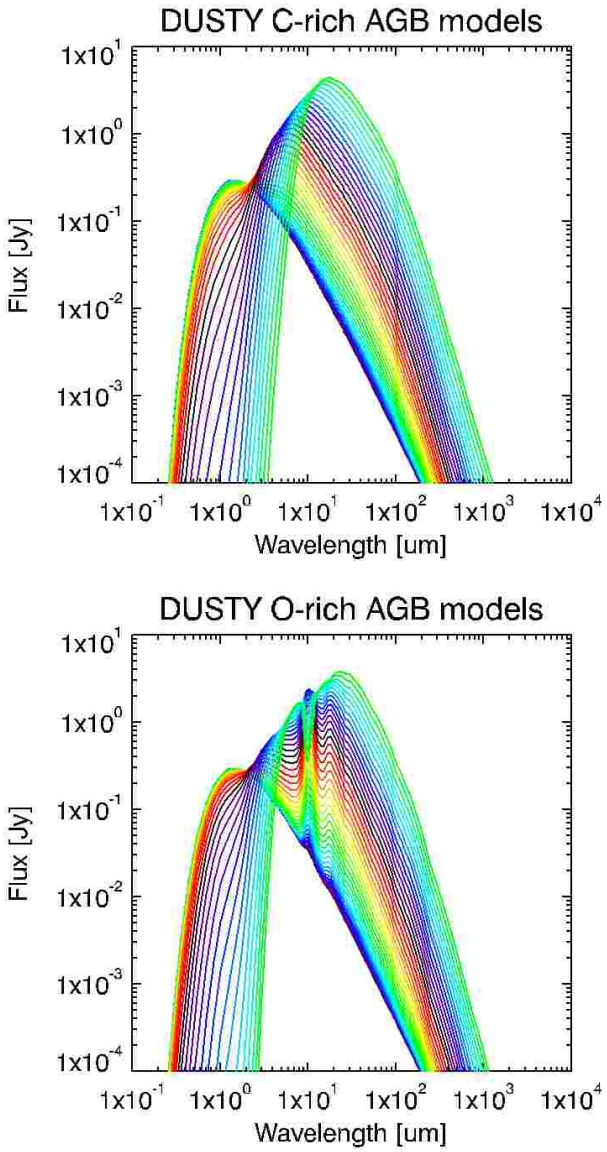

Plotted in Fig. 6.8 are the emergent spectra of the 40 models obtained when running DUSTY with $T_{bb} = 3,500\ K$, $T_1 = 1,000\ K$, $amC - Hn = 1.00$, $q_{MRN} = 3.5$, Y=1,000 and $a_{min} = 0.005\ \mu m$, $a_{max} = 0.25\ \mu m$ (*C-rich AGB star models*). Also plotted are the emergent spectra of the 40 models obtained when running DUSTY with $T_{bb} = 3,500\ K$, $T_1 = 1000\ K$, *Sil-Ow* $= 1.00$, $q_{MRN} = 3.5$, $a_{min} = 0.005\ \mu m$, $a_{max} = 0.25\ \mu m$ and $Y = 1000$ (*O-rich AGB star models*).

6.7.2 Results

The C-rich and O-rich AGB star models generated by DUSTY (see Fig. 6.8) were then used to fit the SED of the 387 Hi-GAL 1 C-rich AGB stars and 817 Hi-GAL 1 O-rich AGB stars that were successfully fitted with 1 Planck function in Sect. 6.6. During the fitting process we made the following observations:

1. In some cases, the model spectra fitted almost perfectly the source's SED (see the top panel of Fig. 6.9 for an example).

2. In other cases, the MIR and FIR tail of the source's SED was well described by the model but in the NIR (i.e. in the 2MASS 1.25 μm, 1.65 μm, 2.17 μm and WISE 4.6 μm bands) the model data points were brighter than those of the source's SED. This can be explained by the fact that at NIR wavelengths the measured fluxes are likely to suffer from interstellar extinction and therefore, they appear to be much fainter than they are in reality. Thus, such overestimation of the NIR model fluxes with respect to the SED fluxes was accepted as a valid fit as long as the model fluxes fell within the extinction-corrected SED fluxes (upper limit) and the SED extinction-uncorrected fluxes (lower limit). In order to correct the SED fluxes from extinction we used the *NASA/IPAC Infrared Science Archive Galactic Dust Reddening and Extinction service*, which provided us with the estimated total Galactic dust extinction (A^c, in mag), as calculated by Schlafly and Finkbeiner (2011), that the sources suffer at multiple wavelengths. The quantities A^c were then subtracted from the SED flux values (in mag) and the resulting flux (in mag) was converted to Jy (see the central panel of Fig. 6.9 for an example).

3. On some occasions, the FIR SED fluxes were brighter than those estimated by the model, i.e. the source presented an excess with respect to the model. This fact can be explained by the possible presence of a detached shell of colder material surrounding the star, which is formed by the dust and gas ejected during the star's thermal pulses (Cox et al. 2012). As this dust shell moves away from the star's photosphere, it increasingly receives less energy input from the star and thus it cools down. With this in mind, such underestimation of the FIR model fluxes with respect to the SED fluxes was accepted as a valid fit (see the bottom panel of Fig. 6.9 for an example).

4. Very often, it was not possible to find a suitable fit between the model spectra and the source SED (see Fig. 6.10 for three examples considered as bad fits).

After examining the fitted SEDs, we established that, in total, 265 Hi-GAL 1 C-rich AGB stars and 465 Hi-GAL 1 O-rich AGB stars were successfully fitted with the DUSTY C and O-rich AGB star models, respectively. Amongst the 265 Hi-GAL 1 C-rich AGB stars, 30 were identified to be reference sources and 235 were confirmed to be non references sources. On the other hand, from the 465 Hi-GAL 1 O-rich AGB stars, 28 were identified to be reference sources and 437 were confirmed to be non references sources.
In the CD accompanying this thesis, one can find two tables containing the complete list of Hi-GAL 1 C-rich and O-rich AGB stars that were successfully modelled with DUSTY together with a summary of the DUSTY output parameters. Included in these tables are:

- The source ID and galactic coordinates l and b (in degrees), as listed in the catalogues of Hi-GAL 1 C-rich and O-rich AGB star candidates.
- A label indicating whether the source is a reference source (*Ref.*) or not (*Non ref.*).
- A label indicating whether the source is classified as a C-rich or an O-rich AGB star.
- The optical depth τ_0, the bolometric flux $Fbol_{in}$ (in $W\ m^{-2}$) at the inner radius, the shell inner radius r_{in} (in cm), the ratio between the shell inner radius r_{in} and the radius of the central source r_{source} (r_{in}/r_{source}), the dust temperature at the envelope's outer edge T_{out} (in K), the mass-loss rate $\dot{M}$ (in $M_{\odot}\ yr^{-1}$), the terminal outflow velocity v (in $km\ s^{-1}$) and the stellar mass upper limit M_{lim} (in $M_{\odot}$) calculated by DUSTY in the selected model.

Also included in the tables are the average values of the parameters previously listed obtained for the Hi-GAL 1 C-rich and O-rich AGB stars. These averages were calculated including both the non reference and the reference sources and are also listed in Table 6.5.

Figure 6.9: Examples of Hi-GAL 1 AGB stars whose SED was successfully reproduced by a DUSTY model.

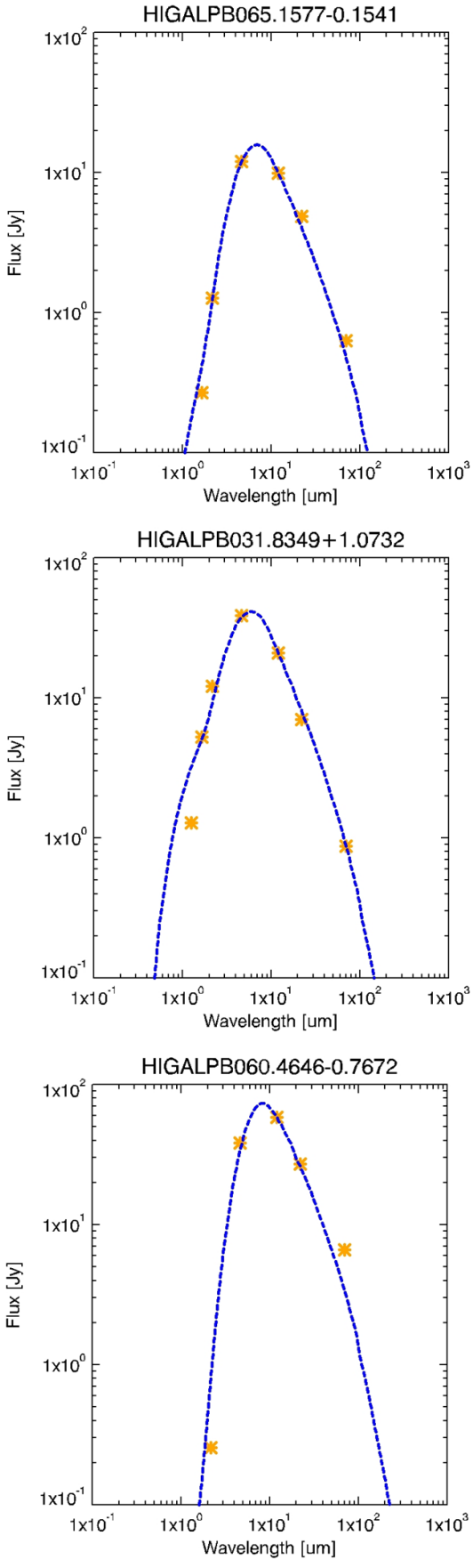

Figure 6.10: Examples of Hi-GAL 1 AGB stars whose SED was not successfully reproduced by a DUSTY model.

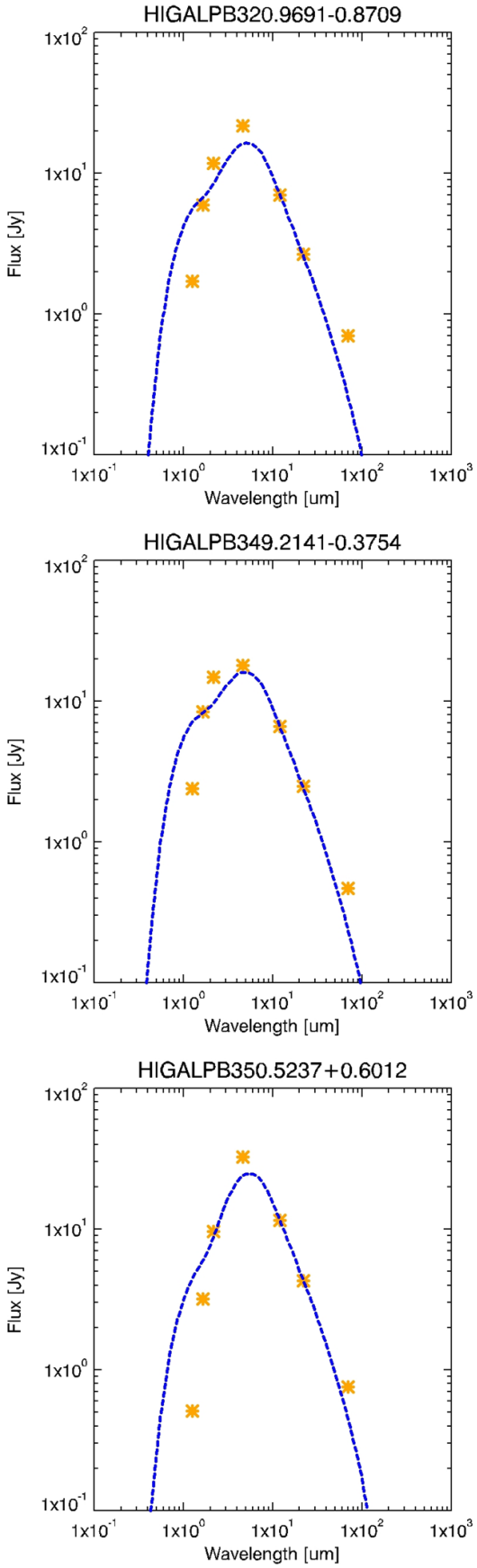

Table 6.5: Mean and STDEV of the optical depth τ_0, the bolometric flux $Fbol_{in}$ (in $W\ m^{-2}$) at the inner radius, the shell inner radius r_{in} (in cm), the ratio between the shell inner radius r_{in} and the radius of the central source r_{source} (r_{in}/r_{source}), the dust temperature at the envelope's outer edge T_{out} (in K), the mass-loss rate $\dot{M}$ (in $M_\odot\ yr^{-1}$), the terminal outflow velocity v (in $km\ s^{-1}$) and the stellar mass upper limit M_{lim} (in $M_\odot$) obtained with DUSTY for the modelled Hi-GAL 1 C and O-rich AGB stars. Indicated within parenthesis is the number of sources considered in the calculation of the parameters' Mean and STDEV.

Hi-GAL 1 C-rich AGB stars		
DUSTY parameters	**Units**	**Mean ± STDEV**
τ_0	–	2.63 ± 2.19 (265)
$Fbol_{in}$	$W\ m^{-2}$	5.73E+04 ± 1.20E+04 (265)
r_{in}	cm	2.35E+14 ± 2.53E+13 (265)
r_{in}/r_{source}	–	12.39 ± 1.34 (265)
T_{out}	K	66 ± 7 (265)
$\dot{M}$	$M_\odot\ yr^{-1}$	5.46E-06 ± 3.51E-06 (265)
v	$km\ s^{-1}$	26.06 ± 3.01 (265)
M_{lim}	$M_\odot$	5.55 ± 1.19 (265)

Hi-GAL 1 O-rich AGB star		
DUSTY parameters	**Units**	**Mean ± STDEV**
τ_0	–	6.71 ± 6.53 (465)
$Fbol_{in}$	$W\ m^{-2}$	2.72E+04 ± 4.36E+03 (465)
r_{in}	cm	3.38E+14 ± 2.88E+13 (465)
r_{in}/r_{source}	–	17.86 ± 1.51 (465)
T_{out}	K	43 ± 3 (465)
$\dot{M}$	$M_\odot\ yr^{-1}$	1.35E-05 ± 7.32E-06 (465)
v	$km\ s^{-1}$	18.17 ± 3.05 (465)
M_{lim}	$M_\odot$	4.69 ± 0.44 (465)

Shown in Fig. 6.11 - 6.16 are the distributions of the optical depth τ_0, the dust shell inner radius r_{in} (in cm), the ratio between the dust shell inner radius r_{in} and the radius of the central source r_{source} (r_{in}/r_{source} ratio), the bolometric flux $Fbol_{in}$ (in $W\ m^{-2}$) at the dust shell inner radius, the dust temperature T_{out} (in K) at the outer edge of the dust shell and the mass-loss rate $\dot{M}$ (in $M_{\odot}\ yr^{-1}$). obtained with DUSTY for the modelled Hi-GAL 1 C-rich and O-rich AGB stars. Also indicated are the average values of the parameters previously listed obtained for the modelled Hi-GAL 1 C-rich and O-rich AGB stars. From the inspection of Fig. 6.11 - 6.16 and Table 6.5 we concluded that:

- It is possible to distinguish the modelled Hi-GAL 1 C-rich AGB stars from O-rich AGB stars by means of: (i) the inner radius r_{in} of the stars' dust shell, (ii) the r_{in}/r_{source} ratio, (iii) the bolometric flux $Fbol_{in}$ at the shell inner radius, (iv) the dust temperature T_{out} at the outer edge of the dust shell and (v) the sources' mass-loss rate $\dot{M}$.

- The optical depth τ_0 found for the modelled Hi-GAL 1 O-rich AGB stars is, in general, greater than that found for the modelled Hi-GAL 1 C-rich AGB stars. This result implies that the O-rich AGB stars are either located at greater distances or that they have larger quantities of dust in their shells. If the latter was true, then these results would suggest that our sample of modelled Hi-GAL 1 O-rich AGB stars are most likely OH/IR-stars, which are known to have very thick dust shells (Justtanont and Tielens 1992). The fact of having used OH/IR-stars as reference objects for the derivation of the colour cuts that we used to separate the Hi-GAL 1 AGB star candidates into C and O-rich AGB stars (see Sect. 5.8.1), would explain why our colour cuts preferably selected OH/IR-stars over other O-rich stellar types.

- The inner radius r_{in} of the dust shell found for the modelled Hi-GAL 1 O-rich AGB stars is much larger than that found for the modelled Hi-GAL 1 C-rich AGB stars, which indicates that the dust shells of the Hi-GAL 1 O-rich AGB stars are more detached from the central source. This result agrees with the structure predicted for OH/IR-stars (Justtanont and Tielens 1992).

- The r_{in}/r_{source} ratio found for the modelled Hi-GAL 1 O-rich AGB stars is much larger than that found for the modelled Hi-GAL 1 C-rich AGB stars, which is a consequence of the previous result.

- The bolometric flux $Fbol_{in}$ at the inner dust shell radius found for the modelled Hi-GAL 1 C-rich AGB stars is much greater than that found for the modelled Hi-GAL 1 O-rich AGB stars. This result can be explained by the greater detachment of the Hi-GAL 1 O-rich AGB dust shells with respect to the central source.

- The dust temperature T_{out} at the outer edge of the dust shell of the modelled Hi-GAL 1 C-rich AGB stars was found to be much greater than that found for the modelled Hi-GAL 1 O-rich AGB stars. This result is a consequence of the greater detachment of the Hi-GAL 1 O-rich AGB dust shells with respect to the central source - the further is the dust shell, the less external radiation will receive from the central source and thus, the colder will the dust shell be.

- Finally, the mass-loss rate $\dot{M}$ found for the modelled Hi-GAL 1 O-rich AGB stars was found to be generally greater than that found for the modelled Hi-GAL 1 C-rich AGB stars. This result agrees with the fact that OH/IR-stars suffer from mass-loss rates stronger than that of C-rich AGB stars (Justtanont and Tielens 1992).

The stellar properties derived in this section were added to the catalogues of Hi-GAL 1 PSC O-rich and C-rich AGB star candidates under columns labelled with the parameters' name.

The agreement found between the stellar properties derived in DUSTY and our classification of the Hi-GAL 1 PSC C-rich and O-rich AGB stars confirms the effectiveness of DUSTY in the obtaining of the stellar properties of AGB stars. It also constitutes the final confirmation that our colour criteria are capable of: (i) successfully separating the AGB stars from the YSOs, HII regions and PNe within the Hi-GAL 1 PSC and (ii) adequately classifying the discriminated AGB stars into C-rich and O-rich AGB types.

Figure 6.11: Distribution of the optical depth τ_0 found with DUSTY for the modelled Hi-GAL 1 C-rich (in blue) and O-rich (in red) AGB stars. Also indicated are the average τ_0 values obtained for the modelled Hi-GAL 1 C-rich (in cyan) and O-rich (in orange) AGB stars.

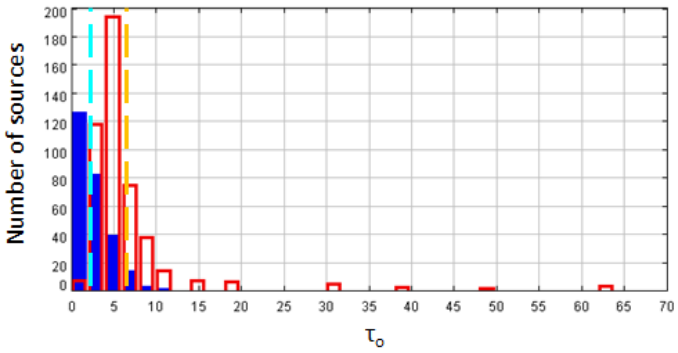

Figure 6.12: Distribution of the inner radius r_{in} (in cm) of the dust shell found with DUSTY for the modelled Hi-GAL 1 C-rich (in blue) and O-rich (in red) AGB stars. Also indicated are the average r_{in} values obtained for the modelled Hi-GAL 1 C-rich (in cyan) and O-rich (in orange) AGB stars.

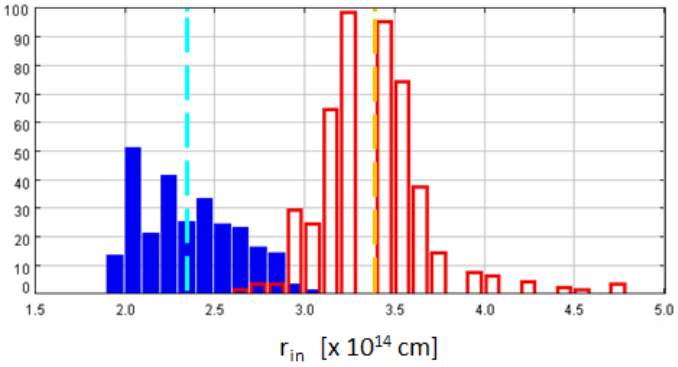

Figure 6.13: Distribution of the ratio between the dust shell inner radius r_{in} and the radius of the central source r_{source} (r_{in}/r_{source} ratio) found with DUSTY for the modelled Hi-GAL 1 C-rich (in blue) and O-rich (in red) AGB stars. Also indicated are the average r_{in}/r_{source} values obtained for the modelled Hi-GAL 1 C-rich (in cyan) and O-rich (in orange) AGB stars.

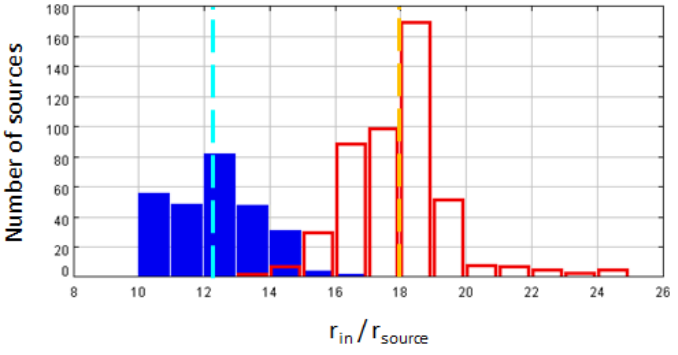

Figure 6.14: Distribution of the bolometric flux $Fbol_{in}$ (in $W\ m^{-2}$) at the inner dust shell radius found with DUSTY for the modelled Hi-GAL 1 C-rich (in blue) and O-rich (in red) AGB stars. Also indicated are the average $Fbol_{in}$ values obtained for the modelled Hi-GAL 1 C-rich (in cyan) and O-rich (in orange) AGB stars.

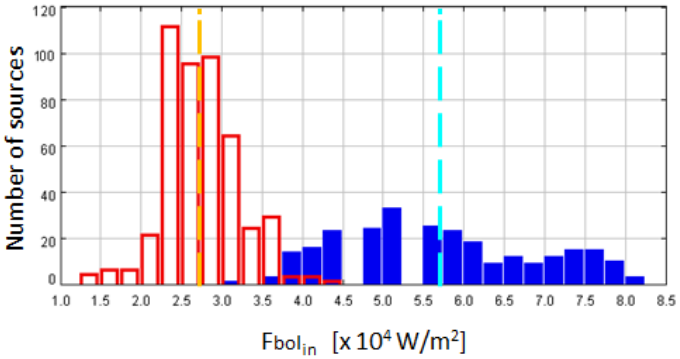

Figure 6.15: Distribution of the dust temperature T_{out} (in K) at the outer edge of the dust shell found with DUSTY for the modelled Hi-GAL 1 C-rich (in blue) and O-rich (in red) AGB stars. Also indicated are the average T_{out} values obtained for the modelled Hi-GAL 1 C-rich (in cyan) and O-rich (in orange) AGB stars.

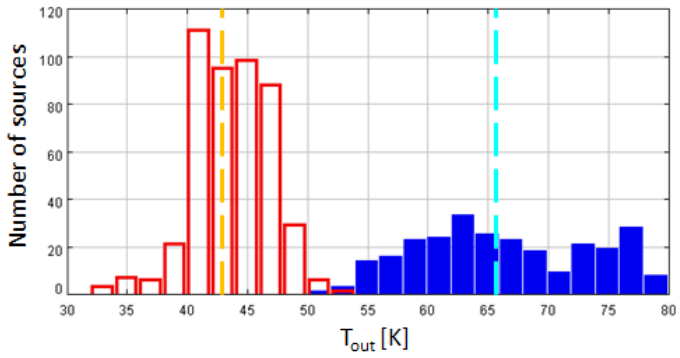

Figure 6.16: Distribution of the mass-loss rate $\dot{M}$ (in $M_{\odot}\ yr^{-1}$) found with DUSTY for the modelled Hi-GAL 1 C-rich (in blue) and O-rich (in red) AGB stars. Also indicated are the average $\dot{M}$ values obtained for the modelled Hi-GAL 1 C-rich (in cyan) and O-rich (in orange) AGB stars.

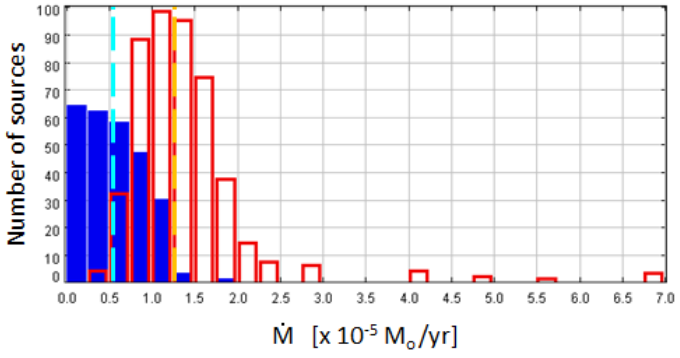

6.8 Establishing relations between the stellar properties

6.8.1 Relation between Tc, T_{bb} and τ_0

In this section we discuss the differences between the colour temperatures Tc and the DUSTY input temperatures T_{bb} and how these temperatures are related to the optical depth τ_0. On the one hand, the Tc temperatures were calculated in Sect. 6.6 by fitting a black body (bb) function to the SEDs of the 761 Hi-GAL 1 C-rich AGB stars and the 1,442 Hi-GAL 1 O-rich AGB stars whose SEDs were classified as *smooth* (see Sect. 6.3). In the case of the Hi-GAL 1 C-rich AGB stars, the average colour temperature was found to be $< Tc >_{C-rich} = 1,271\ K$ whereas in the case of the Hi-GAL 1 O-rich AGB stars, the average colour temperature was found to be $< Tc >_{O-rich} = 812\ K$ (see Table 6.4). On the other hand, the temperature $T_{bb} = 3,500\ K$ is an input of DUSTY, which was defined in Sect. 6.7.1.3 as the temperature of the black body used to describe the emergent spectra of the central source embedded in the dust shell. As we mentioned in Sect. 6.7.1.3, this temperature constitutes an upper limit derived by Bloecker (1995) from theoretical calculations of evolution models of low and intermediate-mass stars and its lower limit is given by $T_{bb} = 2,000\ K$, which corresponds to the minimum temperature necessary to ignite nuclear fusion in the AGB stellar core.

The difference between the Tc and $T_{bb} = 3,500\ K$ temperatures can be explained by the presence of the dust shell around the AGB stars and thus, it is related to the optical depths τ_0 calculated in DUSTY. Let us consider a first case in which an AGB star is embedded in a thin dust shell. In these circumstances, given that the star will be optically thin (τ_0<1), we will be able to detect the radiation coming from the star's photosphere whose spectral shape will be similar to that given by the Planck function at $T_{bb} = [2000, 3500]\ K$.

As a result, in this case, the source temperature Tc obtained from the bb-fitting will be similar to the $T_{bb} = 3,500\ K$ temperature established in DUSTY. Let us now consider a second case in which an AGB star is embedded in a very thick dust shell. In these circumstances, the star will be optically thick (τ_0>1) and thus we will no longer be able to detect the radiation coming from the star's photosphere. Instead, we will detect the dust-processed emergent spectra, which will be shifted to IR wavelengths. As a result, in this case, the source temperature Tc obtained from the bb-fitting will be cooler than the $T_{bb} = 3,500\ K$ temperature established in DUSTY. A clear evidence of the relation between Tc and τ_0 can be seen in Fig. 6.17 where we plotted the τ_0 values obtained in

DUSTY against the Tc values obtained in the bb-fitting for the reference and non reference Hi-GAL 1 C-rich AGB stars modelled with DUSTY. Here, we can see that the lower the sources' optical depth τ_0 found with DUSTY, the greater the sources' Tc temperature obtained from the bb-fitting and the closer is the Tc value to $T_{bb} = [2000, 3500]\ K$. The relation found between the Tc and τ_0 for the modelled Hi-GAL 1 C-rich AGB stars can be expressed by Eq. 6.9.

$$Tc = -402.4\ \ln(\tau_0) + 1464\ [K] \tag{6.9}$$

In the case of the modelled Hi-GAL 1 O-rich AGB stars, the relation between the Tc and the τ_0 values can still be observed as a general trend (see Fig. 6.18) but the values are more spread than in the case of the Hi-GAL 1 C-rich AGB stars. The general relation found between the Tc and τ_0 for the modelled Hi-GAL 1 O-rich AGB stars is best described by Eq. 6.10.

$$Tc = 1543.1\ \tau_0^{-0.362}\ [K] \tag{6.10}$$

6.8.2 Relation between Tc and $\dot{M}$

Our results show that the sources' colour temperatures Tc are also related to the mass-loss rates $\dot{M}$ derived in DUSTY. In the case of the modelled Hi-GAL 1 C-rich AGB stars (see Fig. 6.19), this relation is very well defined and is given by Eq. 6.11.

$$Tc = -535.1\ \ln(\dot{M}) + 2021.5\ [K]\ \ ;\ \ \text{with}\ [\dot{M}] = 10^{-6}\ M_{\odot}/yr \tag{6.11}$$

On the other hand, for the modelled Hi-GAL 1 O-rich AGB stars (see Fig. 6.20), the relation between the Tc and the $\dot{M}$ is more scattered but still, we can see a general correspondence between the two quantities that is best described by Eq. 6.12.

$$Tc = 3032.8\ \dot{M}^{-0.514}\ [K]\ \ ;\ \ \text{with}\ [\dot{M}] = 10^{-6}\ M_{\odot}/yr \tag{6.12}$$

The Eq. 6.11 and 6.12 constitute two very important relations as they could be used to estimate the mass-loss rates of unknown C-rich and O-rich AGB stars from their colour temperatures which, as we showed in Sect. 6.6, are fairly easy to obtain.

Figure 6.17: Relation between the colour temperature Tc and the optical depth τ_0 found with DUSTY for the modelled reference (in blue) and non reference (in red) Hi-GAL 1 C-rich AGB stars. Also shown is the equation (Eq. 6.11) that describes the relation found between the Tc and τ_0 of the modelled Hi-GAL 1 C-rich AGB stars.

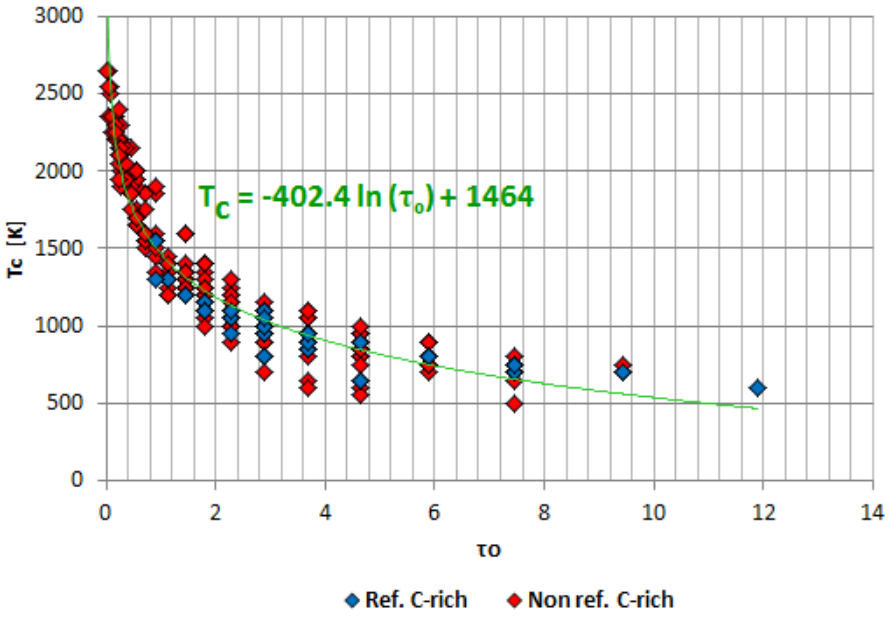

Figure 6.18: Relation between the colour temperature Tc and the optical depth τ_0 found with DUSTY for the modelled reference (in cyan) and non reference (in grey) Hi-GAL 1 O-rich AGB stars. Also shown is the equation (Eq. 6.12) that describes the relation found between the Tc and τ_0 of the modelled Hi-GAL 1 O-rich AGB stars.

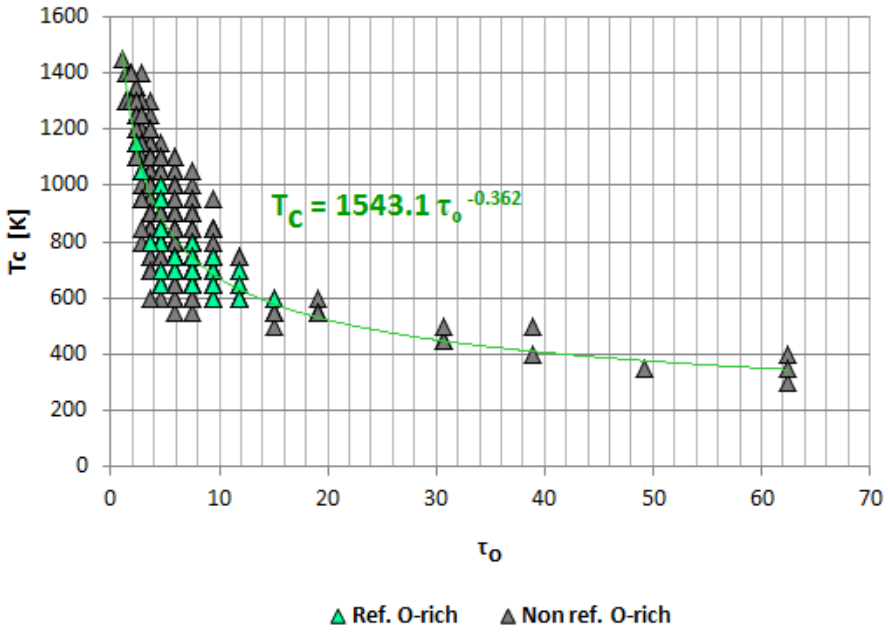

Figure 6.19: Relation between the colour temperature Tc and the mass-loss rate $\dot{M}$ (in units of 10^{-6} $M_{\odot}/yr$) found with DUSTY for the modelled reference (in blue) and non reference (in red) Hi-GAL 1 C-rich AGB stars. Also shown is the equation (Eq. 6.11) that describes the relation found between the Tc and $\dot{M}$ of the modelled Hi-GAL 1 C-rich AGB stars.

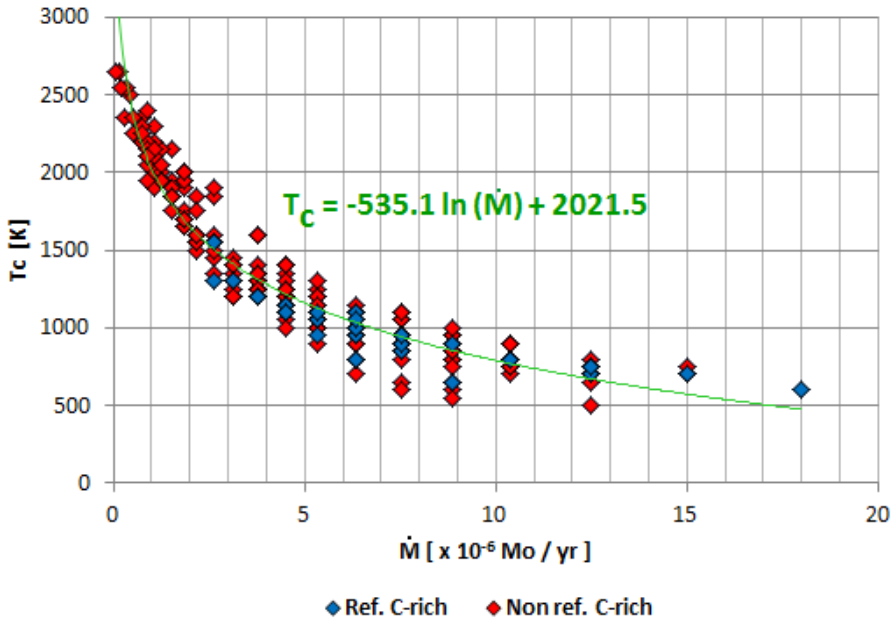

Figure 6.20: Relation between the colour temperature Tc and the mass-loss rates $\dot{M}$ (in units of 10^{-6} $M_{\odot}/yr$) found with DUSTY for the modelled reference (in cyan) and non reference (in grey) Hi-GAL 1 O-rich AGB stars. Also shown is the equation (Eq. 6.12) that describes the relation found between the Tc and $\dot{M}$ of the modelled Hi-GAL 1 O-rich AGB stars.

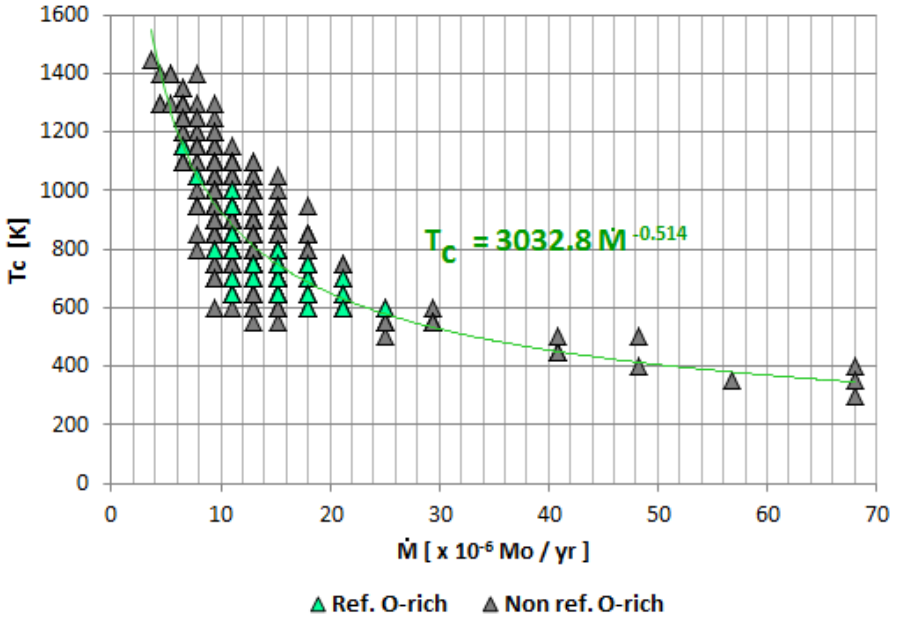

Moreover, we found that for the modelled Hi-GAL 1 C-rich AGB stars, there is a well defined relation between: (i) the mass-loss rates $\dot{M}$ and the outflow velocities v obtained with DUSTY and (ii) the stars' colour temperatures Tc and (iii) luminosities L. This relation can be expressed as:

$$\log Q(Tc) = -1.6\,(\log Tc)^2 + 7.5\,\log Tc - 13.4\;\;[K] \tag{6.13}$$

where the quantity Q(Tc) is given by:

$$Q(Tc) = \left(\frac{\dot{M}}{M_{\odot}\;yr^{-1}}\right)\left(\frac{km\;s^{-1}}{v}\right)\left(\frac{10^6\;L_{\odot}}{L}\right)^{0.7}\;\;;\;\;\text{with}\;L = 10^4\;L_{\odot}. \tag{6.14}$$

In the case of the modelled Hi-GAL 1 O-rich AGB stars (see Fig. 6.22), the relation between the $\log Q$ and $\log Tc$ is more scattered but we can still see a general correspondence between the two quantities that is best described by Eq. 6.12.

$$\log Q(Tc) = 1.7\,(\log Tc)^2 - 12.1\,\log Tc + 15.7\;\;[K] \tag{6.15}$$

The existence of a general relation between the $\log Q(Tc)$ and the $log\dot{M}$ quantities was established by Davidson (1987) when modelling Luminous Blue Variables with a simple radiative diffusion model (see Davidson 1987 for details).

Although the typical luminosities, mass-loss rates and outflow velocities of Luminous Blue Variables ($L \sim 10^{5-6}\;L_{\odot}$, $\dot{M}$>$10^{-4}\;M_{\odot}/yr$, v>$100\;km/s$, Davidson 1987) are much greater than those found for the modelled Hi-GAL 1 C-rich and O-rich AGB stars ($L \sim 10^4\;L_{\odot}$, $\dot{M}_{C-rich} \sim 10^{-6}\;M_{\odot}/yr$ and $\dot{M}_{O-rich} \sim 10^{-5}\;M_{\odot}/yr$, $v_{C-rich} = 26\;km/s$ and $v_{O-rich} = 18\;km/s$), we show here that such relation can also be found for the modelled Hi-GAL 1 C-rich and O-rich AGB stars and it is given by the Eq. 6.13 and 6.15, respectively.

6.8.3 Relation between $\dot{M}$ and T_{bb}

Next, we discuss the relation found by Wachter et al. (2002) between the mass-loss rates of AGB stars and the sources' luminosities L and effective temperatures T_{eff}. In the case of the modelled Hi-GAL 1 C-rich and O-rich AGB stars, the effective temperature of the sources was set to be $T_{bb} = 3,500\;K$ in DUSTY.

Wachter et al. (2002) used pulsating wind models to derive a relation between the effective temperature T_{eff}, the luminosity L and the mass M of C-rich tip-AGB stars.

These models (see Winters et al. 2000 for a description of the code) included: (i) time-dependent hydrodynamics, (ii) chemistry, (iii) radiative transfer and (iv) carbon dust formation, growth and evaporation processes. The models considered C-rich AGB stars with stellar masses within the $M = [0.8, 1.2]\;M_{\odot}$ range, effective temperatures within the

Figure 6.21: Relation between the colour temperature Tc, the mass-loss rate $\dot{M}$, the outflow velocity v and the luminosity L of the modelled reference (in blue) and non reference (in red) Hi-GAL 1 C-rich AGB stars.
The quantity Q is given by:

$$Q(Tc) = \left(\frac{\dot{M}}{M_{\odot}\ yr^{-1}}\right)\left(\frac{km\ s^{-1}}{v}\right)\left(\frac{10^6\ L_{\odot}}{L}\right)^{0.7}$$

Also shown is the equation (Eq. 6.13) that describes the relation found between the $\log Q$ and $\log Tc$ of the modelled Hi-GAL 1 C-rich AGB stars.

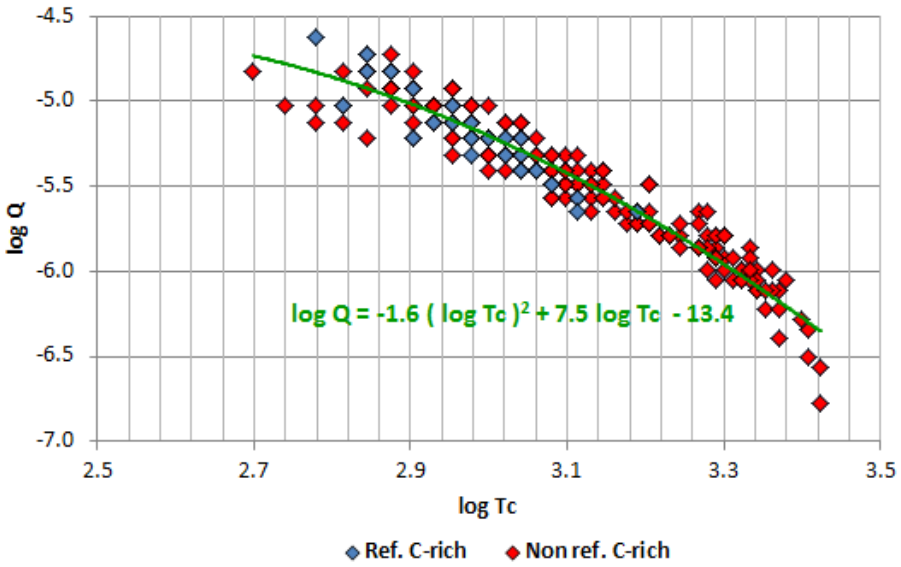

Figure 6.22: Relation between the colour temperature Tc, the mass-loss rate $\dot{M}$, the outflow velocity v and the luminosity L of the modelled reference (in cyan) and non reference (in grey) Hi-GAL 1 O-rich AGB stars. The quantity Q is defined as in Fig. 6.21. Also shown is the equation (Eq. 6.15) that describes the relation found between the $\log Q$ and $\log Tc$ of the modelled Hi-GAL 1 O-rich AGB stars.

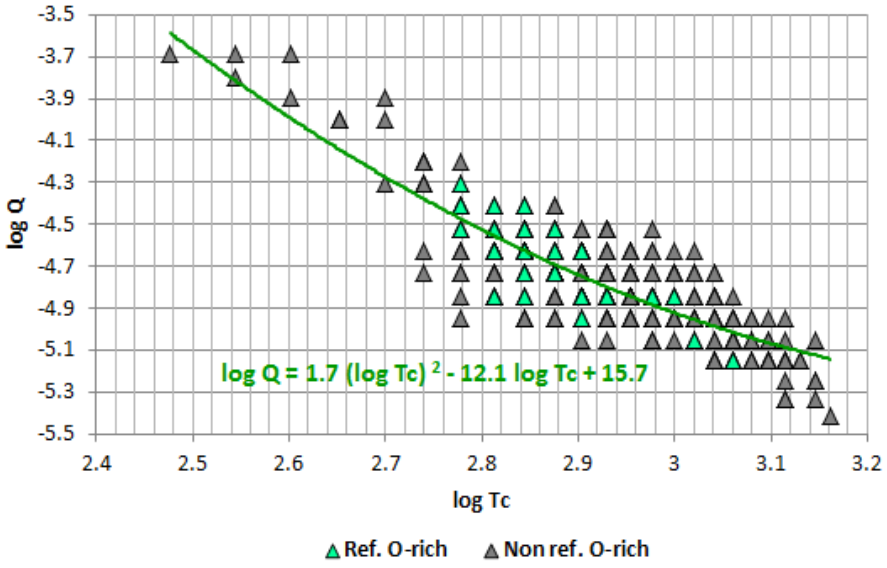

$T_{eff} = [2200, 3000]\ K$ range, luminosities within the $L = [3500, 15000]\ L_{\odot}$ range and pulsation periods (P) of 104 to 1,000 days. The mass-loss rates obtained in the models were then employed to derive the mass-loss formula given in Eq. 6.16, which Wachter et al. (2002) claim it only applies to the mass-loss of Carbon-rich stars that have strong dust-driven winds.

$$\log \dot{M} = -4.52 - 6.81 \log \left(T_{eff}/2600K\right) + 2.47 \log \left(\frac{L}{10^4\ L_{\odot}}\right) - 1.95 \log \left(\frac{M}{M_{\odot}}\right) \tag{6.16}$$

We now compare the mass-loss rates that we obtained in DUSTY for the modelled Hi-GAL 1 C-rich AGB stars to the mass-loss rates that we obtain when using the Eq. 6.16 with: (i) $T_{eff} = T_{bb} = 3,500\ K$, $L = 10^4\ L_{\odot}$ set in DUSTY and with (ii) M equal to the upper limit stellar masses (M_{lim}) derived in DUSTY.

Shown in Fig. 6.23 are the mass-loss rates ($\dot{M}_{DUSTY}$, in $10^{-7}\ \dot{M}/yr$) that we obtained with DUSTY plotted against the mass-loss rates ($\dot{M}_{Wachter}$, in $10^{-7}\ \dot{M}/yr$) that we calculated using the equation from Wachter et al. (2002). Here, we can see that the $\dot{M}_{DUSTY}$ mass-loss rates do not match with the $\dot{M}_{Wachter}$ mass-loss rates. However, there appears to be a relation between these two quantities. This relation is best approximated by Eq. 6.17 for $\dot{M}_{DUSTY} < 7 * 10^{-6}\ \dot{M}/yr$.

$$\dot{M}_{DUSTY} = 70.57\ (\dot{M}_{Wachter})^{\ -1.354}\ [10^{-7}\ \dot{M}/yr] \quad ; \quad \text{valid for } [\dot{M}] < 7 * 10^{-6}\ M_{\odot}/yr \tag{6.17}$$

The origin of such relation is unknown and requires further investigation.

6.8.4 Relation between $\dot{M}$ and [J]-[K]

Finally, we present two expressions that establish a relation between the mass-loss rates $\dot{M}$ derived in DUSTY for the modelled Hi-GAL 1 C-rich and O-rich AGB stars and the sources' [J]-[K] colours.

On the one hand, the modelled Hi-GAL 1 C-rich AGB stars were found to verify that:

$$log\dot{M} = 0.77\ \ln([J] - [K]) - 0.4\ [10^{-6}\ M_{\odot}/yr] \tag{6.18}$$

On the other hand, the modelled Hi-GAL 1 O-rich AGB stars were found to verify that:

$$\log \dot{M} = 0.11\ \ln([J] - [K]) + 0.9\ [10^{-6}\ M_{\odot}/yr] \tag{6.19}$$

The results obtained with the previous two equations are similar to the results found by Le Bertre (1997) and Le Bertre and Winters (1998).

In the case of the C-rich AGB stars, Le Bertre (1997) established that these stars verify that:

$$\log \dot{M} = \frac{-6.0}{([J]-[K])-0.2} + 2.0 \ [10^{-6}\ M_{\odot}/yr] \tag{6.20}$$

$$\text{with } [\dot{M}] = 10^{-6}\ M_{\odot}/yr \ \ , \ \ \dot{M} = [-2,\ 2] \times 10^{-6}\ M_{\odot}/yr \ \text{ and } \ [J]-[K] = [0,\ 9]$$

Le Bertre (1997) derived the previous relation from the mass-loss rates $\dot{M}$ obtained when modelling a total of 23 C-rich AGB stars with the radiative transfer model of Le Bertre et al. (1995), which requires the stars' distance and outflow velocity. While the stellar distances were derived from the Period-Luminosity relation for C-stars of Groenewegen and Whitelock (1996) using the periods observationally measured by Le Bertre (1992), the outflow velocities were taken from the catalogue of Loup et al. (1993) who estimated them *from half the width at zero level of the CO millimetre emission lines.*

In the case of the O-rich AGB stars, Le Bertre and Winters (1998) established that these stars verify that:

$$\log \dot{M} = \frac{-2.5}{([J]-[K])-0.65} + 1.75 \ [10^{-6}\ M_{\odot}/yr] \tag{6.21}$$

$$\text{with } [\dot{M}] = 10^{-6}\ M_{\odot}/yr \text{ and } 1.6 \ \leq \ [J]-[K] \ \leq \ 6.0$$

Le Bertre and Winters (1998) derived the previous relation from the mass-loss rates $\dot{M}$ obtained when modelling a total of 12 O-rich Mira-stars with the radiative transfer model of Le Sidaner and Le Bertre (1993), which requires the stars' distance and outflow velocity. While the stellar distances were derived from the Period-Luminosity relation for O-rich Miras of Feast (1996), *the outflow velocities were estimated from the separation of the OH maser peaks or from the width of the CO (J = 2-1 / 1-0) molecular lines.*

Fig. 6.24 shows the relation between the mass-loss rates $\dot{M}$ found for the modelled Hi-GAL 1 C-rich and O-rich AGB stars and their [J]-[K] colours. Also included in the figure are the trendlines from the mass-loss rates obtained with Eq. 6.20 and 6.21, respectively. From Fig. 6.24, we can see that in our case, the separation between the modelled Hi-GAL 1 C-rich and O-rich AGB stars is not as clear as that of Le Bertre (1997) and Le Bertre and Winters (1998) since the Hi-GAL 1 O-rich AGB stars are lying close to the Hi-GAL 1 C-rich AGB stars. Nevertheless, taking into account the simplicity of the DUSTY radiative transfer solution method, which does not require neither the sources' distances nor the outflow velocities, we concluded that our results constitute a very good approximation.

Figure 6.23: Below, we compare the mass-loss rates found for the modelled reference (in blue) and non reference (in red) Hi-GAL 1 C-rich AGB stars with DUSTY($\dot{M}_{DUSTY}$, in 10^{-7} $M_{\odot}/yr$) with the mass-loss rates ($\dot{M}_{Wachter}$, in 10^{-7} $M_{\odot}/yr$) obtained when using the Eq. 6.16 from Wachter et al. (2002) with: (i) $T_{eff} = T_{bb} = 3,500$ K and $L = 10^4$ $L_{\odot}$ set in DUSTY and with (ii) M equal to the upper limit stellar mass (M_{lim}) derived in DUSTY. Also shown is the equation that approximately describes the relation between $\dot{M}_{Wachter}$ and $\dot{M}_{DUSTY}$ for $\dot{M}_{DUSTY} < 7*$ 10^{-6} $\dot{M}/yr$.

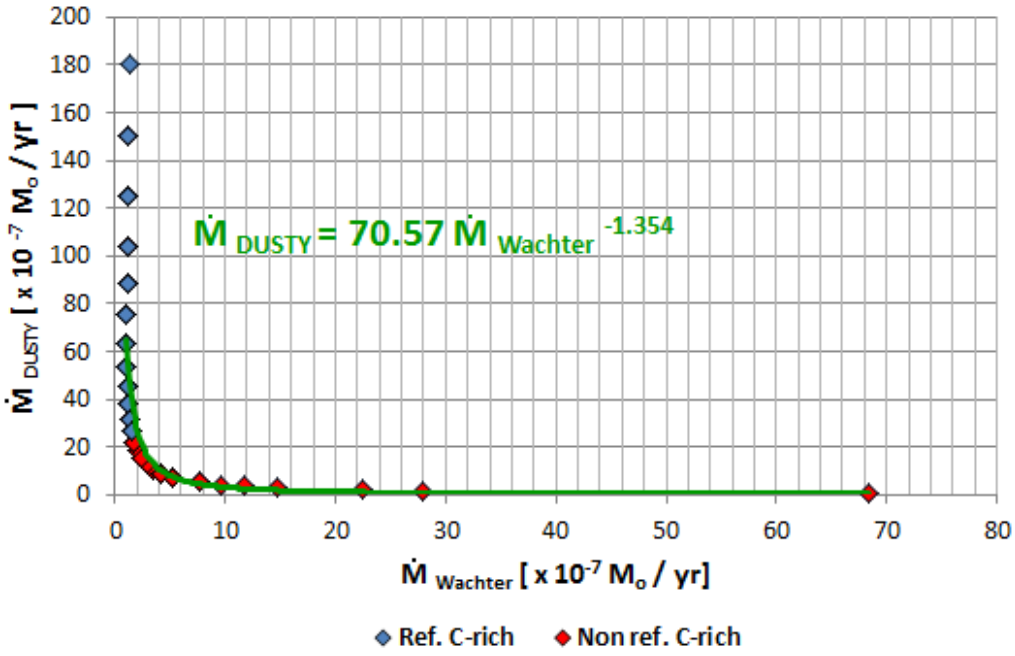

Figure 6.24: Below, we compare the relations between the mass-loss rate and the [J]-[K] colour of C-rich and O-rich AGB stars found by Le Bertre (1997) and Le Bertre and Winters (1998) with the relation we found for the modelled Hi-GAL 1 C-rich and O-rich AGB stars. The trendlines from the mass-loss rates we obtained, (with the equations shown in the diagram), for the modelled Hi-GAL 1 C and O-rich AGB stars are indicated with a cyan and green dashed line, respectively whereas the trendlines from the mass-loss rates of C and O-rich AGB stars derived by Le Bertre (1997) and Le Bertre and Winters (1998) are indicated with a blue and orange solid line, respectively.

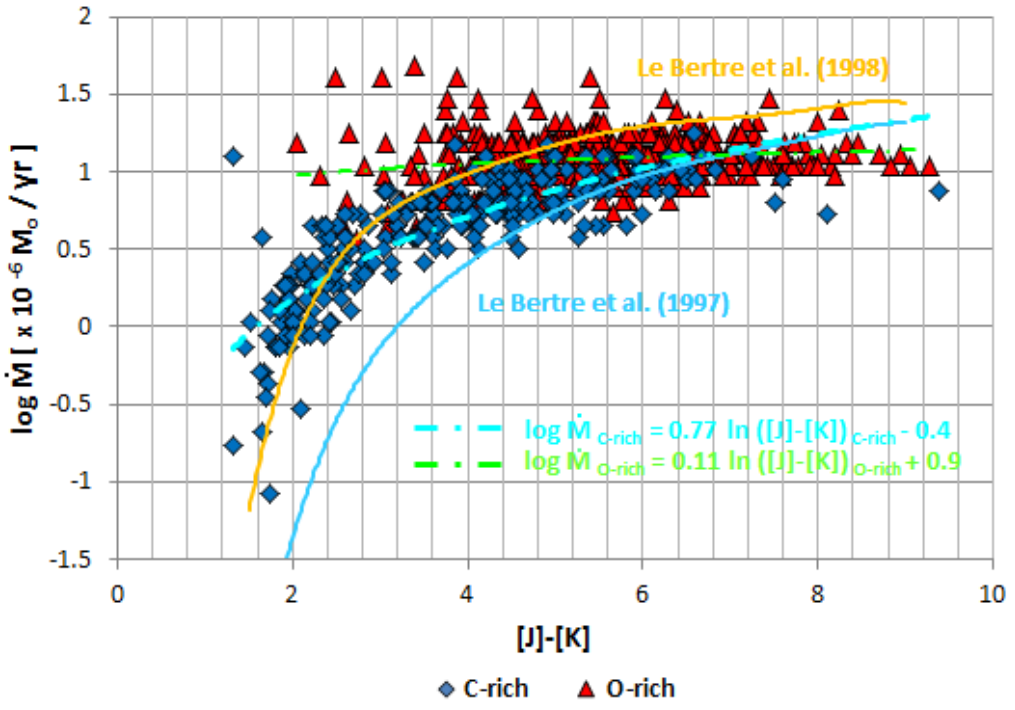

6.9 Summary and conclusions

The purpose of this chapter was to derive the bolometric flux, distance, colour temperature and mass-loss rate (amongst other stellar parameters) for a sub-sample of the 1,721 and 848 sources contained in the catalogues of Hi-GAL 1 PSC O-rich and C-rich AGB star candidates.

In order to accomplish such goal, we first smoothed the sources' Spectral Energy Distributions (SEDs). This was achieved by excluding, from the sources' SEDs, those fluxes: (i) that were measured in bands whose beam size was greater than 18" and (ii) for which more accurate flux measurements were available at a nearby wavelength. The resulting SEDs were then visually inspected in order to detect and reject any SEDs that were left with too few points or were still not sufficiently smooth. After the process, a total of 279 O-rich and 87 C-rich AGB stars were rejected. From the remaining 1,442 O-rich AGB stars, 101 (1,341) stars were identified as being reference (non reference) sources whereas, from the remaining 761 C-rich AGB stars, 55 (706) stars were identified as being reference (non reference) sources. This sub-sample of sources was then used to calculate the stellar properties.

The first stellar property that we derived was the sources' bolometric fluxes F_{bol}. These quantities were calculated through integration of the sources' SEDs over their wavelength range. The results obtained showed that: (i) for the Hi-GAL 1 PSC O-rich AGB stars $F_{bol}^{O-rich} = [2.26E-13,\ 2.69E-10]\, W\, m^{-2}$ while (ii) for the Hi-GAL 1 PSC C-rich AGB stars $F_{bol}^{C-rich} = [1.20E-13,\ 3.90E-10]\, W\, m^{-2}$. The average bolometric flux ($< F_{bol} >$) found for the Hi-GAL 1 PSC C-rich AGB stars ($< F_{bol} >^{C-rich} = 2.75E-11\ W\, m^{-2}$) was found to be 4.4 times greater than that found for the Hi-GAL 1 PSC O-rich AGB stars ($< F_{bol} >^{O-rich} = 6.23E-12\ W\, m^{-2}$), which could be a consequence of the C-rich AGB stars being closer to us.

The second stellar property that we estimated was the sources' nominal distances d. These distances were calculated under the assumption of the sources' bolometric luminosities being $L = 10^4\ L_{\odot}$, as in DUSTY. The results obtained showed that the majority of C-rich AGB stars were found to lie within $d = [2,\ 6]\ kpc$ whereas the O-rich AGB stars expanded over the $d = [4,\ 16]\ kpc$ range. The previous findings led us to the conclusion that the (nominal) distances found for the majority of Hi-GAL 1 O-rich AGB stars were incorrect whereas those found for most of the Hi-GAL 1 C-rich AGB stars were fairly reasonable.

The previous result could be due to the fact that the bolometric luminosities of the Hi-GAL 1 O-rich AGB stars are much lower than the assumed value of $L_{bol} = 10^4\ L_{\odot}$ in reality. Another possibility is that the bolometric fluxes that we derived in Sect. 6.4 for the Hi-GAL 1 PSC O-rich AGB stars could be highly underestimated. The latter hypothesis would imply that the Hi-GAL 1 PSC O-rich AGB stars are heavily extinguished as a result of being further away from us and/or because of the large dust quantities these stars are embedded in. Our results also showed that the number of Hi-GAL 1 C-rich AGB stars found across the Galactic longitudes could be related to Galactic structure.

The third stellar property that we derived was the sources' colour temperatures Tc. These temperatures were obtained by fitting one or two Planck functions to the sources' SEDs. For the one bb-fitted sources, the fit was done over the [1.25, 500] μm range. On the other hand, for the two bb-fitted sources, the fit for the warm SED component was done over the [1.25, 10] μm range whereas the fit for the cold SED component was done over the (10, 500] μm range. From all the 761 Hi-GAL 1 C-rich AGB stars whose SED was classified as *smooth*, only 567 stars (75%) were found to be successfully fitted with one (387 sources) or two (180 sources) Planck functions. On the other hand, from all the 1,442 Hi-GAL 1 O-rich AGB stars whose SED was classified as *smooth*, only 817 stars (57%) were found to be successfully fitted with one Planck function. We found no cases of O-rich AGB stars that were well fitted with two Planck functions.

The results obtained showed that the average colour temperatures ($< Tc >$) found for the reference and non reference Hi-GAL 1 C-rich AGB stars that were fitted with one Planck function ($< Tc >^{C-rich}_{Ref.} = 1,092\ K$ and $< Tc >^{C-rich}_{Non\ ref.} = 1,296\ K$, respectively) were slightly greater than those found for the reference and non reference Hi-GAL 1 O-rich AGB stars ($< Tc >^{O-rich}_{Ref.} = 729\ K$ and $< Tc >^{O-rich}_{Non\ ref.} = 818\ K$, respectively). The higher $< Tc >$ found for the Hi-GAL 1 C-rich AGB stars could be due to the Hi-GAL 1 O-rich AGB stars suffering from more extinction in the NIR for being further from us.

Next, we used the *DUSTY* radiative transfer code to derive: (i) the average optical depth τ_0, (ii) the bolometric flux $Fbol_{in}$ at the inner radius, (iii) the shell inner radius r_{in}, (iv) the dust temperature at the envelope's outer edge T_{out}, (v) the mass-loss rate $\dot{M}$, (vi) the terminal outflow velocity v and (vii) the stellar mass upper limit of a total of 265 C-rich and 465 O-rich Hi-GAL 1 AGB stars. From the inspection of the results obtained with DUSTY for the modelled Hi-GAL 1 PSC C-rich and O-rich AGB stars we concluded that these stars have different: (i) τ_0, (ii) $\dot{M}$, (iii) r_{in}/r_{source}, (iv) Tc and (v) $Fbol_{in}$.

Therefore, it is possible to distinguish the modelled Hi-GAL 1 PSC C-rich AGB stars from the O-rich AGB stars using their stellar properties.

The results also showed that the modelled Hi-GAL 1 PSC O-rich AGB stars are characterised by larger τ_0, further detached shells, lower $Fbol_{in}$, lower Tc and higher $\dot{M}$. The previous results suggest that our sample of modelled Hi-GAL 1 PSC O-rich AGB stars could be OH/IR-stars. The fact of having used OH/IR-stars as reference objects for the derivation of the colour cuts that allowed us to separate the Hi-GAL 1 AGB star candidates into C-rich and O-rich AGB stars, would explain why our colour cuts preferably selected OH/IR-stars over other O-rich stellar types.

The agreement found between the stellar properties derived in DUSTY and our classification of the Hi-GAL 1 C-rich and O-rich AGB stars confirms the effectiveness of DUSTY in the obtaining of the stellar properties of AGB stars. This agreement also constitutes the final confirmation that our colour criteria are capable of successfully separating the AGB stars from the YSOs, HII regions and PNe included in the Hi-GAL 1 PSC and of adequately classifying the discriminated AGB stars into C-rich and O-rich AGB types.

Next, the optical depths τ_0 obtained with DUSTY were proven to be related to the colour temperatures Tc obtained in the bb-fitting. In the case of the modelled Hi-GAL 1 PSC C-rich AGB stars, this relation is given by: $Tc = -402.4\ \ln(\tau_0) + 1464\ [K]$ whereas in the case of the modelled Hi-GAL 1 PSC O-rich AGB stars, this relation is approximately given by: $Tc = 1543.1\ \tau_0^{-0.362}\ [K]$.

We also found a relation between the colour temperatures and the mass-loss rates obtained with DUSTY. In the case of the modelled Hi-GAL 1 PSC C-rich AGB stars, this relation was established to be given by: $Tc = -535.1\ \ln(\dot{M}) + 2021.5\ [K]$ with $[\dot{M}] = 10^{-6}\ M_{\odot}/yr$ while in the case of the modelled Hi-GAL 1 PSC O-rich AGB stars, this relation is approximately given by: $Tc = 3032.8\ \dot{M}^{-0.514}\ [K]$ with $[\dot{M}] = 10^{-6}\ M_{\odot}/yr$.

The previous relations are of great importance since they could be used to estimate the mass-loss rates of unknown C-rich and O-rich AGB stars from their colour temperatures.

In addition, we found that for the modelled Hi-GAL 1 PSC C-rich AGB stars there is a well defined relation between: (i) the mass-loss rates and the outflow velocities obtained with DUSTY and (ii) the stars' colour temperatures and luminosities. This relation can be expressed as: $\log Q(Tc) = -1.6\ (\log Tc)^2 + 7.5\ \log Tc - 13.4\ [K]$ where the quantity *Q(Tc)* is defined as in Davidson (1987). In the case of the modelled Hi-GAL 1 PSC O-rich AGB stars, the relation between the $\log Q$ and the $\log Tc$ was found to be more scattered.

The approximate correspondence between the $\log Q$ and the $\log Tc$ can be described with: $\log Q(Tc) = 1.7\,(\log Tc)^2 - 12.1\ \log Tc + 15.7\ [K]$.

Moreover, we established that the mass-loss rates that we obtained in DUSTY for the modelled Hi-GAL 1 PSC C-rich and O-rich AGB stars can be related to the mass-loss rates calculated with the mass-loss formula in Wachter et al. (2002). This relation is given by: $\dot{M}_{DUSTY} = 70.57\,(\dot{M}_{Wachter})^{-1.354}\ [10^{-7}\ \dot{M}/yr]$, is only valid for $\dot{M} < 7 * 10^{-6}\ M_{\odot}/yr$ and its origin is unknown and requires further investigation.

Finally, we found a relation between the mass-loss rates obtained with DUSTY for the modelled Hi-GAL 1 PSC C-rich and O-rich AGB stars and the sources' NIR [J]-[K] colours. This relation is given by $log\dot{M} = 0.77\ \ln([J]-[K]) - 0.4\ [10^{-6}\ M_{\odot}/yr]$ for the modelled Hi-GAL 1 PSC C-rich AGB stars, and $\log \dot{M} = 0.11\ \ln([J]-[K]) + 0.9\ [10^{-6}\ M_{\odot}/yr]$ for the modelled Hi-GAL 1 PSC O-rich AGB stars. The results obtained with the previous two equations are similar to those found by Le Bertre (1997) and Le Bertre and Winters (1998). However, in our case, the separation found between the modelled Hi-GAL 1 PSC C-rich and O-rich AGB stars is not as clear as that obtained by Le Bertre (1997) and Le Bertre and Winters (1998). Nevertheless, taking into account the simplicity of the DUSTY radiative transfer solution method, which does not require neither the sources' distances nor the outflow velocities, we concluded that our results constitute a very good approximation.

Chapter 7

Summary, Conclusions and Future Work

"...this is just the beginning of all the science that we will get from this mission in the years to come."

Göran Pilbratt

7.1 Introduction

The aim of this chapter is to provide an overview of the contents included in this thesis, to discuss the implications of our findings and their contribution to the field as well as to set the basis of a new line of further research, which could be addressed in future works. In the following sections I present:

(i) a summary of the work presented in each of the previous chapters,

(ii) a synopsis of the conclusions reached in those chapters,

(iii) a discussion of the relevance of our findings and their impact,

(iv) a dissertation of possible future work in the field.

7.2 Summary of this thesis

The aim of this thesis was to use the Hi-GAL 1 Survey data to compile the largest catalogue of Galactic AGB stars (C-rich and O-rich) detected with Herschel existent to date. The building of this catalogue was achieved in four steps, which were described in Chapter 2, 3, 4 and 5 of this thesis and are summarised below.

- Chapter 2

  In this chapter we carried out a comparative study of the different pre-processing and map-making techniques used in the two pipelines currently available to convert the Hi–GAL 1 raw telemetry data into maps: the *Parallel Mode Scan* pipeline and the *ROMAGAL* pipeline. The pipelines' output maps were then compared in order to decide which of the two pipelines generated maps of better quality. The previous results allowed us to establish our preferred pipeline for the creation of the total 315 Hi-GAL 1 maps employed in the following chapters.

- Chapter 3

  In this chapter we described the functioning of a total of five different algorithms: DAOPHOT, SExtractor, the Wiener Filter, CUTEX and TSF. These algorithms were first applied to the original Hi-GAL 1 maps and, if successful, they were then applied to Hi-GAL 1 maps into which we injected artificial sources of known position and flux. These sources were then extracted using the successful algorithms to determine their source-extracting and/or flux-extracting performance, which was characterised by a series of parameters that we introduced. These results were next compared to those that ROMAGAL derived a posteriori. The previous findings allowed us to establish our preferred source and flux extractor for the creation of a total of 315 sourcelists, one for each Hi-GAL 1 map generated in the previous chapter.

- Chapter 4

  In this chapter we explained the process in which the previous sourcelists were combined to build our *SMA Hi-GAL 1 Point Source Catalogue* (PSC): a catalogue containing the position and flux density of all the Hi-GAL 1 sources detected in the 70 μm band. First, we established the series of requirements upon which the catalogue was built. Next, we described how the sourcelists were combined.

Then, we compared our method to that followed by ROMAGAL in the creation of their ROMAGAL Hi-GAL 1 PSC and discussed the benefits of using our catalogue as opposed to theirs. Finally, we determined the source and flux reliability, completeness and photometric coverage of our SMA Hi-GAL 1 PSC and presented the source and flux distribution of the sources contained in the catalogue.

- Chapter 5

  In this chapter we presented a series of colour cuts that allowed us to separate: (i) AGB stars from YSOs, HII regions and PNe and (ii) C-stars (C-rich stars) from OH/IR-stars (O-rich stars). These colour cuts were derived by studying the flux distributions of a total of 205, 178, 95, 59, 101 and 56 Hi-GAL 1 YSOs, HII regions, AGB stars, PNe, OH/IR and C-stars, which were used as reference sources. In order to guarantee the reliability, efficiency and applicability of the colour cuts we only considered those colour cuts that: (i) involved the Herschel 70 μm band, (ii) were testable upon $\geq 70\%$ of our reference samples and (iii) had the maximum verification rate and the minimum contamination rate. Next, we compared the efficiency of these colour cuts to that of the colour cuts derived in previous stellar separation studies. Then, we applied the colour cuts to our SMA Hi-GAL 1 PSC in order to create our catalogues of Hi-GAL 1 PSC AGB, C-rich and O-rich AGB star candidates. Finally, we discussed the catalogues' reliability and source distribution.

- Chapter 6

  Lastly, in Chapter 6 we used the Spectral Energy Distributions (SEDs) of the sources contained in our catalogues of Hi-GAL 1 PSC C-rich and O-rich AGB star candidates to obtain the sources' bolometric luminosity, nominal distance and colour temperature. Next, we employed the DUSTY radiative transfer code to model the sources' SED in order to derive the sources' mass-loss rate, terminal outflow velocity and stellar mass upper limit, amongst other stellar properties. The stellar properties found for the modelled Hi-GAL 1 PSC C-rich AGB stars were then compared to those found for the modelled Hi-GAL 1 PSC O-rich AGB stars in order to establish whether these properties enabled us to separate the two stellar classes. Finally, we derived a series of formulas that establish the relation between some of the stars' properties.

7.3 Conclusions of this thesis

Below we list the conclusions reached in Chapter 2, 3, 4, 5 and 6 of this thesis:

- Chapter 2

  In this chapter we concluded that the quality of the Hi-GAL maps created with the ROMAGAL pipeline (RMP) is better than that of the Hi-GAL maps created with the Parallel Mode Scan pipeline (PMSP). The PMSP-processed maps were found to have a higher presence of artefacts (i.e. Airy rings around bright sources, stripes, glitches, holes and edge defects) than the RMP-processed maps. Also, we showed that the Hi-GAL maps created with the RMP are of much higher resolution and quality than the maps created in the WISE, Spitzer, MSX and IRAS surveys.

- Chapter 3

  In this chapter we concluded that DAOPHOT, SExtractor and the Wiener Filter are inadequate for the Hi-GAL maps since they are not capable of coping with the highly variable foreground and background emission present in the maps. On the contrary, we found that CUTEX and TSF are suitable for the detection (CUTEX) and flux extraction (CUTEX and TSF) of Hi-GAL sources. However, the slightly lower accuracy of the fluxes returned by TSF, added to the fact that TSF does not perform source extraction and only performs flux extraction in three of the five Herschel bands, made us select CUTEX as our preferred algorithm for the detection and flux extraction of sources in the Hi-GAL maps.

  CUTEX source detection was found to be most efficient when extracting sources with fluxes equal to or above 0.5 Jy, 1 Jy, 0.1 Jy, 0.1 Jy and 2 Jy in the 70 μm, 160 μm, 250 μm, 350 μm and 500 μm bands, respectively. This result implies that below these flux levels, which we named *Source Extraction Limits (SEL)*, the sourcelists returned by CUTEX are somewhat incomplete. While our SEL were derived from tests performed on one Hi-GAL field, ROMAGAL's SEL table provides specific SEL for the total 30 fields they performed their tests on. Thus, ROMAGAL's SEL constitute a more complete, but posterior, version of our results. On the other hand, CUTEX fluxes were found to be generally overestimated. This overestimation was found to be systematic in the 70 μm fluxes and thus, could be corrected by multiplying these fluxes by our Flux Correction Factor $FCF_{CUTEX(70)} = 0.77$.

While our FCF considered only the flux uncertainties introduced by the background emission, ROMAGAL's take also into account the deformation that the PSF suffers when the telescope scans in parallel mode at high velocity. As a result, we concluded that ROMAGAL's FCF are preferable to ours. These are: $FCF_{CUTEX(70)} = 1.367$, $FCF_{CUTEX(160)} = 1.153$, $FCF_{CUTEX(250)} = 1.294$, $FCF_{CUTEX(350)} = 1.138$ and $FCF_{CUTEX(500)} = 1.181$ for the 70 μm, 160 μm, 250 μm, 350 μm and 500 μm bands, respectively. Finally, we concluded that the flux uncertainties derived by ROMAGAL are not as accurate as ours since ROMAGAL's do not take into account that the uncertainties associated with CUTEX extracted fluxes depend very strongly on the sources' flux.

- Chapter 4

  In this chapter we established that our SMA Hi-GAL 1 band catalogues - which contain the positions and fluxes of the Hi-GAL 1 sources we detected in the different Herschel bands with CUTEX - are different than those presented by ROMAGAL. On the one hand, we found that the SMA and ROMAGAL Hi-GAL 1 band catalogues include different number of sources. On the other hand, we determined that the fluxes listed for those sources that are common in both catalogues are also different. The previous differences were attributed to ROMAGAL's use of: (i) different maps (theirs being further processed, of better quality and slightly larger than ours), (ii) different thresholds (theirs being higher/lower than ours in the 70 μm band / 160 μm, 250 μm, 350 μm and 500 μm bands) and (iii) different Flux Correction Factors (theirs being preferable to ours). In light of the previous findings, and to ensure we used the most updated catalogues' version, we decided to use the ROMAGAL band catalogues instead of ours. However, these band catalogues were found to have many sources (2%, 5%, 6%, 32% and 45%, respectively) with low flux reliability (i.e. sources with $S/N < 3$), which we decided to exclude from the catalogues. As a result, our modified ROMAGAL Hi-GAL 1 band catalogues are, in general, less complete but have a higher flux reliability than the original ROMAGAL Hi-GAL 1 band catalogues.

  Furthermore, in this chapter we established that our SMA Hi-GAL 1 PSC is very different from ROMAGAL's PSC. In our case, our catalogue includes all the sources detected in the 70 μm modified ROMAGAL Hi-GAL 1 band catalogue and the

corresponding counterparts found lying at a maximum distance (d_{max}) of 1.7" in the modified ROMAGAL 160 μm, 250 μm, 350 μm and 500 μm Hi-GAL 1 band catalogues. Also included are the counterparts found in the IRAS, WISE, MSX, 2MASS, GLIMPSE and AKARI-IRC/FIS PSC lying at a d_{max}=1.7".

In their case, however, the 160 μm, 250 μm, 350 μm and 500 μm counterparts for the 70 μm sources were found allowing a maximum distance of 12", 18", 25" and 37", respectively. Moreover, their catalogue includes also sources that were only detected in one band and therefore, have no counterparts in any other band. Thus, the associations done by ROMAGAL between their band catalogues are of less reliability than those we established in our catalogue. The different methodology used in the building of the two PSC catalogues is responsible for the different number of sources they include. Our results established that, in the 160 μm, 250 μm, 350 μm and 500 μm bands, our SMA Hi-GAL 1 PSC is much less complete than ROMAGAL's - it only includes the 4%, 0.9%, 0.6% and 0.3% of ROMAGAL's sources, respectively. On the contrary, in the 70 μm band, the completeness of our catalogue (96%) is similar to that of the ROMAGAL's. Our results also show that the source reliability of our catalogue, in the 70 μm band, is greater than that of ROMAGAL's. In light of the previous findings, we concluded that, in the 70 μm band, our catalogue is almost as complete as ROMAGAL's yet it has a much higher flux and source reliability.

In terms of photometry, our SMA Hi-GAL 1 PSC was determined to be: (i) $\sim$100% complete for the Herschel 70 μm band, (ii) $\sim$16% complete for the GLIMPSE 3.6 μm and 4.5 μm bands, (iii) $\sim$13% complete for all the 2MASS and WISE bands, (iv) $\sim$11% complete for the GLIMPSE 5.8 μm band and (v) $<$ 10% complete for the remaining bands.

- Chapter 5

  In this chapter we concluded that: (i) the $[70/4.6] < -0.1$ and $[70/12] < -0.1$ and (ii) the $[70/1.65] < 3.5$, $[70/2.17] < 2.6$, $[70/4.6] < 0.5$, $[70/12] < 0.1$, $[70/22] < -0.2$ and (iii) the $[70/4.6] < 0.5$, $[70/12] < 0$ colour cuts efficiently separate AGB stars from (i) YSOs, (ii) HII regions and (iii) PNe, respectively while the $[70/4.6] > -0.8$, $[70/12] > -0.7$, $[4.6/22] < 0.1$, $[12/22] < 0.1$ colour cuts separate OH/IR-stars from C-stars. The application of the previous colour cuts onto our SMA Hi-GAL 1 PSC sources allowed us to classify a total of 3,166, 1,721 and 848 sources as AGB, O-rich

AGB and C-rich AGB star candidates, respectively. These sources are included in our catalogues of Hi-GAL 1 PSC AGB, O-rich AGB and C-rich AGB star candidates, respectively. The Galactic distribution of these sources showed that: (i) the number of O-rich AGB stars detected increases towards the Galactic Centre, (ii) the C-rich AGB stars detected are distributed relatively evenly along the Galactic latitude and longitude and (iii) the ratio between the number of C-rich and O-rich AGB stars detected increases with increasing galactocentric distance.

- Chapter 6

  In this chapter we established that the average bolometric flux ($< F_{bol} >$) of our Hi-GAL 1 PSC C-rich AGB stars ($< F_{bol} >^{C-rich} = 2.75E-11\ W\,m^{-2}$) is 4.4 times greater than that the average bolometric flux found for the Hi-GAL 1 PSC O-rich AGB stars ($< F_{bol} >^{O-rich} = 6.23E-12\ W\,m^{-2}$). This result was attributed to the fact that the Hi-GAL 1 PSC C-rich AGB stars were found to be closer than the Hi-GAL 1 PSC O-rich AGB stars. Also, we found that the average colour temperature ($< Tc >$) derived for the Hi-GAL 1 PSC C-rich AGB stars that were fitted with 1 Planck function ($< Tc >_{1PF}^{C-rich} = 1271\ K$), is 1.6 times greater than that found for the Hi-GAL 1 PSC O-rich AGB stars ($< Tc >_{1PF}^{O-rich} = 812\ K$). This temperature difference was attributed to the fact that the dust shells of the O-rich AGB stars are optically thicker and further detached. On the other hand, for the Hi-GAL 1 PSC C-rich AGB stars that were fitted with 2 Planck functions we found the average colour temperatures to be $< Tc_1 >_{2PF}^{C-rich} = 1759\ K$ and $< Tc_2 >_{2PF}^{C-rich} = 468\ K$. We found no cases of Hi-GAL 1 PSC O-rich AGB stars that were well fitted with two Planck functions.

  Moreover, the results showed that the DUSTY-modelled Hi-GAL 1 PSC O-rich AGB stars are characterised by: (i) larger optical depths τ_0, (ii) further detached shells, (iii) lower inner bolometric fluxes, (iv) lower outer-envelope colour temperatures and (v) higher mass-loss rates $\dot{M}$. The previous results suggest that our sample of modelled Hi-GAL 1 PSC O-rich AGB stars might be OH/IR-stars. The fact of having used OH/IR-stars as reference objects for the derivation of the colour cuts, would explain why our colour cuts preferably selected OH/IR-stars. These results also establish that it is possible to distinguish O-rich AGB stars from C-rich AGB stars by means of the stellar parameters derived with DUSTY.

The τ_0 obtained with DUSTY were proven to be related to the T_c obtained in the blackbody-fitting. In the case of the modelled Hi-GAL 1 PSC C-rich AGB stars, this relation is given by: $Tc = -402.4\ \ln(\tau_0) + 1464\ [K]$ whereas in the case of the modelled Hi-GAL 1 PSC O-rich AGB stars, this relation is approximately given by: $Tc = 1543.1\ \tau_0^{-0.362}\ [K]$.

We also found a relation between the T_c and the $\dot{M}$ obtained with DUSTY. In the case of the modelled Hi-GAL 1 PSC C-rich AGB stars, this relation was established to be given by: $Tc = -535.1\ \ln(\dot{M}) + 2021.5\ [K]$ – with $[\dot{M}] = 10^{-6}\ M_{\odot}/yr$, whereas in the case of the modelled Hi-GAL 1 PSC O-rich AGB stars, this relation is approximately given by: $Tc = 3032.8\ \dot{M}^{-0.514}\ [K]$ – with $[\dot{M}] = 10^{-6}\ M_{\odot}/yr$.

In addition, we found that for the modelled Hi-GAL 1 PSC C-rich AGB stars there is a well defined relation between the mass-loss rates and the outflow velocities obtained with DUSTY and the stars' colour temperatures and luminosities. This relation can be expressed as: $\log Q(Tc) = -1.6(\log Tc)^2 + 7.5 \log Tc - 13.4\,[K]$, where the quantity Q(Tc) is defined as in Davidson (1987). In the case of the modelled Hi-GAL 1 PSC O-rich AGB stars, the relation between the $\log Q(Tc)$ and the $\log Tc$ was found to be more scattered. The approximate correspondence between these two quantities can be described with: $\log Q(Tc) = 1.7\ (\log Tc)^2 - 12.1\ \log Tc + 15.7\ [K]$.

Moreover, we established that the $\dot{M}$ obtained for the Hi-GAL 1 PSC C-rich and O-rich AGB stars modelled with DUSTY can be related to the mass-loss rates calculated from the mass-loss formula in Wachter et al. (2002). This relation is given by: $\dot{M}_{DUSTY} = 70.57(\dot{M}_{Wachter})^{-1.354}\,[10^{-7}\ \dot{M}/yr]$, is only valid for $\dot{M} < 7 * 10^{-6}\ M_{\odot}/yr$ and its origin is unknown and requires further investigation.

Finally, we found that there is a relation between the NIR [J]-[K] colours of the Hi-GAL 1 PSC C-rich and O-rich AGB stars modelled with DUSTY and their $\dot{M}$. This relation is given by: $log\dot{M} = 0.77\ \ln([J]-[K]) - 0.4\ [10^{-6}\ M_{\odot}/yr]$ in the case of the C-rich AGB stars and by: $\log \dot{M} = 0.11\ \ln([J]-[K]) + 0.9\ [10^{-6}\ M_{\odot}/yr]$ in the case of the O-rich AGB stars.

7.4 Relevance of our findings, implications and contribution to the literature

We now discuss the importance, implications and contribution to the literature of the conclusions reached in Chapters 2, 3, 4, 5 and 6 of this thesis:

- Chapter 2

  Our findings in this chapter support the work presented in Traficante et al. (2011) and confirm that, as claimed by Traficante et al. (2011): (i) the maps created with their ROMAGAL Pipeline are of better quality (i.e. they have less stripes, glitches, background noise and pixel–to–pixel offsets) than those created with the standard Parallel Mode Scan Pipeline and (ii) the deglitching operations performed within their pipeline are more efficient than those carried out within the Parallel Mode Scan Pipeline. In light of these results, we recommend all Hi-GAL users to employ the new ROMAGAL pipeline for the processing of the Hi-GAL maps.

- Chapter 3

  The results presented in this chapter give strong evidence that neither DAOPHOT nor SExtractor nor the Wiener Filter are adequate for the source and flux extraction of sources in the Hi-GAL maps. These results confirm that, as suspected by Molinari et al. (2010b), *in the particularly difficult conditions of crowding and variable size sources embedded in variable background regions, the standard methods of aperture photometry or "fixed-template" source fitting may show their limits.*

  Moreover, our findings establish CUTEX as the most efficient and practical point source extractor and flux extractor for the Hi-GAL maps currently available. Thus, we strongly recommend all Hi-GAL users interested in the extraction of point sources to employ CUTEX and to make use of the corresponding flux corrections. Alternatively, for the SPIRE bands, users can also employ TSF, which delivers fluxes of similar accuracy. Finally, users should have in mind that the performance of these two algorithms is maximised for sources with fluxes $\geqslant 1$ Jy and that for sources fainter than 1 Jy the programs often return fluxes with S/N < 3, which have low reliability.

- Chapter 4

  The SMA Hi-GAL 1 PSC built in this chapter constitutes an important alternative to the ROMAGAL Hi-GAL 1 PSC. We have proved that, in the 70 μm band, our catalogue is almost as complete as ROMAGAL's yet it has a much higher source and flux reliability. Thus, we recommend the use of our SMA Hi-GAL 1 PSC over the use of the ROMAGAL Hi-GAL 1 PSC to those Hi-GAL users whose interest lies on the source and flux reliability or on the sources detected in the 70 μm band. On the other hand, those Hi-GAL users whose interest lies on the total number of Galactic sources detected in the Hi-GAL 1 Survey or on the sources detected in the 160 μm, 250 μm, 350 μm and 500 μm bands, are recommended to use the ROMAGAL Hi-GAL 1 PSC, which in these bands, is much more complete than our catalogue.

- Chapter 5

  The colour cuts derived in this chapter are the first colour cuts involving the Herschel 70 μm band that allow the separation between AGB stars and YSOs, PNe and HII regions. We have found that Herschel's 70 μm band is highly effective in distinguishing AGB stars from other stellar types and that this band plays a decisive role on the detection of AGB stars. Moreover, since only the Hi-GAL Survey data contains such accurate 70 μm fluxes we conclude that the Hi-GAL Survey data is crucial for the detection of AGB stars.

  In addition, we have proved that our colour cuts are more efficient in separating our reference AGB stars from our reference YSOs, PNe and HII regions than those established by Ita et al. (2010) and Ishihara et al. (2011). Also, we have established that the $[70/12] > 1.3$ colour cut defined by Anderson et al. (2012b) successfully discriminates our reference PNe from our reference HII regions. The [70/22] colour distribution was also found to provide a good separation but we obtained better results for $[70/22] > 0.5$ than for Anderson's $[70/22] > 0.8$ suggested colour cut.

  In light of these results we recommend the users to employ our colour cuts to separate AGB stars from YSOs, PNe and HII regions.

In this chapter we also derived colour cuts that allow the separation between OH/IR and C-stars and can be used to classify AGB stars into C-rich or O-rich. These colour cuts were found to be more efficient in separating our reference OH/IR-stars from our reference C-stars than those suggested by Ita et al. (2010) and Ishihara et al. (2011). Thus, we recommend the users to employ our colour cuts to separate OH/IR-stars (O-rich stars) from C-stars (C-rich stars).

Our selection of colour cuts prove that the MSX 8.28 μm band, the AKARI 9 μm and 18 μm bands and the WISE 12 μm and 22 μm bands are highly effective in distinguishing OH/IR-stars from C-stars since they cover the silicate features that O-rich AGB stars present around 10 μm and 20 μm and the carbonaceous features that C-rich AGB stars present around 11 μm.

Finally, the SMA catalogues of Hi-GAL 1 PSC O-rich and C-rich AGB star candidates presented here are, to date, the largest catalogues of Galactic O-rich and C-rich AGB stars - they contain 1.4 times and 4.5 times as many O-rich and C-rich AGB stars as the catalogues from Suh and Kwon (2009). The Galactic distributions of our O-rich and C-rich AGB candidates agree with those obtained by Le Bertre et al. (2003b), Lian et al. (2014) and Jura and Kleinmann (1990).

- Chapter 6

  The agreement found between the stellar properties derived in DUSTY and our classification of the Hi-GAL 1 C-rich and O-rich AGB stars confirms the effectiveness of DUSTY in the obtaining of the stellar properties of AGB stars. This agreement also constitutes the final confirmation that our colour criteria successfully separate AGB stars from YSOs, HII regions and PNe and adequately classify AGB stars into C-rich and O-rich AGB types.

  On the other hand, the relation found in this chapter between the stars' colour temperatures and their mass-loss rates is of great importance since it establishes a new direct method to estimate the mass-loss rate of unknown AGB stars from the souces' colour temperatures. The relations found between the stars' colour temperatures and their optical depths, outflow velocities, luminosities and NIR [J]-[K] fluxes are also of interest as they provide us with a method to distinguish C-rich and O-rich AGB stars.

7.5 Future Work

Below, we provide a list of several future projects that follow the line of research established by this thesis. The first direct application of our work would be to apply the colour criteria presented in this thesis to the sources detected in the Hi-GAL 2 and Hi-GAL 3 surveys in order to build a complete catalogue including all the AGB stars detected in the Galactic plane. Then, we could employ the DUSTY radiative transfer code to derive the stellar properties of these sources using the method established in this thesis. The accuracy of the stellar properties could be further improved if we introduced different grain-mixtures in the DUSTY models (instead of using single composition grains) and if we introduced the stars' spectra (instead of describing the stars' emerging spectra as a black body). The results obtained with these additional sources would allow us to confirm the relationship that we found between the colour temperatures and the mass-loss rates of the DUSTY-modelled Hi-GAL 1 PSC C-rich and O-rich AGB stars. Once confirmed, such formulas could be used to estimate the mass-loss rates of Galactic AGB stars from their colour temperatures. Apart from the sources' mass-loss rates, we could also use the k-band extinction values derived by Marshall et al. (2006) in order to estimate the sources' distances. Alternatively, the distances could be inferred from the measurements of the sources' periods for which we would require follow up NIR photometric observations. The obtaining of the stars' periods would allow us in turn to derive their luminosities from the Period-Luminosity relations established by Groenewegen and Whitelock (1996) (for C-rich AGB stars) and Feast (1996) (for O-rich AGB stars). With the stars' distances we could then estimate the total mass of dust in these objects as well as their mass-loss rates. This would allow us to infer the dust production rate at different Galactic regions. Precise distance measurements of the Galactic sources will become available thanks to the *GAIA* mission (Brown et al. 2004), which will enable the study of sources' absolute luminosities, effective temperatures and spectral composition. Finally, the obtaining of the NIR spectra of these objects, would allow us to study the chemistry and grain composition of the C-rich and O-rich AGB stars. Moreover, for those stars with relatively thin dust shells, we could use ALMA (Beasley 2013) observations in an attempt to resolve the size and the shape of the AGB star envelopes. These observations would enable us to track the winds from the stars' photosphere to the ISM, which would provide us with a better understanding of the dynamics of the mass-loss processes that AGB stars undergo.

Appendix A

Conversion from Jy/beam to MJy/sr

Below, we show the necessary steps to convert the SPIRE maps from $\frac{Jy}{beam}$ to $\frac{MJy}{sr}$ units.

1. Calculate the area under the beam in square arsec with:

$$Area\,beam = \frac{\pi\, FWHM(arcsec)^2}{4\,ln2}$$

2. Calculate the area of a pixel in square arsec with:

$$Area\,pixel = size\,pixel(arcsec)^2$$

3. Convert sr into square arsec with:

$$2\,\pi\,rad = 360\,degrees$$
$$1\,rad = \frac{360}{\pi}\,degree = \frac{360}{\pi} \times \frac{3600\,arcsec}{1\,degree}$$
$$1\,sr = 1\,rad^2$$

4. Calculate the ratio of $\frac{Area\,beam}{Area\,pixel}$ and $\frac{Area\,pixel}{sr}$.

5. Multiply the flux in $\frac{Jy}{beam}$ per $\frac{1\,MJy}{10^6\,Jy} \times \frac{Area\,beam}{Area\,pixel} \times \frac{Area\,pixel}{sr}$

Appendix B

Bayesian model selection methods

Below, we give an overview of the general formalism of the *Bayesian methods* that are used in the *SExtractor* (Bertin and Arnouts 1996) algorithm for the detection of the position and the flux of the sources contained in an image. The information presented here uses contents from Savage and Oliver (2007) and is included here only for readability purposes.

In Bayesian model selection methods, a number of models, characterised by several parameters, are defined as a possible representation of the real data that is being analysed. Although at first the value of these parameters is hypothetical, it becomes a realistic approach to the real data after fitting repetitively the model to the real data. The functioning of Bayesian model selection methods is based on the *Baye theorem* which is given by the following expression:

$$P(\theta \mid D, H) = \frac{P(D \mid \theta, H)\, P(\theta, H)}{P(D \mid H)} \tag{B.1}$$

where:

D is the data, θ is the model parameters, H is the hypothesis,
$P(\theta, H)$ represents any prior knowledge about the likely parameter values,
$P(D \mid H)$ is the evidence, which provides a relative measure of the probability of different models being the best fit for the data,
$P(\theta \mid D, H)$ is the posterior probability distribution of the model parameters and
$P(D \mid \theta, H) \equiv \mathcal{L}$ is the likelihood of the data, which can be expressed as:

$$\mathcal{L} \propto exp\,(-\frac{\chi^2}{2}) \qquad ; \qquad \chi^2 = \sum_{i=1}^{N\,pixels} \left[\frac{d_i - m(\theta)_i}{\sigma_i}\right]^2 \tag{B.2}$$

where:

d_i is the value of the i^{th} data pixel of the subset of image pixel under consideration,
m_i is the parametrised value from a model of the signal (flux) and
σ_i is the standard deviation of the Gaussian noise associated with that pixel.

In order to compare how likely different models are and select the one that describes the data the best, a *Bayesian information criterion* (BIC) is introduced. The BIC is defined as:

$$BIC \equiv -2 \ln \mathcal{L}_{max} + \nu \ln N_{data} \tag{B.3}$$

where:

$\mathcal{L}_{max}$ is the maximum likelihood value for a given hypothesis,
ν is the number of free parameters in the model and
N_{data} is the number of data used.

The model that returns the lower BIC value has the higher probability of being the correct one and thus, it is taken as the best description of the real data. The posterior probability distribution of the selected model parameters is then mapped by Markov chain Monte Carlo sampling to take its peak as our most likely parameters solution. Finally, in order to get a single parameter one-dimensional distribution, the task makes a histogram of the samples using the values of that single parameter.

Appendix C

The radiative transfer problem for a spherical dusty medium

Below, we introduce the general equation of radiative transfer and we give an overview of the solution method that the DUSTY code (Ivezic and Elitzur 1997) uses for the calculation of the dust temperature distribution and inner radiation field of a cool star embedded in a dusty shell. In the following demonstrations we use contents from Ivezic and Elitzur (1997), Rybicki and Lightman (1979) and Marengo (2000), which are included here only for readability purposes.

C.1 Equation of radiative transfer

Suppose that we have a set of rays (radiation field) of intensity I_ν and frequency range $d\nu$ passing through a volume of material with cross section dA and length dl in an interval of time dt, whose direction is within a solid angle $d\Omega$. When the rays pass through the matter they will be affected by absorption, scattering and emission. The amount of energy removed by absorption from the incident flux and converted into internal energy of the absorbing material is given by $dE^{(a)}$ (see Eq. C.1) and is a function of the absorption opacity $k_\nu^{(a)}$. On the other hand, the amount of energy removed by scattering from the incident flux and reflected in a different solid angle yet the same wavelength is given by $dE^{(\sigma)}$ (see Eq. C.1) and is a function of the scattering opacity $k_\nu^{(s)}$. Finally, the amount of energy released into the radiation field by the material is given by $dE^{(\epsilon)}$ (see Eq. C.1) and is a function of the emissivity j_ν.

$$dE^{(a)} = k_\nu^{(a)}\, I_\nu\, d\nu\, dt\, d\Omega\, dA\, dl \;\;,\;\; dE^{(\sigma)} = k_\nu^{(\sigma)}\, I_\nu\, d\nu\, dt\, d\Omega\, dA\, dl \;\;,\;\; dE^{(\epsilon)} = j_\nu\, d\nu\, dt\, d\Omega\, dA\, dl \quad \text{(C.1)}$$

By the law of energy conservation, the total variation of the incident flux in the solid angle $d\Omega$ must be equal to the difference between the energy gained from emission and the energy lost by absorption and scattering. Thus:

$$dI_\nu = \frac{dE^{(\epsilon)} - (dE^{(a)} + dE^{(\sigma)})}{d\nu\, dt\, d\Omega\, dA\, dl}$$

If we now group the absorption and scattering opacity into one total opacity so that $k_\nu = k_\nu^{(a)} + k_\nu^{(\sigma)}$ and introduce the source function $S_\nu = \frac{j_\nu}{k_\nu}$, we can re-write the previous equation as:

$$\frac{dI_\nu}{dl} = j_\nu - k_\nu\, I_\nu = k_\nu(S_\nu - I_\nu) \tag{C.2}$$

which constitutes the general equation of radiative transfer. This equation can be simplified if, instead of using the source function S_ν, we use the optical depth τ_ν defined as the total opacity measured along the path P of a travelling ray: $d\tau_\nu = k_\nu\, dl$ *or* $\tau_\nu = \int_P k_\nu\, dl$

Then, Eq. C.2 becomes:

$$\frac{dI_\nu}{d\tau_\nu} = S_\nu - I_\nu \tag{C.3}$$

whose solution is given by:

$$I_\nu(P) = I_\nu(0)\, e^{-\tau_\nu(P)} \; + \int_0^{\tau_\nu} S_\nu(\tau'_\nu)\, e^{-[\tau'_\nu - \tau_\nu(P)]}\, d\tau'_\nu \tag{C.4}$$

where the first term corresponds to the initial intensity diminished by absorption and the second term corresponds to the integrated source diminished by absorption.

C.2 Solution for a dusty medium

In the case of a dusty environment, the second term of Eq. C.4 can be expressed as:

$$S_\nu = \frac{j_\nu}{k_\nu} = \frac{j_\nu^{(\epsilon)} + j_\nu^{(\sigma)}}{k_\nu^{(a)} + k_\nu^{(\sigma)}} \tag{C.5}$$

where $j\nu^{(\epsilon)}$ gives us the dust emission, $j_\nu^{(\sigma)}$ gives us the dust scattering and $k_\nu^{(a)} + k_\nu^{(\sigma)}$ is the total opacity k_ν. The Kirchhoff Law for thermal emission allows the $j_\nu^{(\epsilon)}$ component to be expressed as:

$$j_\nu^{(\epsilon)} = k_\nu^{(a)}\, B_\nu(T_d) \tag{C.6}$$

where $B_\nu(T_d)$ is the Planck function at the dust temperature T_d.

The $j_\nu^{(\sigma)}$ component can be obtained from the integration of the scattered radiation over the solid angle $d\Omega$:

$$j_\nu^{(\sigma)} = \frac{1}{4\pi} \int_{4\pi} k_\nu^\sigma\, I_\nu(\Omega')\, g(\Omega', \Omega)\, d\Omega' \tag{C.7}$$

where $g(\Omega', \Omega)$ is the angular phase function for coherent scattering from the direction Ω' to the direction Ω.

Finally, the total dust opacity k_ν can be expressed as a function of the albedo ϖ_ν :

$$\varpi_\nu = \frac{k_\nu^{(\sigma)}}{k_\nu} \tag{C.8}$$

The introduction of Eq. C.6, C.7 and C.8 into Eq. C.5 results in:

$$S_\nu = (1-\varpi_\nu)\, B_\nu(T_d) + \frac{\varpi_\nu}{4\pi} = \int_{4\pi} I_\nu(\Omega')\, g(\Omega',\Omega)\, d\Omega' \tag{C.9}$$

which, when substituted in Eq. C.3, allows us to solve the radiative transfer problem for a dusty environment provided that we determine the thermal structure of the dust.

C.3 Solution for a dusty medium with spherical geometry

Let us now consider a source of radius r_e and intensity I^e_ν embedded in an spherically-shaped dusty shell, with a radial dust density distribution $\eta(y)$, described by a radial coordinate y and the radial angle θ. Under these circumstances, Ivezic and Elitzur (1994) demonstrated that the solution of the radiative transfer problem given in Eq. C.9 can be re-written as:

$$I_\nu(y,\theta) = I^e_\nu\, e^{\tau_\nu(y)}\, \Theta\left[\frac{\theta^e_1}{y} - \theta\right] + I^d_\nu(y,\theta) \tag{C.10}$$

where θ^e_1 is the angular size of the source, Θ is the step function (1 for positive arguments, 0 for negative arguments) and the second term is the dust component of the radiative intensity I^d_ν, which is given by:

$$I^d_\nu = \int S_\nu(y',\theta)\, e^{-[\tau_\nu(y',\theta)-\tau_\nu(y,\theta)]}\, d\tau_\nu(y',\theta) \tag{C.11}$$

Then, by angular integration of Eq. C.10, the average flux intensity over all solid angles (J_ν) adopts the form of:

$$J_\nu(y) = \frac{F^e_1}{4\pi y^2}\, f^e_\nu\, e^{-\tau_\nu(y)} + J^d_\nu(y) \tag{C.12}$$

where J^d_ν is the dust diffuse average intensity derived from Eq. C.11 and:

$$F^e_1 = \int d\nu \int I^e_\nu \cos\theta\, d\omega = \frac{L^e}{4\pi r_1^2} \equiv \text{Bolometric source flux at the inner shell radius } r_1 \tag{C.13}$$

$$f^e_\nu = \frac{F^e_\nu}{\int F^e_\nu\, d\nu} \equiv \text{Source's spectral shape} \tag{C.14}$$

As explained in Ivezic and Elitzur (1997), the ratio:

$$\Psi = \frac{4\sigma T_1^4}{F^e_1}\ ,\ T_1 \equiv \text{Dust temperature at the shell's inner edge } r_1 \tag{C.15}$$

constitutes a characteristic dimensionless scaling function of the model. Ψ can also be re-written as a function of $J_\nu(y)$:

$$\Psi = \frac{\int k_\nu f^e_\nu\, d\nu}{k_P(T_1)} \times \frac{1}{1-\epsilon} \quad , \quad \epsilon = \frac{\int k_\nu\,(1-\varpi_\nu) J^d_\nu(1)\, d\nu}{\int k_\nu\,(1-\varpi_\nu)\, B_\nu(T_1)\, d\nu} \tag{C.16}$$

where k_P is the Planck averaged opacity and can be obtained from:

$$k_P(T_d)T_d^4 = k_P(T_1)T_1^4\, \frac{\int k_\nu\,(1-\varpi_\nu)\, J_\nu(y)\, d\nu}{k_\nu\,(1-\varpi_\nu)\, J_\nu(1)\, d\nu} \tag{C.17}$$

where T_d is the dust temperature at the shell's outer edge.

With the previous definitions, one can now solve the Eq. C.12 and obtain the values of the parameters that DUSTY returns as an output:

(i) the shell's inner radius r_1,

(ii) the bolometric flux at r_1,

(iii) the ratio between r_1 and the source ratio r_e,

(iv) the angular size of the shell inner diameter θ and

(v) the dust temperature)

using the flux scale Ψ derived in Eq C.16, the dust temperature at the shell's outer edge T_d obtained in Eq C.17 and the parameters that the user must provide to DUSTY as an input:

(i) the dust optical properties k_ν and ϖ_ν,

(ii) the temperature at the shell's inner edge T_1,

(iii) the radial dust density distribution $\eta(y)$ and

(iv) the spectral shape f_ν^e of the star).

Appendix D

The dynamics of dusty winds

Below, we introduce the equation of motion for a supersonic spherical dusty wind and give an overview of the solution method that the DUSTY code (Ivezic and Elitzur 1997) uses for the calculation of the mass-loss rates, outflow velocities and stellar mass limit. In the following demonstrations we use contents from Elitzur and Ivezić (2001), which are included here only for readability purposes.

D.1 Equation of motion

Suppose that we have an AGB star that is undergoing strong stellar winds through which the star returns part of its shell's mass (gas and dust) to the ISM. In order to study the dynamical structure and IR emission of these winds we require a solution of the coupled hydrodynamics and radiative transfer problems. The radiative transfer problem was discussed in Appendix C of this thesis. We now discuss the hydrodynamics problem. In this discussion, the following assumptions are made. Firstly, the winds are assumed to be steady-state (i.e. $\frac{\partial}{\partial t} = 0$) and to have spherical symmetry. Secondly, the dust formation in the star's dust shell is assumed to be completed so that beyond the radius r_1, the properties of individual dust grains do not change. Finally, the winds are assumed to have been initiated and to be moving outwards at supersonic velocities.
Under these assumptions, the equation of motion of this wind is given by:

$$\rho \frac{dv}{dt} = \mathcal{F} \xrightarrow{dt=dr/v} \frac{dv^2}{dy} = 2a_{\mathcal{F}} r_1 \quad , \quad a_{\mathcal{F}} = \frac{\mathcal{F}}{\rho} \equiv \text{acceleration associated with } \mathcal{F} \tag{D.1}$$

where:

v is the gas velocity and y is the scaled radius $y = r/r_1$

$\rho = n_H m_p$ (with $n_H \equiv$ number density of hydrogen nuclei and $m_p \equiv$ proton mass),

$\mathcal{F}$ is the net outward radial force per unit volume that controls the wind movement.

The $\mathcal{F}$ force includes three components: (i) the radiation pressure force - that acts upon the shell dust grains, (ii) the internal drag force - by which dust and gas particles are coupled and (iii) the gravitational force of the star.

- Radiation pressure

  The radiation pressure force per unit volume is described by:

  $$\mathcal{F}_{rad} = \frac{1}{c} n_d \pi a^2 \int Q_{pr,\lambda} F_\lambda d\lambda \tag{D.2}$$

  where n_d is the number density of dust grains, a is the dust grain radius, $Q_{pr,\lambda}$ is the radiation pressure efficiency and F_λ is the local radiative flux.

  The velocity associated with the $\mathcal{F}_{rad}$ is defined as:

  $$v_p^2 = 2r_1 \frac{F_{rad}(r1)}{\rho(r_1)} \quad \xrightarrow{\sigma_g} \quad v_p = \left(\frac{Q_\star \sigma_g L}{2\pi m_p c r_1} \right)^{1/2} \tag{D.3}$$

  where:

  $$Q_\star = \int Q_{pr,\lambda} \frac{F_\lambda(1)}{F(1)} d\lambda = \frac{\pi}{\sigma T_\star^4} \int Q_{pr,\lambda} B_\lambda(T_\star)\, d\lambda \quad ; \quad B_\lambda \equiv \text{Planck function} \tag{D.4}$$

  is the Planck average at the stellar temperature ($T_\star$) of the efficiency coefficient for radiation pressure, σ is the Stefan-Boltzmann constant, σ_g is the dust crossed section area per particle at condensation and L is the stellar luminosity.

  As a result, if we only consider $\mathcal{F}_{rad}$, the equation of motion turns into:

  $$\frac{dv^2}{dy} = \frac{v_p^2}{y^2} \phi(y) \quad , \quad \phi(y) \equiv \text{Reddening profile} = \frac{1}{Q_\star} \int Q_{pr,\lambda} \frac{F_\lambda(y)}{F(y)}\, d\lambda \tag{D.5}$$

  whose solution, when $\phi = 1$, returns the gas velocity v:

  $$v_g^2 = v_T^2 + v_p^2 \left(1 - \frac{1}{y}\right) \quad , \quad v_T \equiv \text{Wind initial velocity} = \left(\frac{kT_k}{m_{H_2}} \right)^{1/2} \tag{D.6}$$

  where m_{H_2} is the mass of the molecular hydrogen and $T_k = T_{k3} \times 1000\ K$ is the kinetic temperature at y=1.

- Drag

  The drag force on a grain moving at the relative velocity v_{rel} through gas with density ρ is described by:

  $$\mathcal{F}_{drag} = \pi a^2 \rho \times \begin{cases} v_{rel}^2 & \text{when } v_{rel} > v_T \text{ (supersonic regime)} \\ v_{rel} v_T & \text{when } v_{rel} < v_T \text{ (subsonic regime)} \end{cases} \tag{D.7}$$

  where:

  $$v_{rel} = \frac{v_m v \phi}{v_T + \sqrt{v_m v \phi}} \quad , \quad v_m \equiv \text{Drift velocity} = \frac{Q_\star L}{\dot{M} c} \quad , \quad \dot{M} \equiv \text{Mass-loss rate} \tag{D.8}$$

- Gravitational force

  Finally, the gravitation pull introduces the escape velocity v_g at r_1:

$$v_g = \left(\frac{2GM}{r_1}\right)^{1/2} \quad , \quad M \equiv \text{Stellar mass} \quad , \quad G \equiv \text{Gravitational constant} \tag{D.9}$$

Adding the effect of the radiation pressure, the drag and the gravitation, the equation of motion becomes:

$$\frac{dv^2}{dy} = \frac{v_p^2}{y^2}\left[\phi(y)\zeta(y) - \frac{1}{\Gamma}\right] \tag{D.10}$$

where:

$$\Gamma = \left.\frac{\mathcal{F}_{rad}}{\mathcal{F}_{grav}}\right|_{r_1} = \frac{v_p^2}{v_g^2} = \frac{Q_\star \sigma_g L}{4\pi G M m_p c} \tag{D.11}$$

$$\zeta(y) \equiv \text{Drift profile} = \frac{v}{v_d} = \frac{v_T + \sqrt{v_m v\phi}}{v_T + v_m\phi + \sqrt{v_m v\phi}} \tag{D.12}$$

which constitutes the complete form of the equation of motion including all the dynamical processes in the wind.

D.2 Coupling with the radiative transfer problem

As we saw in Appendix C, the solution for the radiative transfer problem requires the specification of two independent inputs: the optical depth τ_v and the radial profile of the dust density distribution $\eta(y)$. Thanks to the coupling between the radiative transfer problem and the dynamics problem through the reddening profile ϕ, τ_v and $\eta(y)$ are no longer an input but fully specified by the dynamics problem. These quantities can now be expressed as:

$$\tau_v = Q_V \frac{v_p^2}{2v_m} \int_1^\infty \frac{\zeta}{y^2 v}\, dy \tag{D.13}$$

$$\eta(y) = \frac{\zeta(y)}{y^2 v(y)} \left(\int_1^\infty \frac{\zeta}{y^2 v}\, dy\right)^{-1} \tag{D.14}$$

where Q_V is the absorption efficiency at visual wavelengths.

Thus, given the grain properties and the spectral profile of the stellar radiation, the overall dusty wind dynamics problem is fully determined by the four parameters: v_p, v_m, v_g and v_T.

D.3 Scaling

Using scaling relations, the number of model parameters can be reduced from 4 to 3. These are:

$$w = \frac{v}{v_m} \quad , \quad \theta = \frac{v_T}{v_m} \quad , \quad P = \frac{v_p}{v_m} \tag{D.15}$$

D.4 Solutions

We now list the solutions that Elitzur and Ivezić (2001) obtain when solving the complete full problem. For a detailed description of the steps in which these solutions were derived, we refer the reader to Elitzur and Ivezić (2001).

- Shell inner radius r_1 in cm

$$r_1 = \left(\frac{L\Psi}{16\pi\sigma T_c^4} \right)^{1/2} \tag{D.16}$$

where Ψ is the dimensionless function determined by radiative transfer and T_c is the dust temperature at the inner radius.

- Mass loss rate $\dot{M}_{-6}$ in units of $10^{-6}\ M_{\odot} yr^{-1}$

$$\frac{\dot{M}_{-6}}{L_4^{3/4}} = 1.98\ \frac{Q_\star^{1/2}}{\sigma_{22}^{1/2} T_{c3}}\ P\Psi^{1/4} \tag{D.17}$$

where L_4 is the luminosity in units of $10^4\ L_{\odot}$, σ_{22} is the dust cross-sectional area per particle at condensation in $10^{-22}\ cm^2$ and T_{c3} is the dust temperature at the inner radius in units of $10^3\ K$.

- Outflow velocity v in $km\ s^{-1}$

$$\frac{v_1}{L_4^{1/4}} = c_3 \tau_V^{1/4} K_3(\tau_V) \tag{D.18}$$

where Ψ_0 is the value of Ψ in optically thin winds and:

$$c_3 = 88.9 T_{c_3} (Q_\star \sigma_{22})^{1/2} (Q_V \Psi_0)^{-1/4} \tag{D.19}$$

$$K_3 = \left(\frac{1}{\Phi} \right)^{1/4} \Theta \quad , \quad \Theta^2 \simeq \left[1 + \frac{3}{4} (\tau_V / Q_V)^{1/2} \right] \Phi \tag{D.20}$$

- Upper limit on the stellar mass in $M_{\odot}$ (M_0), derived from the Eddington limit (i.e. all winds must obey $\Gamma > 1$)

$$\frac{L_4}{M_0} Q_\star \sigma_{22} > 2.18 \times 10^{-2} \tag{D.21}$$

Bibliography

Abbott, D. C., Conti, P. S., 1987. Wolf-Rayet stars. Annual Review of Astronomy & Astrophysics 25, 113–150.

Alksnis, A., Balklavs, A., Dzervitis, U., Eglitis, I., Paupers, O., Pundure, I., 2001. General Catalog of Galactic Carbon Stars by C. B. Stephenson. Third Edition. Baltic Astronomy 10, 1–318.

Althaus, L. G., Córsico, A. H., Isern, J., García-Berro, E., Oct. 2010. Evolutionary and pulsational properties of white dwarf stars. Astronomy & Astrophysics Review 18, 471–566.

Anderson, L. D., Bania, T. M., Balser, D. S., Cunningham, V., Wenger, T. V., Johnstone, B. M., Armentrout, W. P., May 2014. The WISE Catalog of Galactic H II Regions. Astrophysical Journal Supplement 212, 1.

Anderson, L. D., Bania, T. M., Balser, D. S., Rood, R. T., Jun. 2011. The Green Bank Telescope H II Region Discovery Survey. II. The Source Catalog. Astrophysical Journal Supplement 194, 32.

Anderson, L. D., Bania, T. M., Balser, D. S., Rood, R. T., Jul. 2012a. The Green Bank Telescope H II Region Discovery Survey. III. Kinematic Distances. Astrophysical Journal 754, 62.

Anderson, L. D., Zavagno, A., Barlow, M. J., García-Lario, P., Noriega-Crespo, A., Jan. 2012b. Distinguishing between HII regions and planetary nebulae with Hi-GAL, WISE, MIPSGAL, and GLIMPSE. Astronomy & Astrophysics 537, A1.

Anderson, L. D., Zavagno, A., Deharveng, L., Abergel, A., Motte, F., André, P., Bernard, J.-P., Bontemps, S., Hennemann, M., Hill, T., Rodón, J. A., Roussel, H., Russeil, D.,

Jun. 2012c. The dust properties of bubble H II regions as seen by Herschel. Astronomy & Astrophysics 542, A10.

André, P., Men'shchikov, A., Bontemps, S., Könyves, V., Motte, F., Schneider, N., Didelon, P., Minier, V., Saraceno, P., Ward-Thompson, D., di Francesco, J., White, G., Molinari, S., Testi, L., Abergel, A., Griffin, M., Henning, T., Royer, P., Merín, B., Vavrek, R., Attard, M., Arzoumanian, D., Wilson, C. D., Ade, P., Aussel, H., Baluteau, J.-P., Benedettini, M., Bernard, J.-P., Blommaert, J. A. D. L., Cambrésy, L., Cox, P., di Giorgio, A., Hargrave, P., Hennemann, M., Huang, M., Kirk, J., Krause, O., Launhardt, R., Leeks, S., Le Pennec, J., Li, J. Z., Martin, P. G., Maury, A., Olofsson, G., Omont, A., Peretto, N., Pezzuto, S., Prusti, T., Roussel, H., Russeil, D., Sauvage, M., Sibthorpe, B., Sicilia-Aguilar, A., Spinoglio, L., Waelkens, C., Woodcraft, A., Zavagno, A., Jul. 2010. From filamentary clouds to prestellar cores to the stellar IMF: Initial highlights from the Herschel Gould Belt Survey. Astronomy & Astrophysics 518, L102.

André, P., Ward-Thompson, D., Barsony, M., Mar. 1993. Submillimeter continuum observations of Rho Ophiuchi A - The candidate protostar VLA 1623 and prestellar clumps. Astrophysical Journal 406, 122–141.

Araya, E., Hofner, P., Churchwell, E., Kurtz, S., Jan. 2002. Arecibo Observations of Formaldehyde and Radio Recombination Lines toward Ultracompact H II Regions. Astrophysical Journal Supplement 138, 63–74.

Avedisova, V. S., Mar. 2002. A Catalog of Star-Forming Regions in the Galaxy. Astronomy Reports 46, 193–205.

Babusiaux, C., Gilmore, G., Apr. 2005. The structure of the Galactic bar. Monthly Notices of the Royal Astronomical Society 358, 1309–1319.

Barlow, M. J., May 1978. The destruction and growth of dust grains in interstellar space. I - Destruction by sputtering. Monthly Notices of the Royal Astronomical Society 183, 367–395.

Beasley, A. J., Jun. 2013. The Atacama Large Millimeter/submillimeter Array: A New Window on the Universe. In: American Astronomical Society Meeting Abstracts. Vol. 222 of American Astronomical Society Meeting Abstracts. p. 205.01.

Bedijn, P. J., Nov. 1987. Dust shells around Miras and OH/IR stars - Interpretation of IRAS and other infrared measurements. Astronomy & Astrophysics 186, 136–152.

Bendo, G. J., Griffin, M. J., Bock, J. J., Conversi, L., Dowell, C. D., Lim, T., Lu, N., North, C. E., Papageorgiou, A., Pearson, C. P., Pohlen, M., Polehampton, E. T., Schulz, B., Shupe, D. L., Sibthorpe, B., Spencer, L. D., Swinyard, B. M., Valtchanov, I., Xu, C. K., Aug. 2013. Flux calibration of the Herschel-SPIRE photometer. Monthly Notices of the Royal Astronomical Society 433, 3062–3078.

Benjamin, R. A., Churchwell, E., Babler, B. L., Bania, T. M., Clemens, D. P., Cohen, M., Dickey, J. M., Indebetouw, R., Jackson, J. M., Kobulnicky, H. A., Lazarian, A., Marston, A. P., Mathis, J. S., Meade, M. R., Seager, S., Stolovy, S. R., Watson, C., Whitney, B. A., Wolff, M. J., Wolfire, M. G., Aug. 2003. GLIMPSE. I. An SIRTF Legacy Project to Map the Inner Galaxy. Publications of the Astronomical Society of the Pacific 115, 953–964.

Bernard, J.-P., Paradis, D., Marshall, D. J., Montier, L., Lagache, G., Paladini, R., Veneziani, M., Brunt, C. M., Mottram, J. C., Martin, P., Ristorcelli, I., Noriega-Crespo, A., Compiègne, M., Flagey, N., Anderson, L. D., Popescu, C. C., Tuffs, R., Reach, W., White, G., Benedettini, M., Calzoletti, L., Digiorgio, A. M., Faustini, F., Juvela, M., Joblin, C., Joncas, G., Mivilles-Deschenes, M.-A., Olmi, L., Traficante, A., Piacentini, F., Zavagno, A., Molinari, S., Jul. 2010. Dust temperature tracing the ISRF intensity in the Galaxy. Astronomy & Astrophysics 518, L88.

Bertin, E., Arnouts, S., Jun. 1996. SExtractor: Software for source extraction. Astronomy and Astrophysics Supplement 117, 393–404.

Billot, N., Noriega-Crespo, A., Carey, S., Guieu, S., Shenoy, S., Paladini, R., Latter, W., Apr. 2010. Young Stellar Objects and Triggered Star Formation in The Vulpecula OB Association. Astrophysical Journal 712, 797–812.

Bloecker, T., May 1995. Stellar evolution of low and intermediate-mass stars. I. Mass loss on the AGB and its consequences for stellar evolution. Astronomy & Astrophysics 297, 727.

Bodenheimer, P., 1989. The impact of stellar evolution on planetary system development. In: Weaver, H. A., Danly, L. (Eds.), The Formation and Evolution of Planetary Systems. pp. 243–268.

Bronfman, L., Nyman, L.-A., May, J., Jan. 1996. A CS(2-1) survey of IRAS point sources with color characteristics of ultra-compact HII regions. Astronomy and Astrophysics Supplement 115, 81.

Brown, R. L., Wild, W., Cunningham, C., Jan. 2004. ALMA - the Atacama large millimeter array. Advances in Space Research 34, 555–559.

Butler, M. J., Tan, J. C., Jul. 2012. Mid-infrared Extinction Mapping of Infrared Dark Clouds. II. The Structure of Massive Starless Cores and Clumps. Astrophysical Journal 754, 5.

Carroll, B. W., Ostlie, D. A., 1996. An Introduction to Modern Astrophysics. Institute for Mathematics and Its Applications.

Chen, P. S., Yang, X. H., Feb. 2012. A Catalog of Galactic Infrared Carbon Stars. Astronomical Journal 143, 36.

Chiosi, C., Maeder, A., 1986. The evolution of massive stars with mass loss. Annual Review of Astronomy & Astrophysics 24, 329–375.

Churchwell, E., Babler, B. L., Meade, M. R., Whitney, B. A., Benjamin, R., Indebetouw, R., Cyganowski, C., Robitaille, T. P., Povich, M., Watson, C., Bracker, S., Mar. 2009. The Spitzer/GLIMPSE Surveys: A New View of the Milky Way. Publications of the Astronomical Society of the Pacific 121, 213–230.

Churchwell, E., Povich, M. S., Allen, D., Taylor, M. G., Meade, M. R., Babler, B. L., Indebetouw, R., Watson, C., Whitney, B. A., Wolfire, M. G., Bania, T. M., Benjamin, R. A., Clemens, D. P., Cohen, M., Cyganowski, C. J., Jackson, J. M., Kobulnicky, H. A., Mathis, J. S., Mercer, E. P., Stolovy, S. R., Uzpen, B., Watson, D. F., Wolff, M. J., Oct. 2006. The Bubbling Galactic Disk. Astrophysical Journal 649, 759–778.

Churchwell, E., Watson, D. F., Povich, M. S., Taylor, M. G., Babler, B. L., Meade, M. R., Benjamin, R. A., Indebetouw, R., Whitney, B. A., Nov. 2007. The Bubbling Galactic Disk. II. The Inner 20^{deg}. Astrophysical Journal 670, 428–441.

Codella, C., Lorenzani, A., Gallego, A. T., Cesaroni, R., Moscadelli, L., May 2004. VizieR Online Data Catalog: Maser and outflows in UC HII region (Codella+, 2004). VizieR Online Data Catalog 341, 70615.

Cox, N. L. J., Kerschbaum, F., van Marle, A.-J., Decin, L., Ladjal, D., Mayer, A., Groenewegen, M. A. T., van Eck, S., Royer, P., Ottensamer, R., Ueta, T., Jorissen, A., Mecina, M., Meliani, Z., Luntzer, A., Blommaert, J. A. D. L., Posch, T., Vandenbussche, B., Waelkens, C., Jan. 2012. A far-infrared survey of bow shocks and detached shells around AGB stars and red supergiants. Astronomy & Astrophysics 537, A35.

Cutri, R. M., et al., 2012. WISE All-Sky Data Release (Cutri+ 2012). VizieR Online Data Catalog 2311, 0.

Davidson, K., Jun. 1987. The relation between apparent temperature and mass-loss rate in hypergiant eruptions. Astrophysical Journal 317, 760–764.

de Graauw, T., Helmich, F. P., Phillips, T. G., Stutzki, J., Caux, E., Whyborn, N. D., Dieleman, P., Roelfsema, P. R., Aarts, H., Assendorp, R., Bachiller, R., Baechtold, W., Barcia, A., Beintema, D. A., Belitsky, V., Benz, A. O., Bieber, R., Boogert, A., Borys, C., Bumble, B., Caïs, P., Caris, M., Cerulli-Irelli, P., Chattopadhyay, G., Cherednichenko, S., Ciechanowicz, M., Coeur-Joly, O., Comito, C., Cros, A., de Jonge, A., de Lange, G., Delforges, B., Delorme, Y., den Boggende, T., Desbat, J.-M., Diez-González, C., di Giorgio, A. M., Dubbeldam, L., Edwards, K., Eggens, M., Erickson, N., Evers, J., Fich, M., Finn, T., Franke, B., Gaier, T., Gal, C., Gao, J. R., Gallego, J.-D., Gauffre, S., Gill, J. J., Glenz, S., Golstein, H., Goulooze, H., Gunsing, T., Güsten, R., Hartogh, P., Hatch, W. A., Higgins, R., Honingh, E. C., Huisman, R., Jackson, B. D., Jacobs, H., Jacobs, K., Jarchow, C., Javadi, H., Jellema, W., Justen, M., Karpov, A., Kasemann, C., Kawamura, J., Keizer, G., Kester, D., Klapwijk, T. M., Klein, T., Kollberg, E., Kooi, J., Kooiman, P.-P., Kopf, B., Krause, M., Krieg, J.-M., Kramer, C., Kruizenga, B., Kuhn, T., Laauwen, W., Lai, R., Larsson, B., Leduc, H. G., Leinz, C., Lin, R. H., Liseau, R., Liu, G. S., Loose, A., López-Fernandez, I., Lord, S., Luinge, W., Marston, A., Martín-Pintado, J., Maestrini, A., Maiwald, F. W., McCoey, C., Mehdi, I., Megej, A., Melchior, M., Meinsma, L., Merkel, H., Michalska, M., Monstein, C., Moratschke, D., Morris, P., Muller, H., Murphy, J. A., Naber, A., Natale, E., Nowosielski, W., Nuzzolo, F., Olberg, M., Olbrich, M., Orfei, R., Orleanski, P., Ossenkopf, V., Peacock, T.,

Pearson, J. C., Peron, I., Phillip-May, S., Piazzo, L., Planesas, P., Rataj, M., Ravera, L., Risacher, C., Salez, M., Samoska, L. A., Saraceno, P., Schieder, R., Schlecht, E., Schlöder, F., Schmülling, F., Schultz, M., Schuster, K., Siebertz, O., Smit, H., Szczerba, R., Shipman, R., Steinmetz, E., Stern, J. A., Stokroos, M., Teipen, R., Teyssier, D., Tils, T., Trappe, N., van Baaren, C., van Leeuwen, B.-J., van de Stadt, H., Visser, H., Wildeman, K. J., Wafelbakker, C. K., Ward, J. S., Wesselius, P., Wild, W., Wulff, S., Wunsch, H.-J., Tielens, X., Zaal, P., Zirath, H., Zmuidzinas, J., Zwart, F., Jul. 2010. The Herschel-Heterodyne Instrument for the Far-Infrared (HIFI). Astronomy & Astrophysics 518, L6.

Deharveng, L., Lefloch, B., Zavagno, A., Caplan, J., Whitworth, A. P., Nadeau, D., Martín, S., Sep. 2003. Triggered massive-star formation at the border of the H II Region Sh 104 408, L25–L28.

Deharveng, L., Zavagno, A., Caplan, J., Apr. 2005. Triggered massive-star formation on the borders of Galactic H II regions. I. A search for "collect and collapse" candidates. Astronomy & Astrophysics 433, 565–577.

Desert, F.-X., Boulanger, F., Puget, J. L., Oct. 1990. Interstellar dust models for extinction and emission. Astronomy & Astrophysics 237, 215–236.

Doi, Y., Komugi, S., Kawada, M., Takita, S., Arimatsu, K., Ikeda, N., Kato, D., Kitamura, Y., Nakagawa, T., Ootsubo, T., Morishima, T., Hattori, M., Tanaka, M., White, G. J., Etxaluze, M., Shibai, H., Nov. 2012. Akari Far-Infrared All-Sky Survey Maps. Publication of Korean Astronomical Society 27, 111–116.

Doi, Y., Takita, S., Ootsubo, T., Arimatsu, K., Tanaka, M., Kitamura, Y., Kawada, M., Matsuura, S., Nakagawa, T., Morishima, T., Hattori, M., Komugi, S., White, G. J., Ikeda, N., Kato, D., Chinone, Y., Etxaluze, M., Cypriano, E. F., Jun. 2015. The AKARI far-infrared all-sky survey maps. pasj 67, 50.

Draine, B. T., 2011. Physics of the Interstellar and Intergalactic Medium. Princeton University Press, 2011. ISBN: 978-0-691-12214-4.

Draine, B. T., Lee, H. M., Oct. 1984. Optical properties of interstellar graphite and silicate grains. Astrophysical Journal 285, 89–108.

Dyson, J. E., Williams, D. A., 1997. The physics of the interstellar medium.

Egan, M. P., Price, S. D., Kraemer, K. E., Mizuno, D. R., Carey, S. J., Wright, C. O., Engelke, C. W., Cohen, M., Gugliotti, M. G., 2003. MSX6C Infrared Point Source Catalog. The Midcourse Space Experiment Point Source Catalog Version 2.3 (October 2003). VizieR Online Data Catalog 5114, 0.

Egan, M. P., Shipman, R. F., Price, S. D., Carey, S. J., Clark, F. O., Cohen, M., Feb. 1998. A Population of Cold Cores in the Galactic Plane. Astrophysical Journal Letters 494, L199.

Elia, D., Molinari, S., Fukui, Y., Schisano, E., Olmi, L., Veneziani, M., Hayakawa, T., Pestalozzi, M., Schneider, N., Benedettini, M., di Giorgio, A. M., Ikhenaode, D., Mizuno, A., Onishi, T., Pezzuto, S., Piazzo, L., Polychroni, D., Rygl, K. L. J., Yamamoto, H., Maruccia, Y., Jul. 2013. The First Hi-GAL Observations of the Outer Galaxy: A Look at Star Formation in the Third Galactic Quadrant in the Longitude Range $216.5° < l < 225.5°$. Astrophysical Journal 772, 45.

Elia, D., Schisano, E., Molinari, S., Robitaille, T., Anglés-Alcázar, D., Bally, J., Battersby, C., Benedettini, M., Billot, N., Calzoletti, L., di Giorgio, A. M., Faustini, F., Li, J. Z., Martin, P., Morgan, L., Motte, F., Mottram, J. C., Natoli, P., Olmi, L., Paladini, R., Piacentini, F., Pestalozzi, M., Pezzuto, S., Polychroni, D., Smith, M. D., Strafella, F., Stringfellow, G. S., Testi, L., Thompson, M. A., Traficante, A., Veneziani, M., Jul. 2010. A Herschel study of YSO evolutionary stages and formation timelines in two fields of the Hi-GAL survey. Astronomy & Astrophysics 518, L97.

Elitzur, M., Ivezić, Ž., Oct. 2001. Dusty winds - I. Self-similar solutions. Monthly Notices of the Royal Astronomical Society 327, 403–421.

Elmegreen, B. G., Lada, C. J., Jun. 1977. Sequential formation of subgroups in OB associations. Astrophysical Journal 214, 725–741.

Evans, N. J., Shirley, Y. L., Mueller, K. E., Knez, C., Oct. 2002. The Formation and Early Evolution of Massive Stars. In: Crowther, P. (Ed.), Hot Star Workshop III: The Earliest Phases of Massive Star Birth. Vol. 267 of Astronomical Society of the Pacific Conference Series. p. 17.

Feast, M. W., Jan. 1996. The pulsation, temperatures and metallicities of Mira and semiregular variables in different stellar systems. Monthly Notices of the Royal Astronomical Society 278, 11–21.

Felli, M., Testi, L., Schuller, F., Omont, A., Sep. 2002. Young massive stars in the ISOGAL survey. II. The catalogue of bright YSO candidates. Astronomy & Astrophysics 392, 971–990.

Giveon, U., Becker, R. H., Helfand, D. J., White, R. L., Jul. 2005. A New Catalog of Radio Compact H II Regions in the Milky Way. II. The 1.4 GHz Data. Astronomical Journal 130, 156–164.

Gray, D. F., Sep. 2005. The Observation and Analysis of Stellar Photospheres. Cambridge University Press, 2005.

Griffin, M. J., Abergel, A., Abreu, A., Ade, P. A. R., André, P., Augueres, J.-L., Babbedge, T., Bae, Y., Baillie, T., Baluteau, J.-P., Barlow, M. J., Bendo, G., Benielli, D., Bock, J. J., Bonhomme, P., Brisbin, D., Brockley-Blatt, C., Caldwell, M., Cara, C., Castro-Rodriguez, N., Cerulli, R., Chanial, P., Chen, S., Clark, E., Clements, D. L., Clerc, L., Coker, J., Communal, D., Conversi, L., Cox, P., Crumb, D., Cunningham, C., Daly, F., Davis, G. R., de Antoni, P., Delderfield, J., Devin, N., di Giorgio, A., Didschuns, I., Dohlen, K., Donati, M., Dowell, A., Dowell, C. D., Duband, L., Dumaye, L., Emery, R. J., Ferlet, M., Ferrand, D., Fontignie, J., Fox, M., Franceschini, A., Frerking, M., Fulton, T., Garcia, J., Gastaud, R., Gear, W. K., Glenn, J., Goizel, A., Griffin, D. K., Grundy, T., Guest, S., Guillemet, L., Hargrave, P. C., Harwit, M., Hastings, P., Hatziminaoglou, E., Herman, M., Hinde, B., Hristov, V., Huang, M., Imhof, P., Isaak, K. J., Israelsson, U., Ivison, R. J., Jennings, D., Kiernan, B., King, K. J., Lange, A. E., Latter, W., Laurent, G., Laurent, P., Leeks, S. J., Lellouch, E., Levenson, L., Li, B., Li, J., Lilienthal, J., Lim, T., Liu, S. J., Lu, N., Madden, S., Mainetti, G., Marliani, P., McKay, D., Mercier, K., Molinari, S., Morris, H., Moseley, H., Mulder, J., Mur, M., Naylor, D. A., Nguyen, H., O'Halloran, B., Oliver, S., Olofsson, G., Olofsson, H.-G., Orfei, R., Page, M. J., Pain, I., Panuzzo, P., Papageorgiou, A., Parks, G., Parr-Burman, P., Pearce, A., Pearson, C., Pérez-Fournon, I., Pinsard, F., Pisano, G., Podosek, J., Pohlen, M., Polehampton, E. T., Pouliquen, D., Rigopoulou, D., Rizzo, D., Roseboom, I. G., Roussel, H., Rowan-Robinson, M., Rownd, B., Saraceno, P., Sauvage, M., Sav-

age, R., Savini, G., Sawyer, E., Scharmberg, C., Schmitt, D., Schneider, N., Schulz, B., Schwartz, A., Shafer, R., Shupe, D. L., Sibthorpe, B., Sidher, S., Smith, A., Smith, A. J., Smith, D., Spencer, L., Stobie, B., Sudiwala, R., Sukhatme, K., Surace, C., Stevens, J. A., Swinyard, B. M., Trichas, M., Tourette, T., Triou, H., Tseng, S., Tucker, C., Turner, A., Vaccari, M., Valtchanov, I., Vigroux, L., Virique, E., Voellmer, G., Walker, H., Ward, R., Waskett, T., Weilert, M., Wesson, R., White, G. J., Whitehouse, N., Wilson, C. D., Winter, B., Woodcraft, A. L., Wright, G. S., Xu, C. K., Zavagno, A., Zemcov, M., Zhang, L., Zonca, E., Jul. 2010. The Herschel-SPIRE instrument and its in-flight performance. Astronomy & Astrophysics 518, L3.

Groenewegen, M. A. T., Whitelock, P. A., Aug. 1996. A revised period-luminosity relation for carbon Miras. Monthly Notices of the Royal Astronomical Society 281, 1347–1351.

Guandalini, R., Busso, M., Sep. 2008. Infrared photometry and evolution of mass-losing AGB stars. II. Luminosity and colors of MS and S stars. Astronomy & Astrophysics 488, 675–684.

Habing, H. J., Olofsson, H. (Eds.), 2003. Asymptotic giant branch stars. Asymptotic giant branch stars, by Harm J. Habing and Hans Olofsson. Astronomy and astrophysics library, New York, Berlin: Springer, 2003.

Hanner, M., Sep. 1988. Grain optical properties. Tech. rep.

Herwig, F., Sep. 2005. Evolution of Asymptotic Giant Branch Stars. Annual Review of Astronomy & Astrophysics 43, 435–479.

Hoare, M. G., Lumsden, S. L., Oudmaijer, R. D., Busfield, A. L., King, T. L., Moore, T. L. J., Dec. 2004. The RMS Survey: A Systematic Search for Massive Young Stars in the Galaxy. In: Clemens, D., Shah, R., Brainerd, T. (Eds.), Milky Way Surveys: The Structure and Evolution of our Galaxy. Vol. 317 of Astronomical Society of the Pacific Conference Series. p. 156.

Ishihara, D., Kaneda, H., Onaka, T., Ita, Y., Matsuura, M., Matsunaga, N., Oct. 2011. Galactic distributions of carbon- and oxygen-rich AGB stars revealed by the AKARI mid-infrared all-sky survey. Astronomy & Astrophysics 534, A79.

Ita, Y., Matsuura, M., Ishihara, D., Oyabu, S., Takita, S., Kataza, H., Yamamura, I., Matsunaga, N., Tanabé, T., Nakada, Y., Fujiwara, H., Wada, T., Onaka, T., Matsuhara,

H., May 2010. AKARI's infrared view on nearby stars. Using AKARI infrared camera all-sky survey, 2MASS, and Hipparcos catalogs. Astronomy & Astrophysics 514, A2.

Ivezic, Z., Elitzur, M., 1994. Infrared Emission and Dynamics of Outflows in Late-Type Stars. In: Caillault, J.-P. (Ed.), Cool Stars, Stellar Systems, and the Sun. Vol. 64 of Astronomical Society of the Pacific Conference Series. p. 711.

Ivezic, Z., Elitzur, M., Jun. 1997. Self-similarity and scaling behaviour of infrared emission from radiatively heated dust - I. Theory. Monthly Notices of the Royal Astronomical Society 287, 799–811.

Ivezic, Z., Nenkova, M., Elitzur, M., Oct. 1999. User Manual for DUSTY. ArXiv Astrophysics e-prints.

Jacoby, G. H., Van de Steene, G., May 2004. Planetary nebulae near the Galactic center: Identifications. Astronomy & Astrophysics 419, 563–582.

Jiménez-Esteban, F. M., García-Lario, P., Engels, D., Perea Calderón, J. V., Feb. 2006. An infrared study of galactic OH/IR stars. II. The "GLMP sample" of red oxygen-rich AGB stars. Astronomy & Astrophysics 446, 773–783.

Jura, M., Kleinmann, S. G., Aug. 1990. Mass-losing M supergiants in the solar neighborhood. Astrophysical Journal Supplement 73, 769–780.

Justtanont, K., Tielens, A. G. G. M., Apr. 1992. Mass loss from OH/IR stars - Models for the infrared emission of circumstellar dust shells. Astrophysical Journal 389, 400–412.

Kang, M., Bieging, J. H., Povich, M. S., Lee, Y., Nov. 2009. Embedded Young Stellar Object Candidates in the Active Star-Forming Complex W51: Mass Function and Spatial Distribution. Astrophysical Journal 706, 83–93.

Karakas, A. I., 2010. Nucleosynthesis of Low and Intermediate-mass Stars. In: Goswami, A., Reddy, B. E. (Eds.), Principles and Perspectives in Cosmochemistry. p. 107.

Kawada, M., Baba, H., Barthel, P. D., Clements, D., Cohen, M., Doi, Y., Figueredo, E., Fujiwara, M., Goto, T., Hasegawa, S., Hibi, Y., Hirao, T., Hiromoto, N., Jeong, W.-S., Kaneda, H., Kawai, T., Kawamura, A., Kester, D., Kii, T., Kobayashi, H., Kwon, S. M., Lee, H. M., Makiuti, S., Matsuo, H., Matsuura, S., Müller, T. G., Murakami, N., Nagata, H., Nakagawa, T., Narita, M., Noda, M., Oh, S. H., Okada, Y., Okuda,

H., Oliver, S., Ootsubo, T., Pak, S., Park, Y.-S., Pearson, C. P., Rowan-Robinson, M., Saito, T., Salama, A., Sato, S., Savage, R. S., Serjeant, S., Shibai, H., Shirahata, M., Sohn, J., Suzuki, T., Takagi, T., Takahashi, H., Thomson, M., Usui, F., Verdugo, E., Watabe, T., White, G. J., Wang, L., Yamamura, I., Yamauchi, C., Yasuda, A., Oct. 2007. The Far-Infrared Surveyor (FIS) for AKARI. pasj 59, 389.

Kim, S.-H., Martin, P. G., Hendry, P. D., Feb. 1994. The size distribution of interstellar dust particles as determined from extinction. Astrophysical Journal 422, 164–175.

Kimeswenger, S., Oct. 2001. Optical Coordinates of Southern Planetary Nebulae. Revista Mexicana de Astronomia y Astrofisica 37, 115–145.

Kohoutek, L., Kühl, D., Jul. 2002. Accurate coordinates of planetary nebulae. Astronomische Nachrichten 323, 484–487.

Kolpak, M. A., Jackson, J. M., Bania, T. M., Clemens, D. P., Dickey, J. M., Jan. 2003. Resolving the Kinematic Distance Ambiguity toward Galactic H II Regions. Astrophysical Journal 582, 756–769.

Krumholz, M. R., McKee, C. F., Feb. 2008. A minimum column density of 1gcm^{-2} for massive star formation. Nature451, 1082–1084.

Kurtz, S., 2005. Hypercompact HII regions. In: Cesaroni, R., Felli, M., Churchwell, E., Walmsley, M. (Eds.), Massive Star Birth: A Crossroads of Astrophysics. Vol. 227 of IAU Symposium. pp. 111–119.

Kurtz, S., Cesaroni, R., Churchwell, E., Hofner, P., Walmsley, C. M., May 2000. Hot Molecular Cores and the Earliest Phases of High-Mass Star Formation. Protostars and Planets IV, 299–326.

Kurtz, S., Churchwell, E., Wood, D. O. S., Apr. 1994. Ultracompact H II regions. 2: New high-resolution radio images. Astrophysical Journal Supplement 91, 659–712.

Kwok, S., Apr. 1994. Planetary nebulae: A modern view. Publications of the Astronomical Society of the Pacific 106, 344–355.

Lada, C. J., 1988. Infrared Energy Distributions and the Nature of Young Stellar Objects. In: Dupree, A. K., Lago, M. T. V. T. (Eds.), NATO ASIC Proc. 241: Formation and Evolution of Low Mass Stars. p. 93.

Lamarre, J. M., Ade, P. R., Benoît, A., de Bernardis, P., Bock, J., Bouchet, F., Bradshaw, T., Charra, J., Church, S., Couchot, F., Delabrouille, J., Efstathiou, G., Giard, M., Giraud-Héraud, Y., Gispert, R., Griffin, M., Lange, A., Murphy, A., Pajot, F., Puget, J. L., Ristorcelli, I., 2000. The High Frequency Instrument of Planck: Design and Performances. Astrophysical Letters and Communications 37, 161.

Le Bertre, T., Aug. 1992. Carbon-star lightcurves in the 1-20 micron range. Astronomy and Astrophysics Supplement 94, 377–398.

Le Bertre, T., Aug. 1997. Optical and infrared observations of 23 carbon-rich stars. Modelling of the circumstellar dust shells. Astronomy & Astrophysics 324, 1059–1070.

Le Bertre, T., Gougeon, S., Le Sidaner, P., Jul. 1995. The properties of the dust in the circumstellar environment of GL 3068. Astronomy & Astrophysics 299, 791.

Le Bertre, T., Tanaka, M., Yamamura, I., Murakami, H., Jun. 2003a. Galactic mass-losing AGB stars probed with the IRTS. II. Astronomy & Astrophysics 403, 943–954.

Le Bertre, T., Tanaka, M., Yamamura, I., Murakami, H., Jun. 2003b. Galactic mass-losing AGB stars probed with the IRTS. II. Astronomy & Astrophysics 403, 943–954.

Le Bertre, T., Winters, J. M., Jun. 1998. On the relations between infrared colors and mass loss rates for Mira stars. Astronomy & Astrophysics 334, 173–180.

Le Sidaner, P., Le Bertre, T., Oct. 1993. Optical and infrared observations of two oxygen-rich miras: Dust shell modelling as a function of phase. Astronomy & Astrophysics 278, 167–178.

Lian, J., Zhu, Q., Kong, X., He, J., Apr. 2014. Characterizing AGB stars in Wide-field Infrared Survey Explorer (WISE) bands. Astronomy & Astrophysics 564, A84.

Lindqvist, M., Winnberg, A., Habing, H. J., Matthews, H. E., Jan. 1992. OH/IR stars close to the Galactic Centre. I - Observational data. Astronomy and Astrophysics Supplement 92, 43–62.

Loup, C., Forveille, T., Omont, A., Paul, J. F., Jun. 1993. CO and HCN observations of circumstellar envelopes. A catalogue - Mass loss rates and distributions. Astronomy and Astrophysics Supplement 99, 291–377.

Lumsden, S. L., Hoare, M. G., Oudmaijer, R. D., Richards, D., Oct. 2002. The population of the Galactic plane as seen by MSX. Monthly Notices of the Royal Astronomical Society 336, 621–636.

Lumsden, S. L., Hoare, M. G., Urquhart, J. S., Oudmaijer, R. D., Davies, B., Mottram, J. C., Cooper, H. D. B., Moore, T. J. T., Sep. 2013. The Red MSX Source Survey: The Massive Young Stellar Population of Our Galaxy. Astrophysical Journal Supplement 208, 11.

Magnier, E. A., Volp, A. W., Laan, K., van den Ancker, M. E., Waters, L. B. F. M., Dec. 1999. Transitional YSOs: candidates from flat-spectrum IRAS sources. Astronomy & Astrophysics 352, 228–238.

Marengo, M., 2000. Mid-ir observations and modeling of astrophysical dust agb circumstellar envelopes and icm dust. Ph.D. thesis, International School for Advanced Studies (SISSA/ISAS).

Marigo, P., Girardi, L., Bressan, A., Apr. 1999. The third dredge-up and the carbon star luminosity functions in the Magellanic Clouds. Astronomy & Astrophysics 344, 123–142.

Marshall, D. J., Robin, A. C., Reylé, C., Schultheis, M., Picaud, S., Jul. 2006. Modelling the Galactic interstellar extinction distribution in three dimensions. Astronomy & Astrophysics 453, 635–651.

Mathis, J. S., Rumpl, W., Nordsieck, K. H., Oct. 1977. The size distribution of interstellar grains. Astrophysical Journal 217, 425–433.

Matteucci, F., Greggio, L., Jan. 1986. Relative roles of type I and II supernovae in the chemical enrichment of the interstellar gas. Astronomy & Astrophysics 154, 279–287.

Miszalski, B., Acker, A., Moffat, A. F. J., Parker, Q. A., Udalski, A., Mar. 2009. Binary planetary nebulae nuclei towards the Galactic bulge. I. Sample discovery, period distribution, and binary fraction. Astronomy & Astrophysics 496, 813–825.

Miszalski, B., Parker, Q. A., Acker, A., Birkby, J. L., Frew, D. J., Kovacevic, A., Feb. 2008. MASH-II: more planetary nebulae from the AAO/UKST Hα survey. Monthly Notices of the Royal Astronomical Society 384, 525–534.

Miville-Deschênes, M.-A., Lagache, G., Apr. 2005. IRIS: A New Generation of IRAS Maps. Astrophysical Journal Supplement 157, 302–323.

Molinari, S., Brand, J., Cesaroni, R., Palla, F., Apr. 1996. Ammonia on YSOs IRAS sources (Molinari+ 1996). VizieR Online Data Catalog 330, 80573.

Molinari, S., Brand, J., Cesaroni, R., Palla, F., Palumbo, G. G. C., May 1998. VizieR Online Data Catalog: VLA observations of ultracompact HII regions (Molinari+ 1998). VizieR Online Data Catalog 333, 60339.

Molinari, S., Schisano, E., Faustini, F., Pestalozzi, M., di Giorgio, A. M., Liu, S., Jun. 2011. Source extraction and photometry for the far-infrared and sub-millimeter continuum in the presence of complex backgrounds. Astronomy & Astrophysics 530, A133.

Molinari, S., Swinyard, B., Bally, J., Barlow, M., Bernard, J.-P., Martin, P., Moore, T., Noriega-Crespo, A., Plume, R., Testi, L., Zavagno, A., Abergel, A., Ali, B., Anderson, L., André, P., Baluteau, J.-P., Battersby, C., Beltrán, M. T., Benedettini, M., Billot, N., Blommaert, J., Bontemps, S., Boulanger, F., Brand, J., Brunt, C., Burton, M., Calzoletti, L., Carey, S., Caselli, P., Cesaroni, R., Cernicharo, J., Chakrabarti, S., Chrysostomou, A., Cohen, M., Compiegne, M., de Bernardis, P., de Gasperis, G., di Giorgio, A. M., Elia, D., Faustini, F., Flagey, N., Fukui, Y., Fuller, G. A., Ganga, K., Garcia-Lario, P., Glenn, J., Goldsmith, P. F., Griffin, M., Hoare, M., Huang, M., Ikhenaode, D., Joblin, C., Joncas, G., Juvela, M., Kirk, J. M., Lagache, G., Li, J. Z., Lim, T. L., Lord, S. D., Marengo, M., Marshall, D. J., Masi, S., Massi, F., Matsuura, M., Minier, V., Miville-Deschênes, M.-A., Montier, L. A., Morgan, L., Motte, F., Mottram, J. C., Müller, T. G., Natoli, P., Neves, J., Olmi, L., Paladini, R., Paradis, D., Parsons, H., Peretto, N., Pestalozzi, M., Pezzuto, S., Piacentini, F., Piazzo, L., Polychroni, D., Pomarès, M., Popescu, C. C., Reach, W. T., Ristorcelli, I., Robitaille, J.-F., Robitaille, T., Rodón, J. A., Roy, A., Royer, P., Russeil, D., Saraceno, P., Sauvage, M., Schilke, P., Schisano, E., Schneider, N., Schuller, F., Schulz, B., Sibthorpe, B., Smith, H. A., Smith, M. D., Spinoglio, L., Stamatellos, D., Strafella, F., Stringfellow, G. S., Sturm, E., Taylor, R., Thompson, M. A., Traficante, A., Tuffs, R. J., Umana, G., Valenziano, L., Vavrek, R., Veneziani, M., Viti, S., Waelkens, C., Ward-Thompson, D., White, G., Wilcock, L. A., Wyrowski, F., Yorke, H. W., Zhang, Q., Jul. 2010a. Clouds, filaments,

and protostars: The Herschel Hi-GAL Milky Way. Astronomy & Astrophysics 518, L100.

Molinari, S., Swinyard, B., Bally, J., Barlow, M., Bernard, J.-P., Martin, P., Moore, T., Noriega-Crespo, A., Plume, R., Testi, L., Zavagno, A., Abergel, A., Ali, B., André, P., Baluteau, J.-P., Benedettini, M., Berné, O., Billot, N. P., Blommaert, J., Bontemps, S., Boulanger, F., Brand, J., Brunt, C., Burton, M., Campeggio, L., Carey, S., Caselli, P., Cesaroni, R., Cernicharo, J., Chakrabarti, S., Chrysostomou, A., Codella, C., Cohen, M., Compiegne, M., Davis, C. J., de Bernardis, P., de Gasperis, G., Di Francesco, J., di Giorgio, A. M., Elia, D., Faustini, F., Fischera, J. F., Fukui, Y., Fuller, G. A., Ganga, K., Garcia-Lario, P., Giard, M., Giardino, G., Glenn, J. ., Goldsmith, P., Griffin, M., Hoare, M., Huang, M., Jiang, B., Joblin, C., Joncas, G., Juvela, M., Kirk, J., Lagache, G., Li, J. Z., Lim, T. L., Lord, S. D., Lucas, P. W., Maiolo, B., Marengo, M., Marshall, D., Masi, S., Massi, F., Matsuura, M., Meny, C., Minier, V., Miville-Deschênes, M.-A., Montier, L., Motte, F., Müller, T. G., Natoli, P., Neves, J., Olmi, L., Paladini, R., Paradis, D., Pestalozzi, M., Pezzuto, S., Piacentini, F., Pomarès, M., Popescu, C. C., Reach, W. T., Richer, J., Ristorcelli, I., Roy, A., Royer, P., Russeil, D., Saraceno, P., Sauvage, M., Schilke, P., Schneider-Bontemps, N., Schuller, F., Schultz, B., Shepherd, D. S., Sibthorpe, B., Smith, H. A., Smith, M. D., Spinoglio, L., Stamatellos, D., Strafella, F., Stringfellow, G., Sturm, E., Taylor, R., Thompson, M. A., Tuffs, R. J., Umana, G., Valenziano, L., Vavrek, R., Viti, S., Waelkens, C., Ward-Thompson, D., White, G., Wyrowski, F., Yorke, H. W., Zhang, Q., Mar. 2010b. Hi-GAL: The Herschel Infrared Galactic Plane Survey. Publications of the Astronomical Society of the Pacific 122, 314–325.

Mottram, J. C., Hoare, M. G., Lumsden, S. L., Oudmaijer, R. D., Urquhart, J. S., Sheret, T. L., Clarke, A. J., Allsopp, J., Dec. 2007. The RMS survey: mid-infrared observations of candidate massive YSOs in the southern hemisphere. Astronomy & Astrophysics 476, 1019–1111.

Mottram, J. C., Hoare, M. G., Urquhart, J. S., Lumsden, S. L., Oudmaijer, R. D., Robitaille, T. P., Moore, T. J. T., Davies, B., Stead, J., Jan. 2011. The Red MSX Source survey: the bolometric fluxes and luminosity distributions of young massive stars. Astronomy & Astrophysics 525, A149.

Müller, T., Balog, Z., Nielbock, M., Lim, T., Teyssier, D., Olberg, M., Klaas, U., Linz, H., Altieri, B., Pearson, C., Bendo, G., Vilenius, E., Jul. 2014. Herschel celestial calibration sources. Four large main-belt asteroids as prime flux calibrators for the far-IR/sub-mm range. Experimental Astronomy 37, 253–330.

Ojha, D. K., Tej, A., Schultheis, M., Omont, A., Schuller, F., Nov. 2007. High mass-loss asymptotic giant branch stars detected by the Midcourse Space Experiment in the 'intermediate' and 'outer' Galactic bulge. Monthly Notices of the Royal Astronomical Society 381, 1219–1234.

Onaka, T., Matsuhara, H., Wada, T., Fujishiro, N., Fujiwara, H., Ishigaki, M., Ishihara, D., Ita, Y., Kataza, H., Kim, W., Matsumoto, T., Murakami, H., Ohyama, Y., Oyabu, S., Sakon, I., Tanabé, T., Takagi, T., Uemizu, K., Ueno, M., Usui, F., Watarai, H., Cohen, M., Enya, K., Ootsubo, T., Pearson, C. P., Takeyama, N., Yamamuro, T., Ikeda, Y., Oct. 2007. The Infrared Camera (IRC) for AKARI – Design and Imaging Performance. pasj 59, 401.

Ortiz, R., Lorenz-Martins, S., Maciel, W. J., Rangel, E. M., Feb. 2005. Evolution from AGB to planetary nebula in the MSX survey. Astronomy & Astrophysics 431, 565–574.

Ossenkopf, V., Henning, T., Mathis, J. S., Aug. 1992. Constraints on cosmic silicates. Astronomy & Astrophysics 261, 567–578.

Paladini, R., Umana, G., Veneziani, M., Noriega-Crespo, A., Anderson, L. D., Piacentini, F., Pinheiro Gonçalves, D., Paradis, D., Tibbs, C. T., Bernard, J.-P., Natoli, P., Dec. 2012. Spitzer and Herschel Multiwavelength Characterization of the Dust Content of Evolved H II Regions. Astrophysical Journal 760, 149.

Parker, Q. A., Acker, A., Frew, D. J., Hartley, M., Peyaud, A. E. J., Ochsenbein, F., Phillipps, S., Russeil, D., Beaulieu, S. F., Cohen, M., Köppen, J., Miszalski, B., Morgan, D. H., Morris, R. A. H., Pierce, M. J., Vaughan, A. E., Nov. 2006. The Macquarie/AAO/Strasbourg Hα Planetary Nebula Catalogue: MASH. Monthly Notices of the Royal Astronomical Society 373, 79–94.

Pegourie, B., Apr. 1988. Optical properties of alpha silicon carbide. Astronomy & Astrophysics 194, 335–339.

Pezzuto, 16-19 November 2010. a new approach to the detection of outliers with the sigma-clipping method applied to pacs photometry observation. Poster presented at The impact of Herschel surveys on ALMA Early Science Garching.

Pilbratt, G. L., Riedinger, J. R., Passvogel, T., Crone, G., Doyle, D., Gageur, U., Heras, A. M., Jewell, C., Metcalfe, L., Ott, S., Schmidt, M., Jul. 2010. Herschel Space Observatory. An ESA facility for far-infrared and submillimetre astronomy. Astronomy & Astrophysics 518, L1.

Poglitsch, A., Waelkens, C., Geis, N., Feuchtgruber, H., Vandenbussche, B., Rodriguez, L., Krause, O., Renotte, E., van Hoof, C., Saraceno, P., Cepa, J., Kerschbaum, F., Agnèse, P., Ali, B., Altieri, B., Andreani, P., Augueres, J.-L., Balog, Z., Barl, L., Bauer, O. H., Belbachir, N., Benedettini, M., Billot, N., Boulade, O., Bischof, H., Blommaert, J., Callut, E., Cara, C., Cerulli, R., Cesarsky, D., Contursi, A., Creten, Y., De Meester, W., Doublier, V., Doumayrou, E., Duband, L., Exter, K., Genzel, R., Gillis, J.-M., Grözinger, U., Henning, T., Herreros, J., Huygen, R., Inguscio, M., Jakob, G., Jamar, C., Jean, C., de Jong, J., Katterloher, R., Kiss, C., Klaas, U., Lemke, D., Lutz, D., Madden, S., Marquet, B., Martignac, J., Mazy, A., Merken, P., Montfort, F., Morbidelli, L., Müller, T., Nielbock, M., Okumura, K., Orfei, R., Ottensamer, R., Pezzuto, S., Popesso, P., Putzeys, J., Regibo, S., Reveret, V., Royer, P., Sauvage, M., Schreiber, J., Stegmaier, J., Schmitt, D., Schubert, J., Sturm, E., Thiel, M., Tofani, G., Vavrek, R., Wetzstein, M., Wieprecht, E., Wiezorrek, E., Jul. 2010. The Photodetector Array Camera and Spectrometer (PACS) on the Herschel Space Observatory. Astronomy & Astrophysics 518, L2.

Polychroni, D., Schisano, E., Elia, D., Roy, A., Molinari, S., Martin, P., André, P., Turrini, D., Rygl, K. L. J., Di Francesco, J., Benedettini, M., Busquet, G., di Giorgio, A. M., Pestalozzi, M., Pezzuto, S., Arzoumanian, D., Bontemps, S., Hennemann, M., Hill, T., Könyves, V., Men'shchikov, A., Motte, F., Nguyen-Luong, Q., Peretto, N., Schneider, N., White, G., Nov. 2013. Two Mass Distributions in the L 1641 Molecular Clouds: The Herschel Connection of Dense Cores and Filaments in Orion A. Astrophysical Journal Letters 777, L33.

Pomarès, M., Zavagno, A., Deharveng, L., Cunningham, M., Jones, P., Kurtz, S., Russeil,

D., Caplan, J., Comerón, F., Feb. 2009. Triggered star formation on the borders of the Galactic Hii region RCW 82. Astronomy & Astrophysics 494, 987–1003.

Povich, M. S., Stone, J. M., Churchwell, E., Zweibel, E. G., Wolfire, M. G., Babler, B. L., Indebetouw, R., Meade, M. R., Whitney, B. A., May 2007. A Multiwavelength Study of M17: The Spectral Energy Distribution and PAH Emission Morphology of a Massive Star Formation Region 660, 346–362.

Povich, M. S., Whitney, B. A., May 2010. Evidence for Delayed Massive Star Formation in the M17 Proto-OB Association. Astrophysical Journal Letters 714, L285–L289.

Rybicki, G. B., Lightman, A. P., 1979. Radiative processes in astrophysics. New York, Wiley-Interscience, 1979. 393 p.

Salaris, M., Cassisi, S., 2006. Evolution of Stars and Stellar Populations.

Savage, R. S., Oliver, S., Jun. 2007. Bayesian Methods of Astronomical Source Extraction. Astrophysical Journal 661, 1339–1346.

Schisano, E., Rygl, K. L. J., Molinari, S., Busquet, G., Elia, D., Pestalozzi, M., Polychroni, D., Billot, N., Carey, S., Paladini, R., Noriega-Crespo, A., Moore, T. J. T., Plume, R., Glover, S. C. O., Vázquez-Semadeni, E., Aug. 2014. The Identification of Filaments on Far-infrared and Submillimiter Images: Morphology, Physical Conditions and Relation with Star Formation of Filamentary Structure. Astrophysical Journal 791, 27.

Schlafly, E. F., Finkbeiner, D. P., Aug. 2011. Measuring Reddening with Sloan Digital Sky Survey Stellar Spectra and Recalibrating SFD. Astrophysical Journal 737, 103.

Schulz, N. S., 2005. From Dust To Stars Studies of the Formation and Early Evolution of Stars.

Seab, C. G., 1988. Grain destruction and growth. In: Bailey, M. E., Williams, D. A. (Eds.), Dust in the Universe. pp. 303–326.

Seab, C. G., Shull, J. M., Dec. 1983. Shock processing of interstellar grains. Astrophysical Journal 275, 652–660.

Sevenster, M. N., May 2002. OH-selected AGB and Post-AGB Objects. I. Infrared and Maser Properties. Astronomical Journal 123, 2772–2787.

Skrutskie, M. F., Cutri, R. M., Stiening, R., Weinberg, M. D., Schneider, S., Carpenter, J. M., Beichman, C., Capps, R., Chester, T., Elias, J., Huchra, J., Liebert, J., Lonsdale, C., Monet, D. G., Price, S., Seitzer, P., Jarrett, T., Kirkpatrick, J. D., Gizis, J. E., Howard, E., Evans, T., Fowler, J., Fullmer, L., Hurt, R., Light, R., Kopan, E. L., Marsh, K. A., McCallon, H. L., Tam, R., Van Dyk, S., Wheelock, S., Feb. 2006. The Two Micron All Sky Survey (2MASS). Astronomical Journal 131, 1163–1183.

Sridharan, T. K., Beuther, H., Schilke, P., Menten, K. M., Wyrowski, F., Feb. 2002. High-Mass Protostellar Candidates. I. The Sample and Initial Results. Astrophysical Journal 566, 931–944.

Stetson, P. B., Mar. 1987. DAOPHOT - A computer program for crowded-field stellar photometry. Publications of the Astronomical Society of the Pacific 99, 191–222.

Suh, K.-W., Kwon, Y.-J., Aug. 2009. A Catalog of AGB Stars in IRAS PSC. Journal of Korean Astronomical Society 42, 81–91.

Suh, K.-W., Kwon, Y.-J., Nov. 2011. Infrared two-colour diagrams for AGB stars using AKARI, MSX, IRAS and near-infrared data. Monthly Notices of the Royal Astronomical Society 417, 3047–3060.

Tauber, J. A., Mandolesi, N., Puget, J.-L., Banos, T., Bersanelli, M., Bouchet, F. R., Butler, R. C., Charra, J., Crone, G., Dodsworth, J., et al., Sep. 2010. Planck pre-launch status: The Planck mission. Astronomy & Astrophysics 520, A1.

Thompson, M. A., Hatchell, J., Walsh, A. J., MacDonald, G. H., Millar, T. J., Jul. 2006. A SCUBA imaging survey of ultracompact HII regions. The environments of massive star formation. Astronomy & Astrophysics 453, 1003–1026.

Tielens, A. G. G. M., Aug. 2005. The Physics and Chemistry of the Interstellar Medium. The Physics and Chemistry of the Interstellar Medium, by A. G. G. M. Tielens, pp. . ISBN 0521826349. Cambridge, UK: Cambridge University Press, 2005.

Traficante, A., Calzoletti, L., Veneziani, M., Ali, B., de Gasperis, G., di Giorgio, A. M., Faustini, F., Ikhenaode, D., Molinari, S., Natoli, P., Pestalozzi, M., Pezzuto, S., Piacentini, F., Piazzo, L., Polenta, G., Schisano, E., Oct. 2011. Data reduction pipeline for the Hi-GAL survey. Monthly Notices of the Royal Astronomical Society 416, 2932–2943.

Urquhart, J. S., Busfield, A. L., Hoare, M. G., Lumsden, S. L., Clarke, A. J., Moore, T. J. T., Mottram, J. C., Oudmaijer, R. D., Jan. 2007a. The RMS survey. Radio observations of candidate massive YSOs in the southern hemisphere. Astronomy & Astrophysics 461, 11–23.

Urquhart, J. S., Busfield, A. L., Hoare, M. G., Lumsden, S. L., Oudmaijer, R. D., Moore, T. J. T., Gibb, A. G., Purcell, C. R., Burton, M. G., Marechal, L. J. L., Nov. 2007b. The RMS survey. ^{13}CO observations of candidate massive YSOs in the southern Galactic plane. Astronomy & Astrophysics 474, 891–901.

Urquhart, J. S., Hoare, M. G., Lumsden, S. L., Oudmaijer, R. D., Moore, T. J. T., Mottram, J. C., Cooper, H. D. B., Mottram, M., Rogers, H. C., Feb. 2012. The RMS survey: resolving kinematic distance ambiguities towards a sample of compact H II regions using H I absorption. Monthly Notices of the Royal Astronomical Society 420, 1656–1672.

Urquhart, J. S., Hoare, M. G., Purcell, C. R., Lumsden, S. L., Oudmaijer, R. D., Moore, T. J. T., Busfield, A. L., Mottram, J. C., Davies, B., Jul. 2009. The RMS survey. 6 cm continuum VLA observations towards candidate massive YSOs in the northern hemisphere. Astronomy & Astrophysics 501, 539–551.

Urquhart, J. S., Thompson, M. A., Moore, T. J. T., Purcell, C. R., Hoare, M. G., Schuller, F., Wyrowski, F., Csengeri, T., Menten, K. M., Lumsden, S. L., Kurtz, S., Walmsley, C. M., Bronfman, L., Morgan, L. K., Eden, D. J., Russeil, D., Oct. 2013. ATLASGAL - properties of compact H II regions and their natal clumps. Monthly Notices of the Royal Astronomical Society 435, 400–428.

van der Veen, W. E. C. J., Habing, H. J., Apr. 1988. The IRAS two-colour diagram as a tool for studying late stages of stellar evolution. Astronomy & Astrophysics 194, 125–134.

Viironen, K., Greimel, R., Corradi, R. L. M., Mampaso, A., Rodríguez, M., Sabin, L., Delgado-Inglada, G., Drew, J. E., Giammanco, C., González-Solares, E. A., Irwin, M. J., Miszalski, B., Parker, Q. A., Rodríguez-Flores, E. R., Zijlstra, A., Sep. 2009. Candidate planetary nebulae in the IPHAS photometric catalogue. Astronomy & Astrophysics 504, 291–301.

Vio, R., Tenorio, L., Wamsteker, W., Aug. 2002. On optimal detection of point sources in CMB maps. Astronomy & Astrophysics 391, 789–794.

Wachter, A., Schröder, K.-P., Winters, J. M., Arndt, T. U., Sedlmayr, E., Mar. 2002. An improved mass-loss description for dust-driven superwinds and tip-AGB evolution models. Astronomy & Astrophysics 384, 452–459.

Walsh, A. J., Burton, M. G., Hyland, A. R., Robinson, G., Dec. 1998. Studies of ultra-compact HII regions - II. High-resolution radio continuum and methanol maser survey. Monthly Notices of the Royal Astronomical Society 301, 640–698.

Watson, C., Povich, M. S., Churchwell, E. B., Babler, B. L., Chunev, G., Hoare, M., Indebetouw, R., Meade, M. R., Robitaille, T. P., Whitney, B. A., Jul. 2008. Infrared Dust Bubbles: Probing the Detailed Structure and Young Massive Stellar Populations of Galactic H II Regions. Astrophysical Journal 681, 1341–1355.

Whittet, D. C. B., 1992. Dust in the galactic environment. Institute of Physics Publishing, 306 p.

Whittet, D. C. B. (Ed.), 2003. Dust in the galactic environment. Bristol: Institute of Physics (IOP) Publishing, 2003 Series in Astronomy and Astrophysics, ISBN 0750306246.

Winters, J. M., Le Bertre, T., Jeong, K. S., Helling, C., Sedlmayr, E., Sep. 2000. A systematic investigation of the mass loss mechanism in dust forming long-period variable stars. Astronomy & Astrophysics 361, 641–659.

Wood, D. O. S., Churchwell, E., Apr. 1989. The morphologies and physical properties of ultracompact H II regions. Astrophysical Journal Supplement 69, 831–895.

Wood, P. R., 1981. The conditions for dredge-up of carbon during the helium shell flash and the production of carbon stars. In: Iben, Jr., I., Renzini, A. (Eds.), Physical Processes in Red Giants. Vol. 88 of Astrophysics and Space Science Library. pp. 135–139.

Wright, N. J., Barlow, M. J., Greimel, R., Drew, J. E., Matsuura, M., Unruh, Y. C., Zijlstra, A. A., Dec. 2009. Near-IR spectra of IPHAS extremely red Galactic AGB stars. Monthly Notices of the Royal Astronomical Society 400, 1413–1426.

Yusef-Zadeh, F., Hewitt, J. W., Arendt, R. G., Whitney, B., Rieke, G., Wardle, M., Hinz, J. L., Stolovy, S., Lang, C. C., Burton, M. G., Ramirez, S., Sep. 2009. Star Formation in the Central 400 pc of the Milky Way: Evidence for a Population of Massive Young Stellar Objects. Astrophysical Journal 702, 178–225.

Zavagno, A., Anderson, L. D., Russeil, D., Morgan, L., Stringfellow, G. S., Deharveng, L., Rodón, J. A., Robitaille, T. P., Mottram, J. C., Schuller, F., Testi, L., Billot, N., Molinari, S., di Gorgio, A., Kirk, J. M., Brunt, C., Ward-Thompson, D., Traficante, A., Veneziani, M., Faustini, F., Calzoletti, L., Jul. 2010a. Star formation triggered by H II regions in our Galaxy. First results for N49 from the Herschel infrared survey of the Galactic plane. Astronomy & Astrophysics 518, L101.

Zavagno, A., Deharveng, L., Comerón, F., Brand, J., Massi, F., Caplan, J., Russeil, D., Jan. 2006. Triggered massive-star formation on the borders of Galactic H II regions. II. Evidence for the collect and collapse process around RCW 79 446, 171–184.

Zavagno, A., Russeil, D., Motte, F., Anderson, L. D., Deharveng, L., Rodón, J. A., Bontemps, S., Abergel, A., Baluteau, J.-P., Sauvage, M., André, P., Hill, T., White, G. J., Jul. 2010b. Star formation triggered by the Galactic H II region RCW 120. First results from the Herschel Space Observatory. Astronomy & Astrophysics 518, L81.

Zhang, K., Jiang, B. W., Li, A., Jul. 2009. On the carriers of the 21μm emission feature in post-asymptotic giant branch stars. Monthly Notices of the Royal Astronomical Society 396, 1247–1256.

Ziurys, L. M., Aug. 2006. The chemistry in circumstellar envelopes of evolved stars: Following the origin of the elements to the origin of life. Proceedings of the National Academy of Science 103, 12274–12279.